DISCRETE AND CONTINUOUS MODELS AND APPLIED COMPUTATIONAL SCIENCE

Volume 34 Number 3 (2026)

Founded in 1993

Founder: PEOPLES' FRIENDSHIP UNIVERSITY OF RUSSIA NAMED AFTER PATRICE LUMUMBA

DOI: 10.22363/2658-4670-2026-34-3

Edition registered by the Federal Service for Supervision of Communications, Information Technology and Mass Media
Registration Certificate: ПИ № ФС 77-76317, 19.07.2019

ISSN 2658-7149 (Online); 2658-4670 (Print)
4 issues per year.
Language: English.

Publisher

Peoples' Friendship University of Russia named after Patrice Lumumba (RUDN University).

Indexed by

- Scopus (https://www.scopus.com),
- Ulrich's Periodicals Directory (http://www.ulrichsweb.com),
- Directory of Open Access Journals (DOAJ) (https://doaj.org),
- Russian Index of Science Citation (https://elibrary.ru),
- RCNI White list.

Aim and Scope

Discrete and Continuous Models and Applied Computational Science arose in 2019 as a continuation of RUDN Journal of Mathematics, Information Sciences and Physics. RUDN Journal of Mathematics, Information Sciences and Physics arose in 2006 as a merger and continuation of the series "Physics", "Mathematics", "Applied Mathematics and Computer Science", "Applied Mathematics and Computer Mathematics".

Discussed issues affecting modern problems of physics, mathematics, queuing theory, the Teletraffic theory, computer science, software and databases development.

It's an international journal regarding both the editorial board and contributing authors as well as research and topics of publications. Its authors are leading researchers possessing PhD and PhDr degrees, and PhD and MA students from Russia and abroad. Articles are indexed in the Russian and foreign databases. Each paper is reviewed by at least two reviewers, the composition of which includes PhDs, are well known in their circles. Author's part of the magazine includes both young scientists, graduate students and talented students, who publish their works, and famous giants of world science.

The Journal is published in accordance with the policies of COPE (Committee on Publication Ethics).

The editors are open to thematic issue initiatives with guest editors. Further information regarding notes for contributors, subscription, and back volumes is available at http://journals.rudn.ru/miph

E-mail: miphj@rudn.ru.

© RUDN University, 2026

Editorial board

Editor-in-Chief

Yury P. Rybakov, Doctor of Sciences in Physics and Mathematics, Professor, Honored Scientist of Russia, Professor of the Institute of Physical Research & Technologies, RUDN University, Moscow, Russia

Vice Editors-in-Chief

Leonid A. Sevastianov, Doctor of Sciences in Physics and Mathematics, Professor, Professor of the Department of Computational Mathematics and Artificial Intelligence, RUDN University, Moscow, Russia

Dmitry S. Kulyabov, Doctor of Sciences in Physics and Mathematics, Docent, Professor of the Department of Probability Theory and Cyber Security, RUDN University, Moscow, Russia

Members of the editorial board

Konstantin E. Samouylov, Doctor of Sciences in Technical Sciences, Professor, Head of Department of Probability Theory and Cyber Security, RUDN University, Moscow, Russia
Yulia V. Gaidamaka, Doctor of Sciences in Physics and Mathematics, Professor, Professor of the Department of Probability Theory and Cyber Security, RUDN University, Moscow, Russia
Gleb Beliakov, PhD, Professor of Mathematics at Deakin University, Melbourne, Australia
Michal Hnatič, DrSc, Professor of Pavol Jozef Safarik University in Košice, Košice, Slovakia
Datta Gupta Subhashish, PhD in Physics and Mathematics, Professor of Hyderabad University, Hyderabad, India
Olli Erkki Martikainen, PhD in Engineering, member of the Research Institute of the Finnish Economy, Helsinki, Finland
Mikhail V. Medvedev, Doctor of Sciences in Physics and Mathematics, Professor of the Kansas University, Lawrence, USA
Raphael Orlando Ramírez Inostroza, PhD, Professor of Rovira i Virgili University (Universitat Rovira i Virgili), Tarragona, Spain
Bijan Saha, Doctor of Sciences in Physics and Mathematics, Leading Researcher in Laboratory of Information Technologies of the Joint Institute for Nuclear Research, Dubna, Russia
Ochbadrah Chuluunbaatar, Doctor of Sciences in Physics and Mathematics, Leading Researcher in the Institute of Mathematics and Digital Technology, Mongolian Academy of Sciences, Ulaanbaatar, Mongolia

Computer Design: *Anna V. Korolkova*, *Dmitry S. Kulyabov*
English Text Editors: *Nikolay E. Nikolaev*, *Ivan S. Zaryadov*, *Konstantin P. Lovetskiy*
Address of editorial board: 3 Ordzhonikidze St, 115419, Moscow, Russia, +7 (495) 955-07-16, e-mail: publishing@rudn.ru
Editorial office: +7 (495) 952-02-50, e-mail: miphj@rudn.ru, site: http://journals.rudn.ru/miph

Approved for printing: 15.09.2026. Published: 25.09.2026.
Paper size 70×100/16. Offset paper. Offset printing. Typeface "Adobe Source."
Conventional printed sheets: 12.17. Printing run 500 copies. Open price. The order: 1021.
PEOPLES' FRIENDSHIP UNIVERSITY OF RUSSIA NAMED AFTER PATRICE LUMUMBA
6 Miklukho-Maklaya St, Moscow, 117198, Russian Federation
Printed at RUDN Publishing House:
3 Ordzhonikidze St, Moscow, 115419, Russian Federation,
+7 (495) 955-08-61; e-mail: publishing@rudn.ru

Discrete & Continuous Models
& Applied Computational Science
ISSN 2658-7149 (Online), 2658-4670 (Print)

2026, 34 (3)
http://journals.rudn.ru/miph

Contents

Editorial

D. S. Kulyabov, A. V. Korolkova, L. A. Sevastianov, Y. P. Rybakov ISO rules for typesetting mathematics: mismath package 283

Computer science

I. E. Ghebrial, I. A. Kochetkova A resource queueing model for equal-rate dynamic spectrum slicing in 5G NR networks 288

I. V. Brak, K. G. Leladze, S. M. Islamova, A. A. Kuzminykh, G. A. Kiselev Reconstructing the volumetric geometry of the cerebral cortex based on magnetic resonance imaging 298

E. A. Khityaev, I. S. Zaryadov, T. A. Milovanova A two-queue JSQ–SLQ service system with absolute preemptive priority and non-zero switch-over times 316

A. A. Tazaeva, E. V. Markova Scenario of priority service for elastic traffic within the network slicing framework 334

D. V. Shilonosov, A. A. Likhtenshtein, V. A. Beschastnyi, Y. V. Gaidamaka An accurate block error rate model for performance analysis of LEO NB-IoT communications systems 345

Modeling and Simulation

A. A. Belov, O. I. Topor, L. V. Borodachev, Z. O. Dombrovskaya Extrapolation of experimental data on thermonuclear reaction cross sections using the global spline method 360

E. B. Laneev, A. M. Gaipova The inverse thermography problem as the inverse potential problem for bodies of constant thickness 369

A. M. Palagashvili, A. M. Ermolayeva, T. R. Velieva Comparative analysis of active queue management algorithms: RED, ARED, Gentle RED 379

M. D. Malykh, I. T. Dulatov, A. L. Sevastianov, Y. Yu On using Rosanes notation to specify quadratic transformations that describe a step of the Kahan difference scheme 396

A. S. Ayriyan, E. A. Ayryan, E. E. Donets, M. P. Veneva Heat-conduction simulation of a wing-like thulium foil for an ion source 408

© RUDN University, 2026

Discrete & Continuous Models
& Applied Computational Science
ISSN 2658-7149 (Online), 2658-4670 (Print)

2026, 34 (3) 283–287
http://journals.rudn.ru/miph

Editorial

DOI: 10.22363/2658-4670-2026-34-3-283-287 EDN: RYSWTL

ISO rules for typesetting mathematics: mismath package

Dmitry S. Kulyabov[1,2], Anna V. Korolkova[1], Leonid A. Sevastianov[1], Yuri P. Rybakov[1]

[1] *RUDN University, 6 Miklukho-Maklaya St, Moscow, 117198, Russian Federation*

[2] *Joint Institute for Nuclear Research, 6 Joliot-Curie St, Dubna, 141980, Russian Federation*

Abstract. We continue to describe tools for simplifying the typesetting of mathematics in accordance with ISO standards. In this article, we briefly describe the mismath package for the LaTeX system.

Key words and phrases: typesetting mathematics standards, ISO, LaTeX

For citation: D. S. Kulyabov, A. V. Korolkova, L. A. Sevastianov, Y. P. Rybakov "ISO rules for typesetting mathematics: mismath package," *Discrete and Continuous Models and Applied Computational Science*, vol. 34, no. 3, pp. 283–287, 2026. DOI: 10.22363/2658-4670-2026-34-3-283-287. EDN: RYSWTL.

1. Mismath package

The `mismath` package provides a set of macros for improving the typesetting of mathematical formulas in accordance with the recommendations of the international standard ISO 80000-2 [1, 2]. Mathematical constants (e, i, π) are typeset in an upright font rather than in italics like variables. Vectors are typeset with arrows above or in bold type. Tensors are typeset in sans-serif bold italic. Uppercase Greek letters are typeset in italics.

The package offers:

- standard operator names;
- useful aliases for frequently used commands;
- improved spacing in mathematical expressions;
- environments for systems of equations and small matrices;
- two-column display-style math output for long calculations involving short expressions.

It is compatible with other packages:

- `amsmath`, `mathtools`: basic mathematical typesetting;
- `esvect`: arrows over vectors;
- `mleftright`: improves spacing for automatic delimiters.

If a command is already defined in previously loaded packages, `mismath` does not redefine it but issues a warning. If you need to force the use of the `mismath` definition, you can reset the command using **`\let\command\relax`** before loading the package.

Recommended package loading order:

```
\usepackage{amsmath}
\usepackage{mathtools}
\usepackage{amssymb}

\usepackage{mismath}
\usepackage{unicode-math}
```

The package automatically loads `mleftright` and `mathtools` (which, in turn, loads `amsmath`). If options need to be passed to these packages, they can be specified for `mismath`, or `amsmath` or `mathtools` can be loaded with the desired options before `mismath`. When using the `unicode-math` package, `mismath` should be loaded before `unicode-math`.

© 2026 D. S. Kulyabov, A. V. Korolkova, L. A. Sevastianov, Y. P. Rybakov

This work is licensed under a Creative Commons "Attribution-NonCommercial 4.0 International" license.

The `mismath` package combines the functions of other packages. All these features are gathered into a single package and configured in a unified style, in accordance with ISO standards.

Alternatives to the `mismath` package:

- Upright constants: `upgreek` (for Greek letters), `fixmath`;
- Vectors with arrows: `esvect`;
- Tensors: `tensor`;
- Improved spacing: `mleftright`, `mathtools`;
- Systems of equations: `amsmath` (`cases` and `matrix` environments);
- Two columns in `displaymath`: `multicol`, `IEEEtrantools`.

2. Package options

Options are specified when loading the package: **`\usepackage`**`[<options>]{mismath}`.

- `nofunction`: disables the loading of additional function and operator definitions.
- `classicReIm`: retains the standard **`\Re`** and **`\Im`** (the symbols $\Re$ and $\Im$) without redefining them as `Re` and `Im`.
- `lineargroups`: loads macros for classical linear groups (**`\GL`**, **`\SL`**, **`\Sp`**, **`\O`**, **`\SO`**, **`\U`**, **`\SU`**).
- `textshortcuts`: adds text shortcuts for mathematics (e.g., **`\ale`** for *almost everywhere*, **`\cc`** for *complex conjugate*, **`\st`** for *such that*, **`\wrt`** for *with respect to*).
- `ibrackets`: loads the `ibrackets` package for improved handling of square brackets.
- `decimalcomma`: loads the `decimalcomma` package to use a comma as the decimal separator in math mode.
- `nosingleletter`: disables all single-letter macros (such as **`\R`**, **`\C`**, **`\e`**, **`\i`**), replacing them with two-letter equivalents (e.g., **`\RR`**, **`\CC`**, **`\ee`**, **`\ii`**). We prefer using double letters to avoid potential conflicts with the author's notation or other packages.

lineargroups option

```
\(\GL(n,\RR)\), \(\SL(2,\CC)\),
↪ \(\Sp(2n,\FF)\), \(\OO(3)\),
↪ \(\SO(n)\), \(\UU(1)\),
↪ \(\SU(2)\)
```

$\mathrm{GL}(n,\mathbb{R})$, $\mathrm{SL}(2,\mathbb{C})$, $\mathrm{Sp}(2n,\mathbb{F})$, $\mathrm{O}(3)$, $\mathrm{SO}(n)$, $\mathrm{U}(1)$, $\mathrm{SU}(2)$

3. Basic commands

3.1. Mathematical constants

Constants are typeset in an upright font, as required by the ISO standard.

Mathematical constants

```
\(\ee\), \(\ii\), \(\jj\)
```

e, i, j

3.2. Vectors, tensors, norms

- **`\vect`**`{argument}`: vector with an arrow above.
- **`\boldvect`**: a switch that renders vectors in bold italics throughout the document or the current group.
- **`\hvect`**`{<argument>}`, **`\hvec`**`{<argument>}`: used to raise the arrows when vectors appear side-by-side (e.g., **`\hvect`**`{u} + `**`\hvect`**`{v}`).
- **`\norm`**`{<argument>}`: norm (double vertical bars).

- **\abs**{<argument>}: absolute value (single vertical bars).
- **\innerprod**{<arg1>}{<arg2>}: inner product (angle brackets).
- **\tensor**{<argument>} (or **\mathbfsfit**): tensor (bold sans-serif italics).

Vectors

```
\(\vect{a}\), { \(\boldvect \vect{a}\) }\\
\(\hvect{u} + \hvect{v}\) \\
\(\norm{a}\), \(\abs{a}\)\\
\(\innerprod{a}{b}\) \\
\(\tensor{F}\)
```

$\vec{a}$, $\boldsymbol{a}$
$\vec{u} + \vec{v}$
$\|a\|$, $|a|$
$\langle a, b \rangle$
$\mathbf{F}$

3.3. Operators

The package defines a set of standard mathematical operators.

3.3.1. Common operators

- **\Re**, **\Im**: real and imaginary parts.
- **\id**: identity operator;
- **\Var**: variance;
- **\Cov**: covariance;
- **\rank**: rank;
- **\tr**: matrix trace;
- **\grad**: gradient;
- **\divg**: divergence;
- **\rot**: curl;
- **\curl**: curl;
- **\End**: endomorphism;
- **\Aut**: automorphism;
- **\di**: differential (upright d with a thin space following it), though it is better to use the more general `derivative` package [2].

Standard operators

```
\(\Re\), \(\Im\) \\
\(\id\),  \(\Var\), \(\Cov\) \\
\(\rank\), \(\tr{A}\) \\
\(\grad{a}\), \(\divg{a}\) \\
\(\rot{a}\),  \(\curl{a}\) \\
\(\End\),  \(\Aut\) \\
\(\di x\), \(\di (x,y)\)
```

Re, Im
id, Var, Cov
rank, tr A
$\overrightarrow{\text{grad}}\, a$, $\operatorname{div} a$
$\overrightarrow{\text{rot}}\, a$, $\overrightarrow{\text{curl}}\, a$
End, Aut
$\mathrm{d}x$, $\mathrm{d}(x,y)$

3.4. Asymptotic notation

Notations for the Bachmann–Landau notation [3, 4].

Asymptotic notation

```
\(n^2 + \bigO (n \log n)\)\\
\(n^2 + \bigo (n \log n)\)\\
\(\ee^{x} = 1 + x + \frac{x^{2}}{2} + \lito
 ↪  (x^{2})\)
```

$n^2 + \mathcal{O}(n \log n)$
$n^2 + \mathrm{O}(n \log n)$
$\mathrm{e}^x = 1 + x + \frac{x^2}{2} + \mathrm{o}(x^2)$

3.4.1. Standard sets

Notation for standard sets. We use the `decimalcomma` option. Following Bourbaki's notation [5], the package uses boldface for sets. However, double-struck letters can also be used, and this is the convention we follow in our work.

Sets

```
{\renewcommand\mathset{\mathbf} \(\RR\),
 ↪  \(\CC\), \(\ZZ\), \(\NN\), \\
\(\QQ\), \(\HH\), \(\FF\), \(\KK\) } \\
{\renewcommand\mathset{\mathbb} \(\RR\),
 ↪  \(\CC\), \(\ZZ\), \(\NN\), \\
\(\QQ\), \(\HH\), \(\FF\), \(\KK\) }
```

$\mathbf{R}$, $\mathbf{C}$, $\mathbf{Z}$, $\mathbf{N}$,
$\mathbf{Q}$, $\mathbf{H}$, $\mathbf{F}$, $\mathbf{K}$
$\mathbb{R}$, $\mathbb{C}$, $\mathbb{Z}$, $\mathbb{N}$,
$\mathbb{Q}$, $\mathbb{H}$, $\mathbb{F}$, $\mathbb{K}$

Author Contributions: The contributions of the authors are equal. All authors have read and agreed to the published version of the manuscript.

Funding: This research received no external funding.

Data Availability Statement: No new data were created or analysed during this study. Data sharing is not applicable.

Conflicts of Interest: The authors declare no conflict of interest.

Declaration on Generative AI: The authors have not employed any Generative AI tools.

References

[1] *Quantities and units – Part 2: Mathematics*, 2nd ed., ISO 80000-2:2019, Geneva, Switzerland: ISO, 2019.
[2] D. S. Kulyabov, A. V. Korolkova, L. A. Sevastianov, and Y. P. Rybakov, "ISO rules for typesetting mathematics," *Discrete and Continuous Models and Applied Computational Science*, vol. 34, no. 2, pp. 155–159, 2026. DOI: 10.22363/2658-4670-2026-34-2-155-159
[3] P. Bachmann, *Analytische Zahlentheorie*, German. Leipzig: Teubner, 1894, vol. 2.
[4] E. Landau, *Handbuch der Lehre von der Verteilung der Primzahlen*, German. Leipzig: B. G. Teubner, 1909.
[5] N. Bourbaki, *Éléments de mathématique. Fascicule III. Livre III: Topologie générale, Chapitres 3 et 4* (Actualités Scientifiques et Industrielles 1143), French, 3rd ed. Paris: Hermann, 1960, 236 pp.

Information about the authors

Kulyabov, Dmitry S.—Professor, Doctor of Sciences in Physics and Mathematics, Professor of Department of Probability Theory and Cyber Security of RUDN University; Senior Researcher of Laboratory of Information Technologies, Joint Institute for Nuclear Research (e-mail: kulyabov-ds@rudn.ru, ORCID: 0000-0002-0877-7063, ResearcherID: I-3183-2013, Scopus Author ID: 35194130800)

Korolkova, Anna V.—Docent, Candidate of Sciences in Physics and Mathematics, Associate Professor of Department of Probability Theory and Cyber Security of RUDN University (e-mail: korolkova-av@rudn.ru, ORCID: 0000-0001-7141-7610, ResearcherID: I-3191-2013, Scopus Author ID: 36968057600)

Sevastianov, Leonid A.—Professor, Doctor of Sciences in Physics and Mathematics, Professor of Department of Computational Mathematics and Artificial Intelligence of RUDN University (e-mail: sevastianov-la@rudn.ru, ORCID: 0000-0002-1856-4643, ResearcherID: B-8497-2016, Scopus Author ID: 8783969400)

Rybakov, Yuri P.—Professor, Doctor of Sciences in Physics and Mathematics, Professor of the Institute of Physical Research and Technologies of RUDN University (e-mail: rybakov-yup@rudn.ru, ORCID: 0000-0002-7744-9725, ResearcherID: S-4813-2018, Scopus Author ID: 16454766600)

RUSSIAN METADATA

DOI: 10.22363/2658-4670-2026-34-3-283-287 EDN: RYSWTL

Правила ISO для набора математики. Пакет mismath

Д. С. Кулябов[1,2], А. В. Королькова[1], Л. А. Севастьянов[1], Ю. П. Рыбаков[1]

[1] *Российский университет дружбы народов, ул. Миклухо-Маклая, д. 6, Москва, 117198, Российская Федерация*

[2] *Объединённый институт ядерных исследований, ул. Жолио-Кюри, д. 6, Дубна, 141980, Российская Федерация*

Аннотация. Мы продолжаем описывать средства для упрощения набора математики, соответствующей правилам ISO. В данной статье мы кратко описываем пакет для системы LaTeX mismath.

Ключевые слова: стандарты набора математики, ISO, LaTeX

Discrete & Continuous Models
& Applied Computational Science
ISSN 2658-7149 (Online), 2658-4670 (Print)

2026, 34 (3) 288–297
http://journals.rudn.ru/miph

Research article

UDC 519.872
PACS 02.50.Ga
DOI: 10.22363/2658-4670-2026-34-3-288-297 EDN: RPKOTU

A resource queueing model for equal-rate dynamic spectrum slicing in 5G NR networks

Ibram E.Z. Ghebrial[1], Irina A. Kochetkova[1, 2]

[1] *RUDN University, 6 Miklukho-Maklaya St, Moscow, 117198, Russian Federation*

[2] *Federal Research Center "Computer Science and Control" of the Russian Academy of Sciences, 44-2 Vavilova St, Moscow, 119333, Russian Federation*

(received: March 31, 2026; revised: April 20, 2026; accepted: May 10, 2026)

Abstract. Background: In fifth-generation (5G) New Radio (NR) network slicing, a mobile network operator leases part of its spectrum to a mobile virtual network operator under service-level agreements. Under equal-rate (Round Robin) scheduling, the base station assigns time-frame shares so that every user in a slice receives the same bitrate regardless of location. Existing analytical queueing frameworks for dynamic spectrum slicing, however, cover only the fixed-power case, and no such framework yet exists for equal-rate scheduling. Purpose: To develop a resource queueing model for dynamic spectrum slicing under equal-rate scheduling, extending the authors' prior fixed-power framework to this regime. Method: We describe each user's channel quality by an inverse spectral efficiency (ISE) and derive its cumulative distribution function from the path-loss model. Under equal-rate scheduling, all users in a slice share a common bitrate equal to the allocated bandwidth divided by the sum of independent, identically distributed ISEs; we characterize this sum exactly through multi-fold convolution and, for computational tractability, approximate it through the central limit theorem. These distributions feed a continuous-time Markov chain (CTMC) that models the joint spectrum partition and per-slice user counts, with state-dependent admission control and stochastic frequency reallocation that preserves isolation guarantees between slices. Results: The framework yields closed-form expressions for the blocking probability, the average per-user bitrate, the average number of active users in each slice, and overall resource utilization. Conclusions: The proposed model provides an analytical tool for spectrum dimensioning and admission control in multi-tenant 5G NR networks under equal-rate scheduling.

Key words and phrases: 5G NR, CTMC, dynamic spectrum management, equal-rate scheduling, network slicing, queueing model, Round Robin

For citation: I. E. Ghebrial, I. A. Kochetkova "A resource queueing model for equal-rate dynamic spectrum slicing in 5G NR networks," *Discrete and Continuous Models and Applied Computational Science*, vol. 34, no. 3, pp. 288–297, 2026. DOI: 10.22363/2658-4670-2026-34-3-288-297. EDN: RPKOTU.

1. Introduction

Network slicing is a cornerstone of fifth-generation (5G) New Radio (NR) architectures, enabling a mobile network operator (MNO) to partition a common radio access network into isolated logical slices, each governed by dedicated service-level agreements (SLAs) [1, 2]. In multi-tenant deployments the MNO simultaneously serves its own subscribers (Slice 1) and leases residual spectrum to a mobile virtual network operator (MVNO, Slice 2), coupling technical resource management with economic objectives [3, 4]. Two intra-slice scheduling strategies are widely studied [5]: the fixed-power (FP) model, which divides the allocated bandwidth equally among active users, and the equal-rate (Round Robin, RR) model, which adjusts per-user time-frame fractions so that every user achieves the same instantaneous bitrate [6, 7]. The FP model inherently discriminates users by location; the RR model eliminates this disparity and is therefore better suited to SLA-governed multi-tenant environments and to mobility-intensive use cases such as high-speed rail and vehicular networks [8, 9].

© 2026 I. E. Ghebrial, I. A. Kochetkova

This work is licensed under a Creative Commons "Attribution-NonCommercial 4.0 International" license.

A complete analytical framework for FP-based dynamic spectrum slicing—combining a continuous-time Markov chain (CTMC) resource queueing model, stochastic frequency reallocation with isolation guarantees, and MNO revenue optimization—was established in [10]. That line of research traces back to queueing and simulation analyses of dynamic slicing [11], a controllable queueing model with elastic traffic and Markov decision process (MDP) formulation [6], and an MDP–artificial neural network combination for policy approximation [12]. However, extending these results to the equal-rate scheduler requires a fundamentally different stochastic characterization of the per-user bitrate, and no prior work has provided such a framework with closed-form performance guarantees.

The present paper fills this gap. The main contributions of our study are as follows:

- Stochastic bitrate model for equal-rate scheduling. The common per-user bitrate under the RR policy is characterized as the ratio of the allocated bandwidth to the sum of independent, identically distributed (i.i.d.) inverse spectral efficiencies. A closed-form cumulative distribution function (CDF) is derived for this random variable, and a tractable Central Limit Theorem (CLT) approximation is established for use in admission control and reallocation computations.
- CTMC resource queueing model with state-dependent control. A complete CTMC over the joint state—spectrum partition, MNO user count, MVNO user count—is formulated, incorporating state-dependent admission probabilities, stochastic frequency reallocation subject to per-slice isolation thresholds. The reallocation policy can be chosen to optimize a given objective, for example MNO revenue maximization as in [10].
- Closed-form performance metrics. Steady-state expressions are derived for blocking probability, average per-user bitrate, average number of active users, and resource utilization.

The remainder of this paper is organized as follows. Section 2 reviews related work. Section 3 describes the system model. Section 4 presents the results—the CTMC queueing model and closed-form performance metrics. Section 6 presents conclusions and future directions.

2. Related work

The architecture and challenges of 5G network slicing are surveyed in [1, 2], covering radio access network (RAN), core, and transport domains. More recent surveys extend this to end-to-end 6G slicing [8] and to smart-city applications of beyond-5G networks [9]. These works establish a consistent taxonomy: while data-driven and optimization-based approaches dominate the recent literature, analytical and model-based methods remain indispensable for deriving closed-form admission control policies and for system dimensioning under SLA constraints. The scheduling layer—covering RR, proportional fairness (PF), and maximum throughput (MT) strategies within sliced architectures—is surveyed in [5], which identifies RR as the preferred policy when uniform per-user quality of service (QoS) is the primary requirement.

Learning-based approaches have become dominant for intra- and inter-slice resource management. A data-driven RAN slicing mechanism for enhanced mobile broadband (eMBB) and ultra-reliable and low latency communications (URLLC) coexistence was proposed in [13], providing a reference architecture for slice-orchestrator-level control. Cooperative multi-agent reinforcement learning (MARL) for flexible RAN slicing in open RAN (O-RAN), capable of handling variable slice counts, was introduced in [14]. Prediction-aided weighted deep reinforcement learning (DRL) for online resource allocation was shown to outperform static and myopic baselines in [15], and a hybrid Double Deep Q-Network with dueling architecture was proposed for 5G network slicing in [16]. The preemptive resource allocation problem in dynamic multi-tenant networks was addressed with a Dueling-DQN approach in [17]. DRL-based dynamic scheduling for LTE (long-term evolution) and eMBB slicing—with explicit comparison of PF, RR, and max-rate rules—was studied in [7]. In the domain of joint allocation and scheduling, the power–subcarrier co-allocation problem for multi-tenant multi-service systems was formulated as a mixed-integer nonlinear program with efficient heuristic decomposition in [18]. A cooperative-aware scheme for cloud RAN was developed in [19], and a QoS-aware multi-cell RAN slicing framework accounting for inter-cell interference and mobility was presented in [20]. While

DRL methods excel in complex dynamic environments, they require extensive training, offer limited interpretability, and do not produce the closed-form expressions needed for system dimensioning.

Guaranteeing strict inter-slice isolation while enabling efficient resource sharing is among the most challenging aspects of multi-tenant slicing. The isolation-aware slicing problem was formulated as a mixed-integer program in [4]. A latency-driven orchestration framework for beyond-5G networks was developed in [21], simultaneously providing latency and throughput guarantees in multi-tenancy environments. Pricing strategies for 5G multi-tenancy—Shapley value, bargaining game, and dynamic pricing—were evaluated using a game-theory framework in [3], highlighting the interplay between isolation requirements, resource efficiency, and economic incentives.

The matrix-analytic foundations for performance evaluation of multi-server queueing systems with state-dependent service rates are provided in [22], which underpins the CTMC-based methodology of the present work. State-dependent service rates and elastic traffic models have been employed to study admission control and capacity planning in sliced networks under various traffic assumptions [6]. The isolation-aware slicing model of [4] demonstrates that analytical formulations can capture the joint technical–economic trade-offs that DRL-based methods leave implicit.

The present paper is the latest contribution to a research program on CTMC-based analytical modeling of dynamic spectrum slicing in 5G NR. The program began with a queueing and simulation study that established the basic framework for modeling the reallocation interaction between an MNO and an MVNO [11]. This was followed by a controllable queueing system with elastic traffic and Poisson control signals, which formulated the spectrum reallocation decision as a Markov decision process (MDP) and provided resource capacity planning guidelines [6]. The MDP formulation was extended in [12] by combining it with an artificial neural network to approximate the optimal reallocation policy in larger state spaces. The most comprehensive prior framework is [10], which integrates a full CTMC resource queueing model with frequency reallocation ensuring per-slice isolation and MNO revenue maximization under the fixed-power scheduling policy. The present work extends [10] to the equal-rate (Round Robin) scheduling model. The key challenge is that the RR policy yields a per-user bitrate that is a random ratio—the allocated bandwidth divided by the sum of i.i.d. inverse spectral efficiencies—whose stochastic characterization differs fundamentally from the fixed-power case. To the best of our knowledge, no existing work has developed a complete resource queueing framework integrating equal-rate scheduling with dynamic spectrum slicing and frequency reallocation in a multi-tenant 5G NR setting.

3. System model

3.1. Network architecture and channel model

We consider a single macrocell served by one base station (BS) shared between an MNO and an MVNO under a network-slicing agreement (Figure 1). The total downlink bandwidth $F = M\Delta f$ is divided into M resource blocks of width Δf. The MNO is allocated m blocks (Slice 1, bandwidth $F_1(m) = m\Delta f$) and leases the remaining $M - m$ blocks to the MVNO (Slice 2, bandwidth $F_2(m) = (M - m)\Delta f$), with the partition constrained to $M_1 \leq m \leq M - M_2$, where M_i is the minimum block reservation for slice i.

Both operators provide broadband data services. PDU (Protocol data unit) session requests in slice i arrive according to independent Poisson processes with rates λ_1 (MNO) and λ_2 (MVNO). The traffic volume per session—the total number of bits to be transferred—is exponentially distributed with mean $1/\mu_i$ bits. Each slice enforces a minimum bitrate guarantee $b_i^{\min}$; in addition, a stricter isolation threshold $b_i^{\text{is}} > b_i^{\min}$ is maintained: a spectrum reallocation is executed only when every active user in the affected slice would receive at least b_i^{is} under the new partition. The MNO controls the partition via a Poisson reallocation signal of rate δ; at each signal epoch the controller selects a target allocation a from the feasible set $\mathcal{A}(m, n_1, n_2)$ defined in Section 4.

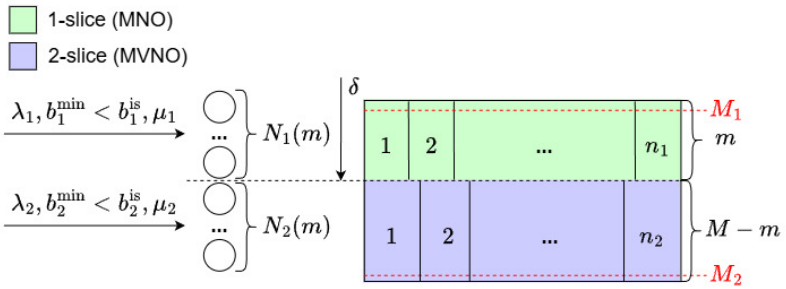


Figure 1. System model

Users are spatially distributed over the macrocell according to a two-dimensional Poisson Point Process (PPP) on the annulus $[R_{\min}, R_{\max}]$. The downlink received SNR (signal-to-noise ratio) is governed by the Friis path-loss model combined with the Shannon–Hartley capacity theorem. With BS transmit power P, antenna gains G_{t} and G_{r}, thermal noise N_0, and background interference I_0, the spectral efficiency (bits/s/Hz) at path loss PL is

$$r(\text{PL}) = \log_2\left(1 + \frac{PG_{\text{t}}G_{\text{r}}}{(N_0 + I_0)\text{PL}}\right).$$

Since $r(\cdot)$ is strictly decreasing in path loss, users near the BS ($\text{PL} = \text{PL}_{\min}$, distance $R_{\min}$) achieve the maximum spectral efficiency (SE) $r(\text{PL}_{\min})$, while cell-edge users ($\text{PL} = \text{PL}_{\max}$, distance $R_{\max}$) achieve the minimum $r(\text{PL}_{\max})$. The general instantaneous bitrate of user j in slice i is

$$b_{ij}(m, n_i) = F_i(m) \cdot \tau_{ij}(m, n_i) \cdot r(\text{PL}_{ij}), \quad j = 1, \dots, n_i, i = 1, 2,$$

where $\tau_{ij}(m, n_i) \in [0, 1]$ is the downlink time-frame fraction allocated to user j.

3.2. Equal-rate scheduling

Under the equal-rate scheduling policy the BS assigns time fractions $\tau_{ij}(m, n_i)$ so that every active user in slice i achieves the same instantaneous bitrate:

$$b_{ij}(m, n_i) = b_i(m, n_i), \quad j = 1, \dots, n_i, \quad i = 1, 2.$$

Substituting the equal-rate condition into the general bitrate expression and solving for the time fraction gives

$$\tau_{ij}(m, n_i) = \frac{b_i(m, n_i)}{F_i(m) \cdot r(\text{PL}_{ij})}, \quad j = 1, \dots, n_i, \quad i = 1, 2.$$

Applying the frame normalization constraint $\sum_{j=1}^{n_i} \tau_{ij}(m, n_i) = 1$ yields the common bitrate:

$$b_i(m, n_i) = \frac{F_i(m)}{\sum\limits_{j=1}^{n_i} 1/r(\text{PL}_{ij})}, \quad i = 1, 2,$$

where $1/r(\text{PL}_{ij})$ is the inverse spectral efficiency (ISE) of user j. Users with poor channel conditions (large ISE) are compensated by a larger time-frame share, so every user in the slice receives the same bitrate regardless of location.

Since user positions are random (PPP), the path loss ξ_{PL} is a random variable with CDF $F_{\xi_{\mathrm{PL}}}(\cdot)$ on $[\mathrm{PL}_{\min}, \mathrm{PL}_{\max}]$. Consequently, $\xi_j^{\mathrm{ISE}} = 1/r(\xi_{\mathrm{PL}})$ are i.i.d. random variables with support $[\mathrm{ISE}_{\min}, \mathrm{ISE}_{\max}]$, where $\mathrm{ISE}_{\min} = 1/r(\mathrm{PL}_{\min})$ and $\mathrm{ISE}_{\max} = 1/r(\mathrm{PL}_{\max})$. The equal-rate bitrate $\xi_i^{\mathrm{b}}(m, n_i)$ is therefore itself a random variable:

$$\xi_i^{\mathrm{b}}(m, n_i) = \frac{F_i(m)}{\sum_{j=1}^{n_i} \xi_j^{\mathrm{ISE}}}, \quad i = 1, 2.$$

Its stochastic characterization—the CDF of ξ_{ISE}, the CLT approximation for the sum $\eta_i(n_i) = \sum_{j=1}^{n_i} \xi_j^{\mathrm{ISE}}$, and the resulting admission and reallocation probabilities—is developed in Section 4.

4. Results: Resource queueing model

4.1. CTMC and transition rates

The system is modeled as a CTMC with state (m, n_1, n_2), where $m \in \{M_1, \dots, M - M_2\}$ is the current spectrum partition and $n_i \geq 0$ is the number of active users in slice i. Under the equal-rate policy the worst-case channel realization (all users at $R_{\min}$, path loss $\mathrm{PL}_{\min}$) determines the maximum admissible occupancy:

$$N_i(m) = \left\lfloor \frac{F_i(m) \cdot r(\mathrm{PL}_{\min})}{b_i^{\min}} \right\rfloor, \quad i = 1, 2.$$

The finite state space is accordingly

$$\mathcal{X} = \big\{(m, n_1, n_2) : \quad 0 \leq n_1 \leq N_1(m), 0 \leq n_2 \leq N_2(m), M_1 \leq m \leq M - M_2\big\}.$$

A Poisson reallocation signal of rate δ triggers a candidate partition change from m to target $a \in \mathcal{A}(m, n_1, n_2)$. To protect both slices, the feasible set $\mathcal{A}(m, n_1, n_2)$ is constructed from the isolation-safe minimum block counts

$$m_i^{\mathrm{is}}(n_i) = \max\left\{M_i, \left\lceil \frac{b_i^{\mathrm{is}} \cdot n_i}{\Delta f \cdot r(\mathrm{PL}_{\min})} \right\rceil\right\}, \quad i = 1, 2,$$

and equals:

$$\begin{aligned}
&\mathcal{A}(m, n_1, n_2) = \varnothing, \quad m < m_1^{\mathrm{is}}(n_1), \quad M - m < m_2^{\mathrm{is}}(n_2),\\
&\mathcal{A}(m, n_1, n_2) = \{m, \dots, M - m_2^{\mathrm{is}}(n_2)\}, \quad m < m_1^{\mathrm{is}}(n_1), \quad M - m \geq m_2^{\mathrm{is}}(n_2),\\
&\mathcal{A}(m, n_1, n_2) = \{m_1^{\mathrm{is}}(n_1), \dots, m\}, \quad m \geq m_1^{\mathrm{is}}(n_1), \quad M - m < m_2^{\mathrm{is}}(n_2),\\
&\mathcal{A}(m, n_1, n_2) = \{m_1^{\mathrm{is}}(n_1), \dots, M - m_2^{\mathrm{is}}(n_2)\}, \quad m \geq m_1^{\mathrm{is}}(n_1), \quad M - m \geq m_2^{\mathrm{is}}(n_2).
\end{aligned}$$

When $\mathcal{A}(m, n_1, n_2) = \varnothing$ no safe reallocation exists and the partition remains at m.

Let $p_i(m, n_i)$ denote the state-dependent admission probability and $p(m, n_1, n_2, a)$ the reallocation success probability; both quantities depend on the CDF of the equal-rate bitrate $\xi_i^{\mathrm{b}}(m, n_i)$ and are derived below. The non-zero off-diagonal transition rates are:

$$\begin{aligned}
&\mathbf{Q}\left[(m, n_1, n_2), (m, n_1 + 1, n_2)\right] = \lambda_1 \cdot p_1(m, n_1), \quad n_1 + 1 \leq N_1(m),\\
&\mathbf{Q}\left[(m, n_1, n_2), (m, n_1, n_2 + 1)\right] = \lambda_2 \cdot p_2(m, n_2), \quad n_2 + 1 \leq N_2(m),\\
&\mathbf{Q}\left[(m, n_1, n_2), (m, n_1 - 1, n_2)\right] = n_1\mu_1 \cdot \mathbb{E}\left[\xi_1^{\mathrm{b}}(m, n_1)\right], \quad n_1 > 0,\\
&\mathbf{Q}\left[(m, n_1, n_2), (m, n_1, n_2 - 1)\right] = n_2\mu_2 \cdot \mathbb{E}\left[\xi_2^{\mathrm{b}}(m, n_2)\right], \quad n_2 > 0,\\
&\mathbf{Q}\left[(m, n_1, n_2), (a, n_1, n_2)\right] = \delta \cdot p(m, n_1, n_2, a), \quad a \in \mathcal{A}(m, n_1, n_2) \setminus \{m\}.
\end{aligned}$$

The first two rates correspond to arrivals: an arriving user in slice i is admitted with probability $p_i(m, n_i)$ and blocked (no state change) when $n_i = N_i(m)$. The third and fourth rates describe service completions, which occur at the elastic rate $n_i\mu_i\mathbb{E}[\xi_i^{\mathrm{b}}(m, n_i)]$: since each session volume is exponentially distributed with mean $1/\mu_i$ bits and the equal-rate scheduler allocates bitrate $\xi_i^{\mathrm{b}}(m, n_i)$, the expected service rate per user is $\mu_i\mathbb{E}[\xi_i^{\mathrm{b}}(m, n_i)]$. The last rate governs reallocation transitions, which fire at each Poisson epoch of rate δ when the controller selects target a and the affected slice passes the isolation check with probability $p(m, n_1, n_2, a)$.

4.2. Performance metrics

The CTMC over $\mathcal{X}$ is irreducible and ergodic. All metrics are expectations over the stationary distribution $\pi(m, n_1, n_2)$. Blocking probability of a request in slice i:

$$P_i^{\mathrm{bl}} = \sum_{m=M_1}^{M-M_2} \sum_{n_1=0}^{N_1(m)} \sum_{n_2=0}^{N_2(m)} [1 - p_i(m, n_i)] \cdot \pi(m, n_1, n_2), \quad i = 1, 2.$$

Average bitrate per user in slice i:

$$\overline{b}_1 = \frac{\sum_{m=M_1}^{M-M_2} \sum_{n_1=1}^{N_1(m)} \mathbb{E}\left[\xi_1^{\mathrm{b}}(m, n_1)\right] \sum_{n_2=0}^{N_2(m)} \pi(m, n_1, n_2)}{\sum_{m=M_1}^{M-M_2} \sum_{n_1=1}^{N_1(m)} \sum_{n_2=0}^{N_2(m)} \pi(m, n_1, n_2)}, \qquad \overline{b}_2 = \frac{\sum_{m=M_1}^{M-M_2} \sum_{n_2=1}^{N_2(m)} \mathbb{E}\left[\xi_2^{\mathrm{b}}(m, n_2)\right] \sum_{n_1=0}^{N_1(m)} \pi(m, n_1, n_2)}{\sum_{m=M_1}^{M-M_2} \sum_{n_2=1}^{N_2(m)} \sum_{n_1=0}^{N_1(m)} \pi(m, n_1, n_2)}.$$

Average number of active users in slice i:

$$\overline{n}_1 = \sum_{m=M_1}^{M-M_2} \sum_{n_1=1}^{N_1(m)} n_1 \sum_{n_2=0}^{N_2(m)} \pi(m, n_1, n_2), \qquad \overline{n}_2 = \sum_{m=M_1}^{M-M_2} \sum_{n_2=1}^{N_2(m)} n_2 \sum_{n_1=0}^{N_1(m)} \pi(m, n_1, n_2).$$

Average resource utilization:

$$\overline{m} = \sum_{m=M_1}^{M-M_2} m \sum_{n_1=0}^{N_1(m)} \sum_{n_2=0}^{N_2(m)} \pi(m, n_1, n_2), \qquad \overline{F}_1 = \Delta f \cdot \overline{m}, \qquad \overline{F}_2 = F - \overline{F}_1.$$

The metrics above require the quantities $p_i(m, n_i)$, $p(m, n_1, n_2, a)$, and $\mathbb{E}[\xi_i^{\mathrm{b}}(m, n_i)]$, all of which depend on the CDF of the equal-rate bitrate $\xi_i^{\mathrm{b}}(m, n_i)$. The next subsection derives this CDF.

4.3. CDF of the equal-rate bitrate

As defined in Section 3, the ISE of a user is the random variable $\xi_{\mathrm{ISE}} = 1/r(\xi_{\mathrm{PL}})$ with support $[\mathrm{ISE}_{\min}, \mathrm{ISE}_{\max}]$. Since $r(\cdot)$ is strictly decreasing, $\xi_{\mathrm{ISE}} \le s$ if and only if $r(\xi_{\mathrm{PL}}) \ge 1/s$, i.e. $\xi_{\mathrm{PL}} \le r^{-1}(1/s)$. Substituting the inverse of r in closed form gives the CDF of the ISE:

$$F_{\xi_{\mathrm{ISE}}}(s) = F_{\xi_{\mathrm{PL}}}\left(\frac{PG_{\mathrm{t}}G_{\mathrm{r}}}{(N_0 + I_0)(2^{1/s} - 1)}\right), \quad s \in [\mathrm{ISE}_{\min}, \mathrm{ISE}_{\max}].$$

Let $\mu_{\mathrm{ISE}} = \mathbb{E}[\xi_{\mathrm{ISE}}]$ and $\sigma^2_{\mathrm{ISE}} = \mathrm{Var}(\xi_{\mathrm{ISE}})$ be the first two central moments computed from $F_{\xi_{\mathrm{ISE}}}(s)$.

With n_i active users, the survival function of ξ_i^{b} is therefore:

$$\Pr\left(\xi_i^{\mathrm{b}}(m, n_i) \ge b\right) = \Pr\left(\eta_i(n_i) \le \frac{F_i(m)}{b}\right) = F^{*n_i}_{\xi_{\mathrm{ISE}}}\left(\frac{F_i(m)}{b}\right), \quad n_i > 0, \quad i = 1, 2,$$

where $F^{*n_i}_{\xi_{\mathrm{ISE}}}$ denotes the n_i-fold convolution of $F_{\xi_{\mathrm{ISE}}}$. While exact, evaluating this convolution for large n_i is computationally intensive.

By the CLT, $\eta_i(n_i)$ is approximately normal with mean $n_i\mu_{\mathrm{ISE}}$ and variance $n_i\sigma^2_{\mathrm{ISE}}$, so the survival function takes the form:

$$\Pr\left(\xi_i^{\mathrm{b}}(m,n_i)\geq b\right)\approx \Phi\left(\frac{F_i(m)/b-n_i\mu_{\mathrm{ISE}}}{\sigma_{\mathrm{ISE}}\sqrt{n_i}}\right),\quad n_i>0,\quad i=1,2,$$

and the CDF is equivalently:

$$F_{\xi_i^{\mathrm{b}}(m,n_i)}(b)\approx 1-\Phi\left(\frac{F_i(m)/b-n_i\mu_{\mathrm{ISE}}}{\sigma_{\mathrm{ISE}}\sqrt{n_i}}\right),\quad n_i>0,\quad i=1,2,$$

where $\Phi(x)$ denotes the standard normal CDF. For $n_i=1$ the CLT approximation reduces to $\Pr(\xi_i^{\mathrm{b}}(m,1)\geq b)=F_{\xi_{\mathrm{ISE}}}(F_i(m)/b)$, which is exact. The expected equal-rate bitrate used in the service-completion rates is $\mathbb{E}\left[\xi_i^{\mathrm{b}}(m,n_i)\right]=\int_{B_i^{\min}(m,n_i)}^{B_i^{\max}(m,n_i)} b\mathrm{d}F_{\xi_i^{\mathrm{b}}(m,n_i)}(b)$, where $B_i^{\min}(m,n_i)=F_i(m)\cdot r(\mathrm{PL}_{\max})/n_i$ and $B_i^{\max}(m,n_i)=F_i(m)\cdot r(\mathrm{PL}_{\min})/n_i$ are the minimum and maximum achievable equal-rate bitrates, corresponding to all users being at the cell edge and all users being at the cell center, respectively.

4.4. Admission and reallocation probabilities

A new arrival to slice i is admitted if and only if all n_i+1 users simultaneously satisfy the minimum bitrate constraint: $\eta_i(n_i+1)\leq F_i(m)/b_i^{\min}$. Conditioning on the current n_i users already being admitted yields the admission probability:

$$p_i(m,n_i)=\frac{\Pr\left(\xi_i^{\mathrm{b}}(m,n_i+1)\geq b_i^{\min}\right)}{\Pr\left(\xi_i^{\mathrm{b}}(m,n_i)\geq b_i^{\min}\right)},\quad n_i>0,\quad i=1,2,$$

and $p_i(m,0)=\Pr(\xi_i^{\mathrm{b}}(m,1)\geq b_i^{\min})$. Substituting the CLT approximation for the survival function gives:

$$p_i(m,n_i)\approx\frac{\Phi\left(\dfrac{F_i(m)/b_i^{\min}-(n_i+1)\mu_{\mathrm{ISE}}}{\sigma_{\mathrm{ISE}}\sqrt{n_i+1}}\right)}{\Phi\left(\dfrac{F_i(m)/b_i^{\min}-n_i\mu_{\mathrm{ISE}}}{\sigma_{\mathrm{ISE}}\sqrt{n_i}}\right)},\quad n_i>0,\quad i=1,2.$$

A reallocation from m to $a\neq m$ succeeds if all n_i users in the affected slice achieve at least the isolation threshold b_i^{is} under the new allocation. Applying the CLT survival function with b_i^{is} in place of $b_i^{\min}$:

$$p(m,n_1,n_2,a)=\frac{\Pr\left(\xi_1^{\mathrm{b}}(a,n_1)\geq b_1^{\mathrm{is}}\right)}{\Pr\left(\xi_1^{\mathrm{b}}(m,n_1)\geq b_1^{\min}\right)}\approx\frac{\Phi\left(\dfrac{F_1(a)/b_1^{\mathrm{is}}-n_1\mu_{\mathrm{ISE}}}{\sigma_{\mathrm{ISE}}\sqrt{n_1}}\right)}{\Phi\left(\dfrac{F_1(m)/b_1^{\min}-n_1\mu_{\mathrm{ISE}}}{\sigma_{\mathrm{ISE}}\sqrt{n_1}}\right)},\quad a<m,\quad n_1>0,$$

$$p(m,n_1,n_2,a)=\frac{\Pr\left(\xi_2^{\mathrm{b}}(a,n_2)\geq b_2^{\mathrm{is}}\right)}{\Pr\left(\xi_2^{\mathrm{b}}(m,n_2)\geq b_2^{\min}\right)}\approx\frac{\Phi\left(\dfrac{F_2(a)/b_2^{\mathrm{is}}-n_2\mu_{\mathrm{ISE}}}{\sigma_{\mathrm{ISE}}\sqrt{n_2}}\right)}{\Phi\left(\dfrac{F_2(m)/b_2^{\min}-n_2\mu_{\mathrm{ISE}}}{\sigma_{\mathrm{ISE}}\sqrt{n_2}}\right)},\quad a>m,\quad n_2>0,$$

with $p(m,n_1,n_2,a)=1$ when the affected slice is empty ($n_1=0$ for $a<m$; $n_2=0$ for $a>m$).

5. Discussion

Unlike the fixed-power model [10], where each user's bitrate depends only on their own path loss, the equal-rate policy couples all users within a slice through the sum $\eta_i(n_i)$: a single cell-edge user lowers the bitrate of every other user in the slice. This coupling is what necessitates the CDF derivation in Section 4—admission and reallocation decisions cannot be made per-user, only for the slice as a whole.

The CLT approximation is exact for $n_i = 1$ and improves as n_i grows, so its main practical value is for slices with several simultaneous users, precisely the regime where the exact n_i-fold convolution becomes too costly to evaluate at each arrival or reallocation epoch.

The isolation-aware set $\mathcal{A}(m, n_1, n_2)$ protects already-admitted users but narrows the range of feasible reallocations under high load in either slice. Because this constraint now operates on a stochastic bitrate rather than a fixed allocation, reallocation decisions under equal-rate scheduling are inherently more conservative than under the fixed-power scheme.

6. Conclusion

This paper has developed a complete resource queueing model for dynamic spectrum slicing in two-operator 5G NR networks under the equal-rate (Round Robin) scheduling policy, where the base station adjusts per-user time-frame fractions so that every active user within a slice achieves the same instantaneous bitrate. The CTMC is formulated with state-dependent arrivals, elastic service completions, and Poisson-triggered reallocation transitions subject to per-slice isolation thresholds. Closed-form steady-state expressions are derived for blocking probability, average per-user bitrate, average number of active users, and resource utilization.

Several directions remain open for future research. First, the numerical validation of the CLT approximation against exact n_i-fold convolution and Monte Carlo simulation across a range of cell radii, load levels, and path-loss exponents would establish practical accuracy bounds. Second, extending the model to more than two slices, to heterogeneous minimum bitrate requirements across user classes, and to non-Poisson arrival processes would broaden its applicability to emerging 5G-Advanced and 6G multi-tenant deployments.

Author Contributions: Conceptualization, supervision, methodology, writing—review and editing, Irina A. Kochetkova; visualization, writing—original draft preparation, Ibram E.Z. Ghebrial; investigation, Ibram E.Z. Ghebrial and Irina A. Kochetkova. All authors have read and agreed to the published version of the manuscript.

Funding: This research received no external funding.

Data Availability Statement: Data sharing is not applicable.

Conflicts of Interest: The authors declare no conflict of interest.

Declaration on Generative AI: During the preparation of this work, the authors used Perplexity AI (Perplexity AI, Inc., 2026) in order to: grammar and spelling check, improve writing style. After using this tool, the authors reviewed and edited the resulting content as needed and take full responsibility for the content of the publication.

References

[1] X. Foukas, G. Patounas, A. Elmokashfi, and M. K. Marina, "Network Slicing in 5G: Survey and Challenges," *IEEE Communications Magazine*, vol. 55, no. 5, pp. 94–100, 2017. DOI: 10.1109/MCOM.2017.1600951

[2] P. Rost, C. Mannweiler, D. S. Michalopoulos, et al., "Network Slicing to Enable Scalability and Flexibility in 5G Mobile Networks," *IEEE Communications Magazine*, vol. 55, no. 5, pp. 72–79, 2017. DOI: 10.1109/MCOM.2017.1600920

[3] S. K. A. Kumar, D. Crawford, and R. Stewart, "Pricing Models for 5G Multi-Tenancy Using Game Theory Framework," *IEEE Communications Magazine*, vol. 62, no. 5, pp. 66–72, 2024. DOI: 10.1109/MCOM.001.2200742

[4] M. Bolourian, N. Limam, M. A. Salahuddin, and R. Boutaba, "5Guard: Isolation-Aware End-to-End Slicing of 5G Networks," *IEEE Transactions on Mobile Computing*, vol. 25, no. 4, pp. 4979–4996, 2026. DOI: 10.1109/TMC.2025.3627066

[5] A. M. Jaradat, M. Alayedi, and H. Arslan, "A Survey of Radio Resource Scheduling for 6G and Future Wireless Networks," *IEEE Open Journal of the Communications Society*, vol. 6, pp. 10 191–10 218, 2025. DOI: 10.1109/OJCOMS.2025.3640408

[6] I. Kochetkova, K. Leonteva, I. Ghebrial, A. Vlaskina, S. Burtseva, A. Kushchazli, and K. Samouylov, "Controllable Queuing System with Elastic Traffic and Signals for Resource Capacity Planning in 5G Network Slicing," *Future Internet*, vol. 16, no. 1, p. 18, 2024. DOI: 10.3390/fi16010018

[7] H. Eddine Benmadani, M. Azni, T. Essa Alharbi, M. S. Alzaidi, and M. Tounsi, "Deep Reinforcement Learning-Based Dynamic Scheduling for Real-Time Applications in LTE and RAN Slicing for eMBB in 5G," *IEEE Access*, vol. 13, pp. 33 555–33 570, 2025. DOI: 10.1109/ACCESS.2025.3541531

[8] S. Ebrahimi, F. Bouali, and O. C. L. Haas, "Resource Management from Single-Domain 5G to End-to-End 6G Network Slicing: A Survey," *IEEE Communications Surveys and Tutorials*, vol. 26, no. 4, pp. 2836–2866, 2024. DOI: 10.1109/COMST.2024.3390613

[9] W. Rafique, J. Rani Barai, A. O. Fapojuwo, and D. Krishnamurthy, "A Survey on Beyond 5G Network Slicing for Smart Cities Applications," *IEEE Communications Surveys and Tutorials*, vol. 27, no. 1, pp. 595–628, 2025. DOI: 10.1109/COMST.2024.3410295

[10] I. Kochetkova, K. Leonteva, I. Ghebrial, and A. Khakimov, "Dynamic Spectrum Management for 5G NR Network Slicing: Frequency Reallocation Ensuring Slice Isolation and Revenue Maximization," *IEEE Access*, vol. 13, pp. 208 414–208 438, 2025. DOI: 10.1109/ACCESS.2025.3640721

[11] I. Kochetkova, A. Vlaskina, S. Burtseva, V. Savich, and J. Hosek, "Analyzing the Effectiveness of Dynamic Network Slicing Procedure in 5G Network by Queuing and Simulation Models," in *Lecture Notes in Computer Science*, vol. 12525, 2020, pp. 71–85. DOI: 10.1007/978-3-030-65726-0_7

[12] I. Ghebrial, K. Leonteva, I. Kochetkova, and S. Shorgin, "Markov Decision Process and Artificial Neural Network for Resource Capacity Planning in 5G Network Slicing," in *Communications in Computer and Information Science*, vol. 2163, 2024, pp. 33–47. DOI: 10.1007/978-3-031-65385-8_3

[13] S. Bakri, P. A. Frangoudis, A. Ksentini, and M. Bouaziz, "Data-Driven RAN Slicing Mechanisms for 5G and Beyond," *IEEE Transactions on Network and Service Management*, vol. 18, no. 4, pp. 4654–4668, 2021. DOI: 10.1109/TNSM.2021.3098193

[14] M. Zangooei, M. Golkarifard, M. Rouili, N. Saha, and R. Boutaba, "Flexible RAN Slicing in Open RAN With Constrained Multi-Agent Reinforcement Learning," *IEEE Journal on Selected Areas in Communications*, vol. 42, no. 2, pp. 280–294, 2024. DOI: 10.1109/JSAC.2023.3336156

[15] Y. Cai, P. Cheng, Z. Chen, M. Ding, B. Vucetic, and Y. Li, "Deep Reinforcement Learning for Online Resource Allocation in Network Slicing," *IEEE Transactions on Mobile Computing*, vol. 23, no. 6, pp. 7099–7116, 2024. DOI: 10.1109/TMC.2023.3328950

[16] Z. Zakariya Saleh, M. F. Abbod, and R. Nilavalan, "Intelligent Resource Allocation via Hybrid Reinforcement Learning in 5G Network Slicing," *IEEE Access*, vol. 13, pp. 47 440–47 458, 2025. DOI: 10.1109/ACCESS.2025.3550518

[17] Y. Xie, Y. Kong, L. Huang, S. Wang, S. Xu, X. Wang, and J. Ren, "Resource Allocation for Network Slicing in Dynamic Multi-Tenant Networks: A Deep Reinforcement Learning Approach," *Computer Communications*, vol. 195, pp. 476–487, 2022. DOI: 10.1016/j.comcom.2022.09.015

[18] S. Tul Muntaha, M. Hafeez, Q. Z. Ahmed, F. A. Khan, Z. D. Zaharis, and P. I. Lazaridis, "RAN Slicing With Joint Resource Allocation for a Multi-Tenant–Multi-Service System," *IEEE Transactions on Cognitive Communications and Networking*, vol. 11, no. 3, pp. 1927–1939, 2025. DOI: 10.1109/TCCN.2024.3490781

[19] S. A. AlQahtani, "Cooperative-Aware Radio Resource Allocation Scheme for 5G Network Slicing in Cloud Radio Access Networks," *Sensors*, vol. 23, no. 11, p. 5111, 2023. DOI: 10.3390/s23115111

[20] A. Papa, A. Jano, S. Ayvasik, O. Ayan, H. M. Gursu, and W. Kellerer, "User-Based Quality of Service Aware Multi-Cell Radio Access Network Slicing," *IEEE Transactions on Network and Service Management*, vol. 19, no. 1, pp. 756–768, 2022. DOI: 10.1109/TNSM.2021.3122230

[21] L. Zanzi, V. Sciancalepore, A. Garcia-Saavedra, H. D. Schotten, and X. Costa-Perez, "LACO: A Latency-Driven Network Slicing Orchestration in Beyond-5G Networks," *IEEE Transactions on Wireless Communications*, vol. 20, no. 1, pp. 667–682, 2021. DOI: 10.1109/TWC.2020.3027963

[22] V. Naumov, Y. Gaidamaka, N. Yarkina, and K. Samouylov, *Matrix and Analytical Methods for Performance Analysis of Telecommunication Systems*. Springer Cham, 2022. DOI: 10.1007/978-3-030-83132-5

Information about the authors

Ghebrial, Ibram E. Z.—Junior Researcher and PhD Student with the Department of Probability Theory and Cyber Security of RUDN University (e-mail: gebrial-ie@rudn.ru, ORCID: 0009-0007-2682-8577, ResearcherID: OKS-6645-2025, Scopus Author ID: 58848551900)

Kochetkova, Irina A.—Doctor of Sciences in Physics and Mathematics, Associate Professor with the Department of Probability Theory and Cyber Security of RUDN University; Senior Researcher with the Federal Research Center "Computer Science and Control" of the Russian Academy of Sciences (e-mail: kochetkova-ia@rudn.ru, ORCID: 0000-0002-1594-427X, ResearcherID: E-3806-2014, Scopus Author ID: 35332169400)

RUSSIAN METADATA

УДК 519.872
PACS 02.50.Ga
DOI: 10.22363/2658-4670-2026-34-3-288-297 EDN: RPKOTU

Ресурсная система массового обслуживания для динамической нарезки радиочастот с равной скоростью в сетях 5G NR

И. Е. З. Гебриал[1], И. А. Кочеткова[1,2]

[1] *Российский университет дружбы народов, ул. Миклухо-Маклая, д. 6, Москва, 117198, Российская Федерация*

[2] *Федеральный исследовательский центр "Информатика и управление" Российской академии наук, ул. Вавилова, д. 44, корп. 2, Москва, 119333, Российская Федерация*

Аннотация. Предпосылки: В сетях 5G NR с нарезкой радиочастот оператор мобильной сети предоставляет часть спектра в аренду виртуальному оператору по соглашению об уровне обслуживания. При планировании с равной скоростью (Round Robin) базовая станция распределяет доли временного кадра так, что каждый пользователь слайса получает одинаковую скорость передачи данных независимо от местоположения. Существующие аналитические модели массового обслуживания для динамической нарезки спектра, однако, охватывают только вариант с фиксированной мощностью, и аналогичной модели для планирования с равной скоростью пока не существует. Цель: Построение ресурсной модели массового обслуживания для динамической нарезки спектра при планировании с равной скоростью, расширяющей ранее разработанную авторами схему с фиксированной мощностью на этот режим. Методы: Качество канала каждого пользователя описывается случайной величиной обратной спектральной эффективности, функция распределения которой выводится из модели затухания радиосигнала. При планировании с равной скоростью все пользователи слайса получают общую скорость передачи данных, равную отношению выделенной полосы пропускания к сумме независимых одинаково распределённых величин обратной спектральной эффективности; эта сумма описывается точно через многократную свёртку и для снижения вычислительной сложности приближается с помощью центральной предельной теоремы. Полученные распределения используются при построении непрерывной марковской цепи (CTMC), описывающей совместную динамику распределения спектра и числа пользователей в каждом слайсе, с зависящим от состояния управлением доступом и стохастическим перераспределением частот, сохраняющим изоляцию между слайсами. Результаты: Модель даёт аналитические выражения для вероятности блокировки, средней скорости передачи данных на пользователя, среднего числа активных пользователей в каждом слайсе и общей занятости ресурсов. Выводы: Построенная модель является аналитическим инструментом для расчёта параметров спектра и управления доступом в мультитенантских сетях 5G NR при планировании с равной скоростью.

Ключевые слова: 5G NR, CTMC, динамическое управление спектром, планирование с равной скоростью, сетевой слайсинг, система массового обслуживания, Round Robin

Discrete & Continuous Models & Applied Computational Science
ISSN 2658-7149 (Online), 2658-4670 (Print)

2026, 34 (3) 298–315
http://journals.rudn.ru/miph

Review

UDC 616.831-07:004.932
PACS 87.61.-c, 87.57.nm, 87.57.ra, 87.19.lf
DOI: 10.22363/2658-4670-2026-34-3-298-315 EDN: ROHGCA

Reconstructing the volumetric geometry of the cerebral cortex based on magnetic resonance imaging

Ivan V. Brak[1,2], Konstantin G. Leladze[1], Saniya M. Islamova[1], Alexey A. Kuzminykh[3], Gleb A. Kiselev[1]

[1] *RUDN University, 6 Miklukho-Maklaya St, Moscow, 117198, Russian Federation*

[2] *Privolzhsky Research Medical University, 178T Gagarina Ave, Nizhny Novgorod, 603107, Russian Federation*

[3] *Novosibirsk State University, 1 Pirogova St, Novosibirsk, 630090, Russian Federation*

(received: June 18, 2025; revised: February 10, 2026; accepted: March 1, 2026)

Abstract. This review article focuses on the analysis of approaches for reconstructing the volumetric geometry of the cerebral cortex and white matter tracts based on magnetic resonance imaging (MRI) data. Particular attention is given to voxel-based morphometry (VBM) and surface-based morphometry (SBM)—two key methodologies for the quantitative analysis of brain structure. The algorithmic principles of each method are considered, along with their advantages, limitations, and metric characteristics, including cortical thickness, surface area, and gyrification index. A separate focus is placed on comparing the sensitivity and accuracy of VBM and SBM in identifying morphological changes related to cognitive and neuropsychiatric traits. Additionally, the article discusses the promising tensor-based surface morphometry (TBSM), which is based on differential geometry methods and provides high spatial resolution without topological distortion. This work emphasizes the importance of accurate and reproducible structural brain reconstruction in the context of biomedical technology and neuroscience development.

Key words and phrases: brain morphometry, SBM, VBM, cortical thickness, MRI, anatomical reconstruction, neuroimaging reproducibility

For citation: I. V. Brak, K. G. Leladze, S. M. Islamova, A. A. Kuzminykh, G. A. Kiselev "Reconstructing the volumetric geometry of the cerebral cortex based on magnetic resonance imaging," *Discrete and Continuous Models and Applied Computational Science*, vol. 34, no. 3, pp. 298–315, 2026. DOI: 10.22363/2658-4670-2026-34-3-298-315. EDN: ROHGCA.

1. Purpose of the article

The purpose of this article is to review existing approaches to modeling brain tissue using MRI data and to identify the key criteria for evaluating the reliability of these models. Special attention is paid to international collaborations, their standards, algorithms, and impact on the reproducibility of neuroimaging research.

2. Introduction

Understanding the structure of the human brain is key to deciphering the physical basis of cognitive functions, mental disorders, and individual differences. Reconstructing an accurate volumetric geometry of the cortex and white matter tracts is not only a technical challenge but also a foundation for a new neuroscience—quantitative, reproducible, and scalable. Modern methods make it possible to reconstruct the three-dimensional morphology and topology of gray and white matter with high resolution based on MRI data, which is fundamentally important for clinical diagnostics, neuroscience, and cognitive research.

To ensure the accuracy and reproducibility of studies, international consortia and national initiatives have been established, which define the standards for processing and analyzing neuroimaging data.

© 2026 I. V. Brak, K. G. Leladze, S. M. Islamova, A. A. Kuzminykh, G. A. Kiselev

This work is licensed under a Creative Commons "Attribution-NonCommercial 4.0 International" license.

3. International collaborations in neuroimaging

In recent years, an increasing number of international organizations and consortia have emerged, focusing on brain research based on morphometric data. Some of the most notable include:

- One of the most notable is the ENIGMA Consortium, a collaborative network of researchers that brings together data from 70 scientific institutions around the world. ENIGMA conducts large-scale meta-analyses of neuroimaging and genetic data from over 12,826 participants (and approximately 25,000 participants when including data from the CHARGE consortium for replication). The main areas of the consortium's work are psychiatric disorders, brain genetics, and neurodevelopment. ENIGMA develops and applies standardized (harmonized) protocols for analyzing MRI data, which allows for consistent measurements and meta-analyses of brain structures in multicenter studies [1].
- The Human Connectome Project (HCP) is an NIH Neuroscience Blueprint-funded interdisciplinary initiative aimed at systematically mapping the macroscopic contours of the human brain and their relationship to behavior in a large population of healthy adults. The project uses multimodal MRI data, including structural MRI, resting-state functional MRI (rfMRI), task-based functional MRI (tfMRI), and diffusion MRI (dMRI). The project develops and optimizes modern algorithms and data processing pipelines for accurate reconstruction of cortical geometry (with a resolution of 0.7 mm isotropically) and white matter tractography [2].
- The Brainnetome Project is a Chinese initiative launched in 2010 by the Ministry of Science and Technology of China. The project aims to create a new functional-anatomical atlas of the brain (brainnetome atlas) based on multimodal MRI data (including structural, diffusion, and functional MRI) and the analysis of structural and functional connectivity patterns. The project develops a highly accurate parcellation of cortical and subcortical regions, taking into account their connections [3, 4].
- CHIMGEN (China Imaging Genetics Project)—a Chinese project that employs structural and functional neuroimaging, genetic analysis, and psychometric testing to build brain models that account for both genetic and environmental factors [5].
- SRPBS (Strategic Research Program for Brain Sciences) is a Japanese national research program that has created one of the largest multicenter databases of multidisciplinary neuroimaging (primarily resting-state fMRI). The program has supported the development of standardized data collection protocols across multiple scanners, as well as methods for harmonizing data between centers to identify biomarkers for mental disorders
- COCORO (Cognitive Genetics Collaborative Research Organization)—a Japanese multicenter project focusing on cognitive disorders and the reconstruction of cortical morphology in patients with psychoses, schizophrenia, and bipolar disorder [6], and bipolar disorder [7].

These projects not only define standards for data acquisition and processing but also provide accessible databases, analysis tools, and software environments (e.g., FreeSurfer [8], FSL, BrainSuite), enabling researchers worldwide to reproduce reconstructions and conduct comparative studies.

However, despite these achievements, a critical evaluation of the employed methodologies remains essential—from voxel- and surface-based morphometry to more complex probabilistic models based on machine learning and deep learning. Even minor artifacts or preprocessing biases can affect the topology of the reconstructed model, and the use of AI may amplify systematic errors. Therefore, the accuracy of structural reconstruction becomes a critical factor in establishing trust in the conclusions of neuroimaging analysis.

4. Computational framework for cortical reconstruction

The technical framework for reconstructing and analyzing the volumetric geometry of the cerebral cortex involves a sophisticated computational pipeline. This study utilizes high-precision software

environments that integrate statistical computing with differential geometry. The primary tools are detailed below:

- Computational Anatomy Toolbox (CAT12): As an advanced extension of the SPM12 (Statistical Parametric Mapping) package within the MATLAB environment, CAT12 provides a streamlined pipeline for both Voxel-Based Morphometry (VBM) and Surface-Based Morphometry (SBM). It employs an Adaptive Maximum A Posterior (AMAP) segmentation approach and a Partial Volume Estimation (PVE) model to account for mixed tissue types. For surface reconstruction, CAT12 utilizes a projection-based thickness (PBT) method, which allows for accurate cortical thickness estimation even in regions with high curvature without the need for manual edits.
- FreeSurfer Suite (v7.4/8.0): An essential tool for creating topologically correct 3D meshes of the brain. The pipeline involves intensity normalization, skull stripping, and the generation of the white matter (inner) and pial (outer) surfaces. FreeSurfer's unique strength lies in its spherical registration system, which aligns cortical folding patterns to a standardized atlas (fsaverage), enabling high-resolution group-level vertex-wise analysis.
- Standardized Neuroanatomical Templates: Spatial normalization and anatomical localization are anchored to the MNI152 (Montreal Neurological Institute) template. For surface-based analysis, the Desikan-Killiany (DK) and Destrieux atlases are utilized to automatically parcellate the cortex into functionally and anatomically distinct regions of interest (ROIs).
- Additional Processing Libraries: The integration of FSL (FMRIB Software Library) for brain extraction (BET) and ANTs (Advanced Normalization Tools) for non-linear registration ensures robust preprocessing and minimizes spatial distortion across diverse MRI datasets.
- TRACULA (TRActs Constrained by UnderLying Anatomy): Integrated within the FreeSurfer environment, this tool is utilized for the automated reconstruction of major white matter pathways using a global probabilistic tractography approach, which accounts for anatomical priors to improve the reliability of connectivity models.

5. Morphometric analysis of the human brain

Brain morphometry refers to a set of quantitative methods aimed at measuring the geometric characteristics of brain structures based on neuroimaging, most commonly magnetic resonance imaging (MRI). Unlike visual assessment, the morphometric approach enables numerical evaluation of volume [9–12], Thickness [9–13], surface area [10–12, 14, 15], and curvature [10–13] of various brain regions, as well as their spatial arrangement (topography) [11, 14, 16, 17] and symmetry [11, 14, 15, 18]. These metrics [19] become particularly important for identifying both individual and group-level differences—within the normative range and in neurodegenerative and neuropsychiatric conditions, such as Alzheimer's disease [20], depressive [2] and schizotypal disorders.

One of the key objectives of morphometry is the construction of anatomically accurate, reproducible, and comparable brain models suitable for both fundamental research and clinical diagnostics. Differences in the morphology of the cortex, subcortical structures, and white matter tracts can reflect a wide spectrum of cognitive, behavioral, and pathological characteristics. For example, the works by Sao et al. [21] and Fischl et al. [13] clearly demonstrate how variations in cortical thickness—both global and local patterns—can predict cognitive status and disease; and study [22] shows that the trajectory of cortical thickness changes correlates with cognitive abilities (memory, attention, executive functions). In [23], it is shown that reductions in gray matter volume in the caudate nucleus and prefrontal cortex in children and adolescents negatively affect executive functioning and cognitive control, which complicates academic performance.

Beyond its diagnostic utility, morphometry plays an important role in understanding the principles of brain organization. When combined with behavioral, genetic, and psychometric data, it enables the identification of links between brain anatomy and function, between biology and psyche. This is especially relevant in the era of big data, where current scientific organizations and consortia are working to identify reproducible patterns of brain organization across thousands and tens of thousands of subjects, developing new—including stochastic—methods for their detection [24–27].

Moreover, morphometric techniques form the foundation of modern approaches to building digital twins of the brain — high-precision models that are becoming increasingly relevant with the integration of artificial intelligence technologies into medicine. The reliability of such models depends on the accuracy of morphometric analysis, the quality of input data, and the correctness of the algorithms used. Therefore, the development and evaluation of morphometric methods is a critical task not only for neuroscience but also for the entire biomedical technology industry [28, 29].

This article reviews the principal approaches to cortical brain morphometry: voxel-based and surface-based, as well as the data quality criteria and processing pipelines that determine the reliability of cortical reconstruction results.

6. MRI-based morphometric approaches to brain reconstruction

The standard approaches in morphometric analysis are voxel-based and surface-based morphometry. Both allow for the assessment of structural brain changes. Voxel-based morphometry analyzes tissue volume at the voxel level, while surface-based morphometry focuses on cortical surface characteristics such as thickness and curvature. Both methods operate within a single spatial scale and do not detect patterns emerging at different levels of organization, which limits their analytical power [21].

6.1. Voxel-based morphometry

Voxel-Based Morphometry (VBM) is a technique for quantitatively assessing anatomical differences in the brain by analyzing brain tissue structure directly in the volume of three-dimensional MRI data at the voxel level.

The general VBM processing pipeline includes the following steps:

1. The VBM workflow begins with spatial normalization, in which individual MRI scans are transformed into a standard anatomical space [14]. This is achieved using non-linear registration algorithms based on image intensities and anatomical templates, allowing for the alignment of corresponding brain regions across individuals.
2. At the next stage, tissue segmentation is performed, dividing brain tissue into major classes: gray matter, white matter, and cerebrospinal fluid. This step employs classification algorithms, most commonly based on statistical modeling of voxel intensity values and their spatial characteristics.
3. The segmented images then undergo spatial smoothing, which increases the sensitivity of statistical analysis by reducing inter-subject variability in the localization of specific structures.
4. In the final step, statistical analysis is carried out to compare the volumes or densities of gray matter at the voxel level either between subject groups or in relation to a continuous variable. The output is a statistical map highlighting brain regions with significant structural differences.

Thus, the VBM pipeline enables automated and objective comparison of anatomical features directly from 3D MRI data, bypassing the surface reconstruction stage that is characteristic of surface-based morphometry.

6.2. Surface-based morphometry

Surface-Based Morphometry (SBM) is an MRI analysis approach focused on the geometry and metrics of the cortical surface. There are several key variations and techniques implementing SBM, differing in analytical goals, types of metrics, and underlying algorithms [30].

SBM is frequently employed for morphometric reconstruction. For instance, study [14] describes the use of this approach for automated segmentation of the cerebral cortex based on structural magnetic resonance imaging data. The input consists of high-quality T1-weighted brain MRI scans, which are first subjected to artifact correction, intensity normalization, skull stripping, and generation of a three-dimensional model of the gray–white matter boundary.

In SBM, cortical surface reconstruction is performed such that each MRI volume is represented as an inflated ("unfolded") surface of the brain, allowing access to structures typically hidden within sulci and gyri. A critical requirement for the input images is high spatial resolution (approximately 1 mm voxel size), minimal motion artifacts, and clear contrast between gray and white matter. Cortical surfaces are matched to one another via mapping to a spherical template [31], followed by automatic registration based on curvature and the geometry of sulcal and gyral patterns [32].

The outputs of the SBM approach are anatomically accurate maps delineating cortical regions of interest, each corresponding to specific gyri or sulci. In [14], 34 such regions were automatically labeled in each hemisphere. These maps exhibit high precision and reproducibility: the average spatial discrepancy between automated and manual labeling does not exceed one millimeter, and the intraclass correlation coefficient (ICC) is approximately 0.835, indicating strong agreement and validity of the developed method. These results highlight the effectiveness of SBM in both research and clinical contexts that require precise and reproducible anatomical localization on the cortical surface.

Like VBM, SBM is highly dependent on the quality of the input data. Study [10] explores surface-based morphometry in depth, with an emphasis on cortical surface reconstruction and cortical thickness estimation. A central focus is the correction of topological defects that arise during cortical surface reconstruction from MRI data. As in [14], the input consists of T1-weighted brain MR images, which must meet high spatial resolution requirements and demonstrate stable intensity characteristics. However, the method is also capable of adapting to intensity variations caused by histological differences and scanner artifacts.

A notable innovation described in the study is the approach to correcting surface topology. Rather than attempting to construct a surface with an assumed correct topology from the outset, the authors begin with a surface that may contain defects and iteratively transform it into a spherical shape. This process enables identification of regions with topological errors, which are then locally corrected. This technique significantly improves the geometric accuracy of the reconstructed model and reduces manual labor, thereby enhancing the automation of the surface reconstruction process and making it suitable for large-scale clinical and research studies [33].

The output of this method is an accurate model of the cortical surfaces, including both the inner (gray–white matter boundary) and outer (pial) surfaces. A key outcome is the high accuracy of cortical thickness measurements—reaching a resolution of less than a quarter millimeter—confirmed by multiple validation studies, including comparison with histological data. This enables the detection of morphometric changes associated with various pathological conditions, age-related differences, or neuropsychological traits with exceptionally high sensitivity and reproducibility.

SBM Results Enable, in Particular, the following:

- Analyzing language lateralization and cortical asymmetry by calculating cortical thickness and other morphometric parameters in regions associated with language function. The resulting data are used to assess structural asymmetry of the brain, enabling precise identification of interhemispheric differences in cortical thickness in language-related areas [18].
- Studying the relationship between cortical folding and the location of cytoarchitectonic fields (Brodmann areas). The authors of [16] use SBM to construct spatial models of cortical surfaces onto which boundaries of cytoarchitectonic fields, derived from postmortem histological studies, are projected. A key finding of the study is that the cortical surface—its folds and gyri—can serve as reliable predictors of the location of different cytoarchitectonic fields.

Thus, a general workflow (processing pipeline) of SBM can be outlined as follows:

1. The input data consist of T1-weighted magnetic resonance images (MRI) of the human brain. During preprocessing, correction of artifacts and distortions is performed, along with intensity inhomogeneity normalization and removal of non-relevant structures such as the skull and meninges, in order to isolate the gray and white matter regions [10, 14].

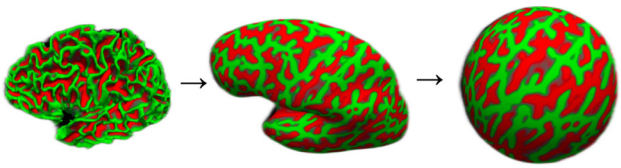


Figure 1. The process of transforming brain geometry into a spherical representation using the inflation procedure (source: compiled by the authors).

2. At the next stage, segmentation and reconstruction of the inner cortical surface are carried out—this surface represents the gray–white matter boundary. It is reconstructed first, as it is the most clearly distinguishable structure in MRI due to the high contrast between gray and white matter and the absence of topological ambiguities that are characteristic of the outer (pial) surface.

   The reconstruction process employs a method of adaptive surface deformation, in which the surface is gradually fitted to the local intensities of gray and white matter [17]. This method involves modifying the geometry by optimizing the following functionals:

   (a) An energy functional is employed to minimize metric distortions (distance-based metric). Specifically, the mean squared error functional J_d is used:

   $$J_d = \frac{1}{V}\sum_{i=1}^{V}\sum_{n\in N(i)}\frac{1}{2}\left(d_{in}^t - d_{in}^0\right)^2,$$

   where V – amount of vertices, d_{in}^t – distance between vertices at time t, d_{in}^0 – initial distance between vertices, and $N(i)$ - neighborhood of vertex i.

   (b) The area-oriented energy functional J_a is used to minimize surface area distortions during surface unfolding:

   $$J_a = \frac{1}{T}\sum_{i=1}^{T}\frac{1}{2}P(A_i^t)\left(A_i^t - A_i^0\right)^2,$$

   where T is the number of triangles in the surface mesh, A_i^t is the area of triangle i at time t, A_i^0 is the initial (reference) area of triangle i, and $P(A_i^t) = \mathbb{I}(A_i^t < 0)$ is a penalty function that activates when the triangle area becomes negative, which indicates the presence of surface folding.

   (c) The total energy functional combines both the metric distortion and surface area preservation terms:

   $$J = \lambda_d \cdot J_d + \lambda_a \cdot J_a,$$

   where λ_d and λ_a are weights that determine the contribution of each component.

3. Next, topological correction of the surface is performed, which constitutes a critical step in the SBM processing pipeline. The initially reconstructed surface may contain topological defects, such as “bridges” between gyri or holes within sulcal surfaces. A specialized approach is applied in which the surface is mapped onto a spherical model [17], enabling straightforward detection and localization of such topological errors. The mapping can be performed either by inflating the cortical surface until it approximates a sphere, or conversely, by deflating the spherical model until it conforms to the pial surface [34, 35].

   The identified defects are then corrected using local algorithms that take into account the intensity profile of the original MRI image, allowing for the restoration of correct surface topology without the loss of meaningful cortical regions [36].

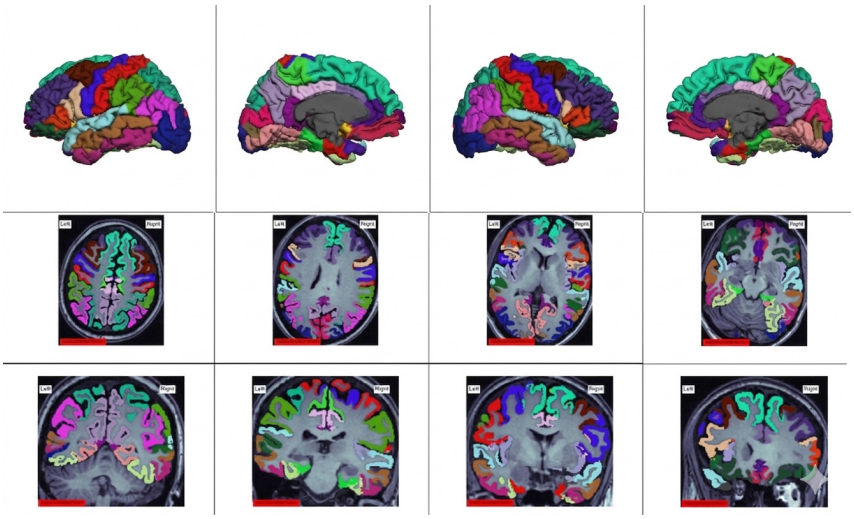


Figure 2. Example of SBM application in the analysis of individual variability in cortical structures in patients with major depressive disorder: lateral and medial views (a); axial and coronal views (b) (source: compiled by the authors).

4. Once a topologically correct inner surface of the brain has been obtained, the outer (pial) surface — representing the external boundary of the gray matter—is reconstructed. This is achieved by progressively deforming the inner surface outward until it reaches the interface between gray matter and cerebrospinal fluid, again using the adaptive algorithms described above, which account for both signal intensity variations and cortical folding curvature. As a result of this stage, two mutually aligned surfaces (the gray–white matter boundary and the pial surface) are formed, enabling precise computation of cortical thickness at any point on the cortical surface [15, 16].
5. The final stage of the SBM pipeline is the morphometric analysis. The reconstructed surfaces are registered and mapped into a standard anatomical space, allowing for statistical comparisons across different subjects and groups. At this stage, the following parameters are computed using numerical methods [13]:
   - Cortical thickness is defined as the shortest distance between the white matter surface and the pial surface. For each point p on the cortical surface, its local thickness is calculated as $T(p) = \text{dist}(S, S_{\text{pial}})$.
   - Cortical volume is computed as the surface integral of cortical thickness over the pial surface: $V = \int T(p)\, dS$.
   - Surface area is calculated as the surface integral over the pial surface: $A = \int dS$.

The accuracy of this method reaches a level of less than a quarter of a millimeter, ensuring high reproducibility and sensitivity to changes that may reflect age-related, pathological, or neuropsychological characteristics of the cerebral cortex.

Below are the main parameters and metrics analyzed using SBM:

- Cortical thickness—the most commonly used SBM parameter, calculated as the distance between the gray–white and gray–CSF boundaries of the cortex [37]. It is used, for example, to study age-related changes, neurodegenerative diseases (including Alzheimer's disease), and neuroplasticity.
- Surface area—reflects both the developmental and individual characteristics of the brain structure.

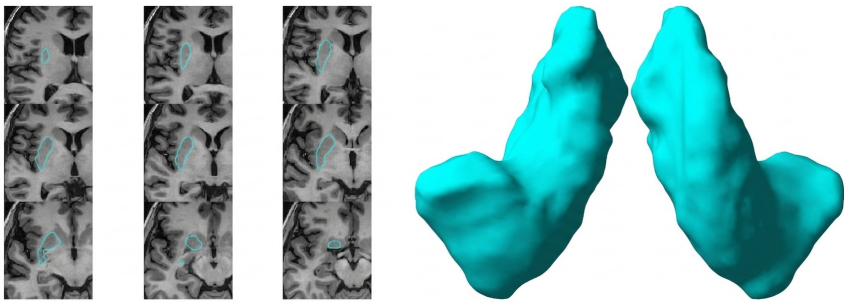


Figure 3. Example of SBM application for analyzing individual variability in subcortical structures of the cerebral hemispheres in patients with major depressive disorder (source: compiled by the authors).

- Gyrification index [6]—quantifies the degree of cortical folding and is calculated as the ratio of the total pial (folded) surface area to the area of its convex hull: $GI = \frac{A}{A_{\text{conv}}}$ [38]. This index is particularly relevant in studies of brain development and psychiatric disorders [39].
- Curvature—describes the shape of the cortex, including convexity and concavity. In [13], curvature is derived directly from the second derivative of the surface, which can be obtained using numerical methods [40].

Several variants of SBM can be distinguished, differing in the operations performed during morphometric analysis:

- Classical approach [10]. Utilizes segmentation of T1-weighted images to build individual surface models; suitable for evaluating cortical thickness, surface area, and curvature.
- Statistical SBM with nonparametric testing [41]. Employs analysis of displacement vector fields along with permutation testing to assess the significance of observed changes.
- Multimodal SBM [39]. Integrates data from functional MRI, diffusion MRI, or metabolic imaging to enable a more comprehensive understanding of structure–function relationships.
- Morphometry of subcortical surfaces [42]. Applied to structures such as the hippocampus and amygdala, using 3D surface modeling and mesh node correspondence.

6.3. Comparison of VBM and SBM

The review article [43] discusses the limitations of Voxel-Based Morphometry (VBM) in detecting distributed brain changes due to its univariate analysis framework. The authors propose the use of multivariate models, such as deformation-based morphometry, to better understand inter-regional dependencies within the brain.

The article also outlines the core characteristics of VBM, emphasizing its nature as a univariate approach that applies statistical parametric mapping to spatially normalized brain images. VBM is designed to detect region-specific structural differences in gray matter after spatial normalization, segmentation, and smoothing.

Importantly, the authors note that VBM is not intended for analyzing dependencies between different brain regions. Rather, it identifies local differences in gray matter that are independent of changes in other areas. They also stress that VBM does not replace shape analysis or provide detailed volumetric evaluation of well-defined anatomical structures. In conclusion, the effectiveness of VBM in neuroanatomical research is acknowledged, but the authors argue that analyzing complex spatial interactions requires multivariate approaches.

Surface-Based Morphometry (SBM), on the other hand, offers several substantial advantages over VBM, especially in the context of cortical analysis [37, 43–45]:

- SBM accounts for the natural geometry and topology of the cortex, enabling more precise and biologically meaningful measurements of thickness, surface area, and curvature. In contrast, VBM operates in a volumetric space without respecting the specific characteristics of sulci and gyri, which reduces sensitivity to subtle local changes in cortical structure.
- SBM provides significantly better spatial registration of anatomical structures across subjects. This is achieved by projecting cortical surfaces onto a spherical model and precisely aligning folds and gyri, thereby minimizing inter-individual variability in cortical folding patterns. VBM, by contrast, relies on less sensitive normalization methods that are not well-suited for fine-scale cortical geometry, often resulting in suboptimal alignment between subjects.
- SBM exhibits higher sensitivity to small-scale changes in cortical thickness associated with both normal and pathological states. Since SBM enables direct measurement of cortical thickness as the distance between the pial surface and the gray-white boundary, it achieves submillimeter accuracy that VBM cannot provide.

Thus, VBM does not utilize information about the specific shape of brain structures—only about their density and volume. It may be susceptible to errors from inaccurate normalization or segmentation and relies on mass univariate testing that ignores inter-regional dependencies [46–48].

In contrast, SBM, due to its superior handling of cortical topology and geometry, more precise spatial registration, and greater sensitivity to subtle morphometric changes, is considered the preferred method for detailed analysis of cortical anatomy and is widely used in tools such as FreeSurfer [10].

Additionally, in a study on traumatic brain injury, SBM demonstrated greater sensitivity than VBM in detecting structural changes associated with neuropsychological test performance. This suggests that SBM may be a more accurate approach for correlating brain anatomy with cognitive functions [9].

6.4. Accuracy of VBM and SBM approaches

Accuracy is a quantitative measure of how well a given approach can detect true morphometric differences between groups or conditions (e.g., patients vs. healthy controls). Several key metrics influence and define accuracy:

- Sensitivity – probability of a type I error (false positive)
- Specificity – probability of a type II error (false negative)
- Reproducibility – stability of results across repeated scans
- Spatial accuracy – how precisely the method localizes the effect

The authors of study [9] claim that SBM has greater sensitivity to cortical changes. In a study involving patients with traumatic brain injury, only SBM was able to detect significant correlations between cortical thickness and cognitive test performance, while VBM did not. This indicates a higher sensitivity of SBM in cortical structure analysis.

Furthermore, study [43] demonstrated that the accuracy of VBM is highly dependent on the quality of spatial normalization and smoothing [49]. Errors at these stages can blur local changes and reduce spatial precision, which limits the reliability of VBM-based findings.

Lastly, the review study [39] shows that SBM is more accurate in measuring cortical thickness and gyrification, whereas VBM may be more effective for assessing subcortical and global volumetric changes. The authors conclude that the best practice is to use both methods in combination for a comprehensive assessment.

A comparison table summarizing the analytic properties of the reviewed morphometric methods is presented below.

Table 1

Comparative analysis of Voxel-Based Morphometry (VBM) and Surface-Based Morphometry (SBM)

Characteristic	**Voxel-Based Morphometry (VBM)**	**Surface-Based Morphometry (SBM)**
Analysis space	Volume (3D voxels)	Surface (vertices, polygons)
Measured parameters	Density, gray matter volume	Thickness, area, curvature, gyrification
Accuracy	Lower for cortical analysis, sensitive to registration	Higher, especially for submillimeter cortical thickness
Application	Assessment of overall volumetric changes	Detailed cortical analysis and folding patterns
Software tools	SPM, FSL, CAT12 (VBM module)	FreeSurfer, CAT12 (SBM module), BrainVISA
Robustness to distortions	Lower due to nonlinear normalization	Higher, performed on native cortical geometry
Computational load	Relatively Lower	Higher; requires intensive surface reconstruction
Anatomical accuracy	Limited (surface features not accounted for)	High (direct vertex-wise analysis)
Sensitivity	Lower after Gaussian smoothing	Higher, uses surface-constrained smoothing
Best use case	Global atrophy, subcortical structures	Subtle cortical changes, neurodevelopment

7. Quality check and reliability of structural reconstruction

To ensure the accuracy and reproducibility of volumetric and surface-based models, a rigorous multi-stage Quality Check (QC) protocol is essential. Structural reconstruction is highly sensitive to image artifacts, and even minor preprocessing biases can lead to significant errors in cortical thickness or volume estimation. The QC framework implemented in modern morphometric studies consists of the following key components:

7.1. Raw data screening and artifact detection

The initial stage involves a systematic evaluation of T1-weighted MRI scans before any automated processing. This includes:

- Motion Artifacts: Identifying “ringing” or “ghosting” effects caused by subject movement, which can blur the gray-white matter boundary.
- Signal-to-Noise Ratio (SNR): Calculating the SNR and Contrast-to-Noise Ratio (CNR) to ensure sufficient image clarity for tissue segmentation.
- Field Inhomogeneity: Correcting for B1 magnetic field non-uniformity (bias field), which can cause intensity variations across the brain.

7.2. Automated quality indices (QA metrics)

Modern tools like CAT12 provide objective numerical indices to evaluate reconstruction quality:

- Weighted Average Image Quality Rating (IQR): A composite score based on noise, resolution, and inhomogeneity. Reconstructions with an IQR below "Satisfactory" (typically < 70%) are excluded from the analysis.
- Euler Number: In surface-based morphometry, the Euler number is used as a quantitative measure of topological complexity. A lower Euler number indicates more topological defects (holes or bridges) in the reconstructed cortical mesh.

7.3. Visual inspection and boundary verification

Despite automated metrics, visual inspection remains the "gold standard". This process involves:

- Segmentation Accuracy: Verifying that the automated tool correctly distinguished between gray matter, white matter, and cerebrospinal fluid (CSF).
- Pial and White Matter Surface Alignment: Ensuring that the reconstructed surfaces accurately follow the anatomical boundaries of the cortex. Particular attention is paid to the temporal lobes and areas near the dural sinuses, where segmentation errors are most frequent.

7.4. Topological correction and statistical robustness

To maintain the integrity of the 3D model, any detected topological defects must be repaired. Spherical inflation and deflation techniques are used to ensure the mesh is a manifold. Finally, the reliability of the measurements is assessed using the Intraclass Correlation Coefficient (ICC), ensuring that the morphometric markers are stable across repeated scans or different processing sessions.

By implementing this comprehensive QC protocol, researchers can minimize the risk of "false positive" structural changes and ensure that the reconstructed geometry reflects true biological variation rather than technical noise.

8. Multiscale approach

The study by [21] introduces a method implementing tensor-based surface morphometry (TBSM), a modern approach for analyzing structural changes in the cerebral cortex. TBSM is based on concepts from differential geometry and tensor calculus, allowing for direct examination of geometric changes in the cortical surface while avoiding distortions inherent in traditional methods that require surface flattening.

The TBSM processing pipeline begins with automatic segmentation of cortical surfaces from T1-weighted MRI scans, which are pre-classified into gray matter, white matter, and cerebrospinal fluid. These surfaces are then modeled as continuous triangular meshes, followed by a mathematical description of surface deformation over time. A key innovation is the use of tensor geometry, which enables the computation of local changes in surface area, cortical thickness, and curvature.

A core advantage of TBSM is its ability to measure local changes in morphometric parameters directly on cortical surfaces with high sensitivity. The approach also incorporates diffusion-based smoothing on cortical surfaces, which improves the signal-to-noise ratio and enhances the accuracy of statistical inference. As a result, TBSM enables precise localization of areas with significant cortical thickness increases or decreases, as well as changes in curvature and surface area—particularly relevant for studies of brain development and neurodegenerative diseases.

Tensor-based surface morphometry (TBSM) differs from traditional surface-based morphometry (SBM) in both its mathematical framework and data analysis methods. While SBM uses classical geometry to reconstruct the cortical surface and evaluate parameters such as thickness, area, and curvature, TBSM relies on more advanced differential and tensor geometry. This allows deformations to be described using tensors, providing greater precision in investigating both local and global changes in brain shape.

Moreover, TBSM avoids distortions typical of traditional methods: in SBM, complex cortical structures are often projected onto simplified forms (e.g., a sphere), which can distort geometric properties [50]. In contrast, TBSM analyzes data directly on the original cortical surface, without simplification, reducing error and enabling more accurate registration.

An additional advantage of TBSM is its heightened sensitivity to subtle morphometric changes. Thanks to diffusion-based smoothing adapted to curved surfaces, this method allows for more precise localization and quantitative assessment of even small changes in cortical shape and thickness—capabilities that are unattainable with standard smoothing in SBM.

Finally, the tensor-based framework of TBSM enables the integration of multiple morphometric characteristics—cortical thickness, curvature, surface area, and volume—into a single analytical model. In traditional SBM, these parameters are typically analyzed separately, which limits the comprehensiveness of the analysis.

Thus, TBSM represents a more advanced analytical method, providing more precise and reliable characterization of structural changes in the cerebral cortex by employing a tensor-based approach and preserving the natural geometry of cortical surfaces.

9. Results

The comparative analysis presented in this review demonstrates that Surface-Based Morphometry (SBM) consistently outperforms Voxel-Based Morphometry (VBM) in the context of cortical structure analysis. SBM achieves submillimeter accuracy in cortical thickness estimation (less than 0.25 mm), whereas VBM is limited by its dependence on spatial normalization and Gaussian smoothing, which reduce spatial precision. As summarized in Table 1, SBM provides higher sensitivity, better anatomical accuracy, and more robust handling of cortical topology compared to VBM.

Furthermore, the emerging Tensor-Based Surface Morphometry (TBSM) approach addresses key limitations of classical SBM by avoiding geometric distortions introduced during spherical projection. TBSM enables the integration of multiple morphometric parameters — cortical thickness, curvature, surface area, and volume — into a unified analytical framework, offering enhanced sensitivity to subtle morphometric changes.

The analysis of international collaborations (ENIGMA, HCP, Brainnetome, CHIMGEN, SRPBS, COCORO) reveals that standardized data acquisition protocols and harmonized processing pipelines are essential for ensuring the reproducibility of morphometric findings across multicenter studies. The Quality Check framework, encompassing raw data screening, automated quality indices, visual inspection, and topological correction, provides a necessary methodological foundation for reliable structural reconstruction.

10. Discussion

The findings of this review highlight several important considerations for the field of brain morphometry. While VBM remains a computationally efficient tool suitable for rapid assessment of global volumetric changes and subcortical structures, its univariate nature and sensitivity to registration errors limit its applicability for fine-grained cortical analysis. In contrast, SBM, by respecting the natural geometry and topology of the cortex, provides more biologically meaningful measurements.

A key observation is that no single morphometric approach is universally optimal. As demonstrated by the reviewed studies, VBM may be more effective for assessing subcortical and global volumetric changes, while SBM excels in detecting subtle cortical thickness variations associated with neurodegenerative and neuropsychiatric conditions. The best practice, as suggested by the literature, is to employ both methods in combination for a comprehensive assessment.

The TBSM approach represents a significant methodological advancement. By operating directly on the original cortical surface without simplification to spherical models, it reduces geometric distortion and enables more precise registration. However, TBSM is still an emerging technique, and further validation across diverse datasets and clinical populations is needed to establish its reliability for routine use.

The importance of rigorous quality control cannot be overstated. Even minor preprocessing biases or image artifacts can propagate through the reconstruction pipeline and lead to erroneous morphometric conclusions. The multi-stage QC protocol described in this review — from raw data screening to topological correction — should be considered a mandatory component of any morphometric study.

11. Conclusion and future work

The main approaches to reconstructing the volumetric geometry of the cerebral cortex based on magnetic resonance imaging have been reviewed, focusing on the comparative analysis of voxel-based morphometry (VBM) and surface-based morphometry (SBM). It has been shown that while VBM remains a computationally efficient tool for rapid assessment of global volumetric changes, it is inherently limited by its univariate nature and dependence on spatial normalization, which often leads to the underestimation of subtle morphological differences. In contrast, SBM provides more accurate and anatomically meaningful results by considering the natural topology and geometry of cortical structures. By directly measuring parameters such as cortical thickness, surface area, and gyrification index, SBM achieves submillimeter precision and increased sensitivity to neurodegenerative and neuropsychiatric changes. Furthermore, the emerging tensor-based surface morphometry (TBSM) approach offers significant prospects for mitigating geometric distortions inherent in traditional methods, allowing for the integration of various morphometric metrics into a unified, multiscale analytical process where cortical deformations are treated as interconnected biological events.

The current review highlights that the transition from traditional voxel-based analysis to surface-oriented and multiscale frameworks is a necessary step for high-precision neuroimaging. However, the field is rapidly moving beyond pure structural metrics toward integrated platforms that combine automated reconstruction with clinical intervention planning. Our future research will be centered around the development and implementation of the NextBrain ecosystem, which aims to bridge the gap between theoretical morphometry and practical neurosurgery. In the upcoming stages of this research, we plan to conduct a comprehensive analysis of automated methods for reconstructing brain white matter tracts, including TRACULA, AFQ, and TractSeg. Particular attention will be given to probabilistic tractography constrained by anatomical priors, enabling the simultaneous reconstruction of the cortical mantle and the underlying white matter connectivity to provide a complete structural connectome.

To ensure the reliability of these complex models, the study will address critical preprocessing steps for diffusion-weighted imaging (DWI), such as motion artifact correction, eddy current compensation, and both affine and non-linear transformations. These technical refinements will allow for the formulation of standardized quality criteria for input data, which is essential for the clinical translation of morphometric markers. A pivotal direction in the NextBrain project is the development of specialized algorithms for anatomical tumor parcellation and mapping. By utilizing the geometric constraints of the reconstructed cortex, we plan to implement automated segmentation of oncological lesions and analyze their spatial relationship with functionally active cortical zones. This level of detail is crucial for personalized medicine, where the anatomical labeling of a tumor is directly linked to its impact on the surrounding neural architecture.

Furthermore, the volumetric models generated via the NextBrain atlas will serve as the technical foundation for stereotactic and functional neurosurgery. By providing high-resolution 3D reconstructions of the pial surface and subcortical structures, the system will enable more accurate trajectory calculation and minimize the risk of damaging eloquent brain areas during invasive procedures. The experimental part of our future work will involve the reconstruction of structural models across multiple international datasets, followed by automatic validation and comparative

analysis of white matter tracts. This rigorous validation process will help identify the most accurate and reproducible solutions suitable for real-time fusion with intraoperative data, creating a dynamic navigation environment for neurosurgeons.

In conclusion, the advancement of tools like NextBrain signifies a fundamental shift toward personalized neuroanatomy. In this emerging paradigm, 3D reconstruction is not merely a research metric but a vital component of clinical decision-making and surgical precision. By integrating multiscale morphometry with tractography and oncological mapping, we move closer to a comprehensive digital model of the human brain that can directly inform and improve patient outcomes in complex neurological conditions.

Author Contributions: Conceptualization, Ivan V. Brak and Saniya M. Islamova; methodology, Ivan V. Brak and Gleb A. Kiselev; software, Alexey A. Kuzminykh; validation, Ivan V. Brak, Konstantin G. Leladze, Saniya M. Islamova, Gleb A. Kiselev and Alexey A. Kuzminykh; formal analysis, Saniya M. Islamova; investigation, Saniya M. Islamova; resources, Ivan V. Brak and Gleb A. Kiselev; data curation, Alexey A. Kuzminykh; writing—original draft preparation, Saniya M. Islamova and Gleb A. Kiselev; writing—review and editing, Ivan V. Brak, Alexey A. Kuzminykh and Gleb A. Kiselev; visualization, Alexey A. Kuzminykh; supervision, Ivan V. Brak; project administration, Gleb A. Kiselev; funding acquisition, Ivan V. Brak. All authors have read and agreed to the published version of the manuscript.

Funding: This research was supported by the strategic project "Innovative Technologies in Strengthening the Mental Health of Children and Adults," "Priority-2030" program of the Privolzhsky Research Medical University.

Data Availability Statement: Data sharing is not applicable to this article as no new datasets were generated or analyzed during the current study. The review is based on previously published research and publicly available neuroimaging protocols.

Acknowledgments: The authors express their gratitude to the administration of the Privolzhsky Research Medical University for the institutional support and the provision of resources necessary for the development of the structural reconstruction frameworks.

Conflicts of Interest: The authors declare no conflict of interest. The funders had no role in the design of the study; in the collection, analyses, or interpretation of data; in the writing of the manuscript; or in the decision to publish the results.

Declaration on Generative AI: The authors have not employed any generative AI tools.

References

[1] S. Hellard et al., "The ENIGMA Consortium: large-scale collaborative analyses of neuroimaging and genetic data," *Brain Imaging and Behavior*, vol. 8, pp. 153–182, 2014.

[2] D. C. Van Essen, S. M. Smith, D. M. Barch, T. E. J. Behrens, E. Yacoub, and K. Ugurbil, "The WU-Minn Human Connectome Project: An overview," *NeuroImage*, vol. 80, pp. 62–79, 2013. DOI: 10.1016/j.neuroimage.2013.05.041

[3] T. Jiang, "Brainnetome: A new -ome to understand the brain and its disorders," *NeuroImage*, vol. 80, pp. 263–272, 2013. DOI: 10.1016/j.neuroimage.2013.04.002

[4] A. Johnson, T. Pollard, L. Shen, et al., "MIMIC-III, a freely accessible critical care database," *Scientific Data*, vol. 3, p. 160 035, 2016. DOI: 10.1038/sdata.2016.35

[5] Q. Xu, L. Guo, J. Cheng, et al., "CHIMGEN: a Chinese imaging genetics cohort to enhance cross-ethnic and cross-geographic brain research," *Molecular Psychiatry*, vol. 25, no. 3, pp. 517–529, 2020. DOI: 10.1038/s41380-019-0627-6

[6] N. Madeira, J. Duarte, R. Martins, G. Costa, A. Macedo, and M. Castelo-Branco, "Morphometry and gyrification in bipolar disorder and schizophrenia: A comparative MRI study," *NeuroImage: Clinical*, p. 102 220, Jan. 2020. DOI: 10.1016/j.nicl.2020.102220

[7] D. Koshiyama, K. Miura, K. Nemoto, et al., "Neuroimaging studies within Cognitive Genetics Collaborative Research Organization aiming to replicate and extend works of ENIGMA," *Human Brain Mapping*, vol. 43, no. 1, pp. 182–193, 2022. DOI: 10.1002/hbm.25040

[8] C. Gaser, R. Dahnke, P. M. Thompson, F. Kurth, E. Luders, and the Alzheimer's Disease Neuroimaging Initiative, "CAT: a computational anatomy toolbox for the analysis of structural MRI data," *GigaScience*, vol. 13, giae049, Aug. 2024. DOI: 10 . 1093 / gigascience / giae049 eprint: https : / / academic . oup . com / gigascience / article - pdf/doi/10.1093/gigascience/giae049/60707960/giae049.pdf.

[9] N. Upadhyay, A. Munivenkatappa, B. I. Devi, D. K. Subbakrishna, and J. Rajeswaran, "Analysis of various automated structural computing methods in patient with early traumatic brain injury," *The Open Access Journal of Science and Technology*, vol. 2, 2014. DOI: 10.11131/2014/101069

[10] B. Fischl, "FreeSurfer," *NeuroImage*, vol. 62, no. 2, pp. 774–781, 2012. DOI: 10.1016/j.neuroimage.2012.01.021

[11] Y. Wang, L. Hao, Y. Zhang, C. Zuo, and D. Wang, "Entorhinal cortex volume, thickness, surface area and curvature trajectories over the adult lifespan," *Psychiatry Research: Neuroimaging*, vol. 292, pp. 47–53, 2019. DOI: 10.1016/j.pscychresns.2019.09.002

[12] N. Makris, J. Kaiser, C. Haselgrove, et al., "Human cerebral cortex: A system for the integration of volume- and surface-based representations," *NeuroImage*, vol. 33, no. 1, pp. 139–153, 2006. DOI: 10.1016/j.neuroimage.2006.04.220

[13] B. Fischl and A. M. Dale, "Measuring the thickness of the human cerebral cortex from magnetic resonance images," *Proceedings of the National Academy of Sciences*, vol. 97, no. 20, pp. 11 050–11 055, 2000. DOI: 10.1073/pnas.200033797

[14] R. S. Desikan, F. Ségonne, B. Fischl, et al., "An automated labeling system for subdividing the human cerebral cortex on MRI scans into gyral based regions of interest," *NeuroImage*, vol. 31, no. 3, pp. 968–980, 2006. DOI: 10.1016/j.neuroimage.2006.01.021

[15] B. Fischl, C. Destrieux, E. Halgren, et al., "Automatically parcellating the human cerebral cortex," *Cerebral Cortex*, vol. 14, no. 1, pp. 11–22, 2004. DOI: 10.1093/cercor/bhg087

[16] B. Fischl, N. Rajendran, E. Busa, et al., "Cortical folding patterns and predicting cytoarchitecture," *Cerebral Cortex*, vol. 18, no. 8, pp. 1973–1980, 2008. DOI: 10.1093/cercor/bhm225

[17] B. Fischl, M. I. Sereno, and A. M. Dale, "Cortical surface-based analysis II: Inflation, flattening, and a surface-based coordinate system," *NeuroImage*, vol. 9, no. 2, pp. 195–207, 1999. DOI: 10.1006/nimg.1998.0396

[18] D. N. Greve, L. Van der Haegen, Q. Cai, et al., "A surface-based analysis of language lateralization and cortical asymmetry," *Journal of Cognitive Neuroscience*, vol. 25, no. 9, pp. 1477–1492, 2013. DOI: 10.1162/jocn_a_00400

[19] A. Klein, S. S. Ghosh, F. S. Bao, et al., "Mindboggling morphometry of human brains," *PLOS Computational Biology*, vol. 13, no. 2, pp. 1–40, Feb. 2017. DOI: 10.1371/journal.pcbi.1005350

[20] Y. He, Y. Huang, Z. Guo, H. Zhu, D. Zhang, C. Xue, X. Hu, C. Xiao, and X. Chai, "MRI-Negative Temporal Lobe Epilepsy: A Study of Brain Structure in Adults Using Surface-Based Morphological Features," *Journal of Integrative Neuroscience*, vol. 23, no. 11, p. 206, 2024. DOI: 10.31083/j.jin2311206

[21] T. Cao, J. C. Pang, A. Segal, Y. C. Chen, K. M. Aquino, M. Breakspear, and A. Fornito, "Mode-based morphometry: A multiscale approach to mapping human neuroanatomy," *bioRxiv*, 2023. DOI: 10.1101/2023.02.26.529328

[22] P. Shaw, D. Greenstein, J. Lerch, et al., "Intellectual ability and cortical development in children and adolescents," *Nature*, vol. 440, pp. 676–679, 2006. DOI: 10.1038/nature04513

[23] A. C. Jagger-Rickels, M. Y. Kibby, and J. M. Constance, "Global gray matter morphometry differences between children with reading disability, ADHD, and comorbid reading disability/ADHD," *Brain Lang.*, vol. 185, pp. 54–66, 2018. DOI: 10.1016/j.bandl.2018.08.004

[24] A. Daoudi and S. Mahmoudi, "Enhancing brain segmentation in MRI through integration of hidden Markov random field model and whale optimization algorithm," *Computers*, vol. 13, no. 5, p. 124, 2024. DOI: 10.3390/computers13050124

[25] P. Kurella, "Convolutional neural networks grid search optimizer based brain tumor detection," *International Transactions on Electrical Engineering and Computer Science*, 2023. DOI: 10.62760/iteecs.2.4.2023.68

[26] R. S. Cruz, L. Lebrat, P. Bourgeat, V. Doré, J. Dowling, J. Fripp, C. Fookes, and O. Salvado, "Going Deeper With Brain Morphometry Using Neural Networks," pp. 711–715, 2021. DOI: 10.1109/ISBI48211.2021.9434039

[27] B. Mosch, V. Hagena, S. Herpertz, and M. Diers, "Brain morphometric changes in fibromyalgia and the impact of psychometric and clinical factors: a volumetric and diffusion-tensor imaging study," *Arthritis Research and Therapy*, vol. 25, 2023. DOI: 10.1186/s13075-023-03064-0

[28] B. Marteau, S. Vashista, M. Chen, et al., "Brain Digital Twin Combining Artificial Intelligence and Extended Reality," pp. 1–8, Dec. 2024. DOI: 10.1109/ICIR64558.2024.10976965

[29] Y. Xiong, B. Liu, D. Wang, T. Zhang, W. Wu, T. Liu, P. Li, G. Shi, and Y. Fan, "Digital Twin Brain: Bridging Biological and Artificial Intelligence via Brain Science," *arXiv preprint arXiv:2308.01941*, 2023.

[30] R. Riccelli, N. Toschi, S. Nigro, A. Terracciano, and L. Passamonti, "Surface-based morphometry reveals the neuroanatomical basis of the five-factor model of personality," *Social cognitive and affective neuroscience*, vol. 12, Jan. 2017. DOI: 10.1093/scan/nsw175

[31] S. Fujita, A. Hagiwara, M. Hori, et al., "Three-dimensional High-resolution Simultaneous Quantitative Mapping of the Whole Brain with 3D-QALAS: An Accuracy and Repeatability Study.," *Magnetic Resonance Imaging*, vol. 63, Aug. 2019. DOI: 10.1016/j.mri.2019.08.031

[32] K. Li, Y. Peng, S. Li, L. Zeng, R. Cao, B. Yu, Y. Zhang, Z. Zhong, and H. Lin, "Correlation between cerebral cortex changes and cognitive dysfunction in patients with obstructive sleep apnea hypopnea syndrome," *Neural Regeneration Research*, vol. 18, no. 11, pp. 2469–2474, 2023. DOI: 10.4103/1673-5374.369493

[33] R. A. Yotter, R. Dahnke, P. M. Thompson, and C. Gaser, "Topological correction of brain surface meshes using spherical harmonics," *Human Brain Mapping*, vol. 32, no. 7, pp. 1109–1124, Jul. 2011, Research supported by NIH grants EB007813, HD050735, EB008432, EB008281. DOI: 10.1002/hbm.21095

[34] B. Fischl, A. Liu, and A. M. Dale, "Automated manifold surgery: constructing geometrically accurate and topologically correct models of the human cerebral cortex," *IEEE Transactions on Medical Imaging*, vol. 20, no. 1, pp. 70–80, Jan. 2001, Research supported by NIH: P41-RR14075, R01-NS39581, R01-RR13609. DOI: 10.1109/42.906426

[35] A. M. Dale, B. Fischl, and M. I. Sereno, "Cortical surface-based analysis. I. Segmentation and surface reconstruction," *NeuroImage*, vol. 9, no. 2, pp. 179–194, Feb. 1999. DOI: 10.1006/nimg.1998.0395

[36] O. Acosta, J. Fripp, V. Doré, et al., "Cortical surface mapping using topology correction, partial flattening and 3D shape context-based non-rigid registration for use in quantifying atrophy in Alzheimer's disease," *Journal of Neuroscience Methods*, vol. 205, no. 1, pp. 96–109, Mar. 2012. DOI: 10.1016/j.jneumeth.2011.12.011

[37] A. C. Evans, "Cortical Surface Morphometry," pp. 157–166, 2015. DOI: 10.1016/B978-0-12-397025-1.00210-4

[38] K. Zilles, E. Armstrong, A. Schleicher, and H. J. Kretschmann, "The human pattern of gyrification in the cerebral cortex," *Anatomy and Embryology*, vol. 179, no. 2, pp. 173–179, 1988. DOI: 10.1007/BF00304699

[39] M. Goto, O. Abe, A. Hagiwara, et al., "Advantages of Using Both Voxel- and Surface-based Morphometry in Cortical Morphology Analysis: A Review of Various Applications," *Magnetic Resonance in Medical Sciences*, vol. 21, no. 1, pp. 41–57, 2022. DOI: 10.2463/mrms.rev.2021-0096

[40] M. Meyer, M. Desbrun, P. Schroder, and A. H. Barr, "Discrete Differential-Geometry Operators for Triangulated 2-Manifolds," pp. 35–57, 2003. DOI: 10.1007/978-3-662-05105-4_2

[41] D. Pantazis, R. M. Leahy, T. E. Nichols, and M. Styner, "Statistical surface-based morphometry using a nonparametric approach," vol. 2, pp. 1283–1286, 2004. DOI: 10.1109/ISBI.2004.1398780

[42] D. P. Devanand, R. Bansal, J. Liu, et al., "MRI hippocampal and entorhinal cortex mapping in predicting conversion to Alzheimer's disease," *NeuroImage*, vol. 60, no. 3, pp. 1622–1629, 2012. DOI: 10.1016/j.neuroimage.2012.01.075

[43] J. A. K.J. Friston, "Generative and recognition models for neuroanatomy," *NeuroImage, Volume 23, Issue 1, 2004, Pages 21-24, ISSN 1053-8119*, vol. 23, no. 1, pp. 21–24, 2004. DOI: 10.1016/j.neuroimage.2004.04.021

[44] N. Voets, M. Hough, G. Douaud, P. Matthews, A. James, L. Winmill, P. J. Webster, and S. M. Smith, "Evidence for abnormalities of cortical development in adolescent-onset schizophrenia," *NeuroImage*, vol. 43, pp. 665–675, 2008. DOI: 10.1016/j.neuroimage.2008.08.013

[45] K. Lai, D. Niddam, J. Fuh, W.-T. Chen, J.-C. Wu, and S.-J. Wang, "Cortical morphological changes in chronic migraine in a Taiwanese cohort: Surface- and voxel-based analyses," *Cephalalgia*, vol. 40, pp. 575–585, 2020. DOI: 10.1177/0333102420920005

[46] J. Ashburner and K. J. Friston, "Voxel-Based Morphometry—The Methods," *NeuroImage*, vol. 11, pp. 805–821, 2000. DOI: 10.1006/nimg.2000.0582

[47] A. Mechelli, C. Price, K. J. Friston, and J. Ashburner, "Voxel-based morphometry of the human brain: Methods and applications," *Current Medical Imaging Reviews*, vol. 1, pp. 105–113, 2005. DOI: 10.2174/1573405054038726

[48] D. Callaert, A. Ribbens, F. Maes, S. Swinnen, and N. Wenderoth, "Assessing age-related gray matter decline with voxel-based morphometry depends significantly on segmentation and normalization procedures," *Frontiers in Aging Neuroscience*, vol. 6, 2014. DOI: 10.3389/fnagi.2014.00124

[49] X. Han, J. Jovicich, D. Salat, A. van der Kouwe, B. Quinn, S. Czanner, E. Busa, J. Pacheco, M. Albert, R. Killiany, et al., "Reliability of MRI-derived measurements of human cerebral cortical thickness: the effects of field strength, scanner upgrade and manufacturer," *NeuroImage*, vol. 32, no. 1, pp. 180–194, Aug. 2006. DOI: 10.1016/j.neuroimage.2006.02.051

[50] M. Chung, "Tensor-Based Surface Morphometry," 2002.

Information about the authors

Brak, Ivan V.—Candidate of Biology Sciences, Senior Lecturer at the Department of Mathematical Modeling and Artificial Intelligence of RUDN University; Researcher of Privolzhsky Research Medical University (e-mail: i.v.brak@gmail.com, ORCID: 0000-0002-5146-0096, ResearcherID: AAM-4659-2021, Scopus Author ID: 24461311200)

Leladze, Konstantin—Student of Department of Mathematical Modeling and Artificial Intelligence of RUDN University (e-mail: 1142230347@pfur.ru)

Islamova, Saniya M.—Student of Department of Mathematical Modeling and Artificial Intelligence of RUDN University (e-mail: 1132249576@rudn.ru, ORCID: 0009-0007-6953-5731)

Kuzminykh, Alexey A.—Student, Novosibirsk State University (e-mail: a.kuzminykh@g.nsu.ru, ORCID: 0009-0008-0642-0328)

Kiselev, Gleb A.—Candidate of Technical Sciences, Senior Lecturer at the Department of Mathematical Modeling and Artificial Intelligence of RUDN University; Researcher of Federal Research Center "Computer Science and Control" of the Russian Academy of Sciences (e-mail: kiselev@isa.ru, ORCID: 0000-0001-9231-8662, ResearcherID: Y-6971-2018, Scopus Author ID: 57195683637)

RUSSIAN METADATA

УДК 616.831-07:004.932
PACS 87.61.-c, 87.57.nm, 87.57.ra, 87.19.lf
DOI: 10.22363/2658-4670-2026-34-3-298-315 EDN: ROHGCA

Восстановление объёмной геометрии коры головного мозга по результатам магнитно резонансной томографии

И. В. Брак[1, 2], К. Г. Леладзе[1], С. М. Исламова[1], А. А. Кузьминых[3], Г. А. Киселёв[1]

[1] *Российский университет дружбы народов, ул. Миклухо-Маклая, д. 6, Москва, 117198, Российская Федерация*

[2] *Приволжский исследовательский медицинский университет, пр. Гагарина, д. 178Т, Нижний Новгород, 603107, Российская Федерация*

[3] *Новосибирский государственный университет, ул. Пирогова, д. 1, Новосибирск, 630090, Российская Федерация*

Аннотация. Настоящая обзорная статья посвящена анализу подходов к восстановлению объёмной геометрии коры головного мозга и проводящих путей на основе данных магнитно-резонансной томографии. Основное внимание уделено воксельно-ориентированной (VBM) и поверхностно-ориентированной (SBM) морфометрии — двум ключевым направлениям в количественном анализе структуры мозга. Рассматриваются алгоритмические принципы каждого подхода, их достоинства, ограничения, а также метрические характеристики, включая толщину коры, площадь поверхности и индекс гирификации. Отдельный акцент сделан на сравнении чувствительности и точности VBM и SBM в выявлении морфологических изменений, связанных с когнитивными и нейропсихическими особенностями. Также рассматривается перспективный тензорно-ориентированный подход (TBSM), опирающийся на методы дифференциальной геометрии и обеспечивающий высокую разрешающую способность без искажения топологии. Работа подчёркивает значимость точной и воспроизводимой структурной реконструкции мозга в контексте развития биомедицинских технологий и нейронауки.

Ключевые слова: морфометрия мозга, SBM, VBM, толщина коры, МРТ, анатомическая реконструкция, воспроизводимость нейровизуализации

Discrete & Continuous Models
& Applied Computational Science
ISSN 2658-7149 (Online), 2658-4670 (Print)

2026, 34 (3) 316–333
http://journals.rudn.ru/miph

Research article

UDC 519.872, 519.217
PACS 02.50.Ey, 02.50.Ga, 07.05.Tp
DOI: 10.22363/2658-4670-2026-34-3-316-333 EDN: RHUTHS

A two-queue JSQ–SLQ service system with absolute preemptive priority and non-zero switch-over times

Evgeny A. Khityaev[1], Ivan S. Zaryadov[1,2], Tatiana A. Milovanova[1]

[1] *RUDN University, 6 Miklukho-Maklaya St, Moscow, 117198, Russian Federation*

[2] *Institute of Informatics Problems, Federal Research Center "Computer Science and Control" of the Russian Academy of Sciences, 44-2 Vavilova St, Moscow, 119333, Russian Federation*

(received: May 10, 2026; revised: June 4, 2026; accepted: June 18, 2026)

Abstract. Purpose. To study a two-queue system with a single server operating under the Join-the-Shortest-Queue (JSQ) routing discipline and the Serve-the-Longest-Queue (SLQ) service discipline, where the destination queue for an arriving customer and the queue to be served are selected according to probabilistic tie-breaking rules when the queue lengths are equal, with absolute preemptive priority and non-zero server switch-over times. Methods. The system is studied using a Markov description, stationary balance equations, conditional probability generating functions, and numerical analysis. Results. The system dynamics are described by a two-dimensional Markov process whose components are the length of the first queue and a phase variable representing the difference between the queue lengths together with the server state. For this process, the stationary balance equations are derived. Conditional probability generating functions are introduced and used to obtain a matrix form of the balance equations and to consider the condition for the existence of a stationary regime. Based on the obtained generating functions, expressions are derived for the main stationary performance measures, including the mean queue lengths, variances, correlation coefficient, effective arrival rates, the probability that the server is in a switch-over state, and the probability that the server is idle. Numerical experiments are performed to evaluate the effect of the arrival rate, service rates, switch-over rates, and probabilistic tie-breaking parameters on the stationary characteristics of the system and on the phase distribution of the underlying Markov process. Conclusions. The results show that the combined use of the JSQ and SLQ disciplines contributes to balancing the queue lengths. However, the system behavior and its stationary characteristics significantly depend on the combination of the arrival rate, service rates, server switch-over rates, and probabilistic tie-breaking parameters.

Key words and phrases: queueing system, join-the-shortest-queue, serve-the-longest-queue, absolute preemptive priority, switch-over times, Markov process, conditional probability generating functions

For citation: E. A. Khityaev, I. S. Zaryadov, T. A. Milovanova "A two-queue JSQ–SLQ service system with absolute preemptive priority and non-zero switch-over times," *Discrete and Continuous Models and Applied Computational Science*, vol. 34, no. 3, pp. 316–333, 2026. DOI: 10.22363/2658-4670-2026-34-3-316-333. EDN: RHUTHS.

1. Introduction

In queueing theory, an important role is played by models that incorporate control mechanisms for customer arrivals and the service process. Such models are widely used in applications where high throughput, efficient load balancing, and low delays are required, in particular in telecommunication networks, data centers, and transportation systems [1–5]. As the load on such systems grows and their structure becomes more complex, dynamic policies that take the current state of the system into account become especially important. These policies make it possible to distribute the customer flow more rationally and to use service resources more efficiently.

© 2026 E. A. Khityaev, I. S. Zaryadov, T. A. Milovanova

This work is licensed under a Creative Commons "Attribution-NonCommercial 4.0 International" license.

One of the classical approaches is the Join-the-Shortest-Queue (JSQ) routing discipline, under which an arriving customer is routed to the subsystem with the shortest queue. This model was first studied in 1958 for a system with two parallel queues and was described by a two-dimensional Markov process [6]. The classical setting assumes Poisson arrivals and exponentially distributed service times, which allows the system to be described in Markovian terms and makes Markov-process methods applicable to its analysis. Since then, the JSQ discipline has been studied in a wide range of queueing models [7–14], including more recent studies [15–19]. The main advantage of the JSQ discipline is that it balances the load by distributing customers among the queues, thereby reducing the risk of overflow in systems with finite buffers and decreasing the mean waiting time [3, 5, 7]. Moreover, it has been shown that in large systems with parallel queues and servers, the mean waiting time under JSQ may converge to zero as the number of queues and servers increases, which illustrates the high efficiency of this discipline [5]. At the same time, JSQ requires information about the current lengths of all queues, which may introduce additional overhead in real systems [20].

Another important approach for improving system performance is the Serve-the-Longest-Queue (SLQ) service discipline, which was considered by Cohen in 1987 [21]. Under this discipline, the server selects the longest queue for service at each decision epoch, which helps equalize queue lengths and prevents individual queues from growing disproportionately. The SLQ discipline was later studied in several related queueing models [22–25]. As a result, SLQ reduces the probability that individual queues become overloaded, which helps to decrease the mean waiting time and, in systems with finite buffers, the loss probability. This is especially important under heavy traffic and in systems with multiple servers, where an uneven distribution of customers may overload some queues even when other servers are idle. In this context, the SLQ discipline has also been studied in the Halfin–Whitt regime [26]. Thus, SLQ can effectively complement routing approaches that balance customer arrivals. At the same time, it requires information about the current queue lengths to select a queue for service.

Combining the JSQ and SLQ disciplines is of particular interest because it allows the routing of arriving customers to be coordinated with the dynamic control of the service process. Models of this type were studied by Perel et al., including a preemptive two-queue system with zero switch-over times [27], a non-preemptive two-queue system with zero and non-zero switch-over times [28], and a preemptive three-queue system with zero switch-over times [29]. In these works, the rule by which the server selects a queue for service is deterministic and based on the comparison of queue lengths: the server selects the longest queue for service. In the preemptive models, the server switches as soon as a non-attended queue becomes longer than the attended one, whereas in the non-preemptive model switching decisions are made only upon service completions. Ties between queues are treated separately. In the two-queue models, when the queue lengths become equal, the server remains at the current queue. In the three-queue model, the same deterministic longest-queue rule is used when there is a unique longest queue; however, if two non-attended queues share the longest length while the attended queue is shorter, the choice between them is made according to a probabilistic tie-breaking rule. Thus, systems in which the server may switch queues even when the queue lengths are equal, according to a probabilistic tie-breaking rule for selecting the queue to be served, are of interest and have not yet been considered. In systems with non-zero switch-over times, preemptive priority may be relative, meaning that an ongoing switch-over cannot be interrupted, or absolute, meaning that the server may interrupt the current switch-over and change its direction of motion.

The present paper considers non-zero switch-over times between the queues and, in contrast to previously studied models, introduces a probabilistic rule for selecting the queue to be served when the queue lengths are equal. This generalization broadens the scope of the model and makes it better suited for systems in which server switching is not purely deterministic.

The proposed model can be used to analyze and optimize systems of this type, including data centers, server clusters, telecommunication networks, and distributed computing systems, where both load distribution and server switch-over times play an important role.

The remainder of the paper is organized as follows. Section 2 describes the model, including the routing and service rules, the switch-over mechanism, and tie-breaking probabilities. In Section 3, a two-dimensional Markov process is introduced and the corresponding stationary balance equations are derived. Section 4 introduces the conditional probability generating functions and discusses the

stability condition for the existence of a stationary regime. Section 5 presents expressions for the main stationary performance measures. Section 6 contains numerical results showing how the main system parameters affect the stationary characteristics and phase probabilities. Section 7 provides a discussion and interpretation of the obtained numerical results. Finally, Section 5 summarizes the results and discusses possible extensions of the model.

2. System description

The system consists of two infinite queues $Q_i,\ i=\overline{1,2}$, a single server, and non-zero server switch-over times between the queues. It operates under an absolute preemptive priority rule, under which the server may interrupt an ongoing switch-over and change its direction.

Customers arrive according to a Poisson process with rate λ. Under the JSQ discipline, each arriving customer joins the currently shortest queue. If the queue lengths are equal, a probabilistic tie-breaking rule is applied: the customer joins queue Q_i with probability $p_i,\ i=\overline{1,2}$, where $p_1+p_2=1$.

Throughout the paper, we use notation partly based on Perel et al. [27–29], adapted to the present model.

Let $L_i(t)$ denote the number of customers in queue $Q_i,\ i=\overline{1,2}$, at time $t>0$.

According to the SLQ discipline, the server selects the longest queue for service. The service time of a customer from queue Q_i is exponentially distributed with rate $\mu_i,\ i=\overline{1,2}$.

Customers in each queue are served according to the First-Come, First-Served (FCFS) discipline. When the server switches over to another queue, the customers remaining in the previous queue stay in the system and wait until the server returns.

The dynamic priority service rule depends on the current queue lengths and is defined as follows.

- If, while the server is serving a customer from queue Q_i, a new customer arrives at queue Q_j, $j\neq i$, and after this arrival $L_j(t)>L_i(t)$, then the server interrupts service in queue Q_i and starts a switch-over to queue Q_j. If after this arrival $L_i(t)=L_j(t)$, then the server continues the current service in queue Q_i with probability q_i or interrupts it and starts a switch-over to queue Q_j with probability $q_j=1-q_i$.
- If, after completing the service of a customer from queue Q_i, the condition $L_i(t)<L_j(t)$, $j\neq i$, is satisfied, then the server starts a switch-over to queue Q_j. If $L_i(t)=L_j(t)$, then the server either remains at the current queue Q_i with probability q_i or switches over to queue Q_j with probability $q_j=1-q_i$.
- Since the priority is absolute, if a new customer arrives at queue Q_i while the server is switching over from queue Q_i to queue Q_j, then, if $L_i(t)>L_j(t)$, the server interrupts the current switch-over and starts switching back from Q_j to Q_i. If $L_i(t)=L_j(t)$, the server either continues switching over to Q_j with probability $q_j=1-q_i$ or returns to queue Q_i with probability q_i.

In all cases, whenever the server starts a switch-over to queue Q_j, the corresponding switch-over time is exponentially distributed with rate $\gamma_j,\ j=\overline{1,2}$.

3. Two-dimensional Markov process and balance equations

Let $D(t)=L_1(t)-L_2(t)$ denote the difference between the numbers of customers in the first and second queues. To describe the position and switch-over state of the server, we introduce the phase variable $J(t)$, which encodes both the value of $D(t)$ and the position or switch-over state of the server. Then the state of the system at time t can be described by the Markov process $\xi(t)=\{L_1(t),J(t)\}$. The probability distribution of this process is defined as follows:

$$P_{n,d}(t)=\mathbb{P}\{L_1(t)=n,J(t)=d\},\quad n\geq 0,\ d\in\mathcal{D},$$

where only admissible pairs (n,d) are considered, and

$$\mathcal{D}=\{1,1_{s_1},0_1,0_{s_1},0_{s_2},0_2,-1_{s_2},-1\}.$$

In each phase, the numerical part of the notation indicates the value of $D(t)$, while the subscript, when present, specifies the position or switch-over state of the server. The phases d are defined as follows:

- 1 means that $D(t) = 1$, the server is located at Q_1, and a new customer joins Q_2.
- 1_{s_1} means that $D(t) = 1$, the server is switching over to Q_1, and a new customer joins Q_2.
- 0_1 means that $D(t) = 0$, the server is located at Q_1, and a new customer joins Q_i with probability $p_i,\ i = \overline{1,2}$, where $p_1 + p_2 = 1$.
- 0_{s_1} means that $D(t) = 0$ and the server is switching over to Q_1.
- 0_{s_2} means that $D(t) = 0$ and the server is switching over to Q_2.
- 0_2 means that $D(t) = 0$, the server is located at Q_2, and a new customer joins Q_i with probability $p_i,\ i = \overline{1,2}$, where $p_1 + p_2 = 1$.
- -1_{s_2} means that $D(t) = -1$, the server is switching over to Q_2, and a new customer joins Q_1.
- -1 means that $D(t) = -1$, the server is located at Q_2, and a new customer joins Q_1.

Under the stability condition, which ensures the existence of a stationary regime, the stationary probabilities are defined by

$$P_{n,d} = \lim_{t\to\infty} P_{n,d}(t), \quad n \geq 0,\ d \in \mathcal{D}. \tag{1}$$

Then the stationary probabilities satisfy the following balance equations.

For the state $(n, 1)$:

$$(\lambda + \mu_1)P_{n,1} = \gamma_1 P_{n,1_{s_1}} + \lambda p_1 P_{n-1,0_1}, \quad n \geq 1.$$

For the state $(n, 1_{s_1})$:

$$(\lambda + \gamma_1)P_{n,1_{s_1}} = \lambda p_1 P_{n-1,0_{s_1}} + \lambda p_1 P_{n-1,0_{s_2}} + \lambda p_1 P_{n-1,0_2} + \mu_2 P_{n,0_2}, \quad n \geq 1.$$

For the state $(n, 0_1)$:

$$\lambda P_{0,0_1} = \mu_1 q_1 P_{1,1} + \gamma_1 P_{0,0_{s_1}}, \quad n = 0,$$

$$(\lambda + \mu_1)P_{n,0_1} = \lambda q_1 P_{n,1} + \mu_1 q_1 P_{n+1,1} + \gamma_1 P_{n,0_{s_1}}, \quad n \geq 1.$$

For the state $(n, 0_{s_1})$:

$$(\lambda + \gamma_1)P_{0,0_{s_1}} = \mu_2 q_1 P_{0,-1}, \quad n = 0,$$

$$(\lambda + \gamma_1)P_{n,0_{s_1}} = \lambda q_1 P_{n,1_{s_1}} + \lambda q_1 P_{n-1,-1_{s_2}} + \lambda q_1 P_{n-1,-1} + \mu_2 q_1 P_{n,-1}, \quad n \geq 1.$$

For the state $(n, 0_{s_2})$:

$$(\lambda + \gamma_2)P_{0,0_{s_2}} = \mu_1 q_2 P_{1,1}, \quad n = 0,$$

$$(\lambda + \gamma_2)P_{n,0_{s_2}} = \lambda q_2 P_{n,1} + \mu_1 q_2 P_{n+1,1} + \lambda q_2 P_{n,1_{s_1}} + \lambda q_2 P_{n-1,-1_{s_2}}, \quad n \geq 1.$$

For the state $(n, 0_2)$:

$$\lambda P_{0,0_2} = \gamma_2 P_{0,0_{s_2}} + \mu_2 q_2 P_{0,-1}, \quad n = 0,$$

$$(\lambda + \mu_2)P_{n,0_2} = \gamma_2 P_{n,0_{s_2}} + \lambda q_2 P_{n-1,-1} + \mu_2 q_2 P_{n,-1}, \quad n \geq 1.$$

For the state $(n, -1_{s_2})$:

$$(\lambda + \gamma_2)P_{n,-1_{s_2}} = \lambda p_2 P_{n,0_1} + \mu_1 P_{n+1,0_1} + \lambda p_2 P_{n,0_{s_1}} + \lambda p_2 P_{n,0_{s_2}}, \quad n \geq 0.$$

For the state $(n, -1)$:

$$(\lambda + \mu_2)P_{n,-1} = \lambda p_2 P_{n,0_2} + \gamma_2 P_{n,-1_{s_2}}, \quad n \geq 0.$$

As a result, we obtain the following system of balance equations:

$$\begin{cases}(\lambda+\mu_1)P_{n,1} &= \gamma_1 P_{n,1_{s_1}} + \lambda p_1 P_{n-1,0_1}, \quad n \geq 1,\\ (\lambda+\gamma_1)P_{n,1_{s_1}} &= \lambda p_1 P_{n-1,0_{s_1}} + \lambda p_1 P_{n-1,0_{s_2}} + \lambda p_1 P_{n-1,0_2} + \mu_2 P_{n,0_2}, \quad n \geq 1,\\ \lambda P_{0,0_1} &= \mu_1 q_1 P_{1,1} + \gamma_1 P_{0,0_{s_1}}, \quad n = 0,\\ (\lambda+\mu_1)P_{n,0_1} &= \lambda q_1 P_{n,1} + \mu_1 q_1 P_{n+1,1} + \gamma_1 P_{n,0_{s_1}}, \quad n \geq 1,\\ (\lambda+\gamma_1)P_{0,0_{s_1}} &= \mu_2 q_1 P_{0,-1}, \quad n = 0,\\ (\lambda+\gamma_1)P_{n,0_{s_1}} &= \lambda q_1 P_{n,1_{s_1}} + \lambda q_1 P_{n-1,-1_{s_2}} + \lambda q_1 P_{n-1,-1} + \mu_2 q_1 P_{n,-1}, \quad n \geq 1,\\ (\lambda+\gamma_2)P_{0,0_{s_2}} &= \mu_1 q_2 P_{1,1}, \quad n = 0,\\ (\lambda+\gamma_2)P_{n,0_{s_2}} &= \lambda q_2 P_{n,1} + \mu_1 q_2 P_{n+1,1} + \lambda q_2 P_{n,1_{s_1}} + \lambda q_2 P_{n-1,-1_{s_2}}, \quad n \geq 1,\\ \lambda P_{0,0_2} &= \gamma_2 P_{0,0_{s_2}} + \mu_2 q_2 P_{0,-1}, \quad n = 0,\\ (\lambda+\mu_2)P_{n,0_2} &= \gamma_2 P_{n,0_{s_2}} + \lambda q_2 P_{n-1,-1} + \mu_2 q_2 P_{n,-1}, \quad n \geq 1,\\ (\lambda+\gamma_2)P_{n,-1_{s_2}} &= \lambda p_2 P_{n,0_1} + \mu_1 P_{n+1,0_1} + \lambda p_2 P_{n,0_{s_1}} + \lambda p_2 P_{n,0_{s_2}}, \quad n \geq 0,\\ (\lambda+\mu_2)P_{n,-1} &= \lambda p_2 P_{n,0_2} + \gamma_2 P_{n,-1_{s_2}}, \quad n \geq 0.\end{cases} \tag{2}$$

4. Conditional probability generating functions

For each phase

$$d \in \mathcal{D} = \{1, 1_{s_1}, 0_1, 0_{s_1}, 0_{s_2}, 0_2, -1_{s_2}, -1\},$$

we introduce the corresponding conditional probability generating function (PGF) $G_d(z)$:

$$G_d(z) = \sum_n P_{n,d}\, z^n, \quad |z| \leq 1. \tag{3}$$

Taking into account the admissible values of n for each phase, definition (3) gives

$$\begin{cases}G_1(z) &= \sum\limits_{n\geq 1} P_{n,1} z^n,\\ G_{1_{s_1}}(z) &= \sum\limits_{n\geq 1} P_{n,1_{s_1}} z^n,\\ G_{0_1}(z) &= \sum\limits_{n\geq 0} P_{n,0_1} z^n,\\ G_{0_{s_1}}(z) &= \sum\limits_{n\geq 0} P_{n,0_{s_1}} z^n,\\ G_{0_{s_2}}(z) &= \sum\limits_{n\geq 0} P_{n,0_{s_2}} z^n,\\ G_{0_2}(z) &= \sum\limits_{n\geq 0} P_{n,0_2} z^n,\\ G_{-1_{s_2}}(z) &= \sum\limits_{n\geq 0} P_{n,-1_{s_2}} z^n,\\ G_{-1}(z) &= \sum\limits_{n\geq 0} P_{n,-1} z^n.\end{cases} \tag{4}$$

Multiplying the corresponding equations of system (2) by z^n, summing over n, and using relations (4), we obtain the following system of equations for the generating functions:

$$\begin{cases}(\lambda+\mu_1)G_1(z)-\gamma_1 G_{1_{s_1}}(z)-\lambda p_1 z\, G_{0_1}(z) & =0,\\ (\lambda+\gamma_1)G_{1_{s_1}}(z)-\lambda p_1 z\, G_{0_{s_1}}(z)-\lambda p_1 z\, G_{0_{s_2}}(z)-(\lambda p_1 z+\mu_2)G_{0_2}(z) & =-\mu_2 P_{0,0_2},\\ -(\lambda z+\mu_1)q_1 G_1(z)+(\lambda+\mu_1)z\, G_{0_1}(z)-\gamma_1 z\, G_{0_{s_1}}(z) & =\mu_1 z\, P_{0,0_1},\\ -\lambda q_1 G_{1_{s_1}}(z)+(\lambda+\gamma_1)G_{0_{s_1}}(z)-\lambda q_1 z\, G_{-1_{s_2}}(z)-(\lambda z+\mu_2)q_1 G_{-1}(z) & =0,\\ -(\lambda z+\mu_1)q_2 G_1(z)-\lambda q_2 z\, G_{1_{s_1}}(z)+(\lambda+\gamma_2)z\, G_{0_{s_2}}(z)-\lambda q_2 z^2 G_{-1_{s_2}}(z) & =0,\\ -\gamma_2 G_{0_{s_2}}(z)+(\lambda+\mu_2)G_{0_2}(z)-(\lambda z+\mu_2)q_2 G_{-1}(z) & =\mu_2 P_{0,0_2},\\ -(\lambda p_2 z+\mu_1)G_{0_1}(z)-\lambda p_2 z\, G_{0_{s_1}}(z)-\lambda p_2 z\, G_{0_{s_2}}(z)+(\lambda+\gamma_2)z\, G_{-1_{s_2}}(z) & =-\mu_1 P_{0,0_1},\\ -\lambda p_2 G_{0_2}(z)-\gamma_2 G_{-1_{s_2}}(z)+(\lambda+\mu_2)G_{-1}(z) & =0,\end{cases}$$

which can be written in matrix form as

$$A(z)\,\vec{G}(z)=\vec{P}(z), \tag{5}$$

where

$$\vec{G}(z)=\big(G_1(z),\, G_{1_{s_1}}(z),\, G_{0_1}(z),\, G_{0_{s_1}}(z),\, G_{0_{s_2}}(z),\, G_{0_2}(z),\, G_{-1_{s_2}}(z),\, G_{-1}(z)\big)^{\mathsf{T}}$$

is the vector of generating functions,

$$\vec{P}(z)=\big(0,\, -\mu_2 P_{0,0_2},\, \mu_1 z P_{0,0_1},\, 0,\, 0,\, \mu_2 P_{0,0_2},\, -\mu_1 P_{0,0_1},\, 0\big)^{\mathsf{T}}$$

is the right-hand side vector containing the unknown boundary probabilities $P_{0,0_1}$ and $P_{0,0_2}$, and the matrix $A(z)$ is given by

$$\begin{pmatrix}
\lambda+\mu_1 & -\gamma_1 & -\lambda p_1 z & 0 & 0 & 0 & 0 & 0\\
0 & \lambda+\gamma_1 & 0 & -\lambda p_1 z & -\lambda p_1 z & -(\lambda p_1 z+\mu_2) & 0 & 0\\
-(\lambda z+\mu_1)q_1 & 0 & (\lambda+\mu_1)z & -\gamma_1 z & 0 & 0 & 0 & 0\\
0 & -\lambda q_1 & 0 & \lambda+\gamma_1 & 0 & 0 & -\lambda q_1 z & -(\lambda z+\mu_2)q_1\\
-(\lambda z+\mu_1)q_2 & -\lambda q_2 z & 0 & 0 & (\lambda+\gamma_2)z & 0 & -\lambda q_2 z^2 & 0\\
0 & 0 & 0 & 0 & -\gamma_2 & \lambda+\mu_2 & 0 & -(\lambda z+\mu_2)q_2\\
0 & 0 & -(\lambda p_2 z+\mu_1) & -\lambda p_2 z & -\lambda p_2 z & 0 & (\lambda+\gamma_2)z & 0\\
0 & 0 & 0 & 0 & 0 & -\lambda p_2 & -\gamma_2 & \lambda+\mu_2
\end{pmatrix}.$$

By Cramer's rule, the generating functions, which are the solutions of system (5), are given by

$$G_d(z)=\frac{|A_d(z)|}{|A(z)|},\quad d\in\mathcal{D},$$

where $|A(z)|$ is the determinant of the matrix $A(z)$, and $|A_d(z)|$ is the determinant of the matrix obtained by replacing the corresponding column of $A(z)$ with the right-hand side vector $\vec{P}(z)$.

We note that the generating functions $G_d(z)$, $d\in\mathcal{D}$, depend on the boundary probabilities $P_{0,0_1}$ and $P_{0,0_2}$, whereas the remaining probabilities at $n=0$ are not independent and can be expressed in terms of these boundary probabilities using the stationary balance equations (2).

The determinant $|A(z)|$ is a sixth-degree polynomial in z and can be written as

$$|A(z)|=z(1-z)h(z),$$

where $h(z)$ is a fourth-degree polynomial in z whose coefficients depend on the system parameters.

The explicit expression for $h(z)$ is omitted because of its considerable length and complex structure.

Setting the determinant $|A(z)|$ equal to zero, we obtain that its roots are $z = 0$, $z = 1$, and the roots of the polynomial $h(z)$. The root $z = 1$ corresponds to the normalization condition for the stationary probabilities:

$$\sum_{d\in\mathcal{D}} G_d(1) = G_1(1) + G_{0_1}(1) + G_{1_{s_1}}(1) + G_{0_{s_1}}(1) + G_{0_2}(1) + G_{0_{s_2}}(1) + G_{-1_{s_2}}(1) + \\ + G_{-1}(1) = \sum_{d\in\mathcal{D}} \lim_{z\to 1} \frac{|A_d(z)|}{|A(z)|} = 1, \quad (6)$$

whereas the factor z corresponding to the root $z = 0$ appears in both the numerator and the denominator of the expressions for the generating functions $G_d(z)$. Since the multiplicity of this root is the same in both, this factor cancels out, and no singularity arises at $z = 0$. Therefore, the root $z = 0$ does not affect the analytic properties of these functions.

Since the generating functions $G_d(z)$ must be analytic and finite for $|z| \le 1$, all roots of the equation $|A(z)| = 0$ that lie inside the unit circle and are different from $z = 1$ must also be roots of $|A_d(z)|$.

Thus, the boundary probabilities are determined from two equations: one follows from the normalization condition (6), while the other follows from the requirement that, after substituting a root of the denominator $|A(z)|$ lying inside the unit circle, the numerators $|A_d(z)|$ also vanish. This ensures that the generating functions $G_d(z)$ remain finite and allows the boundary probabilities $P_{0,0_1}$ and $P_{0,0_2}$ to be determined uniquely.

We further note that a stationary regime exists only if the polynomial $h(z)$ has exactly one root inside the unit circle $|z| < 1$. The location of the remaining roots outside the unit circle does not affect the existence of the stationary regime.

Since, in general, an analytical study of the number of roots of the polynomial $h(z)$ inside the unit circle is difficult due to the complicated dependence of its coefficients on the system parameters, the subsequent analysis is carried out under the assumption that a stationary regime exists (see Section 5).

To determine the stability boundary, we consider the value of polynomial $h(z)$ at $z = 1$ and introduce the notation

$$g(\lambda) = h(1),$$

where $g(\lambda)$ is an eighth-degree polynomial in the parameter λ:

$$g(\lambda) = \sum_{i=0}^{8} \alpha_i \lambda^i = \alpha_8\lambda^8 + \sum_{i=1}^{7} \alpha_i\lambda^i + \alpha_0 = (p_1q_2 + q_1p_2 + p_1q_2q_1p_2)\lambda^8 + \sum_{i=1}^{7} \alpha_i\lambda^i - g_1^2g_2^2\mu_1^2\mu_2^2. \quad (7)$$

Since the stability boundary corresponds to a change in the sign of the polynomial $g(\lambda)$, it is necessary to consider the positive roots of the equation

$$g(\lambda) = 0. \quad (8)$$

However, an analytical determination of these roots is also difficult in the general case due to the complicated dependence of the coefficients of $g(\lambda)$ on the system parameters.

At the same time, it follows from (7) that

$$g(0) < 0, \quad \lim_{\lambda\to+\infty} g(\lambda) = +\infty.$$

Therefore, by the Bolzano–Cauchy theorem, equation (8) has at least one positive root. Since the arrival rate λ is a non-negative parameter, the stability boundary corresponds to the smallest positive root of this equation:

$$\lambda^* = \min\{\lambda > 0 : \ g(\lambda) = 0\}.$$

Thus, the interval $0 < \lambda < \lambda^*$ defines the range of arrival rates for which the existence of a stationary regime is considered. Moreover, for all λ in this interval, the condition

$$g(\lambda) < 0 \quad (9)$$

is satisfied.

In the numerical experiments presented in Section 6, we considered parameter sets for which condition (9) is satisfied. For each such set, we additionally checked that the polynomial $h(z)$ has exactly one root inside the unit circle $|z| < 1$, which ensures the existence of a stationary regime.

5. Stationary performance measures

We use the stationary probabilities defined earlier in (1) and the generating functions introduced in (3).

Then, at $z = 1$, we obtain

$$G_d(1) = \sum_{n\geq 0} P_{n,d}, \quad d \in \mathcal{D}.$$

We determine the values of the first and second derivatives of the generating functions $G_d(z)$ at $z = 1$:

$$G'_d(z) = \frac{d}{dz}\left(\sum_{n\geq 0} P_{n,d} z^n\right) = \sum_{n\geq 0} nP_{n,d}\, z^{n-1} \Rightarrow G'_d(1) = \sum_{n\geq 0} nP_{n,d},$$

$$G''_d(z) = \frac{d}{dz}\left(\sum_{n\geq 0} nP_{n,d}\, z^{n-1}\right) = \sum_{n\geq 0} n(n-1)P_{n,d}\, z^{n-2} \Rightarrow G''_d(1) = \sum_{n\geq 0} n(n-1)P_{n,d}.$$

The stationary marginal probability of phase d is given by

$$P_{\cdot,d} = \lim_{t\to\infty} \mathbb{P}\{J(t) = d\} = \sum_{n\geq 0} P_{n,d} = G_d(1), \quad d \in \mathcal{D}.$$

The stationary marginal probability that queue Q_1 contains n customers is given by

$$P_{n,\cdot} = \lim_{t\to\infty} \mathbb{P}\{L_1(t) = n\} = \sum_{d\in\mathcal{D}} P_{n,d}, \quad n \geq 0.$$

We now compute the mean queue lengths $\mathbb{E}(L_1)$ and $\mathbb{E}(L_2)$, as well as the mean difference $\mathbb{E}(D)$.

Since the numerical part of each phase $d \in \mathcal{D} = \{1, 1_{s_1}, 0_1, 0_{s_1}, 0_{s_2}, 0_2, -1_{s_2}, -1\}$ corresponds to the value of the queue-length difference, by the definition of expectation

$$\mathbb{E}(D) = \sum_{d\in\mathcal{D}} d\, G_d(1) = \sum_{d\in\mathcal{D}} d\, P_{\cdot,d}. \tag{10}$$

Expanding (10) in terms of the generating functions, we obtain

$$\mathbb{E}(D) = 1\cdot G_1(1) + 1\cdot G_{1_{s_1}}(1) + 0\cdot G_{0_1}(1) + 0\cdot G_{0_{s_1}}(1) + 0\cdot G_{0_{s_2}}(1) + 0\cdot G_{0_2}(1) - \\ - 1\cdot G_{-1_{s_2}}(1) - 1\cdot G_{-1}(1) = G_1(1) + G_{1_{s_1}}(1) - G_{-1_{s_2}}(1) - G_{-1}(1).$$

Equivalently, expanding (10) in terms of the marginal phase probabilities, we obtain

$$\mathbb{E}(D) = 1\cdot P_{\cdot,1} + 1\cdot P_{\cdot,1_{s_1}} + 0\cdot P_{\cdot,0_1} + 0\cdot P_{\cdot,0_{s_1}} + 0\cdot P_{\cdot,0_{s_2}} + 0\cdot P_{\cdot,0_2} - \\ - 1\cdot P_{\cdot,-1_{s_2}} - 1\cdot P_{\cdot,-1} = P_{\cdot,1} + P_{\cdot,1_{s_1}} - P_{\cdot,-1_{s_2}} - P_{\cdot,-1}.$$

The mean length of the first queue is given by

$$\mathbb{E}(L_1) = \sum_{n\geq 0} n\, P_{n,\cdot} = \sum_{n\geq 0} n \sum_{d\in\mathcal{D}} P_{n,d} = \sum_{d\in\mathcal{D}} \sum_{n\geq 0} n\, P_{n,d} = \sum_{d\in\mathcal{D}} G'_d(1).$$

The mean length of the second queue can be obtained from the relation between the queue lengths. Since $D = L_1 - L_2$, we have $L_2 = L_1 - D$. Hence, by the linearity of expectation,

$$\mathbb{E}(L_2) = \mathbb{E}(L_1) - \mathbb{E}(D) = \sum_{d\in\mathcal{D}} G'_d(1) - \sum_{d\in\mathcal{D}} d\, G_d(1) = \sum_{d\in\mathcal{D}} \big(G'_d(1) - d\, G_d(1)\big).$$

The covariance of the queue lengths $\mathrm{Cov}(L_1, L_2)$ is defined as

$$\mathrm{Cov}(L_1, L_2) = \mathbb{E}(L_1 L_2) - \mathbb{E}(L_1)\,\mathbb{E}(L_2).$$

Since $L_2 = L_1 - D$, we have

$$\mathbb{E}(L_1 L_2) = \mathbb{E}\big(L_1(L_1 - D)\big) = \mathbb{E}(L_1^2 - L_1 D) = \mathbb{E}(L_1^2) - \mathbb{E}(L_1 D).$$

Therefore,

$$\mathrm{Cov}(L_1, L_2) = \mathbb{E}(L_1^2) - \mathbb{E}(L_1 D) - \mathbb{E}(L_1)\,\mathbb{E}(L_2),$$

where

$$\mathbb{E}(L_1^2) = \sum_{n\geq 0} n^2 P_{n,\cdot} = \sum_{d\in\mathcal{D}}\sum_{n\geq 0} n^2 P_{n,d} = \sum_{d\in\mathcal{D}}\sum_{n\geq 0} n(n-1)P_{n,d} + \sum_{d\in\mathcal{D}}\sum_{n\geq 0} nP_{n,d} =$$
$$= \sum_{d\in\mathcal{D}} G_d''(1) + \sum_{n\geq 0} nP_{n,\cdot} = \sum_{d\in\mathcal{D}} G_d''(1) + \mathbb{E}(L_1) = \sum_{d\in\mathcal{D}} G_d''(1) + \sum_{d\in\mathcal{D}} G_d'(1),$$

$$\mathbb{E}(L_1 D) = \sum_{d\in\mathcal{D}}\sum_{n\geq 0} nd\,P_{n,d} = \sum_{n\geq 0} nP_{n,1} + \sum_{n\geq 0} nP_{n,1_{s_1}} - \sum_{n\geq 0} nP_{n,-1_{s_2}} - \sum_{n\geq 0} nP_{n,-1} =$$
$$= G_1'(1) + G_{1_{s_1}}'(1) - G_{-1_{s_2}}'(1) - G_{-1}'(1).$$

The variances of the numbers of customers in the first and second queues, $\mathrm{Var}(L_1)$ and $\mathrm{Var}(L_2)$, are computed as follows:

$$\mathrm{Var}(L_1) = \mathbb{E}(L_1^2) - (\mathbb{E}(L_1))^2 = \sum_{d\in\mathcal{D}} G_d''(1) + \sum_{d\in\mathcal{D}} G_d'(1) - \left(\sum_{d\in\mathcal{D}} G_d'(1)\right)^2 =$$
$$= \sum_{d\in\mathcal{D}} G_d''(1) + \left(1 - \sum_{d\in\mathcal{D}} G_d'(1)\right)\sum_{d\in\mathcal{D}} G_d'(1),$$

$$\mathrm{Var}(L_2) = \mathbb{E}(L_2^2) - (\mathbb{E}(L_2))^2 = \mathbb{E}\big((L_1 - D)^2\big) - \big(\mathbb{E}(L_1 - D)\big)^2 = \mathbb{E}(L_1^2 - 2L_1 D + D^2) -$$
$$- (\mathbb{E}(L_1) - \mathbb{E}(D))^2 = \mathbb{E}(L_1^2) - 2\,\mathbb{E}(L_1 D) + \mathbb{E}(D^2) - (\mathbb{E}(L_1) - \mathbb{E}(D))^2.$$

Moreover, since

$$D^2 = \begin{cases} 1, & d \in \{1,\ 1_{s_1},\ -1_{s_2},\ -1\}, \\ 0, & d \in \{0_1,\ 0_{s_1},\ 0_{s_2},\ 0_2\}, \end{cases}$$

we have

$$\mathbb{E}(D^2) = G_1(1) + G_{1_{s_1}}(1) + G_{-1_{s_2}}(1) + G_{-1}(1).$$

The correlation coefficient $\mathrm{Cor}(L_1, L_2)$ is computed as

$$\mathrm{Cor}(L_1, L_2) = \frac{\mathrm{Cov}(L_1, L_2)}{\sqrt{\mathrm{Var}(L_1)\,\mathrm{Var}(L_2)}}.$$

Next, we determine the effective arrival rates λ_i^{eff}, $i = \overline{1,2}$, of customers joining queue Q_i, $i = \overline{1,2}$.

For queue Q_1**:** If $L_1 < L_2$, then an arriving customer joins queue Q_1 with probability 1, and the corresponding contribution is $\lambda(P_{\cdot,-1_{s_2}} + P_{\cdot,-1})$. If $L_1 = L_2$, then the customer joins queue Q_1 with probability p_1, and the corresponding contribution is $\lambda p_1(P_{\cdot,0_1} + P_{\cdot,0_{s_1}} + P_{\cdot,0_{s_2}} + P_{\cdot,0_2})$.

Consequently, the effective arrival rate to queue Q_1 is

$$\lambda_1^{\mathrm{eff}} = \lambda\Big(P_{\cdot,-1_{s_2}} + P_{\cdot,-1} + p_1\big(P_{\cdot,0_1} + P_{\cdot,0_{s_1}} + P_{\cdot,0_{s_2}} + P_{\cdot,0_2}\big)\Big).$$

For queue Q_2**:** If $L_1 > L_2$, then an arriving customer joins queue Q_2 with probability 1, and the corresponding contribution is $\lambda(P_{\cdot,1} + P_{\cdot,1_{s_1}})$. If $L_1 = L_2$, then the customer joins queue Q_2 with probability p_2, and the corresponding contribution is $\lambda p_2(P_{\cdot,0_1} + P_{\cdot,0_{s_1}} + P_{\cdot,0_{s_2}} + P_{\cdot,0_2})$.

Consequently, the effective arrival rate to queue Q_2 is

$$\lambda_2^{\mathrm{eff}} = \lambda\Big(P_{\cdot,1} + P_{\cdot,1_{s_1}} + p_2\big(P_{\cdot,0_1} + P_{\cdot,0_{s_1}} + P_{\cdot,0_{s_2}} + P_{\cdot,0_2}\big)\Big).$$

Since the sum of the effective arrival rates to queues Q_1 and Q_2 equals the total arrival rate λ, we have

$$\lambda_1^{\text{eff}} + \lambda_2^{\text{eff}} = \lambda.$$

The effective load factor of queue Q_i, interpreted as the fraction of time during which the server serves this queue, is given by

$$\rho_i^{\text{eff}} = \frac{\lambda_i^{\text{eff}}}{\mu_i}, \quad i = \overline{1,2}.$$

The mean fraction of time during which the server is in a switch-over state is given by

$$P_{\text{sw}} = P_{\cdot,1_{s_1}} + P_{\cdot,0_{s_1}} + P_{\cdot,0_{s_2}} + P_{\cdot,-1_{s_2}}.$$

The probability that the server is idle, that is, neither serving nor switching over, is defined as follows:

$$P_{\text{idle}} = P_{0,0_1} + P_{0,0_2} = 1 - \rho_1^{\text{eff}} - \rho_2^{\text{eff}} - P_{\text{sw}}.$$

Since

$$G_d(z) = \sum_{n=0}^{\infty} P_{n,d}\, z^n = P_{0,d} + P_{1,d} z + P_{2,d} z^2 + \cdots, \quad |z| \le 1,$$

substituting $z = 0$ into the expression for $G_d(z)$ gives

$$G_d(0) = P_{0,d} + P_{1,d} \cdot 0 + P_{2,d} \cdot 0^2 + \cdots = P_{0,d}.$$

It follows that the mean fraction of time during which the server is in a switch-over state while the system is empty is given by

$$P_{\text{sw}_0} = P_{0,0_{s_1}} + P_{0,0_{s_2}} = G_{0_{s_1}}(0) + G_{0_{s_2}}(0).$$

Then the probability that the system is empty, regardless of the server state, is given by

$$P_0 = P_{0,0_1} + P_{0,0_{s_1}} + P_{0,0_{s_2}} + P_{0,0_2} = P_{\text{idle}} + P_{\text{sw}_0}.$$

6. Numerical results

This section presents the numerical results in two groups of tables. Tables 1–4 show how changes in the customer arrival rate, service rates, server switch-over rates, and tie-breaking probabilities affect the main stationary characteristics of the system. These characteristics include the mean queue lengths, the variances of the queue lengths, the correlation coefficient, the effective customer arrival rates, and the fractions of time during which the server is serving, switching over, or idle for different parameter values. Tables 5–7 present the stationary probabilities of the process phases, each of which corresponds to a particular value of the queue-length difference D and a particular server state, and show how these probabilities change as the customer arrival rate λ and the tie-breaking probabilities vary.

We introduce the load parameter

$$\rho = \frac{\lambda}{\lambda^*}, \quad \rho \in (0,1),$$

and set $\lambda = \rho\lambda^*$ for $\rho = 0.3, 0.5, 0.7, 0.85, 0.95$ to evaluate the effect of the arrival rate on the stationary characteristics of the system (see Table 1).

In Tables 2–7, the results are presented for a moderate load, $\rho = 0.7$, that is, for $\lambda = 0.7\lambda^*$, where λ^* is the corresponding stability boundary. This choice makes it possible to illustrate the effect of the model parameters on the system characteristics more clearly. We recall that the parameter $\rho = \frac{\lambda}{\lambda^*}$ characterizes the load level relative to the stability boundary, whereas the quantities ρ_i^{eff} represent the fractions of time during which the server serves the corresponding queues Q_i, $i = 1, 2$.

Table 1

Dependence of the main performance measures on the load parameter ρ for $\lambda^* \approx 1.491719$, $\mu_1 = \mu_2 = 3$, $\gamma_1 = \gamma_2 = 3$, $p_1 = p_2 = q_1 = q_2 = 0.5$.

ρ	λ	$\mathbb{E}(L_1)$	$\mathbb{E}(L_2)$	$\mathrm{Var}(L_1)$	$\mathrm{Var}(L_2)$	$\mathrm{Cor}(L_1, L_2)$	P_{idle}
0.30	0.448	0.172	0.172	0.169	0.169	0.404	0.698
0.50	0.746	0.416	0.416	0.470	0.470	0.667	0.496
0.70	1.044	0.996	0.996	1.630	1.630	0.875	0.295
0.85	1.268	2.459	2.459	7.510	7.510	0.969	0.146
0.95	1.417	8.326	8.326	74.062	74.062	0.997	0.049

Table 2

Influence of the service rates on the main performance measures at $\rho = 0.7$, $\gamma_1 = \gamma_2 = 2$, $p_1 = p_2 = q_1 = q_2 = 0.5$.

μ_1	μ_2	λ^*	$\mathbb{E}(L_1)$	$\mathbb{E}(L_2)$	$\mathrm{Cor}(L_1, L_2)$	ρ_1^{eff}	ρ_2^{eff}	P_{sw}	P_{idle}
0.1	0.2	0.12815	1.189	1.088	0.897	0.403	0.247	0.053	0.297
1	3	0.87537	1.073	0.969	0.881	0.274	0.113	0.320	0.293
5	5	1.51539	1.037	1.037	0.887	0.106	0.106	0.505	0.283
0.5	10	0.76393	1.256	1.017	0.907	0.407	0.033	0.286	0.274

Table 2 shows the effect of the service rates μ_1 and μ_2 on the stationary characteristics of the system.

The influence of the server switch-over rates γ_1 and γ_2 on the system characteristics is shown in Table 3.

Table 4 presents the system characteristics for different combinations of the tie-breaking probabilities p_1 and q_1.

Next, we consider the stationary probabilities of the process phases for different values of the load parameter ρ (see Table 5). Due to rounding, the sums of probabilities in the rows may differ slightly from one.

The effect of the tie-breaking probability p_1 on the stationary distribution over the process phases is shown in Table 6.

Finally, Table 7 shows how the tie-breaking probability q_1 affects the stationary distribution over the process phases.

The numerical results presented in this section are further discussed and interpreted in Section 7.

7. Discussion

The results presented in Table 1 show that, as the load parameter ρ increases, the mean queue lengths $\mathbb{E}(L_1)$ and $\mathbb{E}(L_2)$ grow significantly. As ρ approaches one, the mean queue lengths increase sharply and nonlinearly. This is because the arrival rate λ becomes close to the stability boundary λ^*, so that the server spends less time idle and more time serving customers or switching over between the queues. Under such conditions, even a small increase in the load may lead to customer accumulation in the queues and, consequently, to a sharp increase in the queue lengths.

At the same time, the variances of the queue lengths grow faster than the corresponding mean values, especially for high values of ρ. This indicates that the queue lengths become more variable as the load increases. Together with the growth of the mean queue lengths, this indicates a decrease in the efficiency of the system.

Table 3
Influence of the switch-over rates on the main performance measures at $\rho = 0.7,\ \mu_1 = \mu_2 = 2,\ p_1 = p_2 = q_1 = q_2 = 0.5$.

γ_1	γ_2	λ^*	$\mathbb{E}(L_1)$	$\mathbb{E}(L_2)$	$\mathrm{Cor}(L_1, L_2)$	ρ_1^{eff}	ρ_2^{eff}	P_{sw}	P_{idle}
0.1	0.2	0.15689	1.269	1.174	0.919	0.025	0.030	0.688	0.257
1	3	0.89238	1.063	0.978	0.882	0.143	0.170	0.401	0.287
5	5	1.38724	1.020	1.020	0.877	0.243	0.243	0.213	0.301
0.5	10	0.78691	1.228	1.027	0.904	0.110	0.165	0.463	0.262

Table 4
Influence of tie-breaking probabilities on the main performance measures at $\rho = 0.7,\ \mu_1 = \mu_2 = 2,\ \gamma_1 = \gamma_2 = 2$.

p_1	q_1	λ^*	$\mathbb{E}(L_1)$	$\mathbb{E}(L_2)$	$\mathrm{Cor}(L_1, L_2)$	ρ_1^{eff}	ρ_2^{eff}	P_{sw}	P_{idle}
0.2	0.2	1.02190	0.931	0.932	0.868	0.114	0.244	0.323	0.320
	0.5	0.99603	0.931	1.057	0.880	0.134	0.214	0.355	0.296
	0.8	0.93088	0.877	1.127	0.895	0.146	0.180	0.393	0.281
0.5	0.2	0.97267	1.037	0.909	0.878	0.148	0.192	0.362	0.298
	0.5	0.99447	0.996	0.996	0.875	0.174	0.174	0.357	0.295
	0.8	0.97267	0.909	1.037	0.878	0.192	0.148	0.362	0.298
0.8	0.2	0.93088	1.127	0.877	0.895	0.180	0.146	0.393	0.281
	0.5	0.99603	1.057	0.931	0.880	0.214	0.134	0.355	0.296
	0.8	1.02190	0.932	0.931	0.868	0.244	0.114	0.323	0.320

Table 5
Stationary phase probabilities for different values of ρ at $\lambda^* \approx 1.491719,\ \mu_1 = \mu_2 = 3,\ \gamma_1 = \gamma_2 = 3,\ p_1 = p_2 = q_1 = q_2 = 0.5$.

ρ	$P_{\cdot,1}$	$P_{\cdot,1_{s_1}}$	$P_{\cdot,0_1}$	$P_{\cdot,0_{s_1}}$	$P_{\cdot,0_{s_2}}$	$P_{\cdot,0_2}$	$P_{\cdot,-1_{s_2}}$	$P_{\cdot,-1}$
0.30	0.0596	0.0413	0.3640	0.0351	0.0351	0.3640	0.0413	0.0596
0.50	0.0854	0.0710	0.2867	0.0569	0.0569	0.2867	0.0710	0.0854
0.70	0.1031	0.1009	0.2185	0.0776	0.0776	0.2185	0.1009	0.1031
0.85	0.1120	0.1229	0.1725	0.0925	0.0925	0.1725	0.1229	0.1120
0.95	0.1164	0.1373	0.1441	0.1022	0.1022	0.1441	0.1373	0.1164

Table 6
Stationary phase probabilities for different values of p_1 at $\rho = 0.7,\ \mu_1 = \mu_2 = 3,\ \gamma_1 = \gamma_2 = 3,\ q_1 = 0.5$.

p_1	λ^*	$P_{\cdot,1}$	$P_{\cdot,1_{s_1}}$	$P_{\cdot,0_1}$	$P_{\cdot,0_{s_1}}$	$P_{\cdot,0_{s_2}}$	$P_{\cdot,0_2}$	$P_{\cdot,-1_{s_2}}$	$P_{\cdot,-1}$
0.2	1.459	0.1200	0.1455	0.0901	0.0268	0.1364	0.3444	0.0533	0.0835
0.5	1.491	0.1031	0.1009	0.2185	0.0776	0.0776	0.2185	0.1009	0.1031
0.8	1.459	0.0835	0.0533	0.3444	0.1364	0.0268	0.0901	0.1455	0.1200

Table 7

Stationary phase probabilities for different values of q_1 at $\rho = 0.7$, $\mu_1 = \mu_2 = 3$, $\gamma_1 = \gamma_2 = 3$, $p_1 = 0.5$.

q_1	λ^*	$P_{\cdot,1}$	$P_{\cdot,1_{s_1}}$	$P_{\cdot,0_1}$	$P_{\cdot,0_{s_1}}$	$P_{\cdot,0_{s_2}}$	$P_{\cdot,0_2}$	$P_{\cdot,-1_{s_2}}$	$P_{\cdot,-1}$
0.2	1.494	0.0660	0.0745	0.2081	0.0962	0.0589	0.2298	0.1257	0.1407
0.5	1.491	0.1031	0.1009	0.2185	0.0776	0.0776	0.2185	0.1009	0.1031
0.8	1.494	0.1407	0.1257	0.2298	0.0589	0.0962	0.2081	0.0745	0.0660

The correlation coefficient between the queue lengths also increases with ρ and becomes close to one as the stability boundary is approached. This suggests that the queue lengths vary in a more coordinated way, indicating effective balancing due to the combined use of the JSQ and SLQ disciplines.

The server idle probability, on the contrary, decreases as ρ increases, since the server is less likely to be idle when the arrival rate becomes higher.

Table 2 shows that, in the symmetric case $\mu_1 = \mu_2 = 5$, the mean queue lengths are equal, $\mathbb{E}(L_1) = \mathbb{E}(L_2) = 1.037$, as are the effective load factors, $\rho_1^{\text{eff}} = \rho_2^{\text{eff}} = 0.106$. This is consistent with the symmetry of the model parameters and reflects the symmetric behavior of the two queues.

When the service rates are asymmetric, the load is redistributed between the queues. If the first queue is served more slowly than the second one, its mean length increases. This effect is clearly seen for $\mu_1 = 0.5$, $\mu_2 = 10$, where $\mathbb{E}(L_1) = 1.256$, whereas $\mathbb{E}(L_2) = 1.017$. Along with the increase in the mean queue length, the effective load factor of the first queue also increases to $\rho_1^{\text{eff}} = 0.407$, while the effective load factor of the second queue is much smaller, $\rho_2^{\text{eff}} = 0.033$. Thus, the queue with the lower service rate becomes more heavily loaded.

The values of the correlation coefficient $\text{Cor}(L_1, L_2)$ remain rather high in all the cases considered, which indicates that a positive dependence between the queue lengths is preserved regardless of whether the service rates are symmetric or asymmetric. This effect may be explained by the combined use of the JSQ and SLQ disciplines, which tend to balance the queue lengths by routing new customers to the shortest queue and giving service priority to the longest queue.

It is also important to note how the fraction of time during which the server is in a switch-over state, P_{sw}, changes. In the symmetric case ($\mu_1 = \mu_2 = 5$), it attains the largest value among all the considered cases, $P_{\text{sw}} = 0.505$. This is because, for equal service rates, the queue lengths become equal more often, and the server therefore switches between the queues more frequently. In the asymmetric case, for example, when $\mu_1 = 0.5$ and $\mu_2 = 10$, the fraction of switch-over time decreases to $P_{\text{sw}} = 0.286$, since the server mostly remains at the slower and, consequently, more heavily loaded queue, and switches over less frequently than in the symmetric case.

The idle probability P_{idle} also depends on the combination of service rates, although in the considered cases it remains approximately at the same level, in the range 0.274–0.297. The smallest value, $P_{\text{idle}} = 0.274$, is observed under strong asymmetry, $\mu_1 = 0.5$ and $\mu_2 = 10$. In this case, the first queue is served much more slowly than the second one and therefore becomes more heavily loaded, as reflected by $\rho_1^{\text{eff}} = 0.407$, while $\rho_2^{\text{eff}} = 0.033$. Thus, in the considered examples, changes in the service rates affect the idle probability only moderately.

Table 3 shows that, for small values of γ_1 and γ_2, the server spends most of its time in a switch-over state. For example, when $\gamma_1 = 0.1$ and $\gamma_2 = 0.2$, we have $P_{\text{sw}} = 0.688$. This is due to the long switch-over process. Moreover, because the system operates under absolute preemptive priority, longer switch-overs increase the probability of arrivals during a switch-over, which further increases P_{sw}, the fraction of time spent in switch-over. As a result, in this case the effective load factors of the queues are small, $\rho_1^{\text{eff}} = 0.025$ and $\rho_2^{\text{eff}} = 0.030$, while the mean queue lengths are relatively large.

As the switch-over rates increase, the fraction of time spent in switch-over generally decreases. For example, it decreases from $P_{\text{sw}} = 0.688$ for $\gamma_1 = 0.1$, $\gamma_2 = 0.2$ to $P_{\text{sw}} = 0.213$ for $\gamma_1 = \gamma_2 = 5$. This indicates that faster switch-overs reduce the time spent in switch-over and allow the server to serve

customers more efficiently. Consequently, the mean queue lengths also decrease: from $\mathbb{E}(L_1) = 1.269$ and $\mathbb{E}(L_2) = 1.174$ for $\gamma_1 = 0.1$, $\gamma_2 = 0.2$ to $\mathbb{E}(L_1) = \mathbb{E}(L_2) = 1.020$ for $\gamma_1 = \gamma_2 = 5$.

When the switch-over rates are asymmetric, the fraction of time spent in switch-over may remain rather high, especially when one of the switch-over rates is much smaller than the other. For example, when $\gamma_1 = 0.5$ and $\gamma_2 = 10$, we have $P_{\text{sw}} = 0.463$, which is considerably higher than in the symmetric case $\gamma_1 = \gamma_2 = 5$, where $P_{\text{sw}} = 0.213$. In this case, since $\gamma_1 < \gamma_2$, switch-overs to Q_1 are slower, and queue Q_1 becomes more heavily loaded in terms of its mean length: $\mathbb{E}(L_1) = 1.228$, whereas $\mathbb{E}(L_2) = 1.027$. The effective load factors are also unequal, $\rho_1^{\text{eff}} = 0.110$ and $\rho_2^{\text{eff}} = 0.165$.

The idle probability P_{idle} changes only moderately as the switch-over rates vary. In the considered cases, it remains in the range 0.257–0.301. The largest value, $P_{\text{idle}} = 0.301$, is observed in the symmetric case $\gamma_1 = \gamma_2 = 5$, where the fraction of time spent in switch-over is the smallest. Thus, in these examples, changes in the switch-over rates mainly affect the fraction of time spent in switch-over, whereas the idle probability varies only slightly.

The correlation coefficient $\text{Cor}(L_1, L_2)$, as in Table 2, remains high, which indicates that the queue lengths vary in a coordinated way. This can similarly be explained by the tendency of the JSQ and SLQ disciplines to balance the queue lengths even in the presence of non-zero switch-over times.

When the queue lengths are equal, the parameters p_1 and q_1 define two different tie-breaking mechanisms. The parameter p_1 controls the routing of arriving customers, whereas q_1 controls the server's choice of the queue to be served. As Table 4 shows, when these parameters differ from 0.5, the load tends to shift toward one of the queues. For example, for $(p_1, q_1) = (0.2, 0.8)$, the second queue is more heavily loaded: $\mathbb{E}(L_2) = 1.127$ and $\rho_2^{\text{eff}} = 0.180$, whereas $\mathbb{E}(L_1) = 0.877$ and $\rho_1^{\text{eff}} = 0.146$. Since the remaining parameters are symmetric, the case $(p_1, q_1) = (0.8, 0.2)$ exhibits mirror symmetry: the same numerical values are interchanged between the first and second queues, namely $\mathbb{E}(L_1) = 1.127$, $\rho_1^{\text{eff}} = 0.180$, $\mathbb{E}(L_2) = 0.877$, and $\rho_2^{\text{eff}} = 0.146$.

The correlation coefficient $\text{Cor}(L_1, L_2)$ remains high and positive in all considered cases. This indicates a coordinated behavior of the queue lengths and can be explained in the same way as in the previous tables.

The mean fraction of time during which the server is in a switch-over state, P_{sw}, also depends on the choice of p_1 and q_1, but varies within a moderate range. In the considered cases, it ranges from 0.323 to 0.393. The idle probability P_{idle} is less sensitive to changes in these parameters and remains between 0.281 and 0.320.

Table 5 shows that, for a low load value ($\rho = 0.3$), the largest probabilities correspond to the phases 0_1 and 0_2. This means that the system spends most of the time in a balanced state, where the queue lengths are equal.

As the load increases, the probabilities of the phases 0_1 and 0_2, where the queue lengths are equal and the server is at one of the queues, decrease. At the same time, the probabilities of the phases 1 and -1, as well as those of the switch-over phases 1_{s_1}, 0_{s_1}, 0_{s_2}, and -1_{s_2}, increase. This is because, as the arrival rate increases, the system has less time to restore equality between the queue lengths.

It is important to note that, even as the load increases, a substantial part of the probability mass remains concentrated in the phases with $D = 0$. This reflects the effect of the JSQ and SLQ disciplines, which tend to equalize the queue lengths: arriving customers are routed to the shortest queue, while the server gives priority to the longest queue. As a result, the system regularly returns to phases with equal queue lengths.

As the load parameter ρ approaches one, the probability distribution becomes more evenly spread across the phases, while the probability that the server is in a switch-over phase increases. This is due to more frequent changes in the queue-length difference, which cause the server to switch between the queues more often.

It should also be noted that, due to the symmetry of the model parameters, the probabilities of the corresponding phases for the first and second queues coincide.

Table 6 shows that changing the parameter p_1 leads to a redistribution of probabilities among the process phases. For $p_1 = 0.5$, the distribution is symmetric: the probabilities of the corresponding phases for the first and second queues coincide.

When p_1 deviates from the symmetric value, the probability distribution shifts toward one of the queues. For example, for $p_1 = 0.2$, the total probability of the phases associated with the second queue increases, while the first queue becomes less loaded. For $p_1 = 0.8$, the opposite pattern is observed: the distribution shifts toward the first queue, while the second queue becomes less loaded.

It can also be seen that changing p_1 affects the probabilities of the switch-over phases. As p_1 increases, the probabilities of the phases 0_{s_1} and -1_{s_2} become larger, whereas the probabilities of the phases 1_{s_1} and 0_{s_2} decrease. When p_1 decreases, the opposite pattern is observed: the probabilities of the phases 0_{s_1} and -1_{s_2} become smaller, whereas the probabilities of the phases 1_{s_1} and 0_{s_2} increase.

Thus, the parameter p_1 has a significant effect on the distribution of phase probabilities and determines the direction of the load shift in the system.

Table 7 shows that the parameter q_1 affects the distribution of probabilities over the process phases, although this effect is weaker than that of the parameter p_1 in Table 6.

For $q_1 = 0.5$, as in Table 6, the distribution is symmetric: the probabilities of the corresponding phases for the first and second queues coincide. When q_1 differs from 0.5, the probability mass shifts toward one of the queues. For $q_1 = 0.2$, the system is more often in phases associated with the second queue, whereas for $q_1 = 0.8$, the shift is toward the first queue. These changes are most noticeable in the phases with unequal queue lengths.

Thus, compared with p_1, the parameter q_1 plays a secondary role in the load distribution between the queues.

8. Conclusion

This paper studies a two-queue queueing system with the JSQ–SLQ disciplines, absolute preemptive priority, and non-zero server switch-over times. A Markov model is constructed in terms of the length of the first queue and a phase variable that encodes both the queue-length difference and the server state. This makes it possible to apply the probability generating function method and to obtain analytical expressions for the main stationary characteristics, as well as a condition for the existence of a stationary regime. The obtained analytical results were used to numerically evaluate how the arrival rate, service rates, server switch-over rates, and tie-breaking parameters affect the stationary characteristics and phase probabilities.

The numerical results show that the behavior of the system is shaped by its load, service rates, tie-breaking parameters, and server switch-over times. As the load increases, the mean queue lengths and their variances grow rapidly, which is related to the arrival rate approaching the stability boundary. At the same time, the positive correlation between the queue lengths increases, reflecting the balancing effect of the jointly applied JSQ and SLQ disciplines.

It is shown that the service rates noticeably affect the load distribution between the queues. The queue with the lower service rate becomes more heavily loaded, which is reflected in an increase in its mean length and effective load factor. However, in the considered examples, the idle probability changes only moderately as the service rates vary. The server switch-over times also have a significant effect on the system characteristics. When switching is slow, the server spends a substantial fraction of time in switch-over, which leads to larger mean queue lengths. Faster switching, in contrast, reduces the time spent in switch-over and improves service efficiency.

The tie-breaking parameters also affect the system behavior. The parameter p_1 plays an important role in shifting the load between the queues and noticeably affects the distribution of phase probabilities. The parameter q_1 also affects the phase probabilities, but its effect is weaker than that of p_1, and it plays a secondary role in the load distribution between the queues.

Overall, the combined use of the JSQ and SLQ disciplines provides stable equalization of queue lengths even in the presence of parameter asymmetry. However, the system performance is sensitive to the combination of the routing, service, and switch-over parameters.

Further research may be directed toward generalizing the proposed model to systems with a larger number of queues and servers. Such a generalization would make it possible to analyze multi-server systems with a complex interaction structure, which is typical of distributed computing and telecommunication systems. In addition, it is of particular interest to study other rules for selecting a queue when the queue lengths are equal, as well as systems with different priority mechanisms, including preemptive and non-preemptive variants.

Another relevant direction is the study of systems with more general distributions of service and server switch-over times, as well as non-Poisson arrival processes. This would make it possible to go beyond the Markovian assumptions and extend the applicability of the model.

The model considered in this paper can be used to analyze and optimize queueing systems in which the routing of arriving customers and the selection of a queue for service depend on the current state of the system, for example, in telecommunication networks, data centers, and distributed computing systems.

Author Contributions: Conceptualization, Evgeny A. Khityaev, Ivan S. Zaryadov and Tatiana A. Milovanova; methodology, Evgeny A. Khityaev, Ivan S. Zaryadov and Tatiana A. Milovanova; software, Evgeny A. Khityaev; validation, Evgeny A. Khityaev and Ivan S. Zaryadov; formal analysis, Evgeny A. Khityaev, Ivan S. Zaryadov and Tatiana A. Milovanova; investigation, Evgeny A. Khityaev and Ivan S. Zaryadov; resources, Evgeny A. Khityaev and Ivan S. Zaryadov; data curation, Evgeny A. Khityaev and Ivan S. Zaryadov; writing—original draft preparation, Evgeny A. Khityaev; writing—review and editing, Evgeny A. Khityaev and Ivan S. Zaryadov; visualization, Evgeny A. Khityaev and Ivan S. Zaryadov; supervision, Ivan S. Zaryadov; project administration, Ivan S. Zaryadov. All authors have read and agreed to the published version of the manuscript.

Funding: This research received no external funding.

Data Availability Statement: No new data were created or analysed during this study. Data sharing is not applicable.

Conflicts of Interest: The authors declare no conflict of interest.

Declaration on Generative AI: During the preparation of this work, the authors used ChatGPT-5 for text translation and language editing, as well as for auxiliary assistance with selected mathematical formulations and computational aspects of the study. All AI-assisted materials were reviewed, verified, and edited as needed by the authors, who take full responsibility for the content of the publication.

References

[1] M. A. A. Boon, R. D. Van der Mei, and E. M. M. Winands, "Applications of Polling Systems," *Surveys in Operations Research and Management Science*, vol. 16, no. 2, pp. 67–82, 2011. DOI: 10.1016/j.sorms.2011.01.001

[2] S. Bodas, S. Shakkottai, L. Ying, and R. Srikant, "Scheduling in Multi-Channel Wireless Networks: Rate Function Optimality in the Small-Buffer Regime," *IEEE Transactions on Information Theory*, vol. 60, no. 2, pp. 1101–1125, 2014. DOI: 10.1109/TIT.2013.2293216

[3] V. Gupta, M. Harchol-Balter, K. Sigman, and W. Whitt, "Analysis of Join-the-Shortest-Queue Routing for Web Server Farms," *Performance Evaluation*, vol. 64, no. 9–12, pp. 1062–1081, 2007. DOI: 10.1016/j.peva.2007.06.012

[4] Y. Lu, Q. Xie, G. Kliot, A. Geller, J. R. Larus, and A. Greenberg, "Join-Idle-Queue: A Novel Load Balancing Algorithm for Dynamically Scalable Web Services," *Performance Evaluation*, vol. 68, no. 11, pp. 1056–1071, 2011. DOI: 10.1016/j.peva.2011.07.015

[5] M. Van der Boor, S. C. Borst, J. S. H. Van Leeuwaarden, and D. Mukherjee, "Scalable Load Balancing in Networked Systems: A Survey of Recent Advances," *SIAM Review*, vol. 64, no. 3, pp. 554–622, 2022. DOI: 10.1137/20M1323746

[6] F. A. Haight, "Two Queues in Parallel," *Biometrika*, vol. 45, no. 3–4, pp. 401–410, 1958. DOI: 10.1093/biomet/45.3-4.401

[7] W. Winston, "Optimality of the Shortest Line Discipline," *Journal of Applied Probability*, vol. 14, no. 1, pp. 181–189, 1977. DOI: 10.2307/3213271

[8] A. Hordijk and G. Koole, "On the Optimality of the Generalized Shortest Queue Policy," *Probability in the Engineering and Informational Sciences*, vol. 4, no. 4, pp. 477–487, 1990. DOI: 10.1017/S0269964800001777

[9] S. Halfin, "The Shortest Queue Problem," *Journal of Applied Probability*, vol. 22, no. 4, pp. 865–878, 1985. DOI: 10.2307/3213954

[10] I. J. B. F. Adan, J. Wessels, and W. H. M. Zijm, "Analysis of the Asymmetric Shortest Queue Problem," *Queueing Systems*, vol. 8, no. 1, pp. 1–58, 1991. DOI: 10.1007/BF02412240

[11] J. W. Cohen, "Analysis of the Asymmetrical Shortest Two-Server Queueing Model," *International Journal of Stochastic Analysis*, vol. 11, no. 2, pp. 115–162, 1998. DOI: 10.1155/S1048953398000112

[12] G.-J. Van Houtum, I. Adan, J. Wessels, and W. H. M. Zijm, "Performance Analysis of Parallel Identical Machines with a Generalized Shortest Queue Arrival Mechanism," *OR Spektrum*, vol. 23, no. 4, pp. 411–427, 2001. DOI: 10.1007/PL00013360

[13] H. Yao and C. Knessl, "On the Infinite Server Shortest Queue Problem: Symmetric Case," *Stochastic Models*, vol. 21, no. 1, pp. 101–132, 2005. DOI: 10.1081/STM-200046493

[14] H. Yao and C. Knessl, "On the Infinite Server Shortest Queue Problem: Non-Symmetric Case," *Queueing Systems*, vol. 52, no. 2, pp. 157–177, 2006. DOI: 10.1007/s11134-006-5500-z

[15] I. J. B. F. Adan, O. J. Boxma, S. Kapodistria, and V. G. Kulkarni, "The Shorter Queue Polling Model," *Annals of Operations Research*, vol. 241, no. 1, pp. 167–200, 2016. DOI: 10.1007/s10479-013-1495-0

[16] P. Eschenfeldt and D. Gamarnik, "Join the Shortest Queue with Many Servers. The Heavy-Traffic Asymptotics," *Mathematics of Operations Research*, vol. 43, no. 3, pp. 867–886, 2018. DOI: 10.1287/moor.2017.0887

[17] D. A. Dawson, J. Tang, and Y. Q. Zhao, "Performance Analysis of Joining the Shortest Queue Model Among a Large Number of Queues," *Asia-Pacific Journal of Operational Research*, vol. 36, no. 4, p. 1 950 019, 2019. DOI: 10.1142/S0217595919500192

[18] A. Braverman, "Steady-State Analysis of the Join-the-Shortest-Queue Model in the Halfin–Whitt Regime," *Mathematics of Operations Research*, vol. 45, no. 3, pp. 1069–1103, 2020. DOI: 10.1287/moor.2019.1023

[19] I. Dimitriou, "Analysis of the Symmetric Join the Shortest Orbit Queue," *Operations Research Letters*, vol. 49, no. 1, pp. 23–29, 2021. DOI: 10.1016/j.orl.2020.10.011

[20] W. Weng and W. Wang, "Achieving Zero Asymptotic Queueing Delay for Parallel Jobs," *Proceedings of the ACM on Measurement and Analysis of Computing Systems*, vol. 4, no. 3, pp. 1–36, 2020. DOI: 10.1145/3428327

[21] J. W. Cohen, "A Two-Queue, One-Server Model with Priority for the Longer Queue," *Queueing Systems*, vol. 2, no. 3, pp. 261–283, 1987. DOI: 10.1007/BF01158902

[22] L. Flatto, "The Longer Queue Model," *Probability in the Engineering and Informational Sciences*, vol. 3, no. 4, pp. 537–559, 1989. DOI: 10.1017/S0269964800001376

[23] G.-J. Van Houtum, I. Adan, and J. Van der Wal, "The Symmetric Longest Queue System," *Stochastic Models*, vol. 13, no. 1, pp. 105–120, 1997. DOI: 10.1080/15326349708807416

[24] C. Knessl and H. Yao, "On the Nonsymmetric Longer Queue Model: Joint Distribution, Asymptotic Properties, and Heavy Traffic Limits," *Advances in Operations Research*, vol. 2013, no. 1, p. 680 539, 2013. DOI: 10.1155/2013/680539

[25] R. Pedarsani and J. Walrand, "Stability of Multiclass Queueing Networks under Longest-Queue and Longest-Dominating-Queue Scheduling," *Journal of Applied Probability*, vol. 53, no. 2, pp. 421–433, 2016. DOI: 10.1017/jpr.2016.10

[26] R. Atar and S. Saha, "A Note on Non-Existence of Diffusion Limits for Serve-the-Longest-Queue when the Buffers Are Equal in Size," *Electronic Communications in Probability*, vol. 21, pp. 1–10, 2016. DOI: 10.1214/16-ECP4370

[27] E. Perel, N. Perel, and U. Yechiali, "A Polling System with 'Join the Shortest–Serve the Longest' Policy," *Computers & Operations Research*, vol. 114, p. 104 809, 2020. DOI: 10.1016/j.cor.2019.104809

[28] E. Perel, N. Perel, and U. Yechiali, "The Non-Preemptive 'Join the Shortest Queue–Serve the Longest Queue' Service System with or without Switch-Over Times," *Mathematical Methods of Operations Research*, vol. 99, no. 1, pp. 3–38, 2024. DOI: 10.1007/s00186-023-00848-7

[29] E. Perel, N. Perel, and U. Yechiali, "A 3-Queue Polling System with Join the Shortest–Serve the Longest Policy," *Indagationes Mathematicae*, vol. 34, no. 5, pp. 1101–1120, 2023. DOI: 10.1016/j.indag.2022.11.001

Information about the authors

Khityaev, Evgeny A.—Postgraduate Student of the Department of Probability Theory and Cyber Security of RUDN University (e-mail: evgenykhityaev@yandex.ru, ORCID: 0000-0002-2375-1873, ResearcherID: PYW-1479-2026)

Zaryadov, Ivan S.—Candidate of Physical and Mathematical Sciences, Assistant Professor of the Department of Probability Theory and Cyber Security of RUDN University; Senior Researcher of the Institute of Informatics Problems of the Federal Research Center "Computer Science and Control" of the Russian Academy of Sciences (e-mail: zaryadov-is@rudn.ru, ORCID: 0000-0002-7909-6396, ResearcherID: B-8154-2018, Scopus Author ID: 35294470000)

Milovanova, Tatiana A.—Candidate of Physical and Mathematical Sciences, Assistant Professor of the Department of Probability Theory and Cyber Security of RUDN University (e-mail: milovanova-ta@rudn.ru, ORCID: 0000-0002-9388-9499, ResearcherID: X-6718-2018)

RUSSIAN METADATA

УДК 519.872, 519.217
PACS 02.50.Ey, 02.50.Ga, 07.05.Tp
DOI: 10.22363/2658-4670-2026-34-3-316-333 EDN: RHUTHS

Двухочередная система массового обслуживания с дисциплинами JSQ–SLQ, абсолютным приоритетом и ненулевыми временами перехода прибора

Е. А. Хитяев[1], И. С. Зарядов[1,2], Т. А. Милованова[1]

[1] *Российский университет дружбы народов, ул. Миклухо-Маклая, д. 6, Москва, 117198, Российская Федерация*

[2] *Институт проблем информатики, Федеральный исследовательский центр «Информатика и управление» РАН, ул. Вавилова, д. 44, кор. 2, Москва, 119333, Российская Федерация*

Аннотация. Цель. Исследовать двухочередную систему массового обслуживания с одним прибором, функционирующую в соответствии с дисциплинами выбора кратчайшей очереди и обслуживания длиннейшей очереди, с вероятностным выбором очереди для поступления и обслуживания при равенстве их длин, прерываемым обслуживанием по абсолютному приоритету и ненулевыми временами перехода прибора между очередями. Методы. Для анализа системы используются марковское описание, уравнения глобального баланса для стационарных вероятностей, метод условных производящих функций и численный анализ. Результаты. Построен двумерный марковский процесс, компонентами которого являются длина первой очереди и фазовая переменная, отражающая разность длин очередей и состояние прибора. Для построенного процесса представлена система уравнений глобального баланса для стационарных вероятностей. Введены условные производящие функции, с помощью которых получена матричная форма уравнений баланса и рассмотрено условие существования стационарного режима. Получены выражения для основных стационарных характеристик системы, включая средние длины очередей, дисперсии, коэффициент корреляции, эффективные интенсивности поступления заявок, долю времени, в течение которого прибор находится в состоянии перехода, и вероятность его простоя. Проведён численный анализ влияния интенсивности поступления заявок, интенсивностей обслуживания, интенсивностей перехода прибора и вероятностей выбора очереди при равенстве длин на характеристики системы и распределение фаз процесса. Выводы. Показано, что совместное использование дисциплин выбора кратчайшей очереди и обслуживания длиннейшей очереди способствует выравниванию длин очередей, однако поведение системы и её стационарные характеристики существенно зависят от сочетания параметров маршрутизации, обслуживания, переходов прибора и вероятностей выбора очереди при равенстве длин.

Ключевые слова: система массового обслуживания, выбор кратчайшей очереди, обслуживание длиннейшей очереди, абсолютный приоритет, переход прибора, марковский процесс, условные производящие функции

Discrete & Continuous Models & Applied Computational Science
ISSN 2658-7149 (Online), 2658-4670 (Print)

2026, 34 (3) 334–344
http://journals.rudn.ru/miph

Research article

UDC 519.872, 519.217
DOI: 10.22363/2658-4670-2026-34-3-334-344 EDN: RRPVBC

Scenario of priority service for elastic traffic within the network slicing framework

Anastasia A. Tazaeva[1], Ekaterina V. Markova[1,2]

[1] *RUDN University, 6 Miklukho-Maklaya St, Moscow, 117198, Russian Federation*

[2] *Federal Research Center "Computer Science and Control" of the Russian Academy of Sciences, 44 Vavilova St, bldg 2, Moscow, 119333, Russian Federation*

(received: May 29, 2025; revised: February 20, 2026; accepted: March 3, 2026)

Abstract. *Background.* Network slicing (NS) enables multiple logical slices over shared infrastructure but faces challenges in managing heterogeneous traffic (streaming vs. elastic) with conflicting QoS requirements. *Purpose.* This paper proposes a radio admission control (RAC) scheme with priority service interruption for a two-slice 5G network to balance GBR for streaming traffic and efficient non-GBR elastic traffic service. *Method.* A two-dimensional Markov model is developed. Streaming traffic requires fixed resources; elastic traffic has state-dependent service rate. A full interruption scenario is implemented where elastic traffic preempts streaming traffic within the second slice's guaranteed capacity. Stationary probabilities are obtained numerically. *Results.* As streaming traffic arrival rate increases, elastic traffic interruption probability rises sharply then stabilises. Mean numbers of served requests converge to guaranteed capacities. Elastic traffic blocking remains nearly constant. *Conclusions.* The proposed RAC scheme captures the streaming-elastic trade-off in sliced networks. The full interruption mechanism prioritises elastic traffic under high load. The model provides quantitative guidelines for tuning guaranteed capacities in 5G/6G systems.

Key words and phrases: 5G, network slicing, mobile networks, QoS, GBR services, non-GBR services, key performance indicators, priority service, service interruption, radio resource management, resource allocation

For citation: A. A. Tazaeva, E. V. Markova "Scenario of priority service for elastic traffic within the network slicing framework," *Discrete and Continuous Models and Applied Computational Science*, vol. 34, no. 3, pp. 334–344, 2026. DOI: 10.22363/2658-4670-2026-34-3-334-344. EDN: RRPVBC.

1. Introduction

The rapid advancement of fifth-generation (5G) networks has significantly increased the demand for enhanced Quality of Service (QoS) from service providers. Organizations such as 3GPP and the GSM Association emphasize that 5G networks must support multiaccess capabilities, maintain low and predictable latency with minimal packet loss, and ensure high network resilience [1–3]. These stringent requirements have led to the development of flexible and adaptive network architectures capable of dynamically addressing these challenges [4–7].

One of the fundamental technologies that allows for this flexibility is Network Slicing (NS) [8–11]. NS allows mobile network operators to create multiple logically isolated and customizable network slices within a shared physical infrastructure, such as a base station (BS). These slices, referred to as Network Slice Instances (NSIs), can be dynamically deployed and removed based on real-time technical requirements, facilitating autonomous resource allocation without direct user involvement. Furthermore, NS enables service providers to manage QoS efficiently, enhancing fault tolerance and overall network reliability [12–15].

Each NSI is typically designed to support a specific category of service, such as best effort with minimum guarantee (BG), guaranteed bit rate (GB), or best effort (BE). BG and BE services generate elastic traffic with variable service duration, while GB services generate streaming traffic with fixed duration [16, 17].

© 2026 A. A. Tazaeva, E. V. Markova

This work is licensed under a Creative Commons "Attribution-NonCommercial 4.0 International" license.

This paper proposes a model for the joint servicing of two types of traffic, streaming and elastic with minimum guarantee, within a 5G network utilizing the NS framework. In addition, it evaluates key performance metrics to assess the efficiency of the model.

The remainder of this paper is structured as follows. Section 2 introduces the radio admission control (RAC) scheme for a 5G network, formulated as a queueing system (QS) managing both streaming and elastic traffic. The analysis includes transition intensity diagrams, an infinitesimal generator, and calculations of key performance measures. Finally, Section 3 presents the conclusions.

2. System model

Consider the operation of a base station (BS) cell within a network with a total capacity of C [capacity units, c.u.]. This capacity is distributed between two NSIs, each with capacities C_1 and C_2, respectively, where $\sum_{k=1}^{2} C_k \geqslant C$. The capacity C_k allocated to NSI k consists of two parts: a guaranteed capacity Q_k and a shared capacity available to other NSIs, expressed as $C_k - Q_k$, for $k = 1, 2$. The guaranteed capacities satisfy the condition $\sum_{k=1}^{2} Q_k \leqslant C$, where $0 < Q_k \leqslant C_k \leqslant C$, for $k = 1, 2$.

We assume that the first NSI is for services generating streaming traffic (first-type requests), while the second NSI accommodates services generating elastic traffic (second-type requests). The arrival process for service requests follows a Poisson distribution with an arrival rate λ_k, where $k = 1, 2$. The service time for first-type requests is exponentially distributed with a mean of μ_1^{-1}. In contrast, the duration of the service for second-type requests depends on the system load and the average file length Θ.

Each first-type request requires b_1 c.u., constrained by $b_1 \leqslant Q_1$. Similarly, each second-type request requires a minimum allocation of $b_2^{\min}$ c.u., where $b_2^{\min} \leqslant Q_2$. For simplicity, we set $b_1 = b_2^{\min} = 1$.

Let n_k denote the number of active requests in NSI k ($k = 1, 2$) when the system is in state $n = (n_1, n_2)$. Given the elastic nature of second-type traffic, the number of occupied capacity units is defined as

$$b_2(n_1, n_2) = \frac{\min(C - b_1 n_1, C_2)}{n_2},$$

where $b_2^{\min} \leqslant b_2(n_1, n_2) \leqslant C_2$. The corresponding service time for second-type requests is determined by

$$\mu_2^{-1}(n_1, n_2) = \frac{n_2 \Theta}{b_2(n_1, n_2)}.$$

The key parameters are summarized in Table 1.

Now, let us analyze the request admission process in the system. When a new first-type request arrives, the following conditions apply:

- The request is admitted if the number of ongoing first-type requests is below the maximum allowable limit, given by $N_1^{\max} = C_1/b_1$, and there are sufficient available resources, specifically at least b_1 capacity units.
- If the number of first-type requests is below the threshold supported by the guaranteed capacity, i.e., $N_1^g = Q_1/b_1$, but available resources are insufficient (less than b_1), the request can still be accepted by interrupting a second-type request, provided that at least one second-type request exists within the guaranteed capacity Q_1.
- If neither of the above conditions is met, the request is blocked.

The radio admission control mechanism for second-type requests is structured as follows:

- The request is admitted if the number of ongoing second-type requests is below the maximum permissible limit, given by $N_2^{\max} = C_2/b_2^{\min}$, and there are sufficient available resources, specifically at least $b_2^{\min}$ capacity units.
- If the number of second-type requests is below the threshold supported by the guaranteed capacity, i.e., $N_2^g = Q_2/b_2^{\min}$, but available resources are insufficient (less than $b_2^{\min}$), the request can still be accepted by interrupting a first-type request, provided that at least one first-type request exists within the guaranteed capacity Q_2.

Table 1

Summary of key parameters

Notation	Description
C	The BS's total network capacity (capacity units, c.u.).
C_k	The k-th NSI's overall network capacity, $k \in \{1,2\}$, $C_1 + C_2 \geqslant C$ (c.u.).
Q_k	The k-th NSI's guaranteed network capacity, $Q_k \leqslant C_k$, $Q_1 + Q_2 \leqslant C$ (c.u.).
λ_k	The arrival rate of requests in k-th NSI, $k \in \{1,2\}$ (requests per unit of time).
μ_1^{-1}	The average service time of one request at the first NSI (t.u.).
Θ	The average length of the transmitted file (c.u. $\times$ t.u.).
b_1	The number of resource units required to serve each request of the first type (c.u.).
$b_2^{\min}$	The minimal number of resource units required to serve each request of the second type (c.u.).
n_k	The number of requests in k-th NSI, $k \in \{1,2\}$ (—).
$N_k^{\max}$	The maximum number of requests in k-th NSI, $N_1^{\max} = C_1/b_1$, $N_2^{\max} = C_2/b_2^{\min}$ (—).
N_k^g	The maximum number of requests that can be served using guaranteed network capacity of k-th NSI (—).
$b_2(n_1, n_2)$	The number of resource units available for servicing each request of the second type in the state (n_1, n_2), $b_2^{\min} \leqslant b_2(n_1, n_2) \leqslant C_2$ (c.u.).

– If neither of these conditions is met, the second-type request is blocked.

In cases where resources are insufficient, service interruption for first-type requests can occur through two mechanisms:

1. If the number of ongoing second-type requests is below the guaranteed threshold, i.e., $n_2 < N_2^g$, a first-type request is interrupted to free up the minimum required resources, $b_2^{\min}$, necessary for accommodating a second-type request.
2. If the number of ongoing second-type requests remains below the guaranteed threshold, i.e., $n_2 < N_2^g$, all second-type requests utilizing the guaranteed capacity Q_2 are interrupted.

This study focuses on the second scenario. The system operation is illustrated schematically in Figure 1.

3. Mathematical model

The system behavior is described by a two-dimensional Markov process (MP) $\{(X_1(t), X_2(t)), t > 0\}$, where $X_k(t)$ represents the number of k type requests in the system at time t, $k = 1, 2$, over the state space $\mathbf{X}$:

$$\mathbf{X} = \{(n_1, n_2) : 0 \leqslant n_1 \leqslant N_1^{\max} \wedge 0 \leqslant n_2 \leqslant N_2^{\max} \wedge n_1 b_1 + \\ + n_2 b_2^{\min} \leqslant C \wedge n_2 b_2(n_1, n_2) \cdot \mathbf{I}(n_2 \geqslant 1) \geqslant Q_2\},$$

where I is a characteristic function

$$\mathbf{I}(P) = \begin{cases} 1, & \text{if the condition is satisfied,} \\ 0, & \text{if the condition is not satisfied.} \end{cases}$$

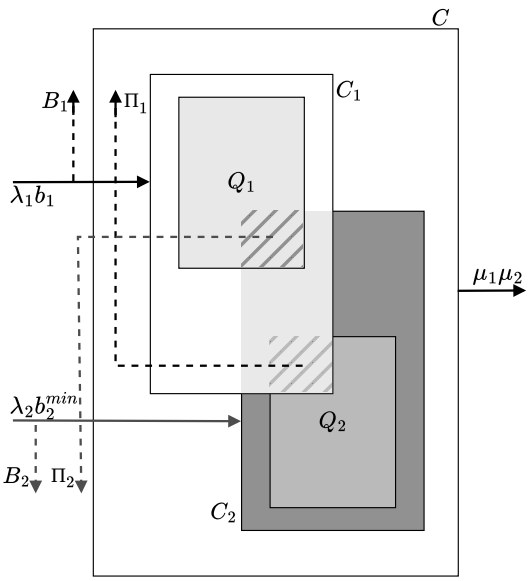


Figure 1. System model representation

The state space $\mathbf{X}$ includes few subsets: interruption subset $\mathbf{V}_i^k$, admission subset $\mathbf{S}_k$, and blocking subset $\mathbf{B}_k$, where $i, k \in \{1, 2\}$, $i \neq k$. Based on the sets, the transition intensity diagram can be represented in the following form (Figure 2).

The interruption subset $\mathbf{V}_1^2$, $\mathbf{V}_2^1$, represents the system states where the service of arriving k-type request has priority over the service of i-type request (in other words, states where the service of i-type request can be interrupted to service one arriving k type request):

$$\mathbf{V}_1^2 = \{(n_1, n_2) \in \mathbf{X} : n_2 = 0 \wedge n_2 b_2(n_1, n_2) < Q_2\},$$

$$\mathbf{V}_2^1 = \{(n_1, n_2) \in \mathbf{X} : n_1 < N_1^g \wedge n_1 b_1 + n_2 b_2^{\min} = C\}.$$

The admission subset $\mathbf{S}_k$, $k = 1, 2$, represents the system states where k-type request will be accepted for service in the k-th NSI:

$$\begin{aligned}\mathbf{S}_1 = \mathbf{V}_2^1 \cup \{(n_1, n_2) \in \mathbf{X} : (0 \leqslant n_1 < N_1^{\max} \wedge (n_1 + 1) b_1 + \\ + n_2 b_2^{\min} \leqslant C \wedge n_2 = 0) \vee (0 \leqslant n_1 < N_1^{\max} \wedge (n_1 + 1) b_1 + \\ + n_2 b_2^{\min} \leqslant C \wedge n_2 > 0 \wedge n_2 b_2(n_1, n_2) > Q_2)\},\end{aligned}$$

$$\mathbf{S}_2 = \mathbf{V}_1^2 \cup \{(n_1, n_2) \in \mathbf{X} : 0 \leqslant n_2 < N_2^{\max} \wedge n_1 b_1 + (n_2 + 1) b_2^{\min} \leqslant C\}.$$

The blocking subset $\mathbf{B}_k$, $k = 1, 2$, represents the system states where arriving k-type requests will be blocked by the system due to insufficient available resources in the k-th NSI:

$$\begin{aligned}\mathbf{B}_1 = \Big\{(n_1, n_2) \in \mathbf{X} : n_1 = N_1^{\max} \vee (N_1^g \leqslant n_1 < N_1^{\max} \wedge \\ \wedge (n_1 + 1) b_1 + n_2 b_2^{\min} > C) \vee (n_2 > 0 \wedge n_2 b_2(n_1 + 1, n_2) < Q_2)\Big\}.\end{aligned}$$

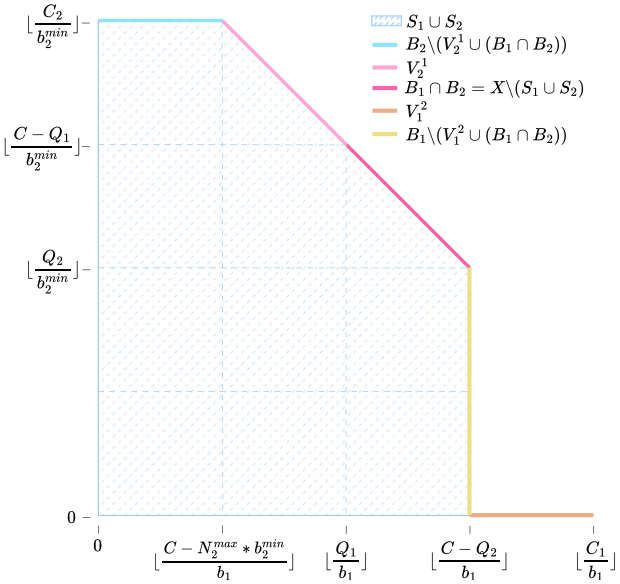


Figure 2. Scheme of the transition intensity diagram

$$\mathbf{B}_2 = \Big\{(n_1, n_2) \in \mathbf{X} : (n_2 = N_2^{\max}) \vee \\ \vee (N_2^g \leqslant n_2 < N_2^{\max} \wedge n_1 b_1 + (n_2+1) b_2^{\min} > C)\Big\}.$$

According to the diagram of transition intensities (Figure 3), the considered process is described by the following system of equilibrium equations:

$$\begin{aligned} & p(n_1, n_2) \cdot \big(\lambda_2 \cdot \mathbf{I}\{(n_1, n_2) \in \mathbf{S}_2/\mathbf{V}_1^2\} + \lambda_1 \cdot \mathbf{I}\{(n_1, n_2) \in \mathbf{V}_2^1\} \\ & \quad + \lambda_1 \cdot \mathbf{I}\{(n_1, n_2) \in \mathbf{S}_1/\mathbf{V}_2^1\} + \lambda_2 \cdot \mathbf{I}\{(n_1, n_2) \in \mathbf{V}_1^2\} \\ & \quad + n_2\mu_2 \cdot \mathbf{I}\{n_2 > 0\} + n_1\mu_1 \cdot \mathbf{I}\{n_1 > 0\}\big) \\ & = \big[\lambda_1 \cdot p(n_1 - 1, n_2) + \lambda_2 \cdot p(n_1, n_2 - 1) + (n_1 + 1)\mu_1 \cdot p(n_1 + 1, n_2) \\ & \quad + (n_2 + 1)\mu_2 \cdot p(n_1, n_2 + 1)\big], \end{aligned}$$

where $p(n_1, n_2)$, $n \in \mathbf{X}$ — stationary probability distribution of system states.

Due to the implementation of the mechanism for interrupting the service of requests, the process $\{(X_1(t), X_2(t)), t > 0\}$, describing the considered system, is not a reversible Markov process. Therefore, the system's stationary probability distribution $\mathbf{p} = \{p(n_1, n_2), (n_1, n_2) \in \mathbf{X}\}$ can be computed using the numerical solution of the equilibrium equations system $\mathbf{p}^T \cdot A = \mathbf{0}^T$, $\mathbf{p}^T \cdot \mathbf{1} = 1$, where A is the infinitesimal generator, and the elements $\mathbf{a}((n_1, n_2), (n_1', n_2'))$ of this generator are determined by the following formulas:

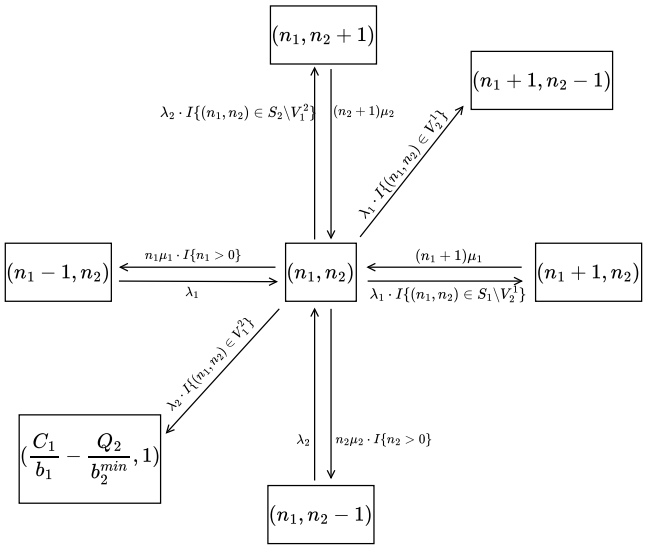


Figure 3. The diagram of transition intensities for an arbitrary system state (n_1, n_2)

$$\mathbf{a}\big((n_1,n_2),(n_1',n_2')\big) = \begin{cases} \lambda_1, n_1' = n_1+1, n_2' = n_2, (n_1,n_2) \in \mathbf{S}_1/\mathbf{V}_2^1, \\ \lambda_1, n_1' = n_1+1, n_2' = n_2-1, (n_1,n_2) \in \mathbf{V}_2^1, \\ \lambda_2, n_1' = n_1, n_2' = n_2+1, (n_1,n_2) \in \mathbf{S}_2/\mathbf{V}_1^2, \\ \lambda_2, n_1' = \frac{C}{b_1} - \frac{Q_2}{b_2^{min}}, n_2' = 1, (n_1,n_2) \in \mathbf{V}_1^2, \\ n_1\mu_1, n_1' = n_1-1, n_2' = n_2, n_1 > 0, \\ n_2\mu_2, n_1' = n_1, n_2' = n_2-1, n_2 > 0, \\ \gamma, n_1' = n_1, n_2' = n_2, \\ 0, \text{otherwise}, \end{cases}$$

where

$$\gamma = -\Big(\lambda_1 \cdot \mathbf{I}\{(n_1,n_2) \in \mathbf{S}_1\} + \lambda_2 \cdot \mathbf{I}\{(n_1,n_2) \in \mathbf{S}_2\} + n_1\mu_1 \mathbf{I}\{(n_1,n_2) \in \mathbf{X} : n_1 > 0\} + n_2\mu_2 \cdot \mathbf{I}\{(n_1,n_2) \in \mathbf{X} : n_2 > 0\}\Big).$$

4. The main performance measures

The main performance measures of the model are the following:

– The mean number N_k of k-type requests served in the k-th NSI

$$N_k = \sum_{(n_1,n_2) \in \mathbf{X}} n_k \cdot p(n_1,n_2), \quad k = 1,2.$$

– The service interruption probability Π_i^k of i type requests served in the i-th NSI when new k-type request arrives at the system

$$\Pi_i^k = \sum_{(n_1,n_2)\in \mathbf{V}_i^k} p(n_1,n_2), \quad i,k=1,2, \quad i\neq k.$$

– The accepting probability S_k of k-th type request for service at k-th NSI

$$S_k = \sum_{(n_1,n_2)\in \mathbf{S}_k} p(n_1,n_2), \quad k=1,2.$$

– The blocking probability B_k of k-th type request

$$B_k = 1 - S_k = \sum_{(n_1,n_2)\in \mathbf{B}_k} p(n_1,n_2), \quad k=1,2.$$

5. Results

Let us now proceed to the numerical analysis. As a case study of a system supporting the joint handling of streaming and elastic traffic, we could consider a 5G network that provides both enhanced Mobile Broadband (eMBB) and Ultra-Reliable Low-Latency Communication (URLLC) services. In this context, eMBB corresponds to elastic traffic, while URLLC represents streaming traffic. We examine how key performance metrics—such as the mean number of active k-type requests, service interruption probability, accepting probability, and blocking probability—vary with changes in the arrival rate, for example, first-type requests.

The parameters used in this numerical example are summarized in Table 2.

Table 2

Main parameters of the numerical example

Notation	**Value**
C	25
C_1	20
C_2	15
Q_1	13
Q_2	10
λ_1	$0 \to 120$
λ_2	100
μ_1	1
Θ	1.5
$b_1 = b_2^{\min}$	1

Figure 4 presents the dependence of the service interruption probability Π_i^k on the arrival rate λ_1. The plot demonstrates that, for the first-type of requests, the interruption probability increases slightly as λ_1 grows. On the contrary, for the second-type requests the probability of interruption increases sharply at first, and then also decreases sharply with an increase in the value of λ_1 and eventually approaches a stable value. This behavior occurs due to the fact that the intensity of the second-type requests is high, and they immediately occupy almost the entire system capacity, and therefore, when first-type requests arrival at the system, the guaranteed network capacity is released and service is interrupted. However, since the number of the second-type requests that can be interrupted is limited by the threshold value of Q_1, then there is a decrease in the interruption probability.

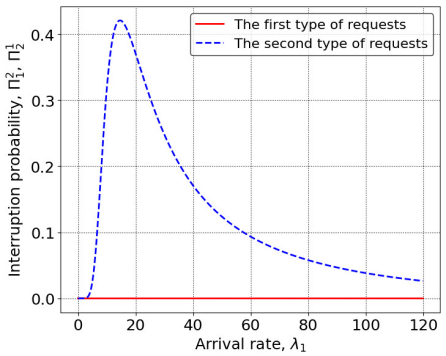


Figure 4. Dependence of the interruption probability on the arrival rate of the first-type requests

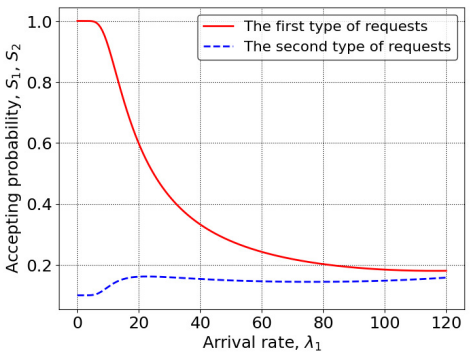


Figure 5. Dependence of the accepting probability on the arrival rate of the first-type requests

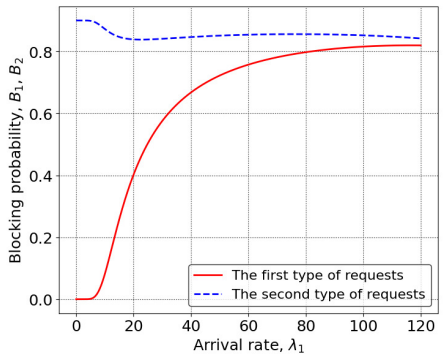


Figure 6. Dependence of the blocking probability on the arrival rate of the first-type requests

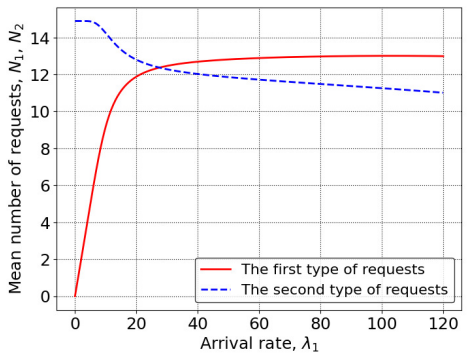


Figure 7. Dependence of the mean number of serviced requests on the arrival rate of the first-type requests

Let's consider the behavior of the accepting probability S_k for each type of requests, depending on the first-type requests arrival rate, λ_1. As shown in Figure 5, at the initial moment of time, with a small λ_1, the accepting probability for the first-type requests is maximum and tends to unity, since requests of each type occupy the capacity of the corresponding NSI and do not affect the QoS for each other. As the arrival rate of requests increases, the accepting probability for both types of requests decreases rapidly. However, since the arrival rate of the second-type requests, (λ_2), remains unchanged, the decrease in S_2 is less pronounced in the graph.

A similar trend is observed in Figure 6, which depicts the blocking probabilities. As λ_1 increases, the blocking probability B_1 grows correspondingly, while the blocking probability B_2 remains nearly constant due to the fixed arrival rate λ_2.

We now turn to the most insightful graph, which illustrates the dependence of the mean number of serviced requests N_k, for $k = 1, 2$, on the arrival rate λ_1 of the first-type requests. As shown in Figure 7, when no first-type requests are present in the system, second-type requests utilize the entire portion of capacity $C_2 = 15$ allocated to them and the number of second-type requests served in the system tends to the maximum value $N_2^{\max} = 15$. As first-type requests begin to arrive, the number of serviced second-type requests N_2 gradually decreases. Under conditions of full system load, the number of serviced requests for both types converges to their respective guaranteed levels $N_1^g = 13$ and $N_2^g = 10$.

6. Discussion

The obtained results highlight the interaction between streaming and elastic traffic in a sliced 5G network. The interruption probability of elastic flows increases sharply in the low-to-medium λ_1 regime, but then stabilizes as the guaranteed resources Q_1 and Q_2 become dominant. This confirms the importance of guaranteed quotas for maintaining predictable service.

Compared to earlier work on preemption-based prioritization [12], our approach explicitly models admission control with guaranteed resource allocation. The findings are consistent with survey studies on slicing performance [4, 5, 7], while extending them by quantifying blocking and interruption trade-offs.

From a practical perspective, the model illustrates how operators can tune Q_1 and Q_2 to balance eMBB and URLLC requirements. Such tuning directly impacts blocking probabilities and guarantees acceptable QoS under varying load conditions. This insight is useful for SLA negotiation and capacity planning.

Naturally, the model has limitations. It assumes Poisson arrivals, exponential service times, and only two slices. Correlations between traffic types, mobility patterns, or more complex slice hierarchies are not captured. Moreover, the interruption mechanism is simplified, focusing only on guaranteed thresholds.

Future extensions could include machine-learning-based controllers for adaptive RAC [18, 19], as well as integration with edge computing and 6G scenarios [16, 20].

7. Conclusions

This paper introduced a radio admission control model for 5G network slicing with priority interruption. The model differentiates between streaming and elastic traffic and evaluates key performance metrics such as blocking, accepting, and interruption probabilities, as well as mean numbers of active requests.

The results demonstrate that the proposed mechanism successfully captures the trade-offs between heterogeneous traffic classes. The analysis provides operators with quantitative guidelines for configuring guaranteed capacities and balancing competing QoS requirements. The presented framework thus offers a foundation for more efficient and fair resource allocation strategies in slice-aware wireless networks.

Author Contributions: Conceptualization, A. Tazaeva and E. Markova; methodology, A. Tazaeva; software, A. Tazaeva; validation, A. Tazaeva and E. Markova; formal analysis, A. Tazaeva; investigation, A. Tazaeva; resources, E. Markova; data curation, A. Tazaeva; writing—original draft preparation, A. Tazaeva; writing—review and editing, A. Tazaeva and E. Markova; visualization, A. Tazaeva; supervision, E. Markova; project administration, A. Tazaeva; funding acquisition, D. Ivanova. All authors have read and agreed to the published version of the manuscript.

Funding: This research was funded by the Russian Science Foundation, project no. 24-19-00804 (https://rscf.ru/en/project/24-19-00804/).

Data Availability Statement: All data generated or analyzed during this study are included in this article. Additional numerical results and simulation scripts are available from the corresponding author upon reasonable request.

Acknowledgments: The authors thank the Department of Probability Theory and Cybersecurity of RUDN University for valuable discussions and methodological support.

Conflicts of Interest: The authors declare no conflict of interest. The funders had no role in the design of the study; in the collection, analyses, or interpretation of data; in the writing of the manuscript; or in the decision to publish the results.

Declaration on Generative AI: The authors have not employed any Generative AI tools.

References

[1] J. Meredith, F. Firmin, and M. Pope, “Release 16 Description; Summary of Rel-16 Work Items,” 3rd Generation Partnership Project (3GPP), Tech. Rep., version 16.2.0, 2022.

[2] M. Zambianco, A. Lieto, I. Malanchini, and G. Verticale, "A Learning Approach for Production-Aware 5G Slicing in Private Industrial Networks," in *Proceedings of the ICC 2022—IEEE International Conference on Communications*, Seoul, Korea, May 2022.

[3] S. Elayoubi, M. Fallgren, P. Spapis, L. Campoy, B. Martinez, A. Mavromatis, and P. Iovanna, "5G Service Requirements and Operational Use Cases: Analysis and Implementation," *IEEE Communications Magazine*, vol. 54, no. 11, pp. 84–90, 2016. DOI: 10.1109/MCOM.2016.1600172CM

[4] X. Foukas, G. Patounas, A. Elmokashfi, and M. Marina, "Network Slicing in 5G: Survey and Challenges," *IEEE Communications Magazine*, vol. 55, no. 5, pp. 94–100, 2017. DOI: 10.1109/MCOM.2017.1600951

[5] H. Zhang, N. Liu, X. Chu, K. Long, A. Aghvami, and V. Leung, "Network Slicing Based 5G and Future Mobile Networks: Mobility, Resource Management, and Challenges," *IEEE Communications Magazine*, vol. 55, no. 8, pp. 138–145, 2017. DOI: 10.1109/MCOM.2017.1600940

[6] M. Richart, J. Baliosian, J. Serrat, and J. Gorricho, "Resource slicing in virtual wireless networks: A survey," *IEEE Transactions on Network and Service Management*, vol. 13, no. 3, pp. 462–476, 2016. DOI: 10.1109/TNSM.2016.2597290

[7] P. Rost, A. Banchs, I. Berberana, M. Breitbach, M. Doll, H. Droste, C. Mannweiler, M. Puente, K. Samdanis, and B. Sayadi, "Network Slicing to Enable Scalability and Flexibility in 5G Mobile Networks," *IEEE Communications Magazine*, vol. 55, no. 5, pp. 72–79, 2017. DOI: 10.1109/MCOM.2017.1600939

[8] V. Tikhvinskiy and G. Bochechka, "Prospects and QoS requirements in 5G networks," *Journal of Telecommunications and Information Technology*, vol. 2015, no. 1, pp. 23–26, 2015.

[9] J. Ordonez-Lucena, P. Ameigeiras, D. Lopez, J. Ramos-Munoz, J. Lorca, and J. Folgueira, "Network Slicing for 5G with SDN/NFV: Concepts, Architectures, and Challenges," *IEEE Communications Magazine*, vol. 55, no. 5, pp. 80–87, 2017. DOI: 10.1109/MCOM.2017.1600935

[10] F. Zhou, R. Hu, Z. Li, and Z. Han, "Network slicing as a service: enabling enterprises' own software-defined cellular networks," in *IEEE Communications Magazine*, vol. 54, 2016, pp. 146–153.

[11] R. Ferrus, O. Sallent, J. Perez-Romero, and R. Agusti, "On 5G Radio Access Network Slicing: Radio Interface Protocol Features and Configuration," *IEEE Communications Magazine*, vol. 56, no. 5, pp. 184–192, 2018. DOI: 10.1109/MCOM.2018.1700659

[12] Y. Adou, E. Markova, and Y. Gaidamaka, "Modeling and analyzing preemption-based service prioritization in 5G networks slicing framework," *Future Internet*, vol. 14, no. 10, p. 299, 2022. DOI: 10.3390/fi14100299

[13] F. Kamoun and L. Kleinrock, "Analysis of shared finite storage in a computer networks node environment under general traffic conditions," *IEEE Transactions on Communications*, vol. 28, no. 7, pp. 992–1003, 1980. DOI: 10.1109/TCOM.1980.1094756

[14] B. Han, V. Gopalakrishnan, L. Ji, and S. Lee, "Network Function Virtualization: Challenges and Opportunities for Innovations," *IEEE Communications Magazine*, vol. 53, no. 2, pp. 90–97, 2015. DOI: 10.1109/MCOM.2015.7045396

[15] I. Parvez, A. Rahmati, I. Guvenc, A. Sarwat, and H. Dai, "A Survey on Low Latency Towards 5G: RAN, Core Network and Caching Solutions," *IEEE Communications Surveys & Tutorials*, vol. 20, no. 4, pp. 3098–3130, 2018. DOI: 10.1109/COMST.2018.2841349

[16] A. Ateya, A. Alhussan, H. Abdallah, M. Al duailij, A. Khakimov, and A. Muthanna, "Edge Computing Platform with Efficient Migration Scheme for 5G/6G Networks," *Computer Systems Science and Engineering*, vol. 45, no. 2, pp. 1775–1787, 2023.

[17] G. Association, "Generic Network Slice Template," GSM Association Official Document NG.116, Tech. Rep., version 1.0, May 2019.

[18] D. Bega, M. Gramaglia, A. Banchs, X. Costa-Pérez, and V. Sciancalepore, "A Machine Learning Approach to 5G Infrastructure Market Optimization," *IEEE Transactions on Mobile Computing*, vol. 19, no. 3, pp. 498–512, 2019. DOI: 10.1109/TMC.2019.2893269

[19] Y. Sun, M. Peng, Y. Zhou, Y. Huang, and S. Mao, "Application of Machine Learning in Wireless Networks: Key Techniques and Open Issues," *IEEE Communications Surveys & Tutorials*, vol. 21, no. 4, pp. 3072–3108, 2019. DOI: 10.1109/COMST.2019.2924243

[20] S. Zhang, J. Xu, W. Wang, and X. Yang, "6G: Connectivity, Networking and Services," *IEEE Internet of Things Journal*, vol. 8, no. 7, pp. 5399–5410, 2021. DOI: 10.1109/JIOT.2020.3037399

Information about the authors

Markova, Ekaterina V.—Docent, Ph.D. in Physics and Mathematics, Associate Professor of Department of Probability Theory and Cyber Security of RUDN University (e-mail: markova-ev@rudn.ru, ORCID: 0000-0002-7876-2801, Scopus Author ID: 56315828200)

Tazaeva, Anastasia A.—Student of Department of Probability Theory and Cyber Security of RUDN University, (e-mail: tazaeva081@gmail.com, ORCID: 0009-0001-4065-0847)

RUSSIAN METADATA

УДК 519.872, 519.217

DOI: 10.22363/2658-4670-2026-34-3-334-344 EDN: RRPVBC

Сценарий приоритетного обслуживания эластичного трафика в рамках концепции сетевой нарезки

А. А. Тазаева[1], Е. В. Маркова[1, 2]

[1] *Российский университет дружбы народов, ул. Миклухо-Маклая, д. 6, Москва, 117198, Российская Федерация*

[2] *Институт проблем информатики, Федеральный исследовательский центр «Информатика и управление» РАН, ул. Вавилова, д. 44, корп. 2, Москва, 119333, Российская Федерация*

Аннотация. *Предпосылки.* Технология сетевой нарезки (NS) позволяет создавать логические слои в рамках общей сетевой инфраструктуры, но сталкивается с проблемой совместного обслуживания разнородного трафика (потокового и эластичного), предъявляющего различные требования к QoS. *Цель.* Разработать и провести анализ схемы управления доступом к радиоресурсам с приоритетным обслуживанием в сети 5G с двумя слоями, которая позволит обеспечить баланс между требованиями к обслуживанию потокового и эластичного трафика. *Метод.* Использованы методы теории массового обслуживания. Разработана двумерная марковская модель. Потоковый трафик предъявляет фиксированное требование к ресурсам; для эластичного трафика требование к ресурсам зависит от состояния системы. Реализован сценарий полного освобождения гарантированной эластичному трафику емкости. Распределение вероятностей состояний системы получено численно. *Результаты.* С ростом интенсивности поступления потокового трафика вероятность прерывания передачи эластичного трафика сначала резко возрастает, затем стабилизируется. Среднее число обслуживаемых запросов стремится к гарантированным числам. Вероятность блокировки эластичного трафика почти не меняется. *Выводы.* Предложенная схема доступа к ресурсам сети представляет собой компромисс при обслуживании разных типов трафика. Модель позволяет получить количественные рекомендации для настройки гарантированных емкостей в системах 5G/6G.

Ключевые слова: 5G, нарезка сети, мобильные сети, QoS, услуги с гарантированным обслуживанием, услуги без гарантий к обслуживанию, показатели производительности, приоритетное обслуживание, прерывание обслуживание, управление доступом к ресурсам, распределение ресурсов

Discrete & Continuous Models & Applied Computational Science
ISSN 2658-7149 (Online), 2658-4670 (Print)

2026, 34 (3) 345–359
http://journals.rudn.ru/miph

Research article

UDC 519.872, 519.217
PACS 07.05.Tp, 02.60.Pn, 02.70.Bf
DOI: 10.22363/2658-4670-2026-34-3-345-359 EDN: RGASAA

An accurate block error rate model for performance analysis of LEO NB-IoT communications systems

Danil V. Shilonosov[1], Alina A. Likhtenshtein[1], Vitalii A. Beschastnyi[1], Yuliya V. Gaidamaka[1,2]

[1] *RUDN University, 6 Miklukho-Maklaya St, Moscow, 117198, Russian Federation*

[2] *Federal Research Center "Computer Science and Control" Russian Academy of Sciences, 44 Vavilova St, bldg 2, Moscow, 119333, Russian Federation*

(received: July 30, 2026; revised: August 10, 2026; accepted: August 15, 2026)

Abstract. *Background:* The extension of NB-IoT to LEO satellite systems enables mMTC in remote areas beyond terrestrial coverage. However, LEO NB-IoT faces significant physical layer challenges, including extreme path loss, rapid orbital dynamics, and blockage by buildings, forests, and hills. Existing Markov chain propagation models fail to capture the fine-grained elevation-dependent variability required for transmission optimization. *Purpose*: This study develops an accurate BLER model for LEO NB-IoT that accounts for elevation angle, deployment-specific shadowing, and scintillation, enabling dynamic scheduling to improve reliability and energy efficiency. *Methods:* We propose a fine-grained model incorporating ITU-R P.681-11 Loo parameterization with PCHIP interpolation for arbitrary elevations, integrating free-space loss, elevation-dependent scintillation, atmospheric absorption, and two-state Markov shadowing with urban/village/rural parameters. The BLER is estimated via Monte Carlo simulations with 10^5 samples and link-budget analysis for repetitions $N_{\text{rep}} \in \{1, 2, 4, 8, 16, 32, 64, 128\}$. *Results:* Elevation angle is the dominant factor: at EIRP=42 dBm and $N_{\text{rep}} = 1$, BLER falls from 1 at 20° to <0.1 at 70°. Deployment conditions have secondary but measurable effects; urban scenarios show up to 0.4 higher BLER than villages at the same elevation. Increasing the number of repetitions to 128 shifts the BLER curves by 8–10 dBm, whereas $N_{\text{rep}} = 4$ yields a near-zero BLER at 50° in all scenarios. *Conclusions:* Fixed-time transmission is suboptimal; UEs can achieve near-zero BLER by waiting for elevations above 50° with moderate repetitions. Our model enables elevation-aware scheduling from ephemeris data without requiring real-time sounding, offering a practical framework for reliable and energy-efficient LEO NB-IoT communications under diverse environmental conditions.

Key words and phrases: mMTC, LEO, shadowing, elevation, NB-IoT, Non-Terrestrial Networks.

For citation: D. V. Shilonosov, A. A. Likhtenshtein, V. A. Beschastnyi, Y. V. Gaidamaka "An accurate block error rate model for performance analysis of LEO NB-IoT communications systems," *Discrete and Continuous Models and Applied Computational Science*, vol. 34, no. 3, pp. 345–359, 2026. DOI: 10.22363/2658-4670-2026-34-3-345-359. EDN: RGASAA.

1. Introduction

While modern networks are pervasive, terrestrial infrastructure fails to cover more than 80% of the Earth's surface [1]. This connectivity gap presents a significant barrier to industrial massive machine-type communication (mMTC) applications, such as maritime logistics, global asset tracking, and remote environmental monitoring, which often operate in isolated territories [2]. To bridge this divide without the prohibitive costs of ground-based expansion, the 3GPP has integrated non-terrestrial networks (NTN) into the 5G framework [3]. By leveraging a multi-layered architecture of high-altitude platforms (HAP) and low/middle/geostationary Earth orbiting satellites, NTNs extend the reach of mMTC services to the most remote corners of the globe [4, 5].

© 2026 D. V. Shilonosov, A. A. Likhtenshtein, V. A. Beschastnyi, Y. V. Gaidamaka

This work is licensed under a Creative Commons "Attribution-NonCommercial 4.0 International" license.

The adaptation of NB-IoT for low-earth orbiting (LEO) constellations is emerging as a definitive solution for ubiquitous IoT connectivity [6]. Although the low-throughput, delay-tolerant traffic design of NB-IoT makes it a prime candidate for NTN integration, the transition from terrestrial to satellite-based architectures introduces formidable physical layer hurdles. The extreme altitudes of spaceborne platforms exacerbate path loss, demanding enhanced link budgets through increased transmit power or higher antenna gains. Furthermore, the rapid orbital velocities of LEO constellations induce significant Doppler shifts and create a highly dynamic environment in which, unlike static terrestrial cells, the base station's continuous movement results in transient visibility and rapidly fluctuating channel states [7].

The mobility of BS, coupled with large communication distances, creates unique problems for NB-IoT operations. Specifically, the elevation angle between the satellite and the User Equipment (UE) is a decisive factor in link reliability. Lower inclinations exacerbate signal attenuation, shadowing, and multipath fading, leading to a significant increase in the block error rate (BLER) and degradation of service quality [8, 9]. This dependency is accurately captured in the 3GPP TR 36.763 specification.

Depending on the UE positioning, additional shadowing can be induced when satellites move over the deployment location [10]. Specifically, when the UE is located in complex propagation conditions, that is, in city centers surrounded by large buildings or in deep forests under the hills, not only do the propagation losses affect the LEO-based narrowband IoT (NB-IoT) communications performance, but also additional losses caused by the so-called shadowing phenomena, which is the partial blockage of the propagation path by large objects in the channel [11]. In 3GPP, these blockage losses are modeled using simple Markov chains with two or three states inherited from ITU-R standards [12]. While these models are appropriate for assessing the average performance of the system, they are not suitable for many practical optimizations, such as choosing the best time instant when the UE needs to send a message to the BS in NTN NB-IoT deployment.

The aim of this study is to evaluate the BLER for the NTN NB-IoT channel with major impairments. To this end, we carefully introduce the 3GPP propagation model with scintillation, shadowing, and elevation-dependent impairments. Our model accounts for user-specific deployments and can be fine-tuned for different deployment conditions, including city centers and deep forests. We then utilized the combined model to assess the BLER experienced by the UE at different elevation angles.

The remainder of this paper is organized as follows. In Section 2 we review the recent progress in the 3GPP standardization of LEO-based NB-IoT systems. The considered system model is introduced in Section 3. The proposed propagation model, which includes the impact of path loss, elevation angle, scintillations, and deployment conditions, is described in Section 4. The BLER estimation algorithm is presented in Section 5. In Section 6 we report our numerical results. Finally, conclusions are drawn in the last section.

2. Background and related work

The evolution of NB-IoT within the NTN framework has been characterized by the systematic adaptation of terrestrial protocols to the distinctive propagation environments of space-borne communications.

The foundational efforts, codified in Releases 13 and 14, focused on establishing the baseline feasibility of satellite-based NB-IoT. These early investigations prioritized the characterization of the non-terrestrial channel, specifically regarding path-loss modeling for the L and S frequency bands. Furthermore, preliminary analyses of timing offsets and Doppler shifts were conducted to determine the constraints for maintaining signal decodability over vast distances associated with various orbital altitudes [13, 14].

Subsequently, Release 15 introduced critical physical layer enhancements to ensure practical deployment stability in the presence of extreme-signal attenuation. This release implements robust synchronization and channel estimation procedures designed to mitigate the high Doppler characteristics typical of non-terrestrial environments. To ensure uplink reliability despite the stringent power constraints of mMTC terminals, the single-carrier frequency division multiple access

(SC-FDMA) waveform was optimized, ensuring that these spaceborne adaptations remained backward-compatible with the existing terrestrial NB-IoT infrastructure [15].

Release 16 expanded the scope of comprehensive system-level integration and mobility management within the broader 5G service architecture. Key advancements include alignment with the 5G core (5GC) and the introduction of refined random-access procedures specifically tailored to track the high-velocity trajectories of LEO satellites. To counteract the volatile and time-varying propagation conditions inherent in low-Earth orbits, enhanced hybrid automatic repeat request (HARQ) schemes and semi-persistent scheduling mechanisms have been integrated to improve link-level resilience [3, 16].

The challenges of intermittent connectivity and sparse constellation coverage were explicitly addressed in Release 17. This release codified the link budget requirements for LEO, medium-earth orbiting (MEO), and geostationary (GEO) constellations, while introducing standardized procedures for coverage recovery. These mechanisms allow the UE to autonomously detect and reconnect after unavoidable "off-coverage" periods. Moreover, advanced beam management and resource allocation strategies have been standardized to mitigate access contention during the short visibility windows characteristic of initial NTN deployments [17].

Under the 5G-Advanced initiative, Release 18 addresses the complexities of highly dynamic network topologies. It introduced refined tracking area and cell identity mechanisms to address the "moving cell" phenomenon, in which a satellite beam footprint shifts rapidly across the terrestrial surface. To accommodate the significant propagation delays associated with higher orbits, the protocol stack was modified with extended Non-Access Stratum (NAS) supervision timers, ensuring stable mobility management across diverse satellite configurations [18].

The ongoing Release 19 represents a shift toward a fully autonomous and intelligent network architecture. This release proposes state-aware reacquisition strategies that enable terminals to maintain operational continuity during prolonged outages without constant reliance on GNSS timing. Furthermore, it integrates AI/ML-assisted beam tracking and adaptive scheduling to minimize control plane overhead. The inclusion of the RedCap device support ensures that low-complexity, cost-efficient terminals can operate effectively within the NTN ecosystem, even under the most stringent link budget and power conditions [19].

Note that the propagation model defined for LEO systems accounts for many physical phenomena, including scintillations and elevation angle, as discussed further in Section 3. However, one critical factor directly related to communication performance, that is, shadowing, is still modeled using simple two- or three-state Markov chain models [12]. These models directly account for additional attenuation in the shadowed state but fail to scale that for a given environment. To this end, in this study, we extend the 3GPP propagation model to the case of deployment-dependent shadowing.

3. System model

In this study, we investigated a communication scenario involving a UE, specifically an NB-IoT device, that establishes a direct link with an LEO satellite for network attachment and the transmission of small data payloads. Similar to [20], the operational context is characterized by intermittent satellite coverage, a prevalent condition during the initial phases of constellation deployment, as illustrated in Figure 1. Consequently, data transmission by the UE is constrained to discrete intervals referred to as contact windows. It is further assumed that the UE has data pending for transmission at the commencement of each contact opportunity. The scope of this analysis is limited to the preamble transmission procedure, which constitutes the initial stage of both the 2-step and 4-step Random Access Channel (RACH) procedures.

During a contact window, the satellite traverses its orbit at an altitude denoted as h_{sat}, with its position relative to the UE parametrized by the elevation angle θ. In the context of NTN for NB-IoT, a minimum elevation angle of $\theta = 10°$ is typically established as a baseline to ensure adequate link budget management, maintain acceptable handover frequencies, and guarantee the signal reliability. While adopting a lower minimum elevation threshold (e.g., $\theta = 5°$) would extend the duration of

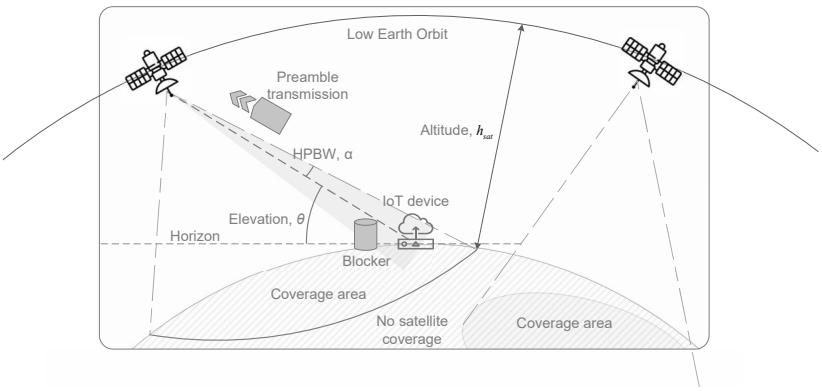


Figure 1. The LEO-based communications system model considered in this paper [20]

the contact window, it would also result in a greater slant range between the UE and satellite. This increased distance leads to heightened path loss and, consequently, a reduced signal power at the receiver. Owing to the $\theta_{\min} = 10°$ minimum elevation requirement combined with the high orbital velocity characteristic of LEO satellites, the effective duration of active contact windows is constrained to approximately 10–15 min per satellite pass for a given UE [21].

The channel gain is a fundamental metric that characterizes the end-to-end signal power attenuation (or occasional amplification) as it propagates from the NB-IoT user equipment (UE) to the LEO satellite. Formally defined as the ratio of the received power to the transmitted power, the channel gain encapsulates all physical phenomena that alter the signal along the path, such as the inverse-square law decay of free-space path loss, large-scale shadowing by buildings or vegetation, and rapid multipath fading caused by reflections and interference.

BLER is the primary reliability metric for preamble transmission in the considered LEO NB-IoT system. The BLER quantifies the probability that a transport block (e.g., preamble message) is incorrectly decoded at the satellite receiver. This study evaluates the BLER as a function of the fine-grained propagation model defined in the following section, the satellite elevation angle, and the number of repetitions N_{rep} used for the transmission. We also report this metric for different UE deployment conditions.

4. Fine-grained propagation model

In this section, we introduce a fine-grained propagation model that captures the fundamental characteristics of the NTN NB-IoT channel. We begin with path loss models, proceed with channel gain characterization, and then account for elevation and shadowing dependent losses.

4.1. Path loss and scintillation models

Satellites and UE are assumed to be equipped with antenna arrays characterized by the receive and transmit gains G_{Tx} and G_{Rx}, respectively, which can be calculated as shown in [22]. Antenna arrays can form a beam with a half-power beamwidth (HPBW) of α degrees.

We model the NTN path loss as

$$PL = 20\log_{10}\left(\frac{4\pi d}{\lambda}\right) - G_{Tx} - G_{Rx} + PL_{Po} + PL_{Sc} + PL_{At},$$

where the free-space term follows the Friis equation [23], d is the satellite-to-device distance (km), λ is the carrier wavelength (m), and the additional loss terms follow ITU-R P.676 [24]:

- PL_{Po}, polarization mismatch loss: 3 dB, typical for cross-polarized IoT terminals;
- PL_{Sc}, ionospheric scintillation loss: 1–3 dB, elevation-dependent, higher at low elevation angles;
- PL_{At}, atmospheric absorption: 0.5–2 dB, frequency- and weather-dependent [24].

The elevation-dependent scintillation is modeled as $PL_{Sc}(\theta) = 3 - 2\sin(\theta)$, for elevation angle $\theta \in [10°, 90°]$, following the recommendations of 3GPP TR 38.811 [25].

A statistical characterization of the channel gain is essential to accurately model the air-to-ground propagation channel for LEO satellite systems. This section presents the generative model for the instantaneous channel gain based on ITU-R P.681 [26], followed by an elevation-dependent parameterization for three representative environments: urban, village, and rural wooded. The analysis focuses on the combined effects of the direct signal and multipath scattering, providing a foundation for Monte Carlo simulations [27] of channel state distributions without temporal correlations.

4.2. Channel gain characterization

The channel gain characterizes the signal power attenuation (or occasionally amplification) as it propagates from the transmitter to the receiver and is expressed as the ratio of the received power to the transmitted power. It encapsulates all physical effects that alter the signal along the path, including the inverse-square law decay of the path loss over distance, large-scale obstruction shadowing from buildings or terrain, and rapid multipath fading caused by signal reflections and interference. Because the wireless environment is dynamic owing to movement, changing obstacles, or atmospheric conditions, the channel gain is inherently time-varying. In our study, the instantaneous channel gain G_{ch} (in dB) represents the combined effects of the direct signal and multipath scattering. Following the generative procedure proposed by [26], we generated independent Monte Carlo samples of the channel state without temporal correlation as follows:

1. Sample direct signal amplitude:

$$A = 10^{(M_A + \Sigma_A \cdot Z_A)/20},$$

   where $Z_A \sim \mathcal{N}(0, 1)$ models the amplitude fluctuations, and the transformation from dB to linear units follows the lower processing path.
2. Compute multipath I/Q standard deviation:

$$\sigma_{mp} = \sqrt{10^{M_P/10}/2},$$

   corresponding to the upper processing path, where the in-phase (I) and quadrature (Q) components represent the two orthogonal dimensions of the complex multipath signal.
3. Sample independent multipath components $n_I, n_Q \sim \mathcal{N}(0, 1)$.
4. Compute received power (Rice+Rayleigh envelope):

$$G_{ch} = 10\log_{10}\left[(A + \sigma_{mp} \cdot n_I)^2 + (\sigma_{mp} \cdot n_Q)^2\right] \text{ (dB)}.$$

Note that for the Monte Carlo simulation, we skip the temporal filtering stages (Doppler spread filter and low-pass correlation filter $H_A(Z)$) as we focus on the evaluation of statistical distributions rather than time-correlated sequences. Figure 2 illustrates the channel gain in urban, village, and rural scenarios as a function of the satellite elevation angle. The horizontal reference line at −3 dB represents a commonly assumed constant shadow fading value in LEO link budget analyses.

4.3. Elevation-dependent parameterization

The ITU-R report [26] provides distribution parameters for five reference elevation angles: $\{20°, 30°, 45°, 60°, 70°\}$ and deployment scenarios at 2.2 GHz. For an arbitrary elevation $\theta \in [20°, 70°]$, we employ a Piecewise Cubic Hermite Interpolating Polynomial (PCHIP) to ensure monotonic interpolation.

We focused on three scenarios for which complete parameter sets were available across all reference angles: urban, village, and rural wooded.

We specifically outline our key observations as follows:

- Urban scenario exhibits severe attenuation at low angles ($\mathbb{E}[G_{ch}] \approx -13$ dB at $\theta = 20°$) due to high buildings creating deep shadowing, improving rapidly with elevation;
- Village shows best performance across all angles due to lower building heights. Rural wooded areas exhibit moderate attenuation with slow improvement, as tree-induced scattering persists even at high angles.

Algorithm 1: Loo Channel Gain Generation (ITU-R P.681-11 Section 6.2)

Input:
- θ – elevation angle (degrees), $\theta \in [20°, 70°]$
- Scenario $\in$ {Urban, Village, Rural wooded}
- ITU-R parameters from Annex 2 (interpolated at θ)

Output: G_{ch} – channel gain (dB)

`// Compute state durations using ITU-R formula (17a)`

Compute $\langle dur \rangle_G, \langle dur \rangle_B$;

`// Compute transition time using ITU-R formulas (17b), (18a), (18b)`

Compute $M_{A,\min,B}$, $M_{A,\max,B}$ using Equations (18a) and (18b);

Compute $\langle dur \rangle_T$ using formula (17b)

`// Compute BAD state probability using ITU-R formula (19b)`

Compute p_B;

`// Sample channel state`

Sample $S \sim \text{Bernoulli}(p_B)$; `// S = 0: ``GOOD'', S = 1: BAD`

`// Generate Loo parameters triplet (ITU-R Table 6)`

if $S = 0$ **then**

  `// ``GOOD'' state`

  Sample $M_A \sim \mathcal{TN}(\mu_{M_{A,G}}, \sigma_{M_{A,G}}, \mu_{M_{A,G}} - 1.645\sigma_{M_{A,G}}, \mu_{M_{A,G}} + 1.645\sigma_{M_{A,G}})$;

  $\Sigma_A = g_{1G} \cdot M_A + g_{2G}$;

  $M_P = h_{1G} \cdot M_A + h_{2G}$ dB;

else

  `// ``BAD'' state`

  Sample $M_A \sim \mathcal{TN}(\mu_{M_{A,B}}, \sigma_{M_{A,B}}, M_{A,\min,B}, M_{A,\max,B})$;

  $\Sigma_A = g_{1B} \cdot M_A + g_{2B}$;

  $M_P = h_{1B} \cdot M_A + h_{2B}$ dB;

`// Generate complex envelope (ITU-R Figure 18, Monte Carlo mode)`

Sample $Z_A \sim \mathcal{N}(0, 1)$;

$A = 10^{(M_A + \Sigma_A \cdot Z_A)/20}$; `// direct signal amplitude`

$\sigma_{mp} = \sqrt{10^{M_P/10}/2}$; `// multipath I/Q std deviation`

Sample independent $n_I, n_Q \sim \mathcal{N}(0, 1)$ Compute $G_{ch} = 10 \log_{10}\left[(A + \sigma_{mp} \cdot n_I)^2 + (\sigma_{mp} \cdot n_Q)^2\right]$ dB

return G_{ch};

4.4. Shadowing model

In this study, we incorporate the stochastic channel model for satellite systems provided in [12]. The model captures both large-scale shadow fading and small-scale multipath effects using a two-state Markov process. The model distinguishes between the “GOOD” and “BAD” channel states, which are

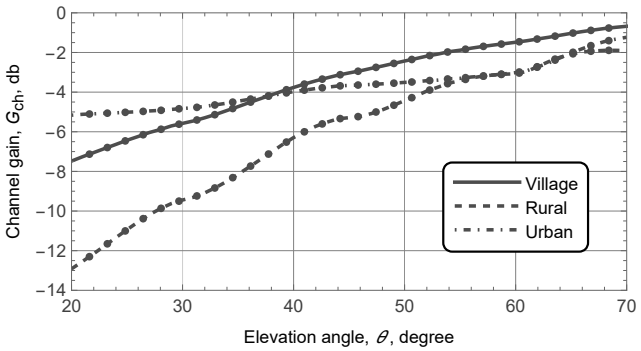


Figure 2. Mean channel gain as function of elevation angle

characterized by distinct statistical distributions of signal attenuation and multipath scattering. The behavior of the model is governed by a set of environment- and geometry-dependent parameters. The primary inputs are the environment type (urban, rural wooded, or village), satellite elevation angle (typically ranging from 10° to 80°), and carrier frequency (between 1.5 and 20GHz). For each combination, ITU-R P.681-11 provides tabulated values of the state transition probabilities p_{GB} and p_{BG}, the mean sojourn times (or the parameters of the log-normal dwell-time distributions) for the good and bad states, and the Loo distribution parameters σ (diffuse power), μ (mean of the log-normal shadowing), and $\sqrt{d_0}$ (standard deviation of the log-normal shadowing) for each state. Additional parameters include the mobile terminal speed (which scales the dwell times by the Doppler effect) and the azimuth angle relative to the satellite, which are neglected in this study.

The steady-state probability of being in the "BAD" state, denoted p_B, is derived from the mean durations of each state and the transition times between them. Following [26], these parameters are characterized as functions of the elevation angle θ and deployment scenario. The mean durations of "GOOD" and "BAD" states are computed from truncated lognormal distributions using (1),

$$\langle dur\rangle_{G,B} = \exp\left(\mu_{G,B} + \frac{\sigma_{G,B}^2}{2}\right)\frac{1-\operatorname{erf}\left(\frac{\log \mathrm{dur}_{\min,B,G}-(\mu_{G,B}+\sigma_{G,B}^2)}{\sqrt{2}}\right)}{1-\operatorname{erf}\left(\frac{\log \mathrm{dur}_{\min,B,G}-\mu_{G,B}}{\sqrt{2}}\right)}, \tag{1}$$

where μ_G, σ_G, $dur_{\min G}$ for the "GOOD" state and μ_B, σ_B, $dur_{\min B}$ for the "BAD" state are scenario-dependent parameters tabulated in [26].

The mean transition time between states is computed using formula (2), which includes a correction term accounting for the statistical bias introduced by truncating the signal attenuation distribution in the "BAD" state.

$$\begin{aligned}\langle dur\rangle_T = f_1 \times (\mu_{M,A,G} - \mu_{M,A,B} - \sigma_{M,A,B}^2 \times \\ \times \frac{p_N(M_{A,\min};\mu_{M,A,B},\sigma_{M,A,B}) - p_N(M_{A,\max};\mu_{M,A,B},\sigma_{M,A,B})}{F_N(M_{A,\min};\mu_{M,A,B}) - F_N(M_{A,\max};\mu_{M,A,B})}) + f_2.\end{aligned} \tag{2}$$

The truncation bounds are defined by (3) and (4), with $p_{B,\min}$ and $p_{B,\max}$ representing the confidence interval range:

$$M_{A,\min,B} = \mu_{M,A,B} + \sqrt{2}\sigma_{M,A,B}\,\overline{\operatorname{erf}}^{-1}(2p_{B,\min}-1), \tag{3}$$

and also

$$M_{A,\max,B} = \mu_{M,A,B} + \sqrt{2}\sigma_{M,A,B}\,\overline{\operatorname{erf}}^{-1}(2p_{B,\max}-1). \tag{4}$$

Finally, the steady-state probabilities p_G and p_B are computed using

$$p_G = \frac{\langle dur\rangle_G + \langle dur\rangle_T}{\langle dur\rangle_G + \langle dur\rangle_B + 2\langle dur\rangle_T},\ p_B = \frac{\langle dur\rangle_B + \langle dur\rangle_T}{\langle dur\rangle_G + \langle dur\rangle_B + 2\langle dur\rangle_T}. \tag{5}$$



Figure 3. Flowchart of the proposed BLER evaluation framework

For each channel state ("GOOD" or "BAD"), the Loo model characterizes three signal components that together define the instantaneous channel realization as follows:

1. Direct signal attenuation (M_A): the direct path experiences attenuation M_A (dB) modeled as a truncated normal distribution. For the "GOOD" state, the truncation range is $[\mu_{M_{A,G}} - 1.645\sigma_{M_{A,G}}, \mu_{M_{A,G}} + 1.645\sigma_{M_{A,G}}]$ as specified in [26]. For the "BAD" state, the truncation bounds are determined by (3) and (4) with the confidence interval $[p_{B,\min}, p_{B,\max}]$ (typically $[0.1, 0.9]$ for Urban at 2.2 GHz).
2. Amplitude fluctuations (Σ_A): the RMS fluctuation of the direct signal amplitude depends linearly on M_A: $\Sigma_A = g_1 \cdot M_A + g_2$, where regression coefficients g_1, g_2 differ between "GOOD" and "BAD" states. This models the variability in shadowing severity within each state.
3. Multipath power (M_P): the multipath scattering power also depends linearly on M_A : $M_P = h_1 \cdot M_A + h_2$, with state-dependent coefficients h_1, h_2. This captures the correlation between direct-path obstruction and multipath richness.

5. BLER estimation

The proposed methodology evaluates the elevation-dependent BLER through a link budget analysis incorporating the Loo channel model and other impairments introduced earlier. Our framework operates through six computational steps executed for each elevation angle $\theta_j \in [20°, 70°]$, as shown in Figure 3.

We began with the parameterization of the considered environment. The physical constants and system parameters were defined in accordance with the NB-IoT specifications for LEO satellite communications. The coding gain for each repetition level is modeled as $G_{\text{code}}(N_{rep}) = 2 \cdot \log_2(N_{rep})$ dB, which is calibrated empirically from link-level simulations [16].

Once the initial parameters are obtained, for each elevation angle θ_j we compute the distance for the communication link employing spherical geometry

$$d_j = \sqrt{(R_E + h_{\text{sat}})^2 - R_E^2 \cos^2 \theta_j} - R_E \sin \theta_j \text{ (km)},$$

and the free-space path loss that follows the Friis equation

$$L_{FSPL}(\theta_j) = 20 \log_{10}(d_j) + 20 \log_{10}(f_c) + 20 \log_{10}(4\pi/c) \text{ (dB)}.$$

We then proceeded to evaluate the channel condition using the Loo channel model. To do this, all ITU-R parameters for the selected scenario are interpolated at every angle value θ_j using PCHIP and the "BAD" state probability $p_B(\theta_j)$ as shown in Algorithm 2. In this phase, the statistical model is prepared for the subsequent Monte Carlo sampling.

After defining the parameter values for the channel model, we began the simulation. We generate N_{MC} independent channel realizations at θ_j using Algorithm 1 and compute the mean channel gain

$$\bar{G}_{ch}(\theta_j) = \frac{1}{N_{MC}} \sum_{i=1}^{N_{MC}} G_{ch,i}.$$

Now we are at evaluation of SNR at θ_j for each repetition number N_{rep} which is given by

$$\text{SNR}(\theta_j, N_{rep}) = P_{TX} - L_{FSPL}(\theta_j) - L_{\text{total}} + G_{RX} - N_0 + \bar{G}_{ch}(\theta_j) + G_{\text{code}}(N_{rep}).$$

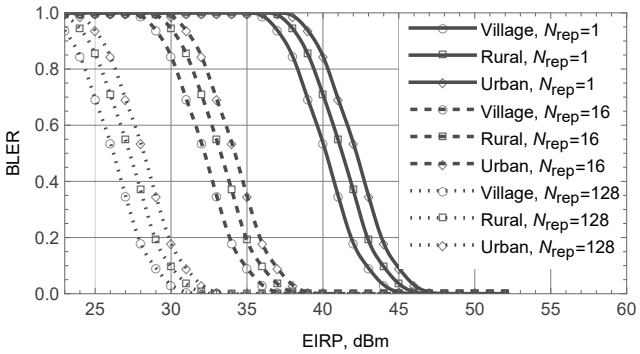


Figure 4. BLER as function of EIRP for 90° elevation angle

The final step involves obtaining the BLER by interpolating link-level simulation data provided in [8]

$$\mathrm{BLER}(\theta_j, N_{rep}) = \mathcal{L}(\mathrm{SNR}(\theta_j, N_{rep})),$$

where $\mathcal{L} : \mathbb{R} \to [0, 1]$ is a PCHIP interpolator constructed from digitized BLER-SNR pairs at $\theta_{\mathrm{ref}} = 50°$ with a transport block size of 408 bits.

Algorithm 2: Loo Channel Model Parameterization

Input:
- θ – elevation angle (degrees), $\theta \in [20°, 70°]$
- Scenario $\in$ {Urban, Village, Rural wooded}

Output: p_B – BAD state probability

`// Interpolate all ITU-R parameters from Annex 2 at` θ

Interpolate μ_G, σ_G, $dur_{\min G}$, μ_B, σ_B, $dur_{\min B}$ via PCHIP;

Interpolate $\mu_{M_{A,G}}$, $\sigma_{M_{A,G}}$, $\mu_{M_{A,B}}$, $\sigma_{M_{A,B}}$ via PCHIP;

Interpolate g_{1G}, g_{2G}, g_{1B}, g_{2B}, h_{1G}, h_{2G}, h_{1B}, h_{2B} using PCHIP Interpolate f_1, f_2 via PCHIP;

`// Compute state durations using ITU-R formula (17a)`

Compute $\langle dur \rangle_G, \langle dur \rangle_B$;

`// Compute transition time using ITU-R formulas (17b), (18a), (18b)`

Compute $M_{A,\min,B}$, $M_{A,\max,B}$ using Equations (18a) and (18b);

Compute $\langle dur \rangle_T$ using formula (17b);

`// Compute BAD state probability using ITU-R formula (19b)`

$p_B = \frac{\langle dur \rangle_B + \langle dur \rangle_T}{\langle dur \rangle_G + \langle dur \rangle_B + 2\langle dur \rangle_T}$;

return p_B;

6. Results

In this section, we present our numerical results. Specifically, we considered the elevation angle, deployment type, and number of repetitions as the main parameters and reported the associated BLER values. The default 3GPP LEO NB-IoT system parameters are listed in Table 1.

We begin in Figure 4 demonstrating the BLER as a function of EIRP for different deployments conditions including rural wooded, urban, and village and different number of repetitions. In this illustration, the elevation angle is set to 90°, that is, the satellite is in the zenith location.

Table 1

Default system parameters

Notation	Description	Value
R_E	Earth radius	6371 km
h_{sat}	Satellite altitude	600 km
f_c	Carrier frequency (NB-IoT uplink, S-band)	2.0 GHz
G_{RX}	Satellite antenna gain	30 dB
L_{total}	System losses	5.3 dB
N_0	Thermal noise floor (15 kHz bandwidth)	-118.4 dBm
P_{TX}	Transmit effective Isotropic Radiated Power	42 dBm
N_{rep}	Number of repetitions	$2^{\{0,\ldots,7\}}$
N_{MC}	Number of samples	10^5

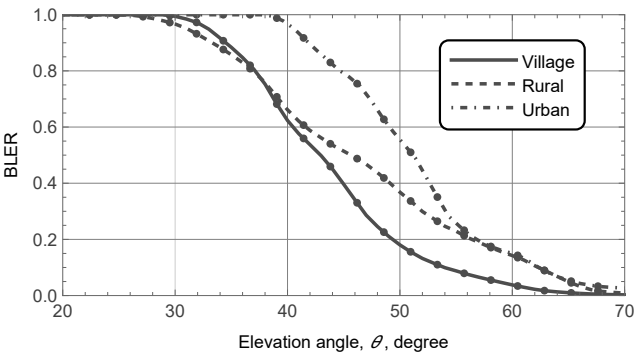


Figure 5. BLER as function of elevation angle for fixed number of repetitions, $N_{\text{rep}} = 1$

By analyzing the results presented in Figure 4 one may observe that the most impact is produced by the number of repetitions utilized at the wireless channel. Specifically, the subsequent increase in the number of repetitions from 1 to 16 and finally to 128 shifts the associated BLER curves by approximately 8–10 dB along the x-axis. However, this improvement is associated with the increased access delay associated with preamble reception and thus successful resolution of the access procedure at the BS side.

The impact of deployment conditions was less pronounced but still noticeable. Specifically, as shown in Figure 4, changing from village to rural wooded and then to urban deployments shifts the BLER curves by around 1–2 dB. In terms of BLER, this may still be noticeable by increasing it by approximately 0.2 with respect to each other. In general, the BLER is very sensitive to both repetitions and deployment conditions and must be considered during the deployment phase.

Yet, another critical parameter for system design is the elevation angle. Its impact on the BLER under different deployment conditions is shown in Figure 5 for the number of repetitions set to 1 and EIRP of 42 dBm. By analyzing the presented results, it can be observed that the elevation angle has a critical

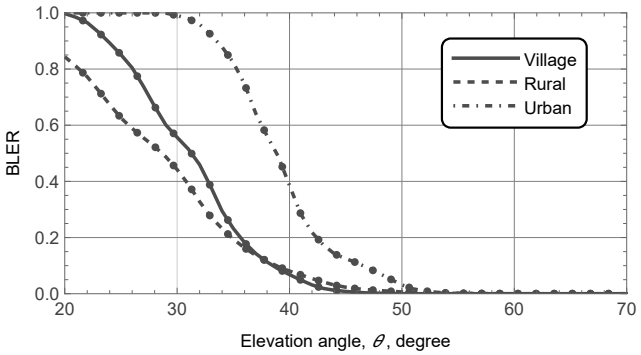


Figure 6. BLER as function of elevation angle for a fixed number of repetitions, $N_{\text{rep}} = 4$

effect on the preamble reception probability. Specifically, for a given number of repetitions, the system may go from a totally unusable regime with a BLER of 1 to perfect conditions with a negligible BLER. This makes the problem of optimal transmission time instant with systems with interrupted LEO coverage important. The impact of deployment conditions is also visible and can amount to 0.4 difference in BLER for a given elevation angle.

Finally, we examine when the number of repetitions may improve the system's performance for the considered elevation angles. To this end, Figure 6 shows the BLER for the number of repetitions set to 4 and EIRP of 42 dBm. By cross-comparing the results presented in this illustration and Figure 5 we see that increasing the number of repetitions from 1 to 4 already have a drastic impact of BLER. Specifically, all the curves move to the left, allowing efficient communication at angles that are totally prohibited with $N_{\text{rep}} = 1$. This is the case, for example, for an elevation angle of 50° the BLER is close to zero for $N_{\text{rep}} = 4$ for all the considered deployment conditions, while it is higher than 0.2 for the best possible village deployment for $N_{\text{rep}} = 1$.

7. Discussion

The primary goal of this study was to evaluate the block error rate (BLER) for LEO-based NB-IoT systems under elevation-dependent channel impairments and deployment-specific shadowing and to determine whether a simple elevation-agnostic propagation model suffices for performance analysis. Our results directly address the questions raised in the Introduction, namely, (i) how severely does the elevation angle affect the BLER across different environments, and (ii) can deployment-dependent shadowing be captured with sufficient accuracy to guide transmission-timing decisions.

The results show that the elevation angle is the dominant factor affecting the BLER. At a fixed number of repetitions ($N_{\text{rep}} = 1$) and an EIRP of 42 dBm, the BLER decreases from approximately 1 at low elevations ($\approx 20°$) to below 0.1 at high elevations ($\approx 70°$) in all three environments (Figure 5). This finding answers the first question: elevation should not be neglected in link budget analysis. Regarding the second question, deployment conditions produced a secondary but measurable effect—urban scenarios exhibited up to 0.4 higher BLER than village environments at the same elevation (Figure 5). Thus, a model that ignores deployment-specific shadowing would systematically overestimate the performance for urban UEs and underestimate it for village deployments. Our fine-grained, parameterized Loo model (Algorithm 1) captures this variability, confirming the hypothesis that environment-dependent parameterization is necessary for an accurate BLER prediction.

The observed strong elevation dependence aligns with 3GPP TR 36.763 and earlier studies [8, 9], which reported that lower elevation angles exacerbate path loss and multipath. However, prior studies using two- or three-state Markov chains [26] treated shadowing as a static or memoryless process without fine-grained elevation-dependent parameter recovery. Our extension, which interpolates ITU-R P.681-11 parameters via PCHIP and derives state probabilities from (5), provides a more accurate

mapping of elevation to channel statistics. The results in Figure 4 also confirms the well-known trade-off between repetitions and reliability: increasing N_{rep} from 1 to 128 shifts the BLER curve by 8–10 dBm, consistent with the coding gain model $G_{\text{code}}(N_{\text{rep}}) = 2\log_2(N_{\text{rep}})$ dB adopted from [8]. No inconsistencies with prior experimental or simulation results were observed.

The elevation dependency can be explained by three coupled mechanisms. First, the slant range $d(\theta)$ increases sharply below 30°, directly increasing the free-space path loss (Friis equation). Second, the scintillation loss $PL_{\text{Sc}}(\theta) = 3 - 2\sin\theta$ amplifies the attenuation at low angles. Third, the "BAD" state probability $p_B(\theta)$ derived from (5) increases as the elevation decreases because the signal path intersects more obstacles. The Loo model's separation of direct signal attenuation M_A (truncated normal) and multipath power M_P (linear regression on M_A) captures the physical reality that heavy shadowing correlates with reduced multipath richness, a feature missing from simpler Markov models.

This study provides a quantitatively validated and deployable model for predicting the BLER in LEO NB-IoT systems across three representative environments. The key practical implication is that fixed-time or random transmission schemes are suboptimal; a UE can reduce its BLER from near 1 to < 0.1 simply by delaying transmission until the satellite reaches a higher elevation angle (e.g., $> 50°$ with $N_{\text{rep}} = 4$). Our model enables such elevation-aware scheduling without requiring real-time channel sounding because the elevation angle is known from ephemeris data.

First, the temporal correlation of the Loo process should be reintroduced to model the burst errors and optimize the HARQ parameters. Second, the model should be extended to lower elevation angles (10°–20°) where the minimum specified in 3GPP TR 38.811 is critical. Third, the interaction between repetitions and elevation can be formulated as an optimization problem: minimize access delay subject to a BLER constraint by jointly selecting N_{rep} and the transmission wait time. Finally, experimental validation using real LEO satellite data will confirm the simulation-based findings presented in this study.

This study aimed to develop a fine-grained model that accounts for satellite NB-IoT channel conditions and estimates the BLER. Our results directly fulfill this aim by providing a complete parameterized algorithm (Algorithms 1–2) and numerical BLER tables for urban, village, and rural wooded scenarios.

8. Conclusion

LEO-based NTN NB-IoT systems provide a convenient way to enable mMTC services in locations that cannot otherwise be covered by terrestrial wireless communication systems. However, the specifics of propagation conditions, including large communication distances modulated by the LEO elevation angle, scintillation, and shadowing caused by different deployment conditions, require careful planning of the link budget to enable efficient random access and data transmission. To this end, in this study, we exhaustively characterized the BLER performance of LEO-based NB-IoT systems.

Our numerical results demonstrated that the elevation angle has the greatest impact on the elevation angle. The effect of the deployment conditions is of second-order importance. Specifically, urban scenarios suffer severe attenuation at low elevation angles (≈ -13 dB at 20°), whereas rural wooded areas exhibit moderate but persistent scattering, and village environments provide the best overall channel conditions. We also showed that the number of repetitions trading off latency for reliability is an efficient way to conceal the deteriorating impact of path loss. However, when latency is critical, one needs to carefully plan the transmission time instants for UEs avoiding low elevation angles.

Author Contributions: Danil V. Shilonosov: methodology, software, investigation; Alina A. Likhtenshtein: validation, formal analysis, writing—original draft preparation; Vitalii A. Beschastnyi: conceptualization, validation, writing—original draft preparation, writing—review and editing, funding acquisition; Yuliya V. Gaidamaka: resources, supervision, project administration, writing—review and editing. All authors have read and agreed to the published version of this manuscript.

Funding: The reported study was funded by RSF, projects no. 25-79-10142, https://rscf.ru/project/25-79-10142/.

Data Availability Statement: Data sharing is not applicable.

Conflicts of Interest: The authors declare no conflict of interest.

Declaration on Generative AI: During the preparation of this work, the authors used Paperpal for grammar and spelling checks. After using this tool, the authors reviewed and edited the content as needed and take full responsibility for the publication's content.

References

[1] ITU-R, *Mobile Network Coverage*, https://www.itu.int/itu-d/reports/statistics/2023/10/10/ff23-mobile-network-coverage/, Accessed: Feb. 2, 2025, 2024.

[2] S. Kavuri, D. Moltchanov, A. Ometov, S. Andreev, and Y. Koucheryavy, "Performance Analysis of Onshore NB-IoT for Container Tracking During Near-the-Shore Vessel Navigation," *IEEE Internet of Things Journal*, vol. 7, no. 4, pp. 2928–2943, 2020.

[3] M. Hosseinian, J. P. Choi, S.-H. Chang, and J. Lee, "Review of 5G NTN Standards Development and Technical Challenges for Satellite Integration with the 5G Network," *IEEE Aerospace and Electronic Systems Magazine*, vol. 36, no. 8, pp. 22–31, 2021.

[4] G. K. Kurt, M. G. Khoshkholgh, S. Alfattani, A. Ibrahim, T. S. Darwish, M. S. Alam, H. Yanikomeroglu, and A. Yongacoglu, "A Vision and Framework for the High Altitude Platform Station (HAPS) Networks of the Future," *IEEE Communications Surveys & Tutorials*, vol. 23, no. 2, pp. 729–779, 2021.

[5] T. D. Le, M. Stusek, R. Dvorak, P. Palurik, P. Masek, D. Moltchanov, and J. Hosek, "Downlink Coverage and Bit Rate Performance of LEO-Based Non-Terrestrial Networks for NB-IoT," in *2025 17th International Congress on Ultra Modern Telecommunications and Control Systems and Workshops (ICUMT)*, IEEE, 2025, pp. 80–86.

[6] H. Alves, K. Mikhaylov, and M. Hoyhtya, *Integration of MTC and Satellites for IoT toward 6G Era*. John Wiley & Sons, 2024.

[7] E. Rastogi, M. K. Maheshwari, A. Rastogi, and J. Jeong, "A Narrowband Internet-of-Things Communications Scheme Over Non-Terrestrial Networks," in *2025 IEEE 11th International Conference on Network Softwarization (NetSoft)*, IEEE, 2025, pp. 240–248.

[8] M. Conti, S. Andrenacci, N. Maturo, S. Chatzinotas, and A. Vanelli-Coralli, "Doppler Impact Analysis for NB-IoT and Satellite Systems Integration," in *ICC 2020 - 2020 IEEE International Conference on Communications (ICC)*, 2020, pp. 1–7. DOI: 10.1109/ICC40277.2020.9149140

[9] R. Barbau, V. Deslandes, G. Jakllari, J. Tronc, J.-F. Chouteau, and A.-L. Beylot, "NB-IoT over GEO Satellite: Performance Analysis," in *2020 10th Advanced Satellite Multimedia Systems Conference and the 16th Signal Processing for Space Communications Workshop (ASMS/SPSC)*, 2020, pp. 1–8. DOI: 10.1109/ASMS/SPSC48805.2020.9268829

[10] R. Dvorak, P. Palurik, T. D. Le, M. Stusek, P. Masek, D. Moltchanov, and J. Hosek, "Verification of Communication Parameters for NTN Communication," in *2025 17th International Congress on Ultra Modern Telecommunications and Control Systems and Workshops (ICUMT)*, IEEE, 2025, pp. 87–93.

[11] A. S. Shurakov, E. V. Mokrov, A. N. Prikhodko, M. I. Ershova, V. O. Begishev, A. A. Khakimov, Y. A. Koucheryavy, and G. N. Gol'tsman, "The recent progress in terahertz channel characterization and system design," *Discrete and Continuous Models and Applied Computational Science*, vol. 32, no. 2, pp. 181–201, 2024.

[12] ITU-R, "Propagation data required for the design systems in the land mobile-satellite service," ITU-R, ITU-R P.681, 2019, P Series; Radiowave propagation.

[13] N. Chuberre and C. Michel, *Satellite Components for the 5G System*, https://www.3gpp.org/news-events/3gpp-news/sat-ntn, Accessed: Mar. 30, 2025, 3GPP, 2018.

[14] 3GPP, "Feasibility Study on New Services and Markets Technology Enablers for Critical Communications; Stage 1," 3GPP, 3GPP TR 22.862 V14.2.0, 2016, Release 14.

[15] M. El Jaafari, N. Chuberre, S. Anjuere, and L. Combelles, "Introduction to the 3GPP-defined NTN Standard: A Comprehensive View on the 3GPP Work on NTN," *International Journal of Satellite Communications and Networking*, vol. 41, no. 3, pp. 220–238, 2023. DOI: 10.1002/sat.1471 eprint: https://onlinelibrary.wiley.com/doi/pdf/10.1002/sat.1471.

[16] P. Palurik, M. Stusek, D. Moltchanov, K. Mikhaylov, P. Masek, R. Dvorak, T. D. Le, R. Mozny, and J. Hosek, "Potential of mMTC Support over Low Earth Orbit Systems: Challenges and Preliminary Assessment," in *ICUMT 2024; 16th International Congress on Ultra Modern Telecommunications and Control Systems and Workshops*, VDE, 2024, pp. 73–79.

[17] G. Masini, P. Reininger, M. El Jaafari, A. Vesely, N. Chuberre, B. Baudry, and J.-M. Houssin, "5G Meets Satellite: Non-terrestrial Network Architecture and 3GPP," *International Journal of Satellite Communications and Networking*, vol. 41, no. 3, pp. 249–261, 2023. DOI: 10.1002/sat.1456 eprint: https://onlinelibrary.wiley.com/doi/pdf/10.1002/sat.1456.

[18] M. M. Saad, M. A. Tariq, M. T. R. Khan, and D. Kim, "Non-Terrestrial Networks: An Overview of 3GPP Release 17 & 18," *IEEE Internet of Things Magazine*, vol. 7, no. 1, pp. 20–26, 2024. DOI: 10.1109/IOTM.001.2300154

[19] X. Lin, "The Bridge Toward 6G: 5G-Advanced Evolution in 3GPP Release 19," *IEEE Communications Standards Magazine*, vol. 9, no. 1, pp. 28–35, 2025. DOI: 10.1109/MCOMSTD.0001.2300063

[20] T. D. Le, M. Stusek, D. Moltchanov, P. Palurik, P. Masek, and J. Hosek, "A Hybrid Analytical Framework for NB-IoT NTN Performance Under Discontinuous LEO Coverage," *IEEE Open Journal of the Communications Society*, 2026.

[21] J. M. Gongora-Torres, C. Vargas-Rosales, A. Aragón-Zavala, and R. Villalpando-Hernandez, "Elevation Angle Characterization for LEO Satellites: First and Second Order Statistics," *Applied Sciences*, vol. 13, no. 7, 2023. DOI: 10.3390/app13074405

[22] D. Moltchanov, E. Sopin, V. Begishev, A. Samuylov, Y. Koucheryavy, and K. Samouylov, "A Tutorial on Mathematical Modeling of 5G/6G Millimeter Wave and Terahertz Cellular Systems," *IEEE Communications Surveys & Tutorials*, vol. 24, no. 2, pp. 1072–1116, 2022. DOI: 10.1109/COMST.2022.3156207

[23] ITU-R, "Calculation of free-space attenuation," International Telecommunication Union, Radiocommunication Sector, Recommendation ITU-R P.525-4, Aug. 2019.

[24] ITU-R, "Attenuation by atmospheric gases and related effects," ITU-R, Tech. Rep. Recommendation ITU-R P.676-13, Aug. 2022.

[25] 3GPP, "Study on New Radio (NR) to support non-terrestrial networks," 3GPP, Technical Report TR 38.811 V15.4.0, Sep. 2020, Release 15.

[26] ITU-R, "Propagation data required for the design systems in the land mobile-satellite service," ITU-R, Tech. Rep. Recommendation ITU-R P.681-11, Aug. 2019.

[27] M. N. Gevorkyan, A. V. Demidova, and D. S. Kulyabov, "Comparative analysis of machine learning methods by the example of the problem of determining muon decay," *Discrete and Continuous Models and Applied Computational Science*, vol. 28, no. 2, pp. 105–119, 2020.

Information about the authors

Shilonosov, Danil V.—Student of the Department of Probability Theory and Cybersecurity, RUDN University (e-mail: shilonosov-dv@rudn.ru, ORCID: 0009-0002-0327-4739)

Likhtenshtein, Alina A.—Student of the Department of Probability Theory and Cybersecurity, RUDN University (e-mail: 1132229533@rudn.ru, ORCID: 0009-0003-4821-2192)

Beschastnyi, Vitalii A.—Candidate of Physical and Mathematical Sciences, assistant professor of the Department of Probability Theory and Cybersecurity, RUDN University (e-mail: beschastnyy-va@rudn.ru, ORCID: 0000-0003-1373-4014, ResearcherID: 3293250, Scopus Author ID: 57192573001)

Gaidamaka, Yuliya V.—Doctor of Physical and Mathematical Sciences, Full Professor of Department of Probability Theory and Cybersecurity, RUDN University; Senior Researcher of Institute of Informatics Problems of Federal Research Center "Computer Science and Control" Russian Academy of Sciences (e-mail: gaydamaka-yuv@rudn.ru, ORCID: 0000-0003-2655-4805, ResearcherID: E-5620-2014, Scopus Author ID: 35106984800)

RUSSIAN METADATA

УДК 519.872, 519.217
PACS 07.05.Tp, 02.60.Pn, 02.70.Bf
DOI: 10.22363/2658-4670-2026-34-3-345-359 EDN: RGASAA

Модель для анализа блочных ошибок в низкоорбитальных системах связи NB-IoT

Д. В. Шилоносов[1], А. А. Лихтенштейн[1], В. А. Бесчастный[1], Ю. В. Гайдамака[1,2]

[1] *Российский университет дружбы народов, ул. Миклухо-Маклая, д. 6, Москва, 117198, Российская Федерация*

[2] *Институт проблем информатики, Федеральный исследовательский центр "Информатика и управление" РАН, ул. Вавилова, д. 44, корп. 2, Москва, 119333, Российская Федерация*

Аннотация. *Актуальность:* Распространение технологии узкополосного интернета вещей (NB-IoT) на низкоорбитальные (LEO) спутниковые системы обеспечило массовые межмашинное взаимодействие (mMTC) в удалённых районах, недоступных для наземных сетей. Однако системы NB-IoT на базе LEO сталкиваются с серьёзными проблемами физического уровня, включая экстремальные потери распространения, быстрое изменение орбитальных параметров и затенение сигнала окружающими объектами, такими как здания, леса и холмы. Существующие модели распространения, основанные на простых марковских цепях, не учитывают изменчивость канала в зависимости от угла места, необходимую для практических задач оптимизации. *Цель*: Данное исследование направлено на разработку точной модели для определения коэффициента блочных ошибок (BLER) в системах связи LEO NB-IoT, учитывающей угол поднятия, затенение и эффекты сцинтилляции, что позволит осуществлять динамическое планирование передачи для повышения надёжности и энергоэффективности. *Методы:* Предложена детерминированная модель распространения, включающая параметризацию канала по модели Loo из рекомендации ITU-R P.681-11 с интерполяцией методом кубических эрмитовых сплайнов (PCHIP) для произвольных углов. Модель объединяет потери в свободном пространстве, сцинтилляционные потери, зависящие от угла места, атмосферное поглощение и двухрежимное марковское затенение с параметрами, зависящими от условий развёртывания (город, деревня, лесистая местность). Оценка BLER выполнялась с помощью моделирования методом Монте-Карло. *Результаты:* Угол поднятия является доминирующим фактором, влияющим на BLER: при фиксированной эквивалентной изотропно-излучаемой мощности (EIRP) 42 дБм и $N_{\text{rep}} = 1$ значение BLER уменьшается с приблизительно 1 при 20° до менее 0.1 при 70°. Условия развёртывания оказывают вторичный, но измеримый эффект: в городских сценариях BLER может быть на 0.4 выше, чем в сельской местности при том же угле. Увеличение числа повторений с 1 до 128 сдвигает кривые BLER на 8–10 дБм, тогда как $N_{\text{rep}} = 4$ обеспечивает надёжную связь (BLER ≈ 0) при 50° во всех рассмотренных условиях. *Заключение:* Предложенная модель BLER, учитывающая угол места и условия развёртывания, показывает, что схемы с фиксированными временными интервалами неоптимальны: абонентские устройства могут достичь почти нулевого BLER, откладывая передачу до моментов с более высокими углами места ($> 50°$) при умеренном числе повторений. Модель представляет собой инструмент планирования передачи на основе эфемеридных данных без необходимости зондирования канала в реальном времени, предлагая практический путь к надёжной и энергоэффективной связи LEO NB-IoT в различных условиях окружающей среды.

Ключевые слова: массовое межмашинное взаимодействие, низкоорбитальные системы связи, затенение, NB-IoT, неназемные сети доступа.

Discrete & Continuous Models
& Applied Computational Science
ISSN 2658-7149 (Online), 2658-4670 (Print)

2026, 34 (3) 360–368
http://journals.rudn.ru/miph

Research article

UDC 519.872:519.217
PACS 07.05.Tp, 02.60.Pn, 02.70.Bf
DOI: 10.22363/2658-4670-2026-34-3-360-368 EDN: RDAZDN

Extrapolation of experimental data on thermonuclear reaction cross sections using the global spline method

Aleksandr A. Belov[2], Oleg I. Topor[1], Leonid V. Borodachev[1], Zhanna O. Dombrovskaya[2]

[1] *M. V. Lomonosov Moscow State University, 1 bld. 2 Leninskie Gory St, Moscow, 119991, Russian Federation*

[2] *RUDN University, 6, Miklukho-Maklaya St, Moscow, 117198, Russian Federation*

(received: October 8, 2025; revised: December 20, 2025; accepted: February 20, 2026)

Abstract. *Background* Modeling processes in thermonuclear targets requires reliable data on the cross sections and rates of thermonuclear reactions. The most reliable source of such data is the regression of experimental measurements. However, existing experiments are conducted for colliding particle energies of 2–3 keV and higher, while target ignition calculations require data at energies starting from 0.1 keV. Therefore, the approximating formula must allow extrapolation to lower energies. The physical basis for such extrapolation is Gamow's formula, according to which the reaction S-factor should tend to a constant. However, the formulas for S-factors given in the literature are applicable within the corresponding experimental intervals. The question of the possibility of their downward extrapolation in energy remains open. *Purpose* In this regard, the aim of this work is to develop a new method for approximating and extrapolating experimental data on thermonuclear reaction cross sections. *Method* The method proposed in this paper is based on constructing a special type of global spline. *Results* Four reactions involving hydrogen and helium isotopes traditionally used in thermonuclear target calculations were processed. The resulting approximations are applicable in the energy range of 0.01 keV to 3.3 MeV. Their accuracy is 0.2–1%. *Conclusions* A comparison of the obtained results with the formulas most commonly used in the literature shows that the accuracy of the proposed method is 2–4 times higher than the world standard.

Key words and phrases: thermonuclear reactions, cross-sections, reactions rates, approximations

For citation: A. A. Belov, O. I. Topor, L. V. Borodachev, Z. O. Dombrovskaya "Extrapolation of experimental data on thermonuclear reaction cross sections using the global spline method," *Discrete and Continuous Models and Applied Computational Science*, vol. 34, no. 3, pp. 360–368, 2026. DOI: 10.22363/2658-4670-2026-34-3-360-368. EDN: RDAZDN.

1. Introduction

Controlled thermonuclear fusion is considered one of the most promising areas of modern energy. A large number of different reactor concepts have been proposed in the literature (see, for example, [1, 2]). Numerical modelling is the main tool used to analyse them. Theoretical calculations of controlled thermonuclear fusion targets predict ignition, but this has not been observed in experiments. Therefore, all components of simulation should be carefully analysed. Ignition conditions are sensitive to the cross-sections of thermonuclear reactions in the temperature range of 0.1–1 keV. The most reliable source of such data is the regression of experimental measurements. However, existing experiments are conducted for colliding particle energies of 2–3 keV and higher [3]. Therefore, the approximating formula must allow extrapolation to lower energies. The physical basis for such extrapolation is Gamow's formula, according to which the S-factor of a reaction should tend toward a constant.

There are dozens of experimental works on measuring cross sections containing thousands of points. A number of articles have carried out statistical processing of such experiments [4–18]. In these articles, a certain a priori dependence of the cross section on energy is selected, and the coefficients of this formula are selected. This method is quite reliable within the limits of experimental energies. The question of whether they can be extrapolated downward in energy remains open. Specialized extrapolation methods for such data have not been developed.

© 2026 A. A. Belov, O. I. Topor, L. V. Borodachev, Z. O. Dombrovskaya

This work is licensed under a Creative Commons "Attribution-NonCommercial 4.0 International" license.

We previously proposed a regularised double-period method [19], which significantly improved the accuracy of the approximation and extrapolation of cross sections and reaction rates. In the present work, an even more reliable method is constructed, based on the use of a special type of global spline. It provides extrapolation of experimental data on cross section by the Gamow's formula [20]. The accuracy achieved is 0.2–1.1%, which is 2 or more times more accurate than the world standard.

2. Method

Global spline Let us consider an array of experimental points: arguments x_i and functions $u_i \pm \delta_i$, $1 \leqslant i \leqslant I$, $I \gg 1$, where δ_i are absolute measurement errors. From the meaning of the problem, it is known that $u(x)$ is a smooth function with not too large higher derivatives, however, experimental errors δ_i can be significant.

Let us construct an approximation on the interval $[x_i, x_I]$. Let us introduce a uniform grid y_n with step h

$$y_n = (x_I - x_i)\frac{n-1}{N}, \quad 1 \leqslant n \leqslant N+1, \quad y_1 = 0, \quad y_{N+1} = x_I.$$

In general, it may be not uniform. We will consider the grid adaptation procedure further. Let us construct an approximation of the form

$$S(x) = a_0 + \sum_{n=1}^{N+1} a_n (x - y_{n-1})_+^3. \tag{1}$$

Here, $a_n, 1 \leqslant n \leqslant N+1$ are the approximation coefficients. The following notation is used

$$(x - y_{n-1})_+^3 = \begin{cases} (x - y_{n-1})^3, & x > y_{n-1}, \\ 0, & x \leqslant y_{n-1}. \end{cases}$$

The first term is the global part of the spline, the terms under the sum are local "additions". Thus, the approximation is continuous along with the second derivative. The coefficients a_n are determined in the standard way using the least squares method. Let us define the relative root mean square deviation per point (RMSD)

$$\Delta = \frac{1}{I - N - 2} \sum_{i=1}^{I} \frac{(S(x_i) - u_i)^2}{\delta_i^2}.$$

Minimising RMSD $\Delta = \min$ leads to a system of algebraic equations for the coefficients a_n

$$\sum_{n=1}^{N} A_{nk} a_n = B_k, A_{nk} = \sum_{i=1}^{I} \frac{1}{\delta_i^2} \varphi_n(x_i)\varphi_k(x_i), B_k = \sum_{i=1}^{I} \frac{1}{\delta_i^2} \varphi_k(x_i) u_i.$$

For brevity, we introduce the following notation for the basis functions

$$\phi_n(x) = \begin{cases} 1, n = 1, \\ (x - y_{n-1})_+^3, \quad 2 \leqslant n \leqslant N+1. \end{cases}$$

Extrapolation Let us note one important circumstance. When extrapolating using traditional methods, the width of the confidence interval increases rapidly as we move away from the end of the experimental range. Thus, for the simplest linear extrapolation, the width of the confidence interval increases proportionally to the square of the "range" of extrapolation (i.e., the length of the segment from the end of the experimental range to the point at which the extrapolant is calculated). The proposed approach does not have this disadvantage. Since the extrapolation is performed by a constant, the width of the confidence interval for the extrapolation is constant and equal to that at the left end of the experimental range. This demonstrates the high reliability of the proposed method.

Calculation of the confidence interval In [19], a procedure for statistically reliable estimation of the accuracy of the obtained curve was developed. It begins with a comparison of the experimental points and the found mean square approximation. In fact, the data from different laboratories are compared and their original accuracy estimates are corrected.

Next, a random "playout" of points is performed. In this case, the mean is determined by the constructed approximation, and the standard deviation is equal to the experimental error. For the new set of "pseudo-experimental" points obtained, a new approximation $\lg S(\lg E)$ is constructed. This procedure is repeated a sufficient number of times. As a result, we obtain a "bundle" of approximating curves. Their standard deviation is a good estimate of the confidence interval of the initial approximation. This procedure was called the virtual experiment method.

If many experimental points are used, the width of the confidence interval turns out to be much smaller than one would expect from experiments conducted by a single laboratory. For well-studied reactions, the errors of the best of known methods are 2%.

Grid adaptation The coordinates of the spline grid nodes are internal parameters of the method. Therefore, they can be adjusted to improve the results.

1) By choosing the position of the leftmost node y_0, we can increase the accuracy of the extrapolation to the left. Let us perform a series of calculations with different positions of the node y_0. For each calculation, we will find the width of the confidence interval and choose the position y_0 at which the specified width is minimal.
2) For a number of reactions, the S-factor turned out to be a rapidly oscillating function. In these cases, a finer spline grid step was selected in the corresponding segments of the experimental range.

3. Reaction rates

Let there be a local thermodynamic equilibrium in the substance with a temperature T. Then the rate of the thermonuclear reaction is determined by the convolution $\sigma(E)\sqrt{(2E/M)}$ with the Maxwellian distribution

$$K(T) = \frac{\pi}{\sqrt{M}}\left(\frac{2}{\pi T}\right)\int_0^\infty \sigma(E)E\exp\left(-\frac{E}{T}\right)dE.$$

The integral was calculated numerically by high-precision quadrature with the substitution of the approximation $\sigma(E)$.

The confidence interval of the dependence $K(T)$ is also determined by the virtual experiment method. For the most studied reactions, accuracy of best of known methods is 1–4% at low temperatures and decreases significantly at high temperatures.

Reaction rate tables are inconvenient to use in gas-dynamic codes. It is desirable to replace them with approximate formulas with a small number of parameters. We constructed such formulas using the double period method [19]. The approximation in physical units is as follows

$$\lg K(T) = \sum_{k=0}^{6}(\xi_k\cos kt + \eta_k\sin kt),\ \text{where } t = \pi/5.3(\lg T - 0.65),\quad -2 \leqslant \lg T \leqslant 3.3. \tag{2}$$

Here, the temperature is taken in keV units.

4. Results

S-factors Traditionally, four key reactions are considered in calculations of controlled thermonuclear fusion

$$\mathrm{D} + \mathrm{D} \to p + \mathrm{T}, \tag{3}$$

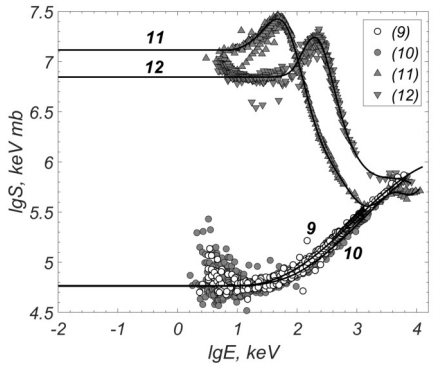


Figure 1. Approximations of the dependence of the S-factor on energy (in c.m.e.) and experimental data [3] for reactions: ∘ — (3), • — (4), ▲ — (5), ▼ — (6)

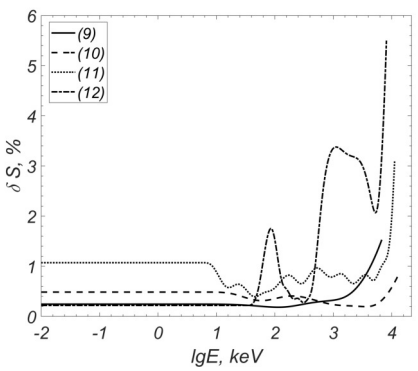


Figure 2. Dependence of S-factor errors on energy (in c.m.s.) for reactions (3)–(6)

$$\mathrm{D} + \mathrm{D} \to n + {}^{3}_{2}\mathrm{He}, \tag{4}$$

$$\mathrm{D} + \mathrm{T} \to n + {}^{4}_{2}\mathrm{He}, \tag{5}$$

$$\mathrm{D} + {}^{3}_{2}\mathrm{He} \to p + {}^{4}_{2}\mathrm{He}. \tag{6}$$

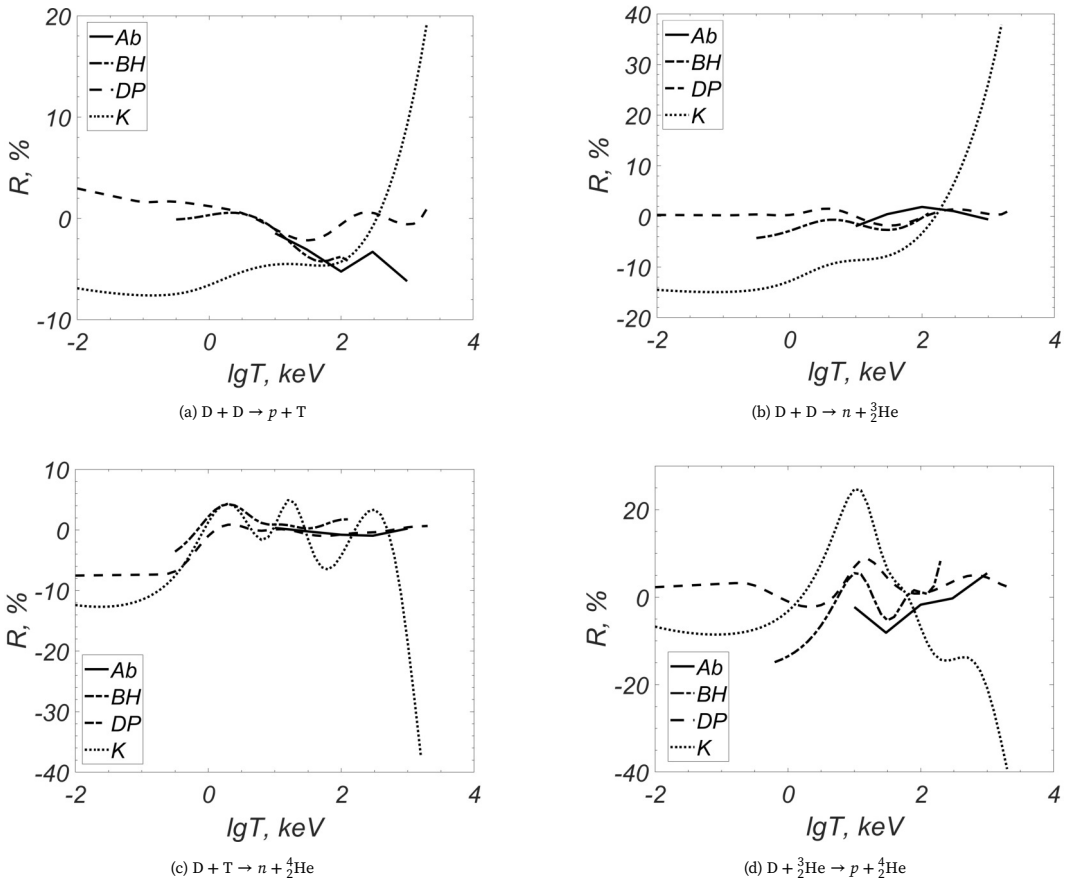
There is a large amount of experimental data available for these reactions (∼ 2000 points for all 4 reactions), collected in the EXFOR library [3]. A number of approximations have been proposed in the literature over the years. In the work [19], approximations were constructed using the regularised double period method. Their accuracy is 0.8. In Russian literature, Kozlov's formulas [18] are widely used, as well as the approximations given in the monograph [21]. Among foreign publications, the work of Bosch and Hale [12] is considered the most authoritative.

Let us process the data on reactions (3)–(6) using the proposed method. The graphs of the constructed approximations for S-factors are shown in Figure 1. The coefficients and nodes of the approximations are given in Table 1. The nature of the dependencies of reactions (3) and (4) is quite simple, so a minimum number of approximation nodes (and coefficients) was used to describe these dependencies (Tab. 1). Reactions (5) and (6) are more complex in nature, with clear resonances in the 45 and 200 keV regions, respectively. An non-uniform grid was used to accurately convey the characteristics of the curves. The number of nodes (and coefficients) reaches 9. Thus, the proposed method allows us to limit ourselves to a small number of approximation parameters. This is convenient for practical application.

Confidence intervals were calculated using the virtual experiment method. They are shown in Figure 2. It can be seen that at the left end of the experimental range, the approximation error is 0.2–1.1% at the left end. This accuracy exceeds the world level by 4 times. The accuracy of extrapolation down the energy scale is also 0.2–1.1%.

Reaction rates The approximation of reaction rates is shown in Figure 3. The approximation coefficients of the tabulated function $K(T)$ are presented in Table 2.

The use of the global spline method made it possible to increase the accuracy of the approximation to values of 0.2–1.1% in the low temperature range. This exceeds previous results several times over.



(a) D + D → p + T

(b) D + D → $n + {}^3_2\mathrm{He}$

(c) D + T → $n + {}^4_2\mathrm{He}$

(d) D + ${}^3_2\mathrm{He}$ → $p + {}^4_2\mathrm{He}$

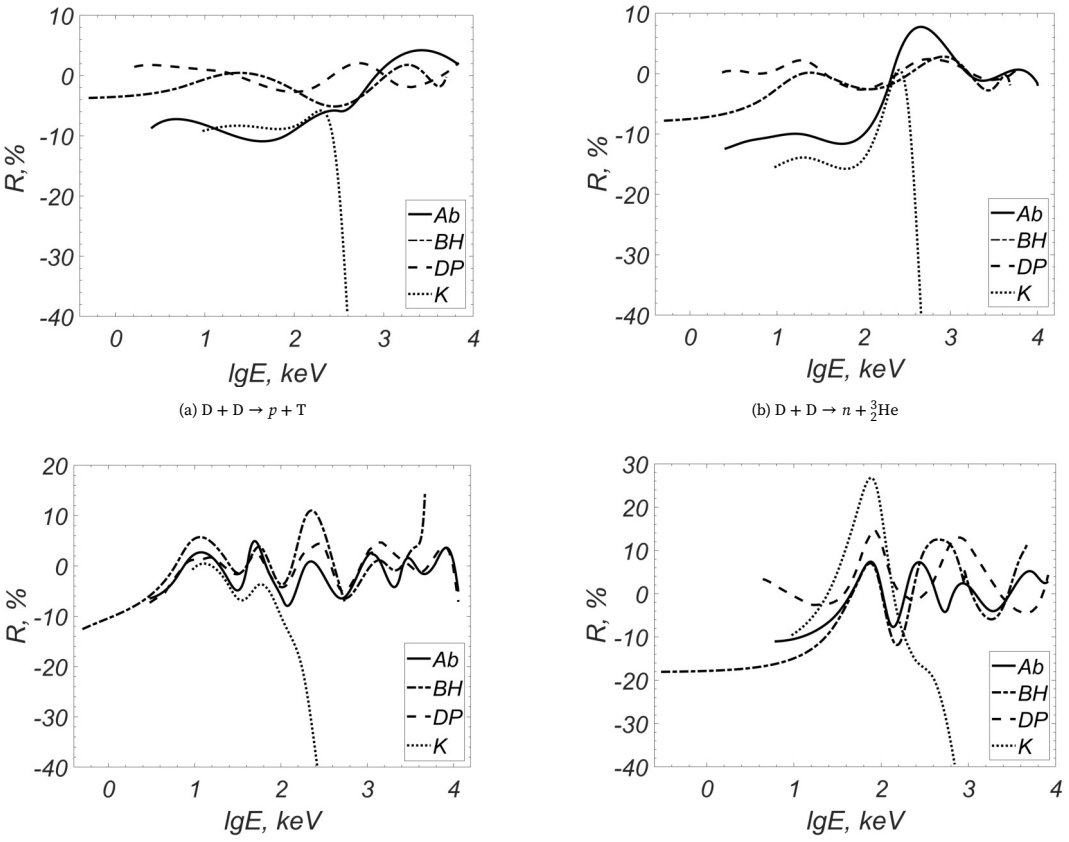
Figure 3. Comparison with other reaction rate approximation formulas: DP — double period method [19], K — Kozlov's formula [18], BH — Bosch-Hale's formula [12] , Ab — Abramovich et al. formula [21]

5. Discussion

Let us compare the obtained results with known approximations for reaction cross-sections and rates. The extremely high accuracy of our approximations allows us to evaluate the accuracy of previously known results, i.e. Kozlov's formulas [18], Bosch–Hale approximations [12], Abramovich et al. approximations [21] and the regularised double-period method [19].

S-factors Figure 4 shows the relative deviation of these approximations from the proposed approximation. Each curve is given in the energy range specified in the original work. We can see that in the low energy range ($E < 100$ keV), the error of Kozlov's formula reaches 20%. The Bosch–Hale and Abramovich et al. formulas have an accuracy of $\sim$ 10–15%. The regularised double-period method provides an accuracy of 1.5–3.5%.

Reactivities Figure 3 shows the relative deviation of known formulas for reaction rates from the curves presented in this work. Kozlov's formulas [18] have an error of $\sim$ 7–15% at temperatures $T \sim 10$ eV. The Bosch–Hale's formulas [12] provide an accuracy of no worse than 5% across the entire temperature range for reactions (3)–(5). For reaction (6), the accuracy is slightly worse and amounts



(a) D + D → p + T

(b) D + D → $n + {}^3_2$He

(c) D + T → $n + {}^4_2$He

(d) D + $^3_2$He → $p + {}^4_2$He

Figure 4. Comparison with other S-factor approximation formulas: DP — double period method [19], K — Kozlov's formula [18], BH — Bosch–Hale's formula [12], Ab — Abramovich et al. formula [21].

to ∼ 10%. The results presented in the monograph by Abramovich et al. [21] have an accuracy of no worse than 10%, but the data on the rates are presented for each reaction only for 4 points lying in the region of fairly high temperatures. The regularised double period method gives an accuracy of 1–3%.

6. Conclusion

A new method for extrapolating the energy dependence of thermonuclear reaction cross sections is proposed, based on the global spline method. The extrapolation is physically justified by the Gamow model, according to which the reaction S-factor tends to a constant at low energies.

The achieved accuracy of 0.2–1.1% for the cross-section and rate dependencies of thermonuclear reactions at low temperatures and energies can significantly improve the accuracy of thermonuclear target calculations in practice. Comparison with known sources indicates that the global spline method exceeds the world standard in accuracy by a factor of 3–4 or more.

Author Contributions: Development and original draft preparation, A. Belov; writing–original draft preparation, O. Topor; manuscript review and editing, Z. Dombrovskaya, L. Borodachev; writing–review and numerical experiments, O. Topor. All authors have read and agreed to the published version of the manuscript.

Funding: This research received no external funding.

Table 1

Values of nodes and approximation coefficients of the S-factor for reactions (3)–(6) used in Eq. (1)

	$D + D \to p + T$		$D + D \to n + {}^3_2He$		$D + T \to n + {}^4_2He$		$D + {}^3_2He \to p + {}^4_2He$	
	y_n	a_n	y_n	a_n	y_n	a_n	y_n	a_n
1	0.7085	4.7622	0.8679	4.7665	0.7761	7.1165	1.4417	6.8466
2	2.0262	0.0608	1.3027	0.1642	0.9243	1.3221	1.7351	0.4836
3	3.8428	-0.1314	2.2375	-0.1821	1.3726	-1.2944	1.9527	3.3702
4					1.8208	-3.7872	2.1704	-12.5360
5					2.2690	8.8008	2.3881	2.9941
6					2.7162	-6.7776	2.6058	16.4896
7					3.1635	3.2060	2.8235	-8.3064
8					3.6107	-4.1709	3.9159	-3.4866
9					4.0579	6.3330		

Table 2

Values of reaction rate approximation coefficients for reactions (3)–(6) used in Eq. (2)

	$D + D \to p + T$	$D + D \to n + {}^3_2He$	$D + T \to n + {}^4_2He$	$D + {}^3_2He \to p + {}^4_2He$
ξ_0	-44.6779	-42.9257	-46.5783	-40.6976
ξ_1	35.0087	31.8969	40.6813	17.2096
η_1	24.3312	24.4850	23.3644	43.9668
ξ_2	-12.7575	-10.5047	-15.4974	10.0461
η_2	-17.0121	-17.1958	-15.3945	-32.5929
ξ_3	4.1990	2.9014	5.9911	-11.3493
η_3	7.6000	7.7764	6.0411	16.6916
ξ_4	-1.2006	-0.6518	-2.1194	6.0740
η_4	-2.5648	-2.6752	-1.2985	-6.6748
ξ_5	0.2616	0.1025	0.5944	-2.1239
η_5	0.5982	0.6421	0.0603	1.9900
ξ_6	-0.0318	-0.0096	-0.1203	0.3707
η_6	-0.0736	-0.0831	0.0822	-0.3894
$\Delta, \%$	0.5193	0.3391	0.0249	0.1233

Data Availability Statement: The source data used in this study are openly available in the EXFOR database of the International Atomic Energy Agency and original scientific works . All numerical results obtained during processing are presented in the tables and graphs of the article; additional derived data can be provided by the authors upon reasonable request.

Acknowledgments: The authors wish to thank the editor and the anonymous referees for their valuable suggestions and comments on the first version of this paper.

Conflicts of Interest: The authors declare no conflict of interest.

Declaration on Generative AI: The author has not employed any generative AI tools.

References

[1] V. Rozanov, "Interaction of laser radiation with a porous medium and formation of a nonequilibrium plasma," *Quantum Electronics*, vol. 27, p. 696, 1997.

[2] V. Rozanov, "Feasibility of spherical fusion target compression under two-beam laser irradiation," *Physics-Uspekhi*, vol. 47, p. 359, 2004.

[3] N. D. Bank, *Nuclear Data Services*, 2023.

[4] R. Brown and N. Jarmie, "Differential cross sections at low energies for ^{2}H(d,p)^{3}H and ^{2}H(d,n)^{3}He," *Physical Review C*, vol. 41, p. 1391, 1990.

[5] L. Hively, "Convenient computational forms for Maxwellian reactivities," *Nuclear Fusion*, vol. 17, p. 873, 1977.

[6] L. Hively, "A Simple Computational Form for Maxwellian Reactivities," *Nuclear Technology-Fusion*, vol. 3, no. 2, pp. 199–200, 1983.

[7] B. Brunelli, "An empirical formula for the (D,T) reaction rate parameter $\langle\sigma v\rangle$," *Nuovo Cimento*, vol. 55, pp. 264–268, 1980.

[8] B. Duane, *Annual Report on CTR Technology (Wolkenhauer W. C., ed.)* Battelle Pacific Northwest Laboratory (Richland, WA), 1972, vol. Rep. BNWL-1685.

[9] G. Dolgoleva and E. Zabrodina, "Comparison of two models of calculation of thermonuclear kinetics," *KIAM Preprint*, vol. 68, pp. 1–14, 2016.

[10] T. Koohrokhi, A. Izadpanah, and S. Hosseini, "Fusion Cross Section of T(d,n)^{4}He and ^{3}He(d,p)^{4}He Reactions by Four Parameters Formula," *Journal of Fusion Energy*, vol. 35, pp. 816–822, 2016.

[11] A. Krauss et al., "Low-energy fusion cross sections of D + D and D + ^{3}He reactions," *Nuclear Physics A*, vol. 465, pp. 150–172, 1987.

[12] H. Bosch and G. Hale, "Improved formulas for fusion cross-sections and thermal reactivities," *Nuclear Fusion*, vol. 32, p. 611, 1992.

[13] A. Peres, "Fusion cross sections and thermonuclear reaction rates," *Journal of Nuclear Materials*, vol. 50, p. 5569, 1979.

[14] G. Sadler and P. Van Belle, "An improved formulation of the D(t,n)^{4}He reaction cross-section," Jet Joint Undertaking, Abingdon, Oxfordshire, Technical Report JET-IR(87)08, 1987.

[15] A. Christopherson et al., "A comprehensive alpha-heating model for inertial confinement fusion," *Physics of Plasmas*, vol. 25, p. 012 703, 2018.

[16] W. Biel et al., "Systems code studies on the optimization of design parameters for a pulsed DEMO tokamak reactor," *Fusion Engineering and Design*, vol. 123, p. 206, 2017.

[17] M. Nocente et al., "Cross section of the d + ^{3}He → a + p reaction of relevance for fusion plasma applications," *Nuclear Fusion*, vol. 50, p. 055 001, 2010.

[18] B. Kozlov, "Rates of thermonuclear reactions," *Soviet Journal of Atomic Energy*, vol. 12, p. 247, 1962.

[19] A. Belov, N. Kalitkin, and I. Kozlitin, "Refinement of thermonuclear reaction rates," *Fusion Engineering and Design*, vol. 141, pp. 51–58, 2019.

[20] A. Gamow, "Essay on the development of the theory of atomic nucleus structure. The theory of radioactive decay," *Physics-Uspekhi*, vol. 10, p. 531, 1930.

[21] S. Abramovich, B. Guszhovskij, V. Zherebtsov, and A. Zvenigorodskij, *Nuclear Physics Constants for Thermonuclear Fusion. A Reference Handbook* (IAEA Report INDC(USSR)). Vienna: IAEA, 1991.

Information about the authors

Belov, Aleksandr A.—Doctor of Physical and Mathematical Sciences, Associate professor of Department of Computational Mathematics and Artificial Intelligence of Peoples' Friendship University of Russia (RUDN University) (e-mail: aa.belov@physics.msu.ru, ORCID: 0000-0002-0918-9263)

Topor, Oleg I.—Postgraduate student of Faculty of Physics, M. V. Lomonosov Moscow State University (e-mail: topor.oi15@physics.msu.ru, ORCID: 0009-0006-9210-4326)

Borodachev, Leonid V.—Doctor of Physical and Mathematical Sciences, Associate professor of Faculty of Physics, M. V. Lomonosov Moscow State University (e-mail: borodach2000@mail.ru, ORCID: 0009-0001-0886-8037)

Domrovskaya, Zhanna O.—Candidate of Physical and Mathematical Sciences, Assistant professor of Department of Computational Mathematics and Artificial Intelligence of Peoples' Friendship University of Russia (RUDN University) (e-mail: dombrovskaya@physics.msu.ru, ORCID: 0000-0003-0609-1065)

RUSSIAN METADATA

УДК 519.872:519.217
PACS 07.05.Tp, 02.60.Pn, 02.70.Bf
DOI: 10.22363/2658-4670-2026-34-3-360-368 EDN: RDAZDN

Экстраполяция экспериментальных данных по сечениям термоядерных реакций методом глобального сплайна

А. А. Белов[1], О. И. Топор[2], Л. В. Бородачев[2], Ж. О. Домбровская[1]

[1] *Российский университет дружбы народов, ул. Миклухо-Маклая, д. 6, Москва, 117198, Российская Федерация*

[2] *Московский государственный университет им. М. В. Ломоносова, Ленинские горы, д. 1, стр. 2, Москва, 119991, Российская Федерация*

Аннотация. *Предпосылки* Для моделирования процессов в термоядерных мишенях требуются достоверные данные по сечениям и скоростям термоядерных реакций. Наиболее надёжным источником таких данных является регрессия экспериментальных измерений. Однако существующие эксперименты проводятся для энергий сталкивающихся частиц 2–3 кэВ и более, в то время как для расчётов зажигания мишеней требуются данные при энергиях от 0,1 кэВ. Поэтому аппроксимирующая формула должна допускать экстраполяцию в сторону меньших энергий. Физическим основанием такой экстраполяции является формула Гамова, согласно которой S-фактор реакции должен стремиться к константе. Однако приведённые в литературе формулы для S-факторов применимы в пределах соответствующих экспериментальных отрезков. Вопрос о возможности их экстраполяции вниз по энергии остается открытым. *Цель* В связи этим, целью данной работы является разработка нового метода аппроксимации и экстраполяции экспериментальных данных по сечениям термоядерных реакций. *Метод* Предложенный в данной работе метод основан на построении глобального сплайна специального вида. *Результаты* Проведена обработка четырёх реакции с участием изотопов водорода и гелия, традиционно используемых в расчетах термоядерных мишеней. Построенные аппроксимации применимы в диапазоне 0,01 кэВ – 3,3 МэВ. Их точность составляет 0,2–1%. *Выводы* Сравнение полученных результатов с наиболее употребительными в литературе формулами показывает, что точность предложенного метода в 2–4 раза превосходит мировой уровень.

Ключевые слова: термоядерные реакции, сечения, скорости реакций, аппроксимации

Discrete & Continuous Models & Applied Computational Science
ISSN 2658-7149 (Online), 2658-4670 (Print)

2026, 34 (3) 369–378
http://journals.rudn.ru/miph

Research article

UDC 519.872, 519.217
PACS 07.05.Tp, 02.60.Pn, 02.70.Bf
DOI: 10.22363/2658-4670-2026-34-3-369-378 EDN: RRILKX

The inverse thermography problem as the inverse potential problem for bodies of constant thickness

Evgeniy B. Laneev, Aigul M. Gaipova

RUDN University, 6 Miklukho-Maklaya St, Moscow, 117198, Russian Federation

(received: June 17, 2026; revised: June 30, 2026; accepted: July 10, 2026)

Abstract. *Background* This paper examines a method for correcting thermographic images used in medical diagnostics. Mathematical processing of thermograms is performed within the framework of a mathematical model of a homogeneous, heat-conducting, semi-infinite cylinder of rectangular cross-section bounded by a general surface and containing time-independent heat sources. We assume that the density function of the source distribution corresponds to a body of constant thickness. Homogeneous conditions of the first kind are specified on the lateral faces of the cylinder, corresponding to zero temperature. Convective heat exchange with the external environment at zero temperature occurs on the surface bounding the cylindrical region. Taking blood flow into account leads to the stationary temperature distribution satisfying the inhomogeneous metaharmonic equation. *Purpose* Within the framework of the chosen model, the inverse problem of reconstructing the unknown density of heat sources from a given temperature distribution function on the surface bounding the cylinder (thermogram) is posed. This inverse problem is formulated as an ill-posed mixed problem for the metaharmonic equation with Cauchy data on the surface bounding the cylindrical region. The desired function is the right-hand side of the metaharmonic equation. *Methods* In this paper, the inverse problem using Green's formulas is reduced to an integral equation of the first kind, corresponding to the inverse potential problem for bodies of constant thickness. An approximate solution to the problem, robust to errors in the thermogram and, consequently, in the Cauchy data, is obtained using Tikhonov's regularization method. *Results* The approximate solution is constructed as a double Fourier series with a regularization factor. Convergence of the approximate solution to the problem is proven when the regularization parameter is matched to the error in the Cauchy data. *Conclusions* The approximate solution to the problem can be viewed as a corrected thermogram. Explicit formulas obtained for the approximate solution can be used to construct efficient computational algorithms.

Key words and phrases: thermogram, ill-posed problem, inverse problem, inverse potential problem, Cauchy problem for the metaharmonic equation, first-kind integral equation, Tikhonov regularization method

For citation: E. B. Laneev, A. M. Gaipova "The inverse thermography problem as the inverse potential problem for bodies of constant thickness," *Discrete and Continuous Models and Applied Computational Science*, vol. 34, no. 3, pp. 369–378, 2026. DOI: 10.22363/2658-4670-2026-34-3-369-378. EDN: RRILKX.

1. Introduction

Digital technologies have penetrated into all branches of human activity, and one of the actual problems is to improve the quality and informativeness of the presentation of research results, in particular the quality of images obtained based on measurement data, by their mathematical (digital) processing. This applies, for example, to images obtained using thermal imaging methods with the help of a thermal imager, which records thermal electromagnetic radiation from the surface of the object under study in the infrared range. In particular, in medicine, thermal imaging has become an effective tool for early diagnosis [1–4]. The image on the thermogram, which is a map of the temperature distribution on the surface of the patient's body, makes it possible to assess functional anomalies in the state of their internal organs. At the same time, the image on the thermogram is sometimes somewhat distorted due to thermal conductivity and heat exchange processes. In the works [5, 6], a method

© 2026 E. B. Laneev, A. M. Gaipova

This work is licensed under a Creative Commons "Attribution-NonCommercial 4.0 International" license.

for correcting the image on a thermogram based on harmonic continuation (similar to problems in geophysics [7]) is proposed. In this paper, within the framework of the chosen mathematical model, the image of the density distribution function of the temperature field sources is considered as the corrected thermogram. It is proposed to obtain this function as the result of solving the corresponding inverse problem of the metaharmonic potential. The inverse potential problem is constructed based on the inverse problem for a certain mixed boundary value problem for the metaharmonic equation. The metaharmonic equation allows one to take into account heat transfer due to blood flow [8, 9]. The inverse problem under consideration is ill-posed, since small errors in the initial data (the initial thermogram) may correspond to significant errors in the solution of the inverse problem. To construct a stable approximate solution, the Tikhonov regularization method is used [10].

2. Problem statement

Let's consider a physical and then a mathematical model, within which we will set up an inverse problem.

The physical model is a homogeneous heat-conducting body in the form of a cylinder of rectangular cross-section, bounded by the surface S and containing heat sources with a density function that does not depend on time, creating a stationary temperature distribution in the body. We associate the density function of heat sources with the object under study. We assume that the lateral faces of the cylinder are maintained at zero temperature, and that there is convective heat exchange with a zero-temperature medium on the surface S, described by Newton's law, according to which the heat flux density at a point on the surface is directly proportional to the temperature difference between the inside and the outside of the body. A metaharmonic equation is used to account for blood flow.

Let us move on to the mathematical model. In an infinite cylinder with a rectangular cross-section

$$D^{\infty} = \{(x,y,z) : 0 < x < l_x,\ 0 < y < l_y,\ -\infty < z < \infty\} \subset \mathbb{R}^3$$

consider a cylindrical region

$$D(F,\infty) = \{(x,y,z) : 0 < x < l_x,\ 0 < y < l_y,\ F(x,y) < z < \infty\},$$

bounded by a surface

$$S = \{(x,y,z) : 0 < x < l_x,\ 0 < y < l_y,\ z = F(x,y) < H\}. \tag{1}$$

Let Γ be the set of side faces of the domain $D(F,\infty)$. In the domain $D(F,\infty)$, consider the following mixed boundary value problem for the metaharmonic equation

$$\begin{aligned} &\Delta u(M) = \rho(M), && M \in D(F,\infty),\\ &\frac{\partial u}{\partial n}\Big|_S = h(U_0 - u)\Big|_S,\\ &u|_{\Gamma} = 0,\\ &u \text{ is bounded when } z \to \infty. \end{aligned} \tag{2}$$

Problem (2) corresponds to a steady-state temperature distribution created by heat sources with a distribution function ρ, on the surface S there is a third boundary condition corresponding to convective heat exchange with a medium at temperature $U_0 = 0$ with a coefficient h, and the boundary Γ has a zero temperature.

We assume that the function ρ is such that the solution of problem (2) exists in

$$C^2(D(F,\infty)) \bigcap C^1(\overline{D(F,\infty)}).$$

In particular, the solution of problem (2) allows us to find the temperature distribution $u|_S$ on the surface S, which we call a thermogram.

Now let's set the inverse problem.

Inverse problem Let the function ρ be unknown in the model (2), but let the function

$$f = u|_S, \tag{3}$$

be given. We need to find the ρ function.

We note that the density recovery is associated with the same difficulties as the solution of the inverse potential problem [11], for which significant restrictions on the classes of uniqueness are known. Here we will consider density functions for bodies of constant thickness

$$\rho(x,y,z) = \tau(x,y)\theta(z-H)\theta(H+s-z), \tag{4}$$

belonging to the Sretensky uniqueness class [12]. In this case, we assume that the depth H and the thickness s are known, and the function $\tau(x,y)$ is the unknown quantity in the inverse problem.

In the model (2), the inverse problem is reduced to the following problem for the functions u and ρ:

$$\begin{aligned} &\Delta u(M) - k^2 u(M) = \rho(M), \quad M \in D(F,\infty), \\ &u|_S = f, \\ &\frac{\partial u}{\partial n}\Big|_S = -hf\Big|_S, \\ &u|_\Gamma = 0. \end{aligned} \tag{5}$$

We assume that the function f in (3), (5) is taken from the set of solutions of the problem (2) for the densities (4), so the solution of the inverse problem with respect to the function τ exists in L_2.

We note that in the problem (5), the Cauchy conditions are specified on the surface S of the form (1), i.e., the boundary values f of the unknown function u and the values of its normal derivative are given, therefore problem (5) has a unique solution [13] with respect to u. As will be shown below, the problem with respect to τ is reduced to an inverse potential problem for the densities (4) belonging to Sretensky's uniqueness class. Problem (5), as a Cauchy problem for an elliptic equation, is not stable with respect to errors in the function f, i.e., it is ill-posed. Methods for regularizing Cauchy problems for elliptic equations are relevant even for simple domains [14, 15].

We will consider the function $\tau(x,y)$ as an adjusted thermogram.

Let's construct an explicit representation of the exact solution to problem (5).

3. Exact solution to the inverse problem

We construct the exact solution of the problem (5) following the scheme of [16–18]. Let us consider the source function $\varphi(M,P)$ of the following Dirichlet problem for the metaharmonic equation in the cylinder D^∞:

$$\begin{aligned} &\Delta_P \varphi(M,P) - k^2 \varphi(M,P) = -\delta_{MP}, \quad M,P \in D^\infty, \\ &\varphi|_{x_P=0,l_x} = 0, \quad \varphi|_{y_P=0,l_y} = 0, \\ &\varphi \to 0 \qquad \text{when} \quad |z_P| \to \infty. \end{aligned}$$

The φ function has the form

$$\varphi(M,P) = \frac{\exp(-kr_{MP})}{4\pi r_{MP}} + W(M,P),$$

where r_{MP} is the distance between points M and P, and $W(M,P)$ is the metaharmonic function of P.

The source function can be obtained by the reflection method as a sum of point source functions with a period of $2l_x$ on x and $2l_y$ on y.

$$\varphi(M,P) = \frac{1}{4\pi} \sum_{n,m=-\infty}^{\infty} \Big(\frac{\exp\{-kr_{1,nm}\}}{r_{1,nm}} - \frac{\exp\{-kr_{2,nm}\}}{r_{2,nm}} - \frac{\exp\{-kr_{3,nm}\}}{r_{3,nm}} + \frac{\exp\{-kr_{4,nm}\}}{r_{4,nm}} \Big),$$

where

$$r_{1,nm} = [(x_M - x_P + 2l_x n)^2 + (y_M - y_P + 2l_y m)^2 + (z_M - z_P)^2]^{1/2},$$
$$r_{2,nm} = [(x_M + x_P + 2l_x n)^2 + (y_M - y_P + 2l_y m)^2 + (z_M - z_P)^2]^{1/2},$$
$$r_{3,nm} = [(x_M - x_P + 2l_x n)^2 + (y_M + y_P + 2l_y m)^2 + (z_M - z_P)^2]^{1/2},$$
$$r_{4,nm} = [(x_M + x_P + 2l_x n)^2 + (y_M + y_P + 2l_y m)^2 + (z_M - z_P)^2]^{1/2},$$

so that $r_{1,00} = r_{MP}$.

Let $M \in D(-\infty, F)$, where

$$D(-\infty, F) = \{(x, y, z) : 0 < x < l_x,\ 0 < y < l_y,\ -\infty < z < F(x, y)\}.$$

Applying the second Green formula in the domain $D(F, \infty)$ to the function $u(P)$ — the solution of the problem (5) and the function $\varphi(M, P)$, we obtain

$$\int\limits_{D(F,\infty)} [\varphi(M,P)\Delta u(P) - u(P)\Delta_P \varphi(M,P)]dv_P =$$
$$= \int\limits_{\partial D(F,\infty)} \Big[\frac{\partial u}{\partial n}(P)\varphi(M,P) - u(P)\frac{\partial}{\partial n_P}\varphi(M,P)\Big]d\sigma_P, \quad M \in D(-\infty, F)$$

or, for the metaharmonic operator

$$\int\limits_{D(F,\infty)} [\varphi(M,P)(\Delta - k^2)u(P) - u(P)(\Delta_P - k^2)\varphi(M,P)]dv_P =$$
$$= \int\limits_{\partial D(F,\infty)} \Big[\frac{\partial u}{\partial n}(P)\varphi(M,P) - u(P)\frac{\partial \varphi}{\partial n_P}(M,P)\Big]d\sigma_P, \quad M \in D(-\infty, F).$$

Since $\varphi(M, P)$ is a metaharmonic function of P, and the function u satisfies the inhomogeneous metaharmonic equation: $(\Delta_P - k^2)u(P) = \rho(P)$, we obtain

$$\int\limits_{D(F,\infty)} \varphi(M,P)\rho(P)dv_P = \int\limits_{\partial D(F,\infty)} \Big[\frac{\partial u}{\partial n}(P)\varphi(M,P) - u(P)\frac{\partial \varphi}{\partial n_P}(M,P)\Big]d\sigma_P, \quad M \in D(-\infty, F).$$

Given the homogeneous boundary conditions for φ and u on the lateral faces Γ of the cylindrical domain $D(F, \infty)$, we obtain

$$\int\limits_{D(F,\infty)} \varphi(M,P)\rho(P)dv_P = \int\limits_{S} \Big[-hf(P)\varphi(M,P) - f(P)\frac{\partial \varphi}{\partial n_P}(M,P)\Big]d\sigma_P, \quad M \in D(-\infty, F). \tag{6}$$

Let us introduce the notation

$$\Phi(M) = \int\limits_{S} \Big[-hf(P)\varphi(M,P) - f(P)\frac{\partial \varphi}{\partial n_P}(M,P)\Big]d\sigma_P, \quad M \in D(-\infty, F). \tag{7}$$

The function Φ is calculated from the known function f and can be considered as a known function. Then (6) can be written as

$$\int\limits_{D(F,\infty)} \varphi(M,P)\rho(P)dv_P = \Phi(M), \quad M \in D(-\infty, F). \tag{8}$$

Given that according to (4) $\rho(x,y,z)=\sigma(x,y)\theta(z-H)\theta(H+s-z)$, we can write the potential in (8) as

$$\int\limits_{D(F,\infty)} \varphi(M,P)\rho(P)dv_P = \int\limits_0^{l_x} dx_P \int\limits_0^{l_y} dy_P \tau(x_P,y_P) \int\limits_H^{H+s} dz_P \varphi(M,P), \quad M\in D(-\infty,F).$$

Let $a<\min\limits_{(x,y)} F(x,y)$ and the point M is located on the rectangle

$$\Pi(a)=\{(x,y,z):\ 0<x<l_x,\ 0<y<l_y,\ z=a\}. \tag{9}$$

Using the representation for the source function φ when $z_P>a$

$$\varphi(M,P)=\frac{2}{l_x l_y}\sum_{n,m=1}^{\infty}\frac{e^{-k_{nm}(z_P-a)}}{k_{nm}}\sin\frac{\pi n x_M}{l_x}\sin\frac{\pi m y_M}{l_y}\sin\frac{\pi n x_P}{l_x}\sin\frac{\pi m y_P}{l_y},$$

we obtain

$$\int\limits_{D(F,\infty)} \varphi(M,P)\rho(P)dv_P = \int\limits_0^{l_x} dx_P \int\limits_0^{l_y} dy_P \tau(x_P,y_P)K(M,P), \quad M\in M\in\Pi(a). \tag{10}$$

where

$$K(M,P)=\frac{4\pi}{l_x l_y}\sum_{n,m=1}^{\infty} K_{nm}\sin\frac{\pi n x_M}{l_x}\sin\frac{\pi m y_M}{l_y}\sin\frac{\pi n x_P}{l_x}\sin\frac{\pi m y_P}{l_y}. \tag{11}$$

$$K_{nm}=\exp\Big\{-k_{nm}(H+\frac{s}{2}-a)\Big\}\frac{\sinh\frac{s}{2}}{k_{nm}^2}, \quad k_{nm}=\pi\Big(\frac{n^2}{l_x^2}+\frac{m^2}{l_y^2}+k^2\Big)^{1/2}. \tag{12}$$

Then, from (10) and (8), we obtain an integral equation of the first kind

$$\int\limits_{\Pi(H)} K(M,P)\tau(P)dx_P dy_P = \Phi(M), \quad M\in\Pi(a). \tag{13}$$

From equation (13), taking into account the expansion (11), when $z_M=a$, we obtain a relation between the Fourier coefficients of the unique solution τ and the Fourier coefficients of the right-hand side

$$\tilde\tau_{nm}K_{nm}=\tilde\Phi_{nm}(a), \tag{14}$$

where $\tilde\Phi_{nm}(a)$ are the Fourier coefficients of the function $\Phi(M)|_{M\in\Pi(a)}$:

$$\tilde\Phi_{nm}(a)=\frac{4}{l_x l_y}\int\limits_{\Pi(a)}\Phi(x,y,a)\sin\frac{\pi n x}{l_x}\sin\frac{\pi m y}{l_y}dxdy.$$

Let us note that formula (14) characterizes the decrease of the Fourier coefficients $\tilde\Phi_{nm}(a)$ with increasing n and m if the function f is such that it ensures the existence of a solution to the problem (5) and, consequently, of the function τ. Expressing the Fourier coefficients $\tilde\tau_{nm}$ from (14), we obtain

$$\tau(x,y)=\sum_{n,m=1}^{\infty}\tilde\Phi_{nm}(a)K_{nm}^{-1}\sin\frac{\pi n x}{l_x}\sin\frac{\pi m y}{l_y}\ . \tag{15}$$

The series (15) converges in L_2 if the solution of problem (5) with respect to τ exists for the given function f.

Formula (15), where the function Φ is of the form (7), gives an explicit expression for solving the inverse problem.

4. Approximate solution to the problem

Let the function f in problem (5) be given with an error, that is, instead of the function f, the function f^δ is given, such that

$$\|f^\delta - f\|_{L_2(S)} \leqslant \delta.$$

We construct an approximate solution of the ill-posed problem (5) that converges to the exact solution when $\delta \to 0$. The function Φ of the form (7) in this case can be obtained approximately:

$$\Phi^\delta(M) = \int\limits_S \Big[- hf^\delta(P)\varphi(M,P) - f^\delta(P)\frac{\partial\varphi}{\partial n_P}(M,P)\Big]d\sigma_P. \tag{16}$$

Applying the Cauchy-Bunyakovsky inequality to the difference of the functions (16) and (7) for $M \in \Pi(a)$, $a < \min\limits_{(x,y)} F(x,y)$, we obtain an estimate for the right-hand side of the integral equation (13)

$$|\Phi^\delta(M) - \Phi(M)|_{M\in\Pi(a)} \leqslant h \max_{M\in\Pi(a)} \Big(\int\limits_S \varphi^2(M,P)d\sigma_P\Big)^{1/2} \|f^\delta - f\|_{L_2(S)} + \\ + \max_{M\in\Pi(a)} \Big(\int\limits_S \Big[\frac{\partial\varphi}{\partial n_P}(M,P)\Big]^2 d\sigma_P\Big)^{1/2} \|f^\delta - f\|_{L_2(S)} \leqslant C\delta. \tag{17}$$

As an approximate solution to equation (13), we will consider the extremal of the Tikhonov functional [10] with a zero-order stabilizer

$$M^\alpha[w] = \Big\| Kw - \Phi^\delta \Big\|^2_{L_2(\Pi(a))} + \alpha\|w\|^2_{L_2(\Pi(H))}, \quad \alpha > 0, \tag{18}$$

where $\Pi(a)$ and $\Pi(H)$ are the domains of the form (9).

The extremal can be obtained as a solution of the Euler equation for the functional (18)

$$K^*Kw + \alpha w = K^*\Phi^\delta(a),$$

which in the Fourier coefficients of the function w has the form

$$K^2_{nm}\tilde{w}_{nm} + \alpha\tilde{w}_{nm} = K_{nm}\tilde{\Phi}^\delta_{nm}(a),$$

where K_{nm} has the form (12) and

$$\tilde{\Phi}^\delta_{nm}(a) = \frac{4}{l_x l_y}\int\limits_{\Pi(a)} \Phi^\delta(x,y,a)\sin\frac{\pi nx}{l_x}\sin\frac{\pi my}{l_y}dxdy$$

— Fourier coefficients of the function $\Phi^\delta(M)|_{M\in\Pi(a)}$.

Solving the equation for the Fourier coefficients of the extremal, we find the approximation w^δ_α to the function τ in the domain $D(-\infty, H)$:

$$w^\delta_\alpha(x,y) = \sum_{n,m=1}^{\infty} \frac{\tilde{\Phi}^\delta_{nm}(a)K^{-1}_{nm}}{1+\alpha K^{-2}_{nm}}\sin\frac{\pi nx}{l_x}\sin\frac{\pi my}{l_y}. \tag{19}$$

We note that the terms of the series (19) differ from the terms of the series (15) by the regularizing factor $(1+\alpha K^{-2}_{nm}\})^{-1}$, which ensures the convergence of the series.

Theorem 1. *Let the solution of problem* (5) *exist. Then for any* $\alpha = \alpha(\delta) > 0$ *such that* $\alpha(\delta) \to 0$ *and* $\delta/\sqrt{\alpha(\delta)} \to 0$ *as* $\delta \to 0$, *the function* $w^\delta_{\alpha(\delta)}$ *of the form* (19) *converges as* $\delta \to 0$ *to the exact solution* τ *in* L_2.

Proof. Let us estimate the difference

$$\|w_\alpha^\delta - \tau\| \leqslant \|w_\alpha^\delta - w_\alpha\| + \|w_\alpha - \tau\|, \tag{20}$$

where w_α is a function of the form (19) with an exact function f

$$w_\alpha(M) = \sum_{n,m=1}^{\infty} \frac{\tilde{\Phi}_{nm}(a)K_{nm}^{-1}}{1+\alpha K_{nm}^{-2}} \sin\frac{\pi n x_M}{l_x} \sin\frac{\pi m y_M}{l_y}.$$

Let us estimate the difference $w_\alpha^\delta - w_\alpha$ in (20) using the estimate (17)

$$\|w_\alpha^\delta(M) - w_\alpha(M)\| = \left|\frac{4}{l_x l_y} \sum_{n,m=1}^{\infty} \left(\frac{K_{nm}^{-1}}{1+\alpha K_{nm}^{-2}}\right)^2 |\tilde{\Phi}_{nm}^\delta(a) - \tilde{\Phi}_{nm}(a)|^2\right|^{1/2} \leqslant$$

$$\leqslant C_1 \max_x \left[\frac{e^x}{1+\alpha e^{2x}}\right] \|\Phi^\delta(a) - \Phi(a)\| \leqslant C_1 \frac{\delta}{\sqrt{2\alpha}}. \tag{21}$$

Let us estimate the difference $w_\alpha - \tau$ in (20)

$$\|w_\alpha - \tau\| \leqslant \left|\frac{4}{l_x l_y} \sum_{n,m=1}^{\infty} \left(\frac{K_{nm}^{-2}}{1+\alpha K_{nm}^{-2}}\right)^2 |K_{nm}\tilde{\Phi}_{nm}(a)|^2\right|^{1/2} = \left|\frac{4}{l_x l_y} \sum_{n,m=1}^{\infty} \left(\frac{K_{nm}^{-2}}{1+\alpha K_{nm}^{-2}}\right)^2 \tilde{\tau}_{nm}^2\right|^{1/2}.$$

Since the series depending on the parameter α is majorized by a convergent numerical series with coefficients $\tilde{\tau}_{nm}^2$, a limit transition in α is possible, and thus

$$\|w_\alpha - \tau\| \to 0 \quad \text{при} \quad \alpha \to 0. \tag{22}$$

From (20), (21), and (22), and the conditions of the theorem, it follows that

$$\|w_{\alpha(\delta)}^\delta - \tau\| \to 0 \quad \text{при} \quad \delta \to 0.$$

5. Results and Discussion

The proven theorem allows us to consider the series (19) as an explicit formula for calculating an approximate solution to problem (5), robust to an error in specifying the thermogram f. Note that for a flat surface S, calculating the integral (16) is significantly simplified. When specifying a non-flat surface S approximately, the results of works [19, 20] on calculating the normal to an approximately specified surface can be used to perform calculations using formula (16).

Conclusion

A stable solution to the inverse problem (5) can be used for mathematical processing of thermograms, particularly in medicine [1], for the purpose of thermal image correction. A thermogram obtained with a thermal imager conveys with varying accuracy the structure of heat sources within the body. Refinement of the thermogram image can be performed within the framework of problem (5). In this case, the function f is compared to the original thermogram, and the function τ can be considered as the result of thermogram processing. Since the function τ represents the intensity distribution of heat sources on the rectangle $\Pi(H)$, one can expect a more accurate reproduction of their image in the calculated thermogram τ compared to the original thermogram f.

Author Contributions: Conceptualization, Evgeniy B. Laneev and Aigul M. Gaipova; methodology, Evgeniy B. Laneev and Aigul M. Gaipova; software, Evgeniy B. Laneev and Aigul M. Gaipova; validation, Evgeniy B. Laneev and Aigul M. Gaipova; formal analysis, Evgeniy B. Laneev and Aigul M. Gaipova; investigation, Evgeniy B. Laneev and Aigul M. Gaipova; resources, Evgeniy B. Laneev and Aigul M. Gaipova; data curation, Evgeniy B. Laneev and Aigul M. Gaipova; writing—original draft preparation, Evgeniy B. Laneev and Aigul M. Gaipova; writing—review and editing, Evgeniy B. Laneev and Aigul M. Gaipova; visualization, Evgeniy B. Laneev and Aigul M. Gaipova; supervision, Evgeniy B. Laneev and Aigul M. Gaipova; project administration, Evgeniy B. Laneev and Aigul M. Gaipova; funding acquisition, Evgeniy B. Laneev and Aigul M. Gaipova. All authors have read and agreed to the published version of the manuscript.

Funding: This research received no external funding.

Data Availability Statement: Data sharing is not applicable.

Conflicts of Interest: The authors declare no conflict of interest.

Declaration on Generative AI: The author has not employed any generative AI tools.

References

[1] G. R. Ivanitskii, "Thermovision in medicine," Russian, *Vestnik RAN*, vol. 76, no. 1, pp. 44–53, 2006.

[2] E. F. J. Ring, "Progress in the measurement of human body temperature," *IEEE Engineering in Medicine and Biology Magazine*, vol. 17, no. 4, pp. 19–24, 1998. DOI: 10.1109/51.687959

[3] E. Y. K. Ng and N. M. Sudarshan, "Numerical computation as a tool to aid thermographic interpretation," *Journal of Medical Engineering and Technology*, vol. 25, no. 2, pp. 53–60, 2001. DOI: 10.1080/03091900110043621

[4] B. F. Jones and P. Plassmann, "Digital infrared thermal imaging of human skin," *IEEE Eng. in Med. Biol. Mag.*, vol. 21, no. 6, pp. 41–48, 2002. DOI: 10.1109/memb.2002.1175137

[5] E. B. Laneev, N. Y. Chernikova, and O. Baaj, "Application of the minimum principle of a Tikhonov smoothing functional in the problem of processing thermographic data," *Advances in Systems Science and Applications*, vol. 21, no. 1, pp. 139–149, 2021. DOI: 10.25728/assa.2021.21.1.1055

[6] E. B. Laneev and A. V. Klimishin, "On an approximate solution to an ill-posed mixed boundary value problem for the Laplace equation in a cylindrical domain with homogeneous conditions of the second kind on the lateral surface of the cylinder," Russian, *Russian Universities Reports. Mathematics*, vol. 29, no. 146, pp. 164–175, 2024. DOI: 10.20310/2686-9667-2024-29-146-164-175

[7] A. N. Tikhonov, V. B. Glasko, O. K. Litvinenko, and V. R. Melihov, "On the continuation of the potential towards disturbing masses based on the regularization method," Russian, *Vestnik RAN*, no. 1, pp. 30–48, 1968.

[8] H. Pennes, "Analysis of tissue and arterial blood temperature in theresting human forearm," *J. Appl. Physiol.*, no. 1, pp. 93–122, 1948.

[9] J. Agnelli, A. Barrea, and C. Turner, "Tumor location and parameter estimation by thermography," *Mathematical and Computer Modelling*, vol. 53, pp. 1527–1534, 2011. DOI: 10.1016/j.mcm.2010.04.003

[10] A. N. Tihonov and V. Y. Arsenin, *Methods for solving ill-posed problems*, Russian. Moscow: Nauka, 1979.

[11] A. I. Prilepko, "Inverse problems of potential theory.," *Math. Notes*, vol. 14, no. 5, pp. 990–996, 1973. DOI: 10.1007/BF01462264

[12] L. N. Sretenskiy, "On the uniqueness of determining the shape of an attractive body by the values of its external potential," Russian, *Dokladi RAN*, vol. 99, no. 1, pp. 21–22, 1954.

[13] E. M. Landis, "Some problems of the qualitative theory of second order elliptic equations (case of several independent variables)," *Russian Math. Surveys*, vol. 18, no. 1, pp. 1–62, 1963. DOI: 10.1070/RM1963v018n01ABEH004124

[14] S. B. Sorokin, "An Efficient Direct Method for Numerically Solving the Cauchy Problem for Laplace's Equation," *Num. Anal. Appl.*, vol. 12, no. 1, pp. 87–103, 2019. DOI: 10.15372/SJNM20190107

[15] M. Joachimiak, "Choice of the regularization parameter for the Cauchy problem for the Laplace equation," *International Journal of Numerical Methods for Heat and Fluid Flow*, vol. 30, no. 10, pp. 4475–4492, 2020. DOI: 10.1108/HFF-10-2019-0730

[16] E. Laneev, "Construction of a Carleman function based on the Tikhonov regularization method in an ill-posed problem for the Laplace equation," *Differential Equations*, vol. 54, no. 4, pp. 476–485, 2018. DOI: 10.1134/S0012266118040055

[17] E. Laneev and C. N.Yu., "Minimum Principle for the Tikhonov Functional in the Problem of Stable Continuation of a Potential Field from a Surface," *Differential Equations*, vol. 59, no. 6, pp. 752–762, 2023. DOI: 10.1134/S001226612306006X

[18] E. Laneev and E. Ponomarenko, "On a linear inverse potential problem with approximate data on the potential field on an approximately given surface," *Eurasian Mathematical Journal*, vol. 14, no. 1, pp. 57–70, 2023. DOI: 10.32523/2077-9879-2023-14-1-55-70

[19] O. Baaj, N. Y. Chernikova, and E. Laneev, "Correction of Thermographic Images Based on the Minimization Method of Tikhonov Functional," *Yugoslav Journal of Operations Research*, vol. 32, no. 3, pp. 407–424, 2022. DOI: 10.2298/YJOR211015026B

[20] E. B. Laneev and A. V. Klimishin, "On the stable approximate solution of the ill-posed boundary value problem for the Laplace equation with homogeneous conditions of the second kind on the edges at inaccurate data on the approximated boundary," *Discrete and Continuous Models and Applied Computational Science*, vol. 1, no. 33, pp. 57–73, 2025. DOI: 10.22363/2658-4670-2023-31-3-228-241

Information about the authors

Laneev, Evgeniy B.—Doctor of Physical and Mathematical Sciences, Professor of the Mathematical Institute named after S. M. Nikolsky of RUDN University (e-mail: elaneev@yandex.ru, ORCID: 0000-0002-4255-9393, ResearcherID: G-7887-2016, Scopus Author ID: 24366681900)

Gaipova, Aigul M.—Post-Graduate student of the Mathematical Institute named after S. M. Nikolsky of RUDN University (e-mail: 1032169239@rudn.ru, ORCID: 0009-0008-1345-6265)

RUSSIAN METADATA

УДК 519.872, 519.217

PACS 07.05.Tp, 02.60.Pn, 02.70.Bf

DOI: 10.22363/2658-4670-2026-34-3-369-378 EDN: RRILKX

Обратная задача термографии как обратная задача потенциала для тел постоянной толщины

Е. Б. Ланеев, А. М. Гаипова

Российский университет дружбы народов, ул. Миклухо-Маклая, д. 6, Москва, 117198, Российская Федерация

Аннотация. *Предпосылки* В работе рассматривается метод коррекции термографических изображений, используемых в медицинской диагностике. Математическая обработка термограмм производится в рамках математической модели однородного теплопроводящего полубесконечного цилиндра прямоугольного сечения, ограниченного поверхностью общего вида и содержащего источники тепла, не зависящие от времени. Мы считаем, что функция плотности распределения источников соответствует телу постоянной толщины. На боковых гранях цилиндра заданы однородные условия первого рода, что соответствует нулевой температуре. На поверхности, ограничивающей цилиндрическую область имеет место конвективный теплообмен со внешней средой нулевой температуры. Учет кровотока приводит к тому, что стационарное распределение температуры удовлетворяет неоднородному метагармоническому уравнению. *Цель* В рамках выбранной модели поставлена обратная задача восстановления неизвестной плотности источников тепла по заданной функции распределения температуры на поверхности, ограничивающей цилиндр (термограмме). Эта обратная задача формулируется как некорректно поставленная смешанная задача для метагаромонического уравнения с данными Коши на поверхности, ограничивающей цилиндрическую область. Искомая функция – правая часть метагармонического уравнения. *Методы* В работе обратная задача с использованием формул Грина сведена к интегральному уравнению первого рода, соответветствущему обратной задаче потенциала для тел постоянной толщины. Приближенное решение поставленной задачи, устойчивое по отношению к погрешности в термограмме и, следовательно, в данных Коши, получено на основе метода регуляризации Тихонова. *Результаты* Приближенное решение построено в виде двойного ряда Фурье с регуляризирующим множителем. Доказана сходимость приближенного решения поставленной задачи при согласовании параметра регуляризации с погрешностью в данных Коши. *Выводы* Приближенное решение задачи может рассматриваться в качестве скорректированной термограммы.

Явные формулы, полученные для приближенного решения, могут быть использованы для построения эффективных вычислительных алгоритмов.

Ключевые слова: термограмма, некорректная задача, обратная задача, обратная задача потенциала, задача Коши для метагармонического уравнения, интегральное уравнение первого рода, метод регуляризации Тихонова

Discrete & Continuous Models
& Applied Computational Science
ISSN 2658-7149 (Online), 2658-4670 (Print)

2026, 34 (3) 379–395
http://journals.rudn.ru/miph

Research article

UDC 004.729, 519.872
PACS 89.20.Ff, 02.60.Pn, 07.05.Tp
DOI: 10.22363/2658-4670-2026-34-3-379-395 EDN: RUDFRI

Comparative analysis of active queue management algorithms: RED, ARED, Gentle RED

Abuli M. Palagashvili, Anna M. Ermolayeva, Tatyana R. Velieva

RUDN University, 6 Miklukho-Maklaya St, Moscow, 117198, Russian Federation

(received: June 28, 2026; revised: July 5, 2026; accepted: July 20, 2026)

Abstract. *Background.* Active Queue Management (AQM) algorithms of the RED family remain widely deployed in network equipment, yet a systematic three-way comparison of RED, Adaptive RED (ARED), and Gentle RED under strictly identical conditions is lacking in the literature. *Purpose.* The aim of this study is to quantify the differences in buffer management dynamics, throughput stability, and congestion signaling among the three algorithms and to formulate practical selection guidelines. *Method.* A dumbbell-topology network model was implemented in the ns-3 discrete-event simulator (version 3.41) with ten TCP bulk-send sources creating sustained congestion at a 2 Mbit/s bottleneck link. All three algorithms were evaluated with identical queue thresholds, load profile, and topology over a 60-second simulation. An extended metric set including EWMA zone distribution and temporal drop structure was applied. *Results.* All algorithms achieved approximately 90% link utilization (mean throughput 1.80 Mbit/s). RED provided the most predictable throughput (coefficient of variation 18.7%) at the cost of the highest drop count (1240 packets). ARED minimized drops (1003 packets, 19% fewer than RED) but produced the largest queue oscillations (p99 of 49 packets). Gentle RED achieved the lowest mean queue length (6.40 packets) with the highest throughput variability (coefficient of variation 24.7%). *Conclusions.* No single algorithm is universally optimal; the choice depends on scenario priorities: Gentle RED for minimum delay, ARED for minimum packet loss, and RED for maximum throughput predictability.

Key words and phrases: active queue management, AQM, RED, Adaptive RED, Gentle RED, congestion control, ns-3, network simulation, bufferbloat

For citation: A. M. Palagashvili, A. M. Ermolayeva, T. R. Velieva "Comparative analysis of active queue management algorithms: RED, ARED, Gentle RED," *Discrete and Continuous Models and Applied Computational Science*, vol. 34, no. 3, pp. 379–395, 2026. DOI: 10.22363/2658-4670-2026-34-3-379-395. EDN: RUDFRI.

1. Introduction

The continuous growth of Internet traffic, driven by the development of cloud computing, video streaming, and 5G/6G networks, imposes increasingly stringent requirements on congestion management mechanisms in network nodes. The traditional approach—tail-drop, in which packets are discarded only when the buffer is completely full—leads to global synchronization of TCP flows, sharp oscillations of throughput, and the bufferbloat effect [1]. The bufferbloat problem—systematic buffer overflow in routers causing end-to-end delay growth by orders of magnitude—has been identified as one of the key threats to quality of service [2].

Active Queue Management (AQM) algorithms, recommended by IETF in RFC 2309 [3], solve this problem by preemptive dropping or marking of packets before buffer overflow [4]. The RED (Random Early Detection) family of algorithms remains the most widely deployed class of AQM mechanisms [5]: RED is implemented in all major network operating systems (Cisco IOS, Linux tc, FreeBSD ALTQ), and its variants—ARED and Gentle RED—are shipped as standard modules in the ns-3 simulator and the Linux kernel. Despite the emergence of new algorithms (CoDel [6], PIE [7]), the choice of a specific RED variant for specific operating conditions still requires experimental justification, since analytical models do not account for all aspects of interaction with heterogeneous TCP traffic.

© 2026 A. M. Palagashvili, A. M. Ermolayeva, T. R. Velieva

This work is licensed under a Creative Commons "Attribution-NonCommercial 4.0 International" license.

1.1. Literature review

The RED algorithm was proposed by Floyd and Jacobson in 1993 [8], building on the foundational work on congestion avoidance [9], and became the first practical AQM mechanism. The authors demonstrated that probabilistic early dropping of packets based on the exponentially weighted moving average (EWMA) of queue length avoids global synchronization of TCP flows and reduces average buffer delay compared to tail-drop.

Practical deployment of RED revealed its main drawback—high sensitivity to parameter tuning. Christiansen et al. [10] showed that RED performance significantly depends on the ratio of $\min_{\text{Th}}$, $\max_{\text{Th}}$, and maxP, with optimal values changing as the number of flows and load level change. To overcome this limitation, Floyd et al. [11] proposed ARED (Adaptive RED), in which the maxP parameter automatically adapts to the current load based on the deviation of the average queue from the target range.

In parallel, Floyd [12] proposed the Gentle RED modification, which eliminates the sharp transition of drop probability from maxP to 1 at $\bar{q} = \max_{\text{Th}}$. Gentle RED introduces an additional linear zone $[\max_{\text{Th}}, 2 \cdot \max_{\text{Th}})$, in which the probability smoothly increases to unity, reducing TCP flow synchronization and decreasing delay variance during short-term bursts. An alternative to packet dropping is Explicit Congestion Notification (ECN) [13], which marks rather than drops packets, though its interaction with RED-family algorithms is outside the scope of this work.

A significant contribution to mathematical modeling of TCP and RED interaction was made by Anna Vladislavovna Korolkova [14], who constructed a mathematical model of the traffic transmission process with dynamic flow intensity regulated by a RED-type algorithm. In her work, using the apparatus of stochastic differential equations with a Poisson process, an autonomous system of three ordinary differential equations was formalized for the first time, describing the joint dynamics of TCP window size, instantaneous queue length, and EWMA average. A method was proposed for determining the region of self-oscillation occurrence, and qualitative analysis of the model was performed using RED, GRED, DSRED, and ARED algorithms in the NS-2 simulator.

The development of this direction was continued by Tatyana Refatovna Velieva [15], who investigated nonlinear phenomena and boundaries of the self-oscillation region in continuous-discrete dynamical models. The key contribution of this work was the adaptation of the Krylov–Bogolyubov method and harmonic linearization method to the continuous-discrete TCP/RED model, which made it possible to analytically determine the amplitude-frequency characteristics of self-oscillations and the boundaries of their occurrence region in the parameter space.

Among alternative approaches to AQM, the BLUE algorithm [16], which controls drop probability based on loss events and link idle events, the SRED algorithm [17], which stabilizes queue behavior through zombie list-based flow identification, and the family of control-theory-based algorithms—the PI controller of Hollot et al. [18] and its development PIE [7]—should be noted. The fluid-based analytical framework of Misra et al. [19] provided theoretical foundations for understanding TCP/AQM interaction dynamics. The CoDel algorithm [6] uses a fundamentally different approach, tracking the sojourn time of a packet in the queue instead of queue length.

Thus, despite extensive research on individual aspects of the RED family algorithms—both analytical (stability, self-oscillations) and experimental—a systematic three-way comparison of RED, ARED, and Gentle RED under strictly identical conditions with an extended set of metrics (including temporal drop structure and zone distribution of the queue) is insufficiently represented in the literature.

1.2. Research objectives

The goal of this work is to conduct a comparative analysis of three algorithms from the RED family (RED, ARED, Gentle RED) under conditions of sustained congestion of a network node and to identify quantitative differences in buffer management dynamics, throughput stability, and the nature of congestion signals.

To achieve this goal, the following tasks are set:

1. Implement a simulation model of a network with dumbbell topology in the ns-3 environment with the ability to switch the AQM algorithm while maintaining other conditions.
2. Conduct a series of experiments with identical queue parameters and load for each of the three algorithms.
3. Compare algorithms by a set of metrics: mean and tail queue length, coefficient of variation of throughput, number and temporal structure of packet drops.
4. Formulate practical recommendations for AQM algorithm selection depending on the priority requirements of the scenario.

1.3. Scientific novelty

The scientific novelty of this work consists of the following:

1. Unlike the works of Floyd and Jacobson [8], Floyd [11, 12], and Christiansen et al. [10], where each algorithm was analyzed in isolation or in pairwise comparison with tail-drop, this work conducts a systematic three-way comparison of RED, ARED, and Gentle RED under strictly identical conditions (unified topology, identical thresholds, identical load profile), which eliminates the influence of methodological differences on results.
2. Unlike the analytical approach of Korolkova [14], who studied self-oscillation modes using ODE systems, and Velieva [15], who applied the harmonic linearization method to determine stability boundaries, this work proposes an extended set of *experimental* evaluation metrics, including zone distribution of EWMA average operating time and temporal structure of drops (median interval, clustering), which allows characterizing not only static indicators but also the dynamics of control actions in the simulation model.
3. Unlike the works of Hollot et al. [18] and Feng et al. [16], focused on comparing RED with fundamentally different AQM approaches (PI controller, BLUE), this work focuses on *intra-family* comparison of RED variants and for the first time quantitatively describes the fundamental trade-off between throughput predictability (RED, CV = 18.7%), drop minimization (ARED, −19%), and buffer delay minimization (Gentle RED, average queue 6.40 pkt).

1.4. RED family algorithms

Active queue management algorithms begin dropping or marking packets *preemptively*—before the buffer overflows—based on average queue length statistics. TCP connections receive congestion signals earlier and reduce their sending rate more smoothly, preventing collapse.

1.4.1. RED (Random Early Detection)

RED is the base AQM algorithm proposed by Floyd and Jacobson in 1993 [8]. The algorithm computes the exponentially weighted moving average of queue length (EWMA) and makes drop decisions based on it.

Average queue update on each arriving packet:

$$\bar{q} = (1 - w_q)\,\bar{q} + w_q\,q,$$

where q is the instantaneous queue length, $w_q \in (0, 1)$ is the filter weight.

Drop probability is determined by three zones:

$$p(\bar{q}) = \begin{cases} 0, & \bar{q} < \min_{\text{Th}} \\ \text{maxP} \cdot \dfrac{\bar{q} - \min_{\text{Th}}}{\max_{\text{Th}} - \min_{\text{Th}}}, & \min_{\text{Th}} \le \bar{q} < \max_{\text{Th}} \\ 1, & \bar{q} \ge \max_{\text{Th}} \end{cases}$$

The hard forced drop above $\max_{\text{Th}}$ ensures fast reaction but synchronizes TCP flows and creates sawtooth queue oscillations.

1.4.2. ARED (Adaptive RED)

ARED extends RED with an adaptive mechanism [11]: the maxP parameter is periodically recomputed every T_{interval} depending on the deviation of the average queue from the target range:

$$\text{maxP} = \begin{cases} \text{maxP} + \alpha, & \bar{q} > \dfrac{\min_{\text{Th}} + \max_{\text{Th}}}{2} \\ \text{maxP} - \beta, & \bar{q} < \dfrac{\min_{\text{Th}} + \max_{\text{Th}}}{2} \end{cases}$$

where α and β are increment and decrement coefficients ($\alpha > \beta$). The value of maxP is bounded within an admissible range. This allows the algorithm to adapt to changing load without manual tuning; however, the adaptation introduces additional inertia and may lead to wide queue oscillations.

1.4.3. Gentle RED

Gentle RED [12] modifies RED behavior in the zone above $\max_{\text{Th}}$: instead of immediate forced drop, the algorithm continues the probabilistic approach up to $2 \cdot \max_{\text{Th}}$:

$$p(\bar{q}) = \begin{cases} 0, & \bar{q} < \min_{\text{Th}} \\ \text{maxP} \cdot \dfrac{\bar{q} - \min_{\text{Th}}}{\max_{\text{Th}} - \min_{\text{Th}}}, & \min_{\text{Th}} \le \bar{q} < \max_{\text{Th}} \\ \text{maxP} + (1 - \text{maxP}) \cdot \dfrac{\bar{q} - \max_{\text{Th}}}{\max_{\text{Th}}}, & \max_{\text{Th}} \le \bar{q} < 2\max_{\text{Th}} \\ 1, & \bar{q} \ge 2\max_{\text{Th}} \end{cases}$$

In the zone $[\max_{\text{Th}},\ 2 \cdot \max_{\text{Th}})$ the probability linearly grows from maxP to 1, and forced drop occurs only at $\bar{q} \ge 2 \cdot \max_{\text{Th}}$. This softens the reaction to short-term bursts, reduces TCP flow synchronization, and decreases the average queue length—at the cost of somewhat greater throughput variability.

2. Methods

2.1. Simulation environment

2.1.1. Discrete-event network simulation

The study of network protocols and congestion control mechanisms can be conducted using three principal methodologies: analytical modeling, physical experimentation on real hardware, and simulation. Analytical models (such as the fluid models of TCP/RED interaction used by Korolkova [14] and Velieva [15]) provide closed-form insights into system stability but require significant simplifying assumptions that limit their applicability to complex multi-flow scenarios. Physical testbeds provide maximum realism but suffer from poor reproducibility, high cost, and limited scalability. *Simulation*—and specifically *discrete-event simulation* (DES)—occupies the middle ground: it models the behavior of each individual packet traversing the network at a chosen level of abstraction while maintaining full control over experimental conditions.

In discrete-event simulation, the simulator does not advance time in fixed increments. Instead, it maintains a priority queue of future events (packet arrivals, timer expirations, state transitions), each tagged with its scheduled virtual time. The simulation engine processes events in chronological order: it dequeues the earliest event, advances the simulation clock to that event's time, executes the associated callback (which may schedule new events), and repeats. Between events, no computation occurs—the simulation clock "jumps" directly to the next event. This event-driven approach provides several critical properties for network research:

– Exact reproducibility. Given identical initial conditions, random seeds, and parameters, the simulation produces bitwise-identical results on any platform—a prerequisite for controlled comparative studies.
– Arbitrary instrumentation. Any internal state variable (instantaneous queue length, EWMA average, TCP congestion window, drop probability) can be sampled at any point in simulated time without introducing probe traffic or measurement overhead that would perturb the system.
– Time compression. A 60-second simulation of a network with dozens of nodes completes in seconds of wall-clock time, enabling systematic parameter sweeps that would require days on physical hardware.
– Perfect isolation. Unlike emulation or physical experiments, simulation results are unaffected by host OS scheduling jitter, hardware variability, or background traffic.

2.1.2. The ns-3 simulator

For conducting the experiments in this work, the discrete-event network simulator ns-3 (Network Simulator 3) version 3.41 was used [20]. ns-3 is an open-source simulation platform designed for research and education in the field of computer networks. It is developed and maintained by an international consortium of universities and research laboratories, distributed under the GNU GPLv2 license, and has been cited in thousands of peer-reviewed publications since its first release in 2008.

ns-3 is implemented entirely in C++ with optional Python bindings for scripting convenience. The simulator is organized into a set of *modules*, each implementing a specific protocol layer or network technology:

– `internet`—IPv4/IPv6 stacks, TCP (NewReno, Cubic, BBR), UDP, ARP, routing;
– `traffic-control`—queue disciplines including `RedQueueDisc` (RED, ARED, Gentle RED), CoDel, PIE, FQ-CoDel;
– `point-to-point`, `csma`, `wifi`, `lte`—link-layer and physical-layer models;
– `applications`—traffic generators (BulkSend, OnOff, PacketSink) and application-layer protocols.

The `RedQueueDisc` module, used in this work, implements all three algorithms of the RED family within a single class controlled by configuration attributes: `ARED` (boolean flag enabling adaptive maxP), `Gentle` (boolean flag enabling the gentle mode with extended probability zone), and standard threshold parameters (`MinTh`, `MaxTh`, `MaxSize`, `QW`). This unified implementation guarantees that algorithm comparison is not confounded by differences in code quality, timer resolution, or packet processing paths.

Key reasons for choosing ns-3 in this work:

– Protocol fidelity. The TCP implementation in ns-3 models the full state machine (slow start, congestion avoidance, fast retransmit, fast recovery) with segment-level granularity, matching the behavior of real kernel stacks.
– Native AQM support. All three RED variants are available as standard modules with validated implementations referenced in the ns-3 documentation and regression test suite.
– Scalability. Simulating tens of nodes and hundreds of flows is feasible on a single workstation; the event-driven core consumes memory proportional to the number of active events, not simulated time.
– Tracing framework. ns-3 provides a hierarchical tracing system that allows attaching callbacks to any state change (enqueue, dequeue, drop, congestion window update) without modifying simulator source code.
– Active development. ns-3 receives regular releases (3–4 per year), maintains backwards compatibility of simulation APIs, and has extensive documentation including a tutorial, manual, and model library reference.

Table 1

Architectural comparison of ns-2 and ns-3

Aspect	**ns-2**	**ns-3**
Language	C++ core + OTcl scripting	C++ throughout (Python optional)
Architecture	Split object model (C++/OTcl)	Unified object model
IP model	Abstract addressing	Real IP stack (BSD-like)
Packet format	Simulated headers	Serialized byte buffers
Emulation	Limited	Real-time scheduler, tap bridges
Maintenance	Frozen (last release 2011)	Active (latest release 2024)
Validation	Community scripts	Regression test suite per module

2.1.3. Comparison with ns-2 and other simulation tools

ns-2 (Network Simulator 2) is the predecessor of ns-3 and was the dominant network simulation tool from the mid-1990s through the 2000s. While ns-3 inherits the research mission of ns-2, it is a complete rewrite with a fundamentally different architecture. Table 1 summarizes the key differences.

The split-object architecture of ns-2 required researchers to maintain parallel class hierarchies in C++ and OTcl, leading to steep learning curves and frequent synchronization bugs between the two layers. ns-3 eliminates this duality: simulation scripts are written in the same C++ (or Python) that implements the models. Furthermore, ns-2 used abstract 32-bit node addresses and simplified packet headers, while ns-3 models real IPv4/IPv6 headers with proper checksums and fragmentation—enabling direct validation against packet captures from physical networks.

A critical practical consideration is that ns-2 has not received official updates since 2011 and its RED implementation lacks the ARED adaptive mechanism as a standard module. In ns-3, all three algorithms are maintained, tested, and documented within the `traffic-control` module.

Other simulation and emulation environments:

- *OMNeT++* [21] is a modular discrete-event simulation framework. Network protocols are provided by the separate INET library. OMNeT++ uses NED (Network Description) language for topology specification and has a graphical IDE. While powerful, it requires learning an additional domain-specific language and the INET RED implementation is less extensively validated than ns-3's.
- *GNS3* and *Mininet* are network *emulators* rather than simulators: they run real protocol implementations (Linux kernel network stack, actual router firmware images) in virtualized or containerized environments. Emulators provide maximum protocol realism but sacrifice reproducibility (results depend on host CPU scheduling, memory pressure, and I/O latency) and scalability (each node requires real OS resources).
- *OPNET Modeler* (now Riverbed Modeler) is a commercial discrete-event simulator with a graphical drag-and-drop interface, widely used in industry for network planning. Its proprietary license and closed-source nature limit its use in academic reproducibility contexts.

Table 2 provides a summary comparison of simulation tools across dimensions relevant to this work.

2.1.4. Installation and setup

ns-3 is distributed as source code and can be built on Linux (Ubuntu, Fedora, CentOS) and macOS. The build system requires a C++17-compatible compiler (GCC $\geq$ 9 or Clang $\geq$ 11), CMake $\geq$ 3.13, and Python 3. The minimal installation procedure is:

```
git clone https://gitlab.com/nsnam/ns-3-dev.git ns-3.41
cd ns-3.41
```

Table 2

Comparison of network simulation/emulation environments

Property	ns-3	ns-2	OMNeT++	Mininet	OPNET
Type	DES	DES	DES	Emulation	DES
License	GPLv2	GPLv2	Academic/Comm.	BSD	Commercial
RED family support	Full	Partial	INET	Kernel	Yes
Reproducibility	Exact	Exact	Exact	Approximate	Exact
Active development	Yes	No	Yes	Yes	Yes

```
./ns3 configure --enable-examples --enable-tests
./ns3 build
```

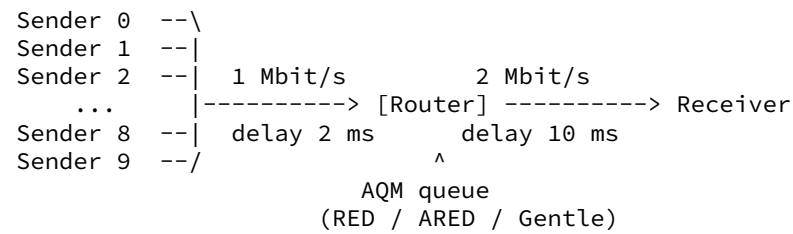
The `./ns3 configure` step detects available optional dependencies (GTK for visualization, SQLite for statistics, MPI for distributed simulation) and generates the build system. The `./ns3 build` step compiles all enabled modules into shared libraries. After building, simulation scripts are placed in the `scratch/` directory and executed via:

```
./ns3 run "scratch/<script-name> [--command-line-arguments]"
```

For this work, a dedicated subdirectory `scratch/red-experiments/` was created containing the simulation source code, configuration files, and analysis scripts.

2.2. Experimental topology

The experiment uses a dumbbell topology: multiple senders are connected to a common router through fast links, and the router is connected to a single receiver through a narrow bottleneck link with limited bandwidth. The narrow link is the only possible congestion point, and the AQM queue discipline is installed on its outgoing interface.



Each of the ten senders establishes one TCP connection (using TCP CUBIC [22]) with the receiver and continuously transmits data (BulkSend). The total incoming load on the router potentially reaches 10×1 Mbit/s $= 10$ Mbit/s, which is 5 times the bottleneck link capacity. This ensures sustained congestion and allows evaluation of AQM algorithm behavior under real buffer saturation conditions.

Topology parameters are listed in Table 3.

2.3. AQM configuration

All three algorithms are launched with identical threshold parameters (Table 4).

2.4. Instrumentation

The discrete-event network simulator ns-3 version 3.41 was used. Simulation scripts are placed in the `scratch/` directory. For this experiment, a subdirectory was created with the following structure:

Table 3

Topology and simulation parameters

Parameter	Value	Description
`nSenders`	10	Number of TCP senders
`fastRate`	1 Mbit/s	Sender → router link speed (delay 2 ms)
`bottleneckRate`	2 Mbit/s	Bottleneck link speed (router → receiver)
`bottleneckDelay`	10 ms	Bottleneck link delay
`simTime`	60.0	Simulation duration (s)
Transport	TCP BulkSend	Segment size 512 bytes

Table 4

Unified threshold parameters for RED, ARED, and Gentle RED

Parameter	Value	Description
`minTh`	5 packets	Lower average queue threshold—no drops below
`maxTh`	10 packets	Upper threshold; above it RED/ARED drop all packets
`MaxSize`	100 packets	Hard buffer limit

```
ns-3.41/
+-- scratch/
    +-- red-experiments/
        +-- red.cc
        +-- configs/
        |   +-- red.txt
        |   +-- ared.txt
        |   +-- gentle.txt
        +-- analysis/
            +-- vis.py
            +-- ...
```

Configuration files specify the AQM type and queue parameters. Example `configs/red.txt`:

```
aqmType=red
minTh=5
maxTh=10
MaxSize=100
```

Analogous files for ARED (`aqmType=ared`) and Gentle RED (`aqmType=gentle`) differ only in the `aqmType` field value.

Simulations were launched with:

```
./ns3 run "scratch/red-experiments/red.cc
 ↪  --config=configs/<algorithm>.txt"
```

Upon completion of each simulation, three CSV files were generated:

- `<algorithm>_queue.csv`—queue length sampled every 100 ms;
- `<algorithm>_drops.csv`—timestamps of each packet drop;
- `<algorithm>_throughput.csv`—throughput sampled every 100 ms.

For plotting, the script `vis.py` with moving average smoothing (window of 30 samples) was used:

```
// 1. Create network nodes
NodeContainer senders(10), router(1), receiver(1);

// 2. Configure access links (sender -> router)
PointToPointHelper accessLink;
accessLink.SetRate("1Mbps");
accessLink.SetDelay("2ms");
for (int i = 0; i < 10; i++)
    accessLink.Install(senders[i], router);

// 3. Configure bottleneck link (router -> receiver)
PointToPointHelper bottleneck;
bottleneck.SetRate("2Mbps");
bottleneck.SetDelay("10ms");
bottleneck.Install(router, receiver);

// 4. Install IP stack on all nodes
InternetStackHelper stack;
stack.InstallAll();

// 5. Install AQM queue discipline on bottleneck
TrafficControlHelper tch;
tch.SetRootQueueDisc("ns3::RedQueueDisc",
    "MinTh",    DoubleValue(5),
    "MaxTh",    DoubleValue(10),
    "MaxSize",  QueueSizeValue("100p"),
    "ARED",     BooleanValue(aredFlag),
    "Gentle",   BooleanValue(gentleFlag));
tch.Install(bottleneckDevice);
```

Listing 1: Topology construction and AQM installation (pseudocode)

```
python vis.py --algorithms red ared gentle --window 30
```

2.5. Simulation script structure

To illustrate the experimental setup, Listings 1–3 present simplified pseudocode of the main simulation stages.

Listing 1 demonstrates the key step distinguishing the three experiments: the `ARED` and `Gentle` boolean flags passed to `RedQueueDisc`. When both are `false`, standard RED is used; setting `ARED=true` enables adaptive maxP; setting `Gentle=true` enables the extended probability zone. All other parameters (thresholds, topology, traffic pattern) remain identical across runs.

Listing 2 shows the traffic generation pattern: ten BulkSend applications, each sending an unlimited stream of 512-byte segments over TCP, creating sustained congestion at the bottleneck.

Listing 3 illustrates the instrumentation approach: ns-3's tracing framework allows attaching callbacks to queue state changes and scheduling periodic sampling without modifying the protocol implementation code. The three output CSV files are produced by these callbacks.

3. Results

The experiment consisted of three sequential simulations—one for each algorithm. Each algorithm was launched with identical queue parameters (Table 4) for 60 seconds (the first second is warm-up, excluded from analysis).

```
// 6. Install TCP BulkSend on each sender
BulkSendHelper bulkSend("ns3::TcpSocketFactory",
    InetSocketAddress(receiverAddr, port));
bulkSend.SetAttribute("SendSize", UintegerValue(512));
bulkSend.SetAttribute("MaxBytes", UintegerValue(0)); // unlimited

ApplicationContainer senderApps;
for (int i = 0; i < 10; i++)
    senderApps.Add(bulkSend.Install(senders[i]));

// 7. Install PacketSink on receiver
PacketSinkHelper sink("ns3::TcpSocketFactory",
    InetSocketAddress(Ipv4Address::GetAny(), port));
sink.Install(receiver);

// 8. Schedule start/stop
senderApps.Start(Seconds(0.0));
senderApps.Stop(Seconds(60.0));
```

Listing 2: Traffic generation setup (pseudocode)

Table 5

Algorithm evaluation metrics

Metric	Data source	What it characterizes
Mean and median queue length	`*_queue.csv`	Average buffer delay
p90 / p99 queue length	`*_queue.csv`	Tail delays
Fraction of time with empty queue	`*_queue.csv`	Link underutilization
Mean throughput	`*_throughput.csv`	Link utilization
Coefficient of variation (CV)	`*_throughput.csv`	Flow stability
Total drop count	`*_drops.csv`	Load on TCP congestion mechanism
Median inter-drop interval	`*_drops.csv`	Nature of control signals

3.1. Queue dynamics

Figure 1 shows the queue length dynamics for the three algorithms over the entire simulation time.

Two phases are clearly distinguishable on the plot.

Slow-start phase ($t = 0$–4 s). All TCP connections simultaneously enter slow-start and saturate the buffer within seconds. The queue for all algorithms reaches peak values: ARED—up to 100 packets, RED and Gentle RED—up to 84 packets. This burst is identical for all three, since the AQM algorithm has not yet accumulated sufficient statistics to react.

Steady-state regime ($t > 5$ s). After the initial burst dissipates, the algorithms diverge in behavior.

RED (blue curve) maintains the queue in the range of 5–26 packets with relatively regular oscillations. The curve rarely touches zero (empty queue only 13.4% of time): the forced drop at `m_qAvg >= maxTh` reacts quickly and keeps the queue "in check", but at the cost of constant pressure on TCP flows.

ARED (orange curve) demonstrates the largest oscillation amplitude and the most chaotic pattern. Periodically the queue grows to 30–35 packets in steady state and sharply collapses to zero. This is a consequence of maxP adaptation: the algorithm alternately "releases" and "tightens" the drop

```
// 9. Queue length sampling (every 100 ms)
void SampleQueue(Ptr<QueueDisc> qdisc, ofstream& out) {
    double t = Simulator::Now().GetSeconds();
    uint32_t qLen = qdisc->GetCurrentSize().GetValue();
    out << t << "," << qLen << "\n";
}
ScheduleEvery(Seconds(0.1), &SampleQueue, redQueue, queueFile);

// 10. Drop event tracing
void OnDrop(ofstream& out, Ptr<const QueueDiscItem> item) {
    out << Simulator::Now().GetSeconds() << "\n";
}
redQueue->TraceConnectWithoutContext("Drop",
    MakeBoundCallback(&OnDrop, dropFile));

// 11. Throughput sampling (every 100 ms)
void SampleThroughput(Ptr<PacketSink> sink, ofstream& out,
                      uint64_t& prevBytes) {
    uint64_t curr = sink->GetTotalRx();
    double tput = (curr - prevBytes) * 8.0 / 0.1; // bits/s
    out << Simulator::Now().GetSeconds() << "," << tput << "\n";
    prevBytes = curr;
}
ScheduleEvery(Seconds(0.1), &SampleThroughput, sink, tputFile,
              prevBytes);

// 12. Run simulation
Simulator::Stop(Seconds(60.0));
Simulator::Run();
Simulator::Destroy();
```

Listing 3: Trace callbacks for metric collection (pseudocode)

Table 6

Queue length statistics in steady-state regime

Algorithm	Mean (pkt)	Std. dev.	Median	p90	p99	Empty (%)
RED	7.74	7.45	6	18	26	13.4%
ARED	9.57	11.94	4	25	49	22.3%
Gentle	6.40	8.86	1	19	34	26.6%

probability, producing wide irregular cycles. p99 = 49 packets—the highest value among the three algorithms.

Gentle RED (green curve) returns to zero most frequently (26.6% of time the queue is empty, median = 1 packet). The smooth probabilistic function in the zone `[maxTh, 2*maxTh]` allows TCP flows to desynchronize their windows, leading to deeper but shorter queue “dips”.

Steady-state queue statistics are presented in Table 6.

The time distribution across EWMA average $\bar{q}$ operating zones is shown in Table 7.

RED spends 34.1% of time in the forced drop zone (`m_qAvg >= maxTh`), explaining its high average queue. ARED spends 19.7% of time in the $\bar{q} \geq 2 \cdot \max_{\text{Th}}$ zone where all packets are dropped—hence its

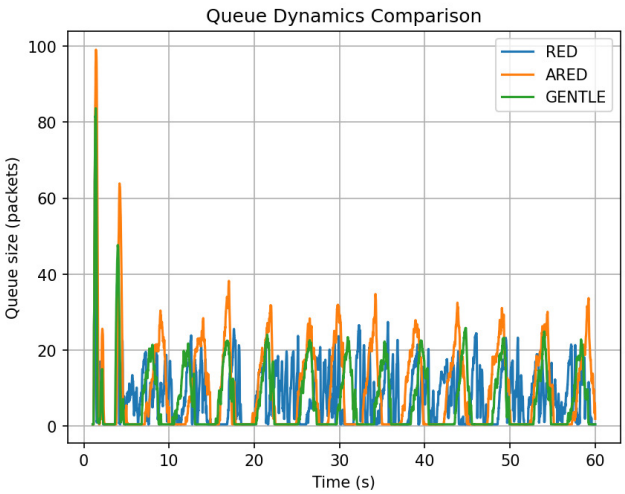


Figure 1. Queue length dynamics for RED, ARED, and Gentle RED

Table 7

Fraction of time in each queue management zone

Algorithm	$\bar{q} < \min_{\text{Th}}$	$[\min_{\text{Th}}, \max_{\text{Th}})$	$[\max_{\text{Th}}, 2\max_{\text{Th}})$	$\bar{q} \geq 2\max_{\text{Th}}$
RED	46.0%	19.8%	29.3%	4.8%
ARED	52.6%	8.0%	19.6%	19.7%
Gentle	60.8%	11.8%	19.8%	7.7%

anomalously high p99. Gentle RED most frequently stays below minTh (60.8%) and least frequently enters the hard drop zone (7.7%).

3.2. Throughput

The throughput plot (Figure 2) is constructed with moving average smoothing (window of 30 samples), thus displaying data starting from $t \approx 29$ s. The Y-axis is intentionally compressed to the range 1.74–1.86 Mbit/s, allowing examination of differences invisible on the full scale.

All three algorithms stably maintain throughput near 1.80–1.81 Mbit/s (~90% of the nominal 2 Mbit/s link capacity). This means that the choice of AQM algorithm at these parameters does not affect bandwidth utilization: all three mechanisms equally effectively "fill" the link.

The characteristic peak around $t = 33$ s (all curves reach ~1.86 Mbit/s) represents synchronous recovery of TCP flows after the initial wave of drops: congestion windows simultaneously begin growing, creating a short-term excess flow.

Despite identical means, RED demonstrates the lowest variability (CV = 18.7%) [23]: hard synchronous drops keep all TCP flows in step, making throughput predictable. Gentle RED has the highest CV (24.7%)—asynchronous window management creates more "ripple", although the mean does not suffer.

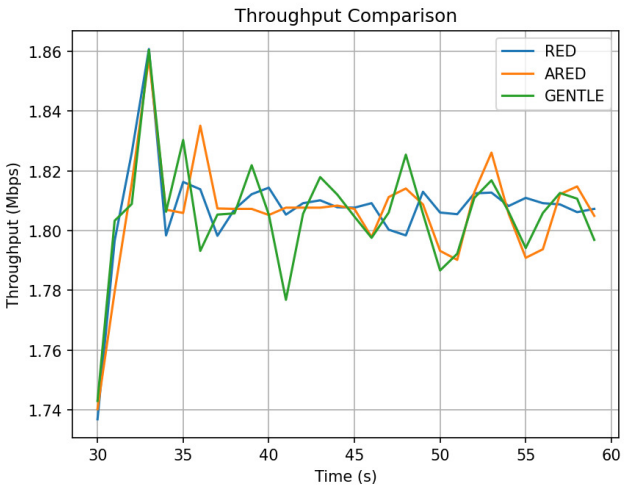


Figure 2. Throughput comparison: RED, ARED, and Gentle RED

Table 8

Throughput statistics (CV—coefficient of variation)

Algorithm	Mean (Mbit/s)	Std. dev.	Min.	Max.	CV
RED	1.8047	0.3380	0.533	3.621	18.7%
ARED	1.8039	0.3950	0.553	3.293	21.9%
Gentle	1.7998	0.4444	0.352	3.654	24.7%

3.3. Packet drops

The plot (Figure 3) presents drop moments as a scatter diagram: each point is one dropped packet. Three horizontal bands correspond to the three algorithms.

RED (bottom band, blue)—the densest and most continuous band: points fill virtually the entire simulation time, with only rare small gaps. RED actively drops in 47 out of 58 seconds with a median inter-drop interval of only 2.3 ms. The forced drop at `m_qAvg >= maxTh` creates a continuous stream of dropped packets each time the average queue exceeds the threshold.

ARED (middle band, orange)—clearly visible drop clusters separated by noticeable pauses. The algorithm is active in 33 out of 58 seconds. The maxP adaptation periodically reduces drop probability to zero, giving flows a "break". However, when drops occur, their density within a cluster is high (maximum burst—276 drops per second).

Gentle RED (top band, green)—the most pronounced cluster structure with the longest pauses between clusters. The algorithm is active in only 27 out of 58 seconds. Within each cluster, drops are dense (maximum burst—305/s), but between them—extended "quiet" intervals.

Drop statistics summary is presented in Table 9.

RED generates 19–21% more drops than the competitors. The median inter-drop interval for RED (2.3 ms) is 4–5 times smaller than for ARED and Gentle—RED practically continuously drops packets during congestion periods, while ARED and Gentle operate in "pulses".

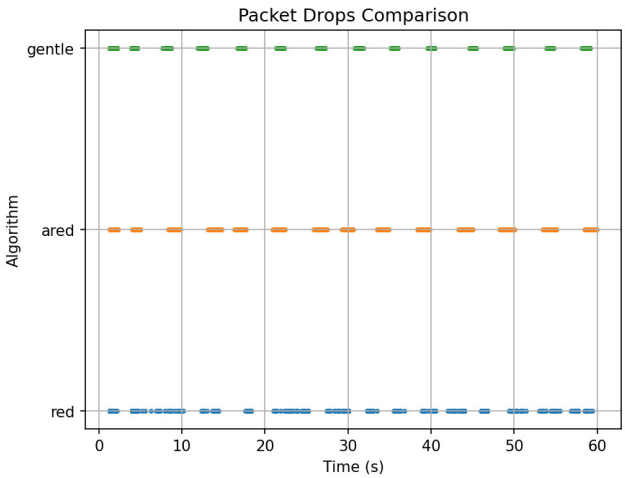


Figure 3. Packet drop moments for each algorithm

Table 9

Packet drop statistics

Algorithm	Total drops	Rate (drops/s)	Median interval	Active seconds	Max. burst
RED	1240	21.34	2.3 ms	47	321
ARED	1003	17.11	11.3 ms	33	276
Gentle	1026	17.75	9.1 ms	27	305

4. Discussion

The final comparison of algorithms across all key metrics is presented in Table 10.

RED provides the most predictable and stable throughput (CV = 18.7%) but achieves this at the cost of the highest number of drops (1240) and the highest average queue. The continuous nature of drops synchronizes TCP flows, creating rigid, “quantized” congestion management dynamics.

ARED minimizes the number of drops (1003, −19% vs. RED) and least frequently disturbs flows. However, maxP adaptation creates significant queue instability (std. = 11.94, p99 = 49 packets) with periods of excessive buffer growth—potentially undesirable from a delay perspective.

Gentle RED achieves the lowest average queue (6.40 packets) and the highest fraction of empty buffer (26.6%). The number of drops is comparable to ARED (1026), but they are distributed in the most compact pulses with long pauses between them. The cost is the highest throughput variability (CV = 24.7%) due to TCP flow desynchronization.

5. Conclusion

The conducted experiment showed that all three AQM algorithms—RED, ARED, and Gentle RED—provide practically the same average throughput (∼1.80 Mbit/s, ∼90% of link capacity), but fundamentally differ in the nature of buffer management and the load on the TCP congestion control mechanism.

Table 10

Summary comparison of RED, ARED, and Gentle RED algorithms

Metric	RED	ARED	Gentle RED
Mean throughput	1.8047 Mbit/s	1.8039 Mbit/s	1.7998 Mbit/s
Throughput CV	18.7%	21.9%	24.7%
Mean queue	7.74 pkt	9.57 pkt	6.40 pkt
Queue std. dev.	7.45	11.94	8.86
p99 queue	26 pkt	49 pkt	34 pkt
Empty queue (%)	13.4%	22.3%	26.6%
Total drops	1240	1003	1026
Drop pattern	continuous	clustered	pulsed
Median inter-drop interval	2.3 ms	11.3 ms	9.1 ms

The key difference lies in the trade-off between predictability and aggressiveness of queue management. RED acts most aggressively: forced drop upon exceeding $\max_{\text{Th}}$ keeps the queue "in check" (mean 7.74 packets) and ensures minimum throughput variability (CV = 18.7%), but at the cost of the highest number of drops (1240) and continuous pressure on TCP flows. ARED, conversely, sacrifices queue stability for reduced drops: maxP adaptation decreases drops by 19% compared to RED, but produces wide oscillations (std. = 11.94, p99 = 49 packets), unacceptable for delay-sensitive applications. Gentle RED occupies an intermediate position, achieving the lowest average queue (6.40 packets) due to a smoother drop function that desynchronizes TCP flows and reduces buffer occupancy—but increasing throughput variability (CV = 24.7%).

The obtained results confirm that AQM algorithm selection is determined by specific scenario requirements: there is no single "best" solution—each algorithm is optimal for its target metric.

Application recommendations:

- When minimum buffer delay is priority—Gentle RED (lowest average queue 6.40 pkt).
- When minimum drop count is priority—ARED (19% fewer drops than RED).
- When predictable throughput is priority—RED (lowest CV 18.7%).

6. Code availability

The simulation source code and analysis scripts are publicly available at: https://github.com/fibersel/dcm-paper.

Author Contributions: The author confirms sole responsibility for the following: study conception and design, implementation of the simulation model, data collection, analysis and interpretation of results, and manuscript preparation. All authors have read and agreed to the published version of the manuscript.

Funding: This research received no external funding.

Data Availability Statement: The simulation data and analysis scripts generated during this study are available at: https://github.com/fibersel/dcm-paper.

Conflicts of Interest: The authors declares no conflict of interest.

Declaration on Generative AI: During the preparation of this work, the authors used Claude (Anthropic) in order to: grammar and spelling check, text translation, and improve writing style. After using these tools, the authors reviewed and edited the content as needed and takes full responsibility for the publication's content.

References

[1] J. Gettys and K. Nichols, "Bufferbloat: Dark Buffers in the Internet," *Communications of the ACM*, vol. 55, no. 1, pp. 57–65, 2012. DOI: 10.1145/2063176.2063196

[2] K. Nichols, V. Jacobson, A. McGregor, and J. Iyengar, *Controlled Delay Active Queue Management*, RFC 8289, 2018.

[3] B. Braden, D. Clark, J. Crowcroft, et al., *Recommendations on Queue Management and Congestion Avoidance in the Internet*, RFC 2309, 1998.

[4] R. Adams, "Active Queue Management: A Survey," *IEEE Communications Surveys & Tutorials*, vol. 15, no. 3, pp. 1425–1476, 2013. DOI: 10.1109/SURV.2012.082212.00018

[5] A. V. Korolkova, D. S. Kulyabov, and T. I. Tchernyshev, "On the Classification of RED Algorithm Modifications," *Bulletin of Peoples' Friendship University of Russia. Series: Mathematics, Informatics, Physics*, vol. 26, no. 3, pp. 305–316, 2018.

[6] K. Nichols and V. Jacobson, "Controlling Queue Delay," *ACM Queue*, vol. 10, no. 5, pp. 20–34, 2012. DOI: 10.1145/2209249.2209264

[7] R. Pan, P. Natarajan, C. Piglione, M. S. Prabhu, V. Subber, F. Khan, and K. Athiappan, "PIE: A Lightweight Control Scheme to Address the Bufferbloat Problem," in *Proceedings of IEEE International Conference on High Performance Switching and Routing (HPSR)*, 2013, pp. 148–155. DOI: 10.1109/HPSR.2013.6602305

[8] S. Floyd and V. Jacobson, "Random Early Detection Gateways for Congestion Avoidance," *IEEE/ACM Transactions on Networking*, vol. 1, no. 4, pp. 397–413, 1993. DOI: 10.1109/90.251892

[9] V. Jacobson, "Congestion Avoidance and Control," *ACM SIGCOMM Computer Communication Review*, vol. 18, no. 4, pp. 314–329, 1988. DOI: 10.1145/52325.52356

[10] M. Christiansen, K. Jeffay, D. Ott, and F. D. Smith, "Tuning RED for Web Traffic," *IEEE/ACM Transactions on Networking*, vol. 9, no. 3, pp. 249–264, 2001. DOI: 10.1109/90.929849

[11] S. Floyd, R. Gummadi, and S. Shenker, "Adaptive RED: An Algorithm for Increasing the Robustness of RED's Active Queue Management," ICSI, Tech. Rep., 2001.

[12] S. Floyd. "Recommendation on using the "gentle" variant of RED. "[Online]. Available: https://www.icir.org/floyd/red/gentle.html

[13] K. K. Ramakrishnan, S. Floyd, and D. Black, *The Addition of Explicit Congestion Notification (ECN) to IP*, RFC 3168, 2001.

[14] A. V. Korolkova, *Mathematical Model of Traffic Transmission with Dynamic Flow Intensity Regulated by a RED-type Algorithm: PhD Thesis*. Moscow: RUDN University, 2010.

[15] T. R. Velieva, *Analysis of Self-Oscillation Modes in Continuous-Discrete Dynamical Models: PhD Thesis*. Moscow: RUDN University, 2019.

[16] W.-c. Feng, D. D. Kandlur, D. Saha, and K. G. Shin, "BLUE: A New Class of Active Queue Management Algorithms," University of Michigan, Tech. Rep. CSE-TR-387-99, 2002.

[17] T. J. Ott, T. V. Lakshman, and L. H. Wong, "SRED," in *Proceedings of IEEE INFOCOM*, vol. 3, 1999, pp. 1346–1355. DOI: 10.1109/INFCOM.1999.752153

[18] C. V. Hollot, V. Misra, D. Towsley, and W.-B. Gong, "On Designing Improved Controllers for AQM Routers Supporting TCP Flows," in *Proceedings of IEEE INFOCOM*, 2001, pp. 1726–1734. DOI: 10.1109/INFCOM.2001.916670

[19] V. Misra, W.-B. Gong, and D. Towsley, "Fluid-based Analysis of a Network of AQM Routers Supporting TCP Flows with an Application to RED," *ACM SIGCOMM Computer Communication Review*, vol. 30, no. 4, pp. 151–160, 2000. DOI: 10.1145/347059.347421

[20] T. ns-3 Project. "ns-3: A Discrete-Event Network Simulator." Version 3.41. [Online]. Available: https://www.nsnam.org/

[21] A. Varga and R. Hornig, "An Overview of the OMNeT++ Simulation Environment," in *Proceedings of the 1st International Conference on Simulation Tools and Techniques (SIMUTools)*, 2008, pp. 1–10. DOI: 10.4108/ICST.SIMUTOOLS2008.3027

[22] S. Ha, I. Rhee, and L. Xu, "CUBIC: A New TCP-Friendly High-Speed TCP Variant," in *ACM SIGOPS Operating Systems Review*, vol. 42, 2008, pp. 64–74. DOI: 10.1145/1400097.1400105

[23] R. Jain, "Throughput Fairness Index," *IEEE 802.11-98/S41*, 1999.

Information about the authors

Palagashvili, Abuli M.—PhD Student of Department of Department of Probability Theory and Cyber Security of RUDN University (e-mail: 1042250185@rudn.ru, ORCID: 0009-0007-7009-7038)

Ermolayeva, Anna M.—Assistent Professor of Department of Probability Theory and Cyber Security of RUDN University (e-mail: ermolaeva-am@rudn.ru, ORCID: 0000-0001-6107-6461)

Velieva, Tatyana R.—Candidate of Physical and Mathematical Sciences, Associate Professor of Department of Probability Theory and Cyber Security of RUDN University (e-mail: velieva-tr@rudn.ru, ORCID: 0000-0003-4466-8531)

RUSSIAN METADATA

УДК 004.729, 519.872
PACS 89.20.Ff, 02.60.Pn, 07.05.Tp
DOI: 10.22363/2658-4670-2026-34-3-379-395 EDN: RUDFRI

Сравнительный анализ алгоритмов активного управления очередями: RED, ARED, Gentle RED

А. М. Палагашвили, А. М. Ермолаева, Т. Р. Велиева

Российский университет дружбы народов, ул. Миклухо-Маклая, д. 6, Москва, 117198, Российская Федерация

Аннотация. *Предпосылки.* Алгоритмы активного управления очередями (AQM) семейства RED широко применяются в сетевом оборудовании, однако систематическое трёхстороннее сравнение RED, Adaptive RED (ARED) и Gentle RED в строго идентичных условиях недостаточно представлено в литературе. *Цель.* Целью данного исследования является количественное определение различий в динамике управления буфером, стабильности пропускной способности и характере сигналов перегрузки между тремя алгоритмами, а также формулировка практических рекомендаций по их выбору. *Метод.* Реализована модель сети с топологией «гантель» в среде дискретно-событийного симулятора ns-3 (версия 3.41) с десятью TCP-источниками, создающими устойчивую перегрузку узкого канала (2 Мбит/с). Все три алгоритма оценены с идентичными порогами очереди, профилем нагрузки и топологией в течение 60 секунд моделирования. Применён расширенный набор метрик, включающий зональное распределение EWMA-средней и временну́ю структуру сбросов. *Результаты.* Все алгоритмы обеспечили приблизительно 90% утилизации канала (средняя пропускная способность 1,80 Мбит/с). RED показал наиболее предсказуемую пропускную способность (коэффициент вариации 18,7%) ценой наибольшего числа сбросов (1240 пакетов). ARED минимизировал сбросы (1003 пакета, на 19% меньше RED), но породил наибольшие осцилляции очереди (p99 = 49 пакетов). Gentle RED достиг наименьшей средней длины очереди (6,40 пакета) при наибольшей вариабельности пропускной способности (коэффициент вариации 24,7%). *Выводы.* Универсально оптимального алгоритма не существует; выбор определяется приоритетами сценария: Gentle RED для минимальной задержки, ARED для минимальных потерь пакетов, RED для максимальной предсказуемости пропускной способности.

Ключевые слова: активное управление очередями, AQM, RED, Adaptive RED, Gentle RED, управление перегрузкой, ns-3, сетевое моделирование, bufferbloat

Discrete & Continuous Models & Applied Computational Science
ISSN 2658-7149 (Online), 2658-4670 (Print)

2026, 34 (3) 396–407
http://journals.rudn.ru/miph

Research article

UDC 51-72.530.145
PACS 07.05.Tp
DOI: 10.22363/2658-4670-2026-34-3-396-407 EDN: RFAXLG

On using Rosanes notation to specify quadratic transformations that describe a step of the Kahan difference scheme

Mikhail D. Malykh[1,2], Il'shat T. Dulatov[1], Anton L. Sevastianov[1], Ying Yu[3]

[1] *RUDN University, 6 Miklukho-Maklaya St, Moscow, 117198, Russian Federation*

[2] *Joint Institute for Nuclear Research, 6 Joliot-Curie St, Dubna, 141980, Russian Federation*

[3] *Kaili University, Kaiyuan Road 3, Kaili, 556011, China*

(received: July 10, 2026; revised: July 16, 2026; accepted: July 22, 2026)

Abstract. Kahan's method allows approximating a dynamical system with a quadratic right-hand side using a difference scheme whose step is described by a quadratic Cremona transformation. To study such transformations, it has been proposed to use the notation of Rosanes (1870), which provides a bridge between matrix theory, which is well developed, and the theory of quadratic Cremona transformations written in projective coordinates. In this approach, the eigenvalue problem for a matrix bundle becomes the problem of finding the fundamental points of the Cremona transformation and reduces the determination of these points to a standard algebraic problem. Applying this to standard examples of dynamical systems with a quadratic right-hand side revealed a surprising observation: a common feature of the Volterra–Lotka system and the $\wp$-oscillator is that in both cases, the fundamental points have coordinates in the field of fractions of the polynomial ring $\mathbb{Q}[\Delta t]$. Explicit formulas for the fundamental points in these examples are given. This property is not typical for dynamical systems with quadratic right-hand sides and is not related to the existence of algebraic integrals.

Key words and phrases: finite difference method, eigenvalue problem, Cremona transformations, birational map, eigenvalue problem

For citation: M. D. Malykh, I. T. Dulatov, A. L. Sevastianov, Y. Yu "On using Rosanes notation to specify quadratic transformations that describe a step of the Kahan difference scheme," *Discrete and Continuous Models and Applied Computational Science*, vol. 34, no. 3, pp. 396–407, 2026. DOI: 10.22363/2658-4670-2026-34-3-396-407. EDN: RFAXLG.

1. Introduction

Consider the xy-plane, two equations

$$f(x,y;\hat{x},\hat{y})=0, \quad g(x,y;\hat{x},\hat{y})=0, \tag{1}$$

connect two pairs of variables, (x,y) and $(\hat{x},\hat{y})$ and, in the non-degenerate case, define an algebraic correspondence on the plane: given a point (x,y) in this system, one can find several corresponding points $(\hat{x},\hat{y})$, and vice versa.

If Eqs. (1) are linear with respect to the variables $x,y,\hat{x},\hat{y}$, then the correspondence is called linear (affine). For example, the equations

$$x+y=\hat{x}+2\hat{y}+1, \quad x-y=3\hat{y}+4\hat{x}+1,$$

define a linear transformation, which is usually written by expressing $\hat{x}$ and $\hat{y}$ in terms of x and y.

If Eqs. (1) are linear in both x,y and $\hat{x},\hat{y}$, then the correspondence will still remain one-to-one, but will no longer be linear. Traditionally, this is called the quadratic Cremona transformation [1]. For example, the equations

$$x\hat{x}=1, \quad y\hat{y}+x=2$$

© 2026 M. D. Malykh, I. T. Dulatov, A. L. Sevastianov, Y. Yu

This work is licensed under a Creative Commons "Attribution-NonCommercial 4.0 International" license.

define a one-to-one transformation, in which the point (x, y) is associated with a point with coordinates

$$\hat{x} = \frac{1}{x}, \quad \hat{y} = \frac{2 - x}{y},$$

and the point $(\hat{x}, \hat{y})$ is associated with a point with coordinates

$$x = \frac{1}{\hat{x}}, \quad y = \frac{2\hat{x} - 1}{\hat{x}\hat{y}}.$$

Thus, a birational correspondence is obtained.

We encountered quadratic Cremona transformations while studying difference schemes for dynamical systems obtained using Kahan's method [2, 3]. In such schemes, each time step is described by a quadratic Cremona transformation. For example, the Riccati equation

$$\frac{dx}{dt} = a + bx + cx^2$$

can be approximated by the scheme

$$\hat{x} - x = \left(a + b\frac{x + \hat{x}}{2} + cx\hat{x}\right)\Delta t.$$

In this case, $\hat{x}$ is expressed fractional-linearly in terms of x and the scheme itself is symmetric under time reversal. The trick of replacing x^2 with $\hat{x}x$ was probably known in soliton theory as early as the mid-20th century, but the first publication on this scheme should be considered the report of 1993 by W. Kahan [4]. Independently of Kahan, the same technique was applied to the motion of a top by Hirota and Kimura in 1999 [5–7]; they were also the first to study the inheritance of integrals of motion by schemes of this kind. The inheritance of the energy integral in the case of a Hamiltonian system was proved in [8], and the study of integral curves in the case of a one-dimensional Hamiltonian system is presented in [9]. Following these publications, the name "Kahan's method" became established, and it was realized that the main advantage of Kahan's method is that it defines a birational mapping between the old and new positions of a dynamical system.

Obviously, there is no convenient notation for Cremona transformations. It is doubly surprising that matrix notation for quadratic Cremona transformations was proposed as early as the 1870s by J. Rosanes [10]. Unfortunately, this work went unnoticed. It is mentioned in thick reviews spanning half a century [11, 12], but no attention to Rosanes's notation is paid. It should be noted that matrix notation was just coming into use at that time, and Rosanes's presentation is not quite consistent. In particular, he fails to note the remarkable fact that fundamental points are eigenvectors of the matrix bundle describing the transformation. (Theorem 2 below). At that time, there were no matrix bundles, nor any notion of a generalized eigenvalue problem.

In this paper, we describe in detail the Rosanes notation and apply it to the study of Cremona transformations that define the steps of classical models of dynamical systems — the Volterra–Lotka system and the Hamiltonian system.

2. Quadratic Cremona transformation in Rosanes notation

In addition to the Cartesian coordinates of a point (x, y), we will use homogeneous coordinated $(u : v : w)$, setting

$$x = \frac{u}{w}, \quad y = \frac{v}{w}.$$

When multiplying matrices, we will consider homogeneous coordinates as a column $\mathfrak{u} = (u, v, w)^T$. Two matrices A and B of dimension 3×3 define a quadratic transformation

$$\hat{\mathfrak{u}}^T A\mathfrak{u} = 0, \quad \hat{\mathfrak{u}}^T B\mathfrak{u} = 0, \tag{2}$$

since these equations are linear in both $\mathfrak{u}$ and $\hat{\mathfrak{u}}$. It is only important that any value of $\mathfrak{u}$ corresponds to a unique value of $\hat{\mathfrak{u}}$, and vice versa.

For a given value $\mathfrak{u}$ to correspond to a unique point $\hat{\mathfrak{u}}$, it is necessary and sufficient that the equations of system (2) be linearly independent, i.e., that columns $A\mathfrak{u}$ and $B\mathfrak{u}$ differ by more than a multiplicative constant. In other words, a value $\mathfrak{u}$ corresponds to several points $\hat{\mathfrak{u}}$ if and only if there exist numbers μ, λ, one of which is nonzero, such that

$$\mu A\mathfrak{u} = \lambda B\mathfrak{u}. \tag{3}$$

For a given value $\hat{\mathfrak{u}}$ to correspond to a single point $\hat{\mathfrak{u}}$, it is necessary and sufficient that the columns $\hat{\mathfrak{u}}^T A\mathfrak{u}$ and $\hat{\mathfrak{u}}^T B$ differ by more than a multiplicative constant. In other words, the value $\hat{\mathfrak{u}}$ corresponds to several points $\mathfrak{u}$ if and only if there exist numbers μ, λ, one of which is nonzero, such that

$$\mu A^T\mathfrak{u} = \lambda B^T\mathfrak{u}. \tag{4}$$

From this, we can find both the conditions under which a pair of matrices defines a quadratic transformation and the conditions on the singular points of a quadratic transformation.

2.1. Conditions under which a pair of matrices defines a quadratic transformation

Condition (3) is satisfied for an arbitrary $\mathfrak{u}$ if and only if the matrices are proportional to each other, that is, $\mu A = \lambda B$. The same condition holds for (4) for arbitrary $\hat{\mathfrak{u}}$. This yields the first theorem.

Theorem 1. *If nonzero matrices A and B of dimension 3×3 differ by more than a multiplicative constant, then Eqs.* (2) *define a quadratic transformation.*

The linear space spanned by two nonzero matrices A and B, differing from each other by more than a multiplicative constant, has dimension 2. The elements of this space can be written as $\mu A - \lambda B$, where $\mu, \lambda \in k$. In operator theory, such a linear space is called a matrix bundle [13, 14]. If we take any basis A and B of the matrix bundle L, then the system (2) defines a quadratic transformation that does not change if we take another basis of this bundle.

Indeed, let A' and B' be another basis of the same matrix bundle L. Since A, B is a basis of the bundle L, the matrices A', B' are expressed linearly in terms of A, B, that is,

$$A' = \mu A - \lambda B, \quad B' = \mu' A - \lambda' B,$$

where $\mu, \ldots, \lambda'$ are constants. Therefore, the equations

$$\hat{\mathfrak{u}}^T A'\mathfrak{u} = 0, \quad \hat{\mathfrak{u}}^T B'\mathfrak{u} = 0 \tag{5}$$

follow from (2). Since A', B' is a basis of the bundle L, the matrices A, B are expressed linearly in terms of A', B' and therefore Eqs. (2) follow from (5). Thus, Eqs. (2) and (5) are equivalent to each other and therefore define the same transformation of the plane.

Theorem 1 can be reformulated as follows: there is a one-to-one correspondence between bundles of 3×3 matrices and quadratic transformations.

2.2. Fundamental points of the transformation

Let us now consider the conditions (3) and (4) as conditions that indicate singular points of the transformation, i.e., the points at which the uniqueness of the transformation is violated. These points have long been called fundamental points (*punti fondamentali*) [1, n. 15].

To formulate the corresponding theorem, it is necessary to bring the terminology used into line with that generally accepted in matrix theory. Let A, B be a basis of some matrix bundle. Condition (3) can be treated as a generalized eigenvalue problem for the bundle [13, 14]. Since we are interested in the case where at least one of the quantities μ, λ is nonzero, it is natural to pass from the pair of numbers (μ, λ) to the point $(\mu : \lambda)$ on the projective straight line. Such a point will be called an eigenvalue of the pair of matrices A, B if there exists a nontrivial column $\mathfrak{u}$ such that (3) for such μ, λ and $\mathfrak{u}$ becomes a true equality. The column itself will be called an eigencolumn or the vector corresponding to this eigenvalue.

Theorem 2. *Quadratic transformation* (2) *is not unique only at those points* $\mathbf{u}$ *that are eigenvectors of the eigenvalue problem* (3). *The quadratic transformation* (2) *is not uniquely invertible only at those points* $\hat{\mathbf{u}}$ *that are eigenvectors of the eigenvalue problem* (4)

Of course, the eigenvalues of the problems (3) and (4) coincide and are the zeros of the determinant

$$\det(\mu A - \lambda B) = 0. \tag{6}$$

This is an algebraic equation of degree 3 with respect to μ/λ, so it has, generally speaking, three complex roots. If the determinant of the matrix A is zero, then among them there is a root $(\mu : \lambda) = (1 : 0)$, which we interpret as infinitely large.

If the polynomial

$$\det(\mu A - \lambda B)$$

is factored over a field k, then one of the factors is linear. Therefore, in this case, there must be at least one fundamental point. However, we cannot rule out the case where the eigenvalue is multiple and the problem has associated vectors.

Example 1. Let A be a matrix containing a Jordan block:

$$A = \begin{pmatrix} 0 & 0 & 0 \\ 1 & 0 & 0 \\ 0 & 0 & 1 \end{pmatrix}, \quad B = \begin{pmatrix} 1 & 0 & 0 \\ 0 & 1 & 0 \\ 0 & 0 & 1 \end{pmatrix}.$$

In this case, the bundle has two eigenvectors and one associated vector. However, Eqs. (2) for this case have the form

$$\hat{v}u + \hat{w}w = 0, \quad \hat{u}u + \hat{v}v + \hat{w}w = 0$$

or in Cartesian coordinators

$$\hat{y}x + 1 = 0, \quad \hat{x}x + \hat{y}y + 1 = 0$$

and define a birational transformation of the plane.

However, in our study of the Kahan difference scheme, we did not encounter multiple eigenvalues.

3. The case when the characteristic equation factors into three different linear factors

Suppose that the left-hand side of Eq. (6) factorizes into three linear factors. Then there are three distinct eigenvalues, corresponding to three eigenvectors $\mathbf{u}_1, \mathbf{u}_2, \mathbf{u}_3$ of problem (3) and three distinct eigenvectors $\hat{\mathbf{u}}_1, \hat{\mathbf{u}}_2, \hat{\mathbf{u}}_3$ of problem (4). By Theorem 2, the uniqueness of the corresponding quadratic transformation is violated at exactly three distinct points in the xy-plane and three points in the $\hat{x}\hat{y}$-plane. These points are called the fundamental points of the quadratic transformation.

3.1. Fundamental lines

Let $\mathbf{u}_i$ be an eigenvector corresponding to the eigenvalue $(\mu_i : \lambda_i)$, then in the system of equations linear with respect to $\hat{\mathbf{u}}$

$$\hat{\mathbf{u}}^T A \mathbf{u}_i = 0, \quad \hat{\mathbf{u}}^T B \mathbf{u}_i = 0,$$

one of the equations is a consequence of the other. Therefore, the point $\mathbf{u}_i$ corresponds to a straight line given by the equation

$$\hat{\mathbf{u}}^T A \mathbf{u}_i = 0. \tag{7}$$

These straight lines are called fundamental straight lines of the quadratic transformation [1, n. 15]. In this case, we say that the fundamental point $\mathbf{u}_i$ is broken by a quadratic transformation and transformed into a fundamental straight line (7).

The fundamental straight line can be described using the well-known properties of eigenvector orthogonality. Indeed, for a pair of eigenvectors $\mathbf{u}_i$ and $\hat{\mathbf{u}}_j$ corresponding to different eigenvalues, we have

$$\mu_i A\mathbf{u}_i = \lambda_i B\mathbf{u}_i,$$

whence

$$\mu_i \hat{\mathbf{u}}_j^T A\mathbf{u}_i = \lambda_i \hat{\mathbf{u}}_j^T B\mathbf{u}_i.$$

In other words,

$$\hat{\mathbf{u}}_j^T A\mathbf{u}_i \,:\, \hat{\mathbf{u}}_j^T B\mathbf{u}_i = \lambda_i \,:\, \mu_i.$$

Similarly, from

$$\mu_j \hat{\mathbf{u}}_j^T A = \lambda_j \hat{\mathbf{u}}_j^T B$$

it follows that

$$\hat{\mathbf{u}}_j^T A\mathbf{u}_i \,:\, \hat{\mathbf{u}}_j^T B\mathbf{u}_i = \lambda_j \,:\, \mu_j.$$

These equalities are possible simultaneously only when

$$\hat{\mathbf{u}}_j^T A\mathbf{u}_i = \hat{\mathbf{u}}_j^T B\mathbf{u}_i = 0.$$

Therefore, on the fundamental straight line (7), generated by the point $\mathbf{u}_i$, the fundamental points $\hat{\mathbf{u}}_j$ and $\hat{\mathbf{u}}_k$ lie, which correspond to eigenvalues different from $(\mu_i : \lambda_i)$.

Let us now consider the mapping in the opposite direction: $\hat{\mathbf{u}} \to \mathbf{u}$. The points of the fundamental straight line $\hat{\mathbf{u}}^T A\mathbf{u}_3$, passing through the fundamental points $\hat{\mathbf{u}}_1$ and $\hat{\mathbf{u}}_2$, and different from the three fundamental points $\hat{\mathbf{u}}_1$, $\hat{\mathbf{u}}_2$, and $\hat{\mathbf{u}}_3$, are ordinary for the Cremona transformation under consideration and therefore map to a single well-defined point. We know this point: it is the fundamental point $\mathbf{u}_3$.

Theorem 3. *Let the equation* (6) *have three different roots*

$$(\mu_i : \lambda_i), \quad i = 1, 2, 3.$$

Then the quadratic transformation (2) *is uniquely defined at all points except three points in the* $\mathbf{u}$ *plane, the eigenvalues* $\mathbf{u}_1, \mathbf{u}_2, \mathbf{u}_3$ *of problem* (3)*, and three points in the* $\hat{\mathbf{u}}$ *plane, the eigenvalues* $\hat{\mathbf{u}}_1, \hat{\mathbf{u}}_2, \hat{\mathbf{u}}_3$ *of problem* (4)*. In this case, the quadratic transformation transforms the point* $\mathbf{u}_i$ *into a straight line passing through* $\hat{\mathbf{u}}_j$ *and* $\hat{\mathbf{u}}_k$ *(*$i \neq j$*,* $i \neq k$*).*

3.2. Natural coordinates

Note now that the eigenvectors $\mathbf{u}_1, \mathbf{u}_2, \mathbf{u}_3$ form a basis dual to the basis composed of the vectors $\hat{\mathbf{u}}_1, \hat{\mathbf{u}}_2, \hat{\mathbf{u}}_3$ [14]. Let

$$\mathbf{u} = \nu_1 \mathbf{u}_1 + \nu_2 \mathbf{u}_2 + \nu_3 \mathbf{u}_3,$$

and

$$\hat{\mathbf{u}} = \hat{\nu}_1 \hat{\mathbf{u}}_1 + \hat{\nu}_2 \hat{\mathbf{u}}_2 + \hat{\nu}_3 \hat{\mathbf{u}}_3.$$

Then, firstly,

$$\nu_i = \frac{\hat{\mathbf{u}}_i^T A\mathbf{u}}{\hat{\mathbf{u}}_i^T A\mathbf{u}_i},$$

and, secondly,

$$\hat{\mathbf{u}}^T A\mathbf{u} = \sum_{i,j} \hat{\nu}_i \nu_j \hat{\mathbf{u}}_i^T A\mathbf{u}_j = \sum_{i=1}^{3} \hat{\nu}_i \nu_i \hat{\mathbf{u}}_i^T A\mathbf{u}_i.$$

We set

$$a_i = \hat{\mathbf{u}}_i^T A\mathbf{u}_i, \quad b_i = \hat{\mathbf{u}}_i^T B\mathbf{u}_i,$$

then

$$\mu_i a_i = \lambda_i b_i$$

or

$$a_i : b_i = \lambda_i : \mu_i.$$

In this case, Eqs. (2) can be rewritten as

$$\begin{cases} \hat{v}_1 v_1 a_1 + \hat{v}_2 v_2 a_2 + \hat{v}_3 v_3 a_3 = 0, \\ \hat{v}_1 v_1 b_1 + \hat{v}_2 v_2 b_2 + \hat{v}_3 v_3 b_3 = 0. \end{cases}$$

The solution of this system with respect to $\mathfrak{v}$ is the vector product

$$\mathfrak{v} = \det \begin{pmatrix} i & j & k \\ a_1\hat{v}_1 & a_2\hat{v}_2 & a_3\hat{v}_3 \\ b_1\hat{v}_1 & b_2\hat{v}_2 & b_3\hat{v}_3 \end{pmatrix},$$

and with respect to $\hat{\mathfrak{v}}$ it is the vector product

$$\hat{\mathfrak{v}} = \det \begin{pmatrix} i & j & k \\ a_1 v_1 & a_2 v_2 & a_3 v_3 \\ b_1 v_1 & b_2 v_2 & b_3 v_3 \end{pmatrix}.$$

For example,

$$v_1 = (a_2 b_3 - a_3 b_2)\hat{v}_2\hat{v}_3.$$

Actually, it is now clear why the transformation is called quadratic. This notation for a quadratic transformation is used in [1, n. 17] as the definition of a quadratic transformation.

3.3. Network of straight lines

A network of straight lines in the xy-plane is defined by the equation

$$c_1 v_1 + c_2 v_2 + c_3 v_3 = 0,$$

where $(c_1 : c_2 : c_3)$ are arbitrary parameters. This network is transformed into a network of lines

$$\det \begin{pmatrix} c_1 & c_2 & c_3 \\ a_1\hat{v}_1 & a_2\hat{v}_2 & a_3\hat{v}_3 \\ b_1\hat{v}_1 & b_2\hat{v}_2 & b_3\hat{v}_3 \end{pmatrix} = 0.$$

This network is a network of second-order curves generated by three lines of the second order:

$$\hat{v}_1\hat{v}_2 = 0, \quad \hat{v}_1\hat{v}_3 = 0, \quad \hat{v}_2\hat{v}_3 = 0.$$

Each of these lines breaks up into a pair of fundamental straight lines. For example,

$$\hat{v}_1 = 0$$

can be written in old coordinates as

$$\hat{\mathfrak{u}}^T A \mathfrak{u}_1 = 0.$$

This is exactly the straight line that the fundamental point $\mathfrak{u}_1$ maps to. Now it is easy to see that each of these second-order lines passes through three fundamental points; therefore, the network is formed by of second-order curves passing through three fundamental points.

Initially, Cremona [15] described a quadratic transformation exactly as such a transformation of a plane that transforms a network of straight lines into a network of conic sections homologous to the original one.

3.4. Image of a line of arbitrary order

An arbitrary monomial of degree r with respect to the original Cartesian coordinates x, y transforms into a linear combination of monomials of the same degree with respect to ν_1, ν_2, ν_3, say,

$$\nu_1^{r_1}\nu_2^{r_2}\nu_3^{r_3}, \quad r_1 + r_2 + r_3 = r.$$

A quadratic transformation consists of replacing ν_1 with $\nu_2\nu_3$, and so on. Therefore, this monomial maps to

$$\hat{\nu}_1^{r_2+r_3}\hat{\nu}_2^{r_1+r_3}\hat{\nu}_3^{r_1+r_2}.$$

This monomial defines a line of order $2r$ consisting of fundamental straight lines. This line passes through fundamental points, e.g., through the point u_1, and has multiplicity $r_1 + r_3 + r_1 + r_2 = r + r_1$ there. Therefore, a line of order r maps to a line of order $2r$, which passes through fundamental points of multiplicity r or higher. In particular, the linear family of all lines of order r maps to a linear family of lines of order $2r$ passing through three fundamental points of order r.

Earlier authors derived this by considering infinitely close points [1, n. 17].

4. Kahan's method

Consider a dynamical system with a quadratic right-hand side.

$$\frac{dx}{dt} = f(x,y), \quad \frac{dy}{dt} = g(x,y).$$

We assume that

$$f(x,y) = f_{11}x^2 + 2f_{12}xy + f_{22}y^2 + 2f_{13}x + 2f_{23}y + f_{33},$$

denote the symmetric matrix (f_{ij}) as F, and adopt a similar relation for the quadratic function g. According to Kahan's method [2, 9], this system can be approximated by a difference scheme defining a birational transformation of the plane:

$$\begin{aligned} \hat{x} - x &= (f_{11}x\hat{x} + f_{12}(x\hat{y} + \hat{y}x) + f_{22}y\hat{y} + f_{13}(x + \hat{x}) + f_{23}(y + \hat{y}) + f_{33})\Delta t, \\ \hat{y} - y &= (g_{11}x\hat{x} + \dots)\Delta t. \end{aligned} \tag{8}$$

To write this transformation in Rosanes notation, we rewrite these relations in homogeneous coordinates

$$\begin{aligned} w\hat{u} - u\hat{w} &= (f_{11}u\hat{u} + f_{12}(u\hat{v} + \hat{v}u) + \dots + f_{33}w\hat{w})\Delta t, \\ w\hat{v} - v\hat{w} &= (g_{11}u\hat{u} + \dots)\Delta t. \end{aligned}$$

We introduce

$$E_1 = \begin{pmatrix} 0 & 0 & 1 \\ 0 & 0 & 0 \\ -1 & 0 & 0 \end{pmatrix}, \quad E_2 = \begin{pmatrix} 0 & 0 & 0 \\ 0 & 0 & 1 \\ 0 & -1 & 0 \end{pmatrix},$$

then in Rosanes's notation, the transformation (8) is defined by two matrices

$$A = E_1 + F\Delta t, \quad B = E_2 + G\Delta t.$$

We emphasize that F and G are symmetric matrices of the quadratic functions f and g in the generally accepted notation.

Like the original differential equations, the Kahan scheme has t-symmetry: when replacing

$$x \to \hat{x}, \quad y \to \hat{y}, \quad \Delta t \to -\Delta t$$

the scheme transforms into itself. Therefore, the inverse Cremona transformation can be calculated by replacing Δt with $-\Delta t$.

We consider two of the most well-known dynamical systems of dimension 2 with a quadratic right-hand side. For the calculations, we used the Sage system [16], and we collected the procedures used in the `rosanes` module, which we added to the FDM for Sage package [17].

4.1. Volterra–Lotka System

The Volterra–Lotka system is defined by the system of equations

$$\frac{dx}{dt} = (a - by)x, \quad \frac{dy}{dt} = (-c + dx)y.$$

The Kahan scheme for this system is given by two matrices

$$A = E_1 + \frac{\Delta t}{2}\begin{pmatrix} 0 & -b & a \\ -b & 0 & 0 \\ a & 0 & 0 \end{pmatrix}, \quad B = E_2 + \frac{\Delta t}{2}\begin{pmatrix} 0 & d & 0 \\ d & 0 & -c \\ 0 & -c & 0 \end{pmatrix}.$$

Since $\det A = \det B = 0$, there are two eigenvalues $(\mu : \lambda) = (0 : 1)$ and $(1 : 0)$. The third eigenvalue is calculated directly from (6); it is $(d : -b)$. Although all three eigenvalues are independent of Δt, the eigenvectors depend on the step.

Let us list the eigenvalues and eigenvectors.

1. The eigenvalue $(\mu : \lambda) = (1 : 0)$ corresponds to the fundamental points

$$\mathfrak{u}_1 = (0 : a\Delta t + 2 : b\Delta t), \quad \hat{\mathfrak{u}}_1 = (0 : a\Delta t - 2 : b\Delta t).$$

2. The eigenvalue $(\mu : \lambda) = (0 : 1)$ corresponds to the fundamental points

$$\mathfrak{u}_2 = (c\Delta t - 2 : 0 : d\Delta t), \quad \hat{\mathfrak{u}}_2 = (c\Delta t + 2 : 0 : d\Delta t).$$

3. The eigenvalue $(\mu : \lambda) = (d : -b)$ corresponds to the fundamental points

$$\mathfrak{u}_3 = (bc\Delta t + 2b : ad\Delta t - 2d : 0), \quad \hat{\mathfrak{u}}_3 = (bc\Delta t - 2b : ad\Delta t + 2d : 0).$$

When Δt is replaced by $-\Delta t$, the fundamental points corresponding to the same eigenvalue transform into each other:

$$\mathfrak{u}_i \to \hat{\mathfrak{u}}_i, \quad (i = 1, 2, 3).$$

It should also be noted that the points $\mathfrak{u}_3$ and $\hat{\mathfrak{u}}_3$ are at infinity for any Δt, while the remaining fundamental points go to infinity as $\Delta t \to 0$.

4.2. $\wp$-oscillator

Let us consider the $\wp$-oscillator, that is, a Hamiltonian system with Hamiltonian

$$h = dy^2 + ax^3 + bx^2 + cx.$$

As is known, this dynamical system is integrated exactly in Weierstrass elliptic functions [18], and Kahan's scheme imitates this property of the dynamical system [9, 19, 20]. A step of the Kahan scheme is described by a quadratic transformation with matrices

$$A = \begin{pmatrix} 0 & 0 & 1 \\ 0 & 0 & d\Delta t \\ -1 & d\Delta t & 0 \end{pmatrix}, \quad B = \begin{pmatrix} -3\,a\Delta t & 0 & -b\Delta t \\ 0 & 0 & 1 \\ -b\Delta t & -1 & -c\Delta t \end{pmatrix}.$$

The eigenvalue problem has three distinct roots.

1. The eigenvalue $(1 : d\Delta t)$ corresponds to the fundamental points

$$\mathfrak{u}_1 = (-2bd^2\Delta t^3 - 2d\Delta t : (b^2d^2 - 3acd^2)\Delta t^4 - 1 : 6ad^2\Delta t^3), \quad \hat{\mathfrak{u}}_1 = (0 : 1 : 0).$$

2. The eigenvalue $(1 : 0)$ corresponds to the fundamental points

$$\mathfrak{u}_2 = (d\Delta t : 1 : 0), \quad \hat{\mathfrak{u}}_2 = (-d\Delta t : 1 : 0).$$

3. The eigenvalue $(1 : -d\Delta t)$ corresponds to the fundamental points

$$\mathfrak{u}_3 = (0 : 1 : 0), \quad \hat{\mathfrak{u}}_3 = (-2bd^2\Delta t^3 - 2d\Delta t : (-b^2d^2 + 3acd^2)\Delta t^4 + 1 : 6ad^2\Delta t^3).$$

It is easy to calculate the determinants of the matrices whose rows are the coordinates of the fundamental points found. Some of these determinants are equal to zero, meaning that the corresponding triple of points lies on a straight line. In this way, we discovered that the triples of points

$$\mathfrak{u}_1, \hat{\mathfrak{u}}_3, \mathfrak{u}_3 = \hat{\mathfrak{u}}_1$$

and

$$\mathfrak{u}_2, \hat{\mathfrak{u}}_2, \mathfrak{u}_3 = \hat{\mathfrak{u}}_1$$

lie on a straight line.

When Δt is replaced by $-\Delta t$, the fundamental points corresponding to the same eigenvalue transform into each other, but the rule is more sophisticated than in the case of the Volterra–Lotka system:

$$\mathfrak{u}_1 \to \hat{\mathfrak{u}}_3, \quad \mathfrak{u}_3 = \hat{\mathfrak{u}}_1, \quad \mathfrak{u}_2 \to \hat{\mathfrak{u}}_2.$$

It should be noted that there are only 5 distinct fundamental points, 3 of which are at infinity, and the remaining two go to infinity as $\Delta t \to 0$.

The energy integral of the Hamiltonian system is inherited by the Kahan difference scheme: the points of approximate solutions on the xy phase plane are aligned along lines that are the level lines of the modified Hamiltonian $h_m(x, y, \Delta t)$, which is a rational function of degree 3 [8, 9]. Since under the Cremona transformation considered, the points of the approximate solution are mapped to points of the same solution, the isolines of the modified Hamiltonian are invariant curves of the Cremona transformation. Therefore, there is a linear pencil of cubic lines invariant under the considered Cremona transformation.

On the other hand, as noted above in Section 3.4, a line of the 3rd order under the action of a quadratic transformation transforms into a line of the order $6 - r_1 - r_2 - r_3$, where r_1, r_2, r_3 are the multiplicities with which this line passes through the fundamental points $\mathfrak{u}_1, \mathfrak{u}_2, \mathfrak{u}_3$. For a line of the 3rd order to transform into a line of the 3rd order, it is necessary that $r_1 + r_2 + r_3 = 3$. The simplest implementation of this equality is the assumption that the cubic line passes through these three points. Since the cubic line will also be invariant under the inverse Cremona transformation ($\hat{\mathfrak{x}} \to \mathfrak{x}$), an invariant cubic line must pass through all fundamental points of the Cremona transformation. In this case, there are five of these. In other words, the five fundamental points found are base points for the pencil of isolines of the modified Hamiltonian.

We verified this statement by direct calculation. In Refs. [8, 9], an explicit expression for the modified Hamiltonian is given: h_m is a rational function of x, y, whose numerator is a polynomial of degree 3:

$$3ax^3 - 3ad^2\Delta t^2xy^2 + (3acd\Delta t^2 - b^2d\Delta t^2 + 3b)x^2 + (3d - bd^2\Delta t^2)y^2 + (3c - bcd\Delta t^2)x - c^2d\Delta t^2,$$

and the denominator is a polynomial of degree 1:

$$9ad\Delta t^2x + 3bd\Delta t^2 + 3.$$

The isolines of the Hamiltonian are cubic lines that indeed pass through all 5 fundamental points found above.

4.3. System with a cubic Hamiltonian

It is easy to find an example of a Hamiltonian system for which the roots of the characteristic equation are not rational. For example, consider

$$h = y^3 - x^3.$$

Then two of the three roots of Eq. (6) will not be elements of the field of quotients of the ring $\mathbb{Q}[\Delta t]$.

5. Discussion and results

Rosanes' notation bridges the gap between well-developed matrix theory and the theory of quadratic Cremona transformations. The eigenvalue problem for a matrix bundle turns out to be a problem of finding the fundamental points of the Cremona transformation and provides a simple method for finding these points. Applying this approach to standard examples of dynamical systems with a quadratic right-hand side yields a surprising observation: the Volterra–Lotka system and the $\wp$-oscillator have in common that in both cases the fundamental points have coordinates in the field of quotients of the ring $\mathbb{Q}[\Delta t]$. This property is not typical for dynamical systems with a quadratic right-hand side and is not related, as one might think, to the existence of algebraic integrals. Nevertheless, the formulas for the fundamental points are very simple. It can be said that classical oscillators—the Volterra–Lotka system and the $\wp$-oscillator—are particularly simple from the point of view of Kahan's schemes.

Author Contributions: Conceptualization, M. Malykh; methodology, A. Sevastianov; software, I. Dulatov; validation, I. Dulatov and Yu Ying; writing—original draft preparation, I. Dulatov; writing—review and editing, A. Sevastianov; supervision, M. Malykh; project administration, A. Sevatianov. All authors have read and agreed to the published version of the manuscript.

Funding: This research received no external funding.

Data Availability Statement: Data sharing is not applicable.

Conflicts of Interest: The author declares no conflict of interest.

Declaration on Generative AI: The author has not employed any generative AI tools.

References

[1] F. Severi, *Lezioni di geometria algebrica*. Padova: Angelo Graghi, 1908.

[2] M. Malykh, M. Gambaryan, O. Kroytor, and A. Zorin, "Finite Difference Models of Dynamical Systems with Quadratic Right-Hand Side," *Mathematics*, vol. 12, no. 1, p. 167, 2024. DOI: 10.3390/math12010167

[3] M. Malykh, E. Ayryan, L. Lapshenkova, and L. Sevastianov, "Difference Schemes for Differential Equations with a Polynomial Right-Hand Side, Defining Birational Correspondences," *Mathematics*, vol. 12, no. 17, p. 2725, 2024. DOI: 10.3390/math12172725

[4] J. M. Sanz-Serna, "An unconventional symplectic integrator of W. Kahan," *Applied Numerical Mathematics*, vol. 16, pp. 245–250, 1994.

[5] R. Hirota and K. Kimura, "Discretization of the Lagrange Top," *Journal of the Physical Society of Japan*, vol. 69, no. 10, pp. 3193–3199, 2000.

[6] R. Hirota and K. Kimura, "Discretization of the Euler Top," *Journal of the Physical Society of Japan*, vol. 69, no. 3, pp. 627–630, 2000.

[7] M. Petrera and Y. B. Suris, "On the Hamiltonian structure of Hirota-Kimura discretization of the Euler top," *Math. Nachr.*, vol. 283, no. 11, pp. 1654–1663, 2010. DOI: 10.1002/mana.200711162

[8] E. Celledoni, R. I. McLachlan, B. Owren, and G. R. W. Quispel, "Geometric properties of Kahan's method," *J. Phys. A: Math. Theor.*, vol. 46, p. 025 201, 2013. DOI: 10.1088/1751-8113/46/2/025201

[9] M. Petrera, J. Smirin, and Y. B. Suris, "Geometry of the Kahan discretizations of planar quadratic Hamiltonian systems," *Proc. R. Soc. A*, vol. 475, p. 20 180 761, 2019. DOI: 10.1098/rspa.2018.0761

[10] J. Rosanes, "Ueber diejenigen rationalen Substitutionen, welche eine rationale Umkehrung zulassen," *Journal für die reine und angewandte Mathematik*, vol. 73, pp. 101–114, 1870.

[11] L. Godeaux, "Les transformations birationnelles du plan," in *Mémorial des sciences mathématiques*, vol. 122, 1953.

[12] K. A. Shramov, "Finite groups of automorphisms of algebraic and complex varieties," Doctor of Sciences dissertation, Steklov Mathematical Institute of Russian Academy of Sciences, Moscow, 2020.

[13] M. V. Keldysh, *Selected works. Mathematics*. Moscow: Nauka, 1985.

[14] I. C. Gohberg and M. G. Krein, *Introduction to the theory of linear nonselfadjoint operators in Hilbert space*. American Mathematical Soc., 1969.

[15] L. Cremona, *Opere matematiche di Luigi Cremona*. Milano: U. Hoepli, 1915, vol. 2.
[16] T. S. Developers, W. Stein, D. Joyner, D. Kohel, J. Cremona, and B. Eröcal, *SageMath, version 10.9*, 2026.
[17] A. Baddour, M. M. Gambaryan, L. Gonzalez, and M. D. Malykh, "On Implementation of Numerical Methods for Solving Ordinary Differential Equations in Computer Algebra Systems," *Programming and Computer Software*, vol. 49, no. 5, pp. 47–58, 2023. DOI: 10.31857/S013234742302005X
[18] Y. S. Sikorski, *Elements of theories of elliptic functions with applications to mechanics*. Moscow, Leningrad: ONTI, 1936.
[19] E. A. Airyan, M. M. Gambaryan, M. D. Malykh, and L. A. Sevastyanov, "On Trajectories of Dynamical Systems with Quadratic Right-Hand Side Computed by Reversible Difference Schemes," *Zap. Nauchn. Semin. POMI*, vol. 517, pp. 17–35, 2022.
[20] E. A. Airyan, M. M. Gambaryan, M. D. Malykh, and L. A. Sevastyanov, "Reversible Difference Schemes for Elliptic Oscillators," *Zap. Nauchn. Semin. POMI*, vol. 528, pp. 54–78, 2023.

Information about the authors

Malykh, Mikhail D.—DSc., Head of Department of Computational Mathematics and Artificial Intelligence of RUDN University; Senior Researcher of Joint Institute for Nuclear Research (e-mail: malykh-md@rudn.ru, ORCID: 0000-0001-6541-6603, ResearcherID: P-8123-20168, Scopus Author ID: 6602318510)

Dulatov, Il'shat T.—PhD Student of Department of Computational Mathematics and Artificial Intelligence of RUDN University (e-mail: dulatov-it@rudn.ru, ORCID: 0009-0009-2167-6177)

Sevastianov, Anton L.—Ph.D., Department of Computational Mathematics and Artificial Intelligence of RUDN University (e-mail: alsevastyanov@gmail.com, ORCID: 0000-0002-0280-485X)

Yu, Ying—Ph.D., Assistant Professor of Department of Mathematics and Applied Mathematics, Kaili University, China (e-mail: 45384377@qq.com, ORCID: 0000-0002-4105-2566)

RUSSIAN METADATA

УДК 51-72.530.145
PACS 07.05.Tp
DOI: 10.22363/2658-4670-2026-34-3-396-407 EDN: RFAXLG

Об использовании нотации Розанеса для описания квадратичных преобразований, описывающих шаг разностной схемы Кагана

М. Д. Малых[1, 2], И. Т. Дулатов[1], А. Л. Севастьянов[1], Ин Юй[3]

[1] *Российский университет дружбы народов, ул. Миклухо-Маклая, д. 6, Москва, 117198, Российская Федерация*

[2] *Объединённый институт ядерных исследований, ул. Жолио-Кюри, д. 6, Дубна, 141980, Российская Федерация*

[3] *Университет Кайли, 3, Кайюань Роуд, Кайли, 556011, Китай*

Аннотация. Метод Кагана позволяет аппроксимировать динамическую систему с квадратичной правой частью разностной схемой, шаг которой описывается квадратичным преобразованием Кремоны. Для исследования таких преобразований предложено использовать нотацию Розанеса (1870), которая перекидывает мостик между теорией матриц, которая хорошо разработана, и теорий квадратичных преобразований Кремоны, записанных в проективных координатах. При этом задача на собственные значения для матричного пучка оказывается задачей об отыскании фундаментальных точек преобразования Кремоны и сводит отыскание этих точек к стандартной алгебраической задаче. Применение этого приёма к стандартным примерам динамических систем с квадратичной правой частью позволило сделать неожиданное наблюдение: систему Вольтерры–Лотки и $\wp$-осциллятор объединяет то, что в обоих случаях фундаментальные точки имеют координаты в поле частных полиномиального кольца $\mathbb{Q}[\Delta t]$. Приведены явные формулы для фундаментальных точек в этих примерах. Это свойство не является типичным для динамических систем с квадратичной правой частью и не связано с существованием алгебраических интегралов.

Ключевые слова: метод конечных разностей, задача на собственные значения, преобразования Кремоны, бирациональные преобразования, задача на собственные значения

Discrete & Continuous Models
& Applied Computational Science
ISSN 2658-7149 (Online), 2658-4670 (Print)

2026, 34 (3) 408–429
http://journals.rudn.ru/miph

Research article

UDC 519.63, 536.2
PACS 44.10.+i, 07.05.Tp, 02.70.Bf
DOI: 10.22363/2658-4670-2026-34-3-408-429 EDN: QXTTKT

Heat-conduction simulation of a wing-like thulium foil for an ion source

Alexander S. Ayriyan[1,2], Edik A. Ayryan[1], Eugeny E. Donets[1], Milena P. Veneva[3]

[1] *Joint Institute for Nuclear Research, 6 Joliot-Curie St, Dubna, 141980, Russian Federation*

[2] *Alikhanyan National Science Laboratory (YerPhI), 2 Alikhanyan Brothrs St., Yerevan, 0036, Armenia*

[3] *RIKEN Center for Computational Science, 7-1-26 Minatojima-minami-machi, Chuo-ku, Kobe, Hyogo 650-0047, Japan*

(received: July 28, 2026; revised: August 10, 2026; accepted: August 12, 2026)

Abstract. *Background.* Metal foils heated by an electric current are commonly used as evaporation elements in ion sources. Because the evaporation rate is highly sensitive to temperature, predicting the temperature distribution accurately and efficiently is essential for choosing the foil geometry and operating conditions. *Purpose.* This study develops a two-dimensional electric-thermal model of a wing-shaped thulium foil and evaluates numerical strategies for repeated simulations. *Methods.* Owing to symmetry, only one quarter of the foil is included in the computational domain. The current paths are determined by solving a Laplace problem with constant electrical conductivity. The resulting field is then scaled to the prescribed total current and used to calculate the spatially varying Joule heat source. The transient heat equation accounts for the temperature dependence of density, heat capacity, thermal conductivity, and electrical resistivity, as well as radiative and evaporative heat losses from both faces of the foil. The equation is discretized on a masked Cartesian grid and integrated using an alternating-direction implicit scheme, with Picard iterations applied at each half-step. *Results.* At a current of 2.5 A and a contact temperature of 78 K, the stationary maximum temperature is 829.803 K. All tested tridiagonal solvers produce the same converged temperature field. The fastest partition solver, combined with a CUDA task graph, completes the simulation in 36.3 s, giving a 24.1-fold speedup over the serial central-processing-unit implementation. *Conclusions.* The model accounts for nonuniform electric heating and nonlinear heat losses in the foil. Its graphics-processing-unit implementation is sufficiently efficient for repeated optimization of the foil geometry and operating current.

Key words and phrases: nonlinear heat conduction, Joule heating, alternating-direction implicit method, tridiagonal solver, partition methods, CUDA

For citation: A. S. Ayriyan, E. A. Ayryan, E. E. Donets, M. P. Veneva "Heat-conduction simulation of a wing-like thulium foil for an ion source," *Discrete and Continuous Models and Applied Computational Science*, vol. 34, no. 3, pp. 408–429, 2026. DOI: 10.22363/2658-4670-2026-34-3-408-429. EDN: QXTTKT.

1. Introduction

Current-heated metallic foils are commonly used as evaporation elements in ion sources [1]. Their operating temperature is set by the competition between Joule heating, conduction to the cooled contacts, radiation, and evaporation. Because the evaporation rate is strongly temperature dependent, even a moderate error in the predicted temperature field can lead to a large error in the estimated material flux.

We consider a thulium foil with rectangular side wings. The wings enlarge the heated area but also disturb the current paths, particularly at the abrupt changes in width. The resulting problem is nonlinear: density, heat capacity, thermal conductivity, and electrical resistivity all vary with temperature, while radiation and evaporation introduce additional temperature-dependent losses.

An earlier formulation ranked candidate geometries by the area lying within a specified temperature interval [2]. For an evaporation source, the surface flux is a more direct performance measure. We therefore compute the stationary temperature field and evaluate the local evaporation rate from a vapor-pressure correlation and the Hertz–Knudsen formula [3–5].

© 2026 A. S. Ayriyan, E. A. Ayryan, E. E. Donets, M. P. Veneva

This work is licensed under a Creative Commons "Attribution-NonCommercial 4.0 International" license.

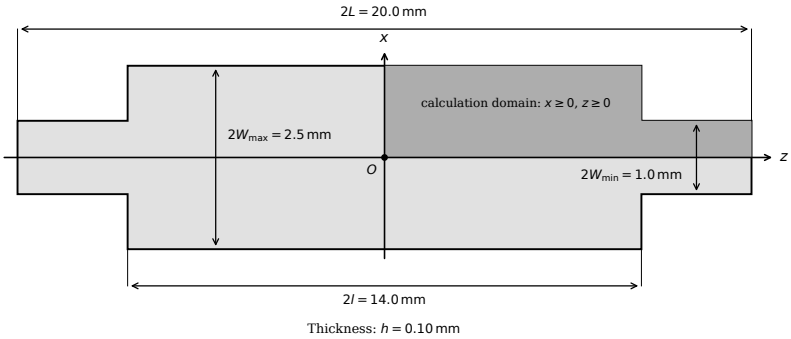


Figure 1. Geometry of the wing-shaped thulium foil in the (x, z) plane. The plate is symmetric about both the x- and z-axes: the wide central region of full width $2W_{\max} = 2.5$ mm and length $2l = 14.0$ mm narrows to the terminal contacts of width $2W_{\min} = 1.0$ mm, giving a total length $2L = 20.0$ mm and a uniform thickness $h = 0.10$ mm. Due to the symmetry, the computations are restricted to one quarter of the plate ($x \geq 0$, $z \geq 0$; shaded region) only, with the origin O at the centre

The optimization itself requires many solutions for different wing lengths and currents. This paper addresses the direct problem that underlies those repeated evaluations. We discretize one quarter of the symmetric foil on a masked Cartesian grid and use an alternating-direction implicit (ADI) scheme. Each half-step produces independent tridiagonal systems along rows or columns, which we solve in batches on a CUDA-capable GPU. The calculation returns the stationary field, the maximum foil temperature, and the total evaporation flux; these quantities will serve as the objective and constraint data in the subsequent optimization.

2. Mathematical model and direct heat-conduction problem

The model couples electric conduction to transient heat conduction in a thin thulium foil of prescribed geometry. Radiation and evaporation enter the thermal balance as losses from the two broad faces of the foil.

2.1. Rectangular wing-shaped foil

We use the one-parameter foil geometry introduced in Ref. [2]. The foil has total length $2L$ and minimum width $2W_{\min}$. Two symmetric rectangular wings increase the width to $2W_{\max}$ over a half-length l, with $0 \leq l \leq L$. The limits $l = 0$ and $l = L$ give uniform rectangles of widths $2W_{\min}$ and $2W_{\max}$, respectively.

The local half-width of the foil is defined as

$$W_l(z) = \begin{cases} W_{\max}, & |z| \leq l, \\ W_{\min}, & l < |z| \leq L \end{cases}.$$

The corresponding two-dimensional domain is

$$\Omega_l = \{(x, z) : -L \leq z \leq L, \quad -W_l(z) \leq x \leq W_l(z)\}.$$

All four geometrical parameters are fixed for a single direct calculation (see Figure 1).

2.2. Heat-conduction problem

For a prescribed shape $W_l(z)$ and current I, the temperature satisfies

$$\rho_m(T)c_p(T)\frac{\partial T}{\partial t} = \nabla \cdot (\lambda(T)\nabla T) + \rho_e(T)|\mathbf{j}(x, z; I, l)|^2 - Q_{\text{loss}}(T). \tag{1}$$

Here ρ_m, c_p, λ, and ρ_e denote the mass density, specific heat capacity, thermal conductivity, and electrical resistivity of thulium, and $\mathbf{j}$ is the in-plane current-density field.

The foil thickness h is small relative to its in-plane dimensions, so the temperature is taken to be uniform through the thickness. We nevertheless retain both in-plane coordinates. A one-dimensional approximation, $j(z) = I/[2hW_l(z)]$, cannot resolve current crowding at the steps in foil width; the current field is therefore obtained from a separate two-dimensional potential problem.

2.3. Electric-current distribution

The current distribution is computed once for each geometry, before thermal integration begins. This auxiliary problem uses constant conductivity because only the geometry of the current paths is required. The normalized potential $\phi(x, z)$ satisfies

$$\nabla \cdot (\sigma_0 \nabla \phi) = 0, \quad \sigma_0 = 1,$$

on the same quarter-domain mask as the heat problem.

Because the equation is homogeneous, σ_0 does not affect the potential shape. Setting $\sigma_0 = 1$ simply fixes an auxiliary normalization; the field is later rescaled to I in Eq. (2). Temperature dependence enters only through $\rho_e(T)$ in the Joule source.

In the quarter-domain calculation, $z = 0$ is the mid-plane of the full foil and is assigned $\phi = 0.5$; the right terminal at $z = L$ is assigned $\phi = 0$ for $x \le W_{\min}$.

All remaining free boundaries are insulating. This boundary-value problem can be effectively solved by using the over-relaxation method [6, 7]. Numerically, fluxes through faces without an active neighboring node are omitted.

The unscaled current-density field is

$$\mathbf{j}_0 = -\sigma_0 \nabla \phi.$$

The total current carried by the computed quarter-domain field through the terminal section is evaluated as

$$I_0^{(1/4)} = h \int_0^{W_{\min}} |(\mathbf{j}_0)_z(x, L)|\, dx.$$

The physical field used in the Joule source is then obtained by scaling $\mathbf{j}_0$ to the prescribed total current I:

$$\mathbf{j}(x, z; I, l) = \frac{I/2}{I_0^{(1/4)}}\, \mathbf{j}_0(x, z). \tag{2}$$

The Joule source is then

$$q_J(x, z, T) = \rho_e(T) |\mathbf{j}(x, z; I, l)|^2.$$

The loss term combines radiation with the energy carried by evaporated atoms. Surface fluxes from the two broad faces are converted to a volumetric rate by dividing by the foil thickness:

$$Q_{\text{loss}}(T) = \frac{2}{h} \left[\varphi_{\text{rad}}(T) + \varphi_{\text{evap}}(T) \right].$$

The radiative heat flux from one surface [8] is written as

$$\varphi_{\text{rad}}(T) = \varepsilon \sigma_{\text{SB}} \left(T^4 - T_{\text{env}}^4 \right),$$

where ε is the effective hemispherical emissivity, σ_{SB} is the Stefan–Boltzmann constant, and T_{env} is the effective radiation temperature of the chamber.

The heat flux carried away by evaporation from one surface is estimated as

$$\varphi_{\text{evap}}(T) = \Gamma(T) \frac{\Delta H_{\text{sub}}}{N_A}.$$

Here $\Gamma(T)$ is the evaporation flux, ΔH_{sub} is the molar enthalpy of sublimation, and N_A is Avogadro's constant. We use a constant reference value for ΔH_{sub}.

Table 1
Saturated vapor pressure and estimated evaporation flux of metallic thulium. The flux was calculated using the Hertz–Knudsen relation with the evaporation coefficient taken equal to unity. The vapor-pressure relation is recommended for 298 K to 1400 K; values below 298 K are shown only as a formal extrapolation.

T (K)	P_{sat} (Pa)	Γ (atom cm^{-2} s^{-1})
100	1.88×10^{-111}	3.82×10^{-93}
200	2.17×10^{-50}	3.12×10^{-32}
298	2.22×10^{-30}	2.61×10^{-12}
300	4.16×10^{-30}	4.87×10^{-12}
400	5.30×10^{-20}	5.37×10^{-2}
500	5.84×10^{-14}	5.30×10^{4}
600	6.04×10^{-10}	5.00×10^{8}
678	1.21×10^{-7}	9.42×10^{10}
700	4.35×10^{-7}	3.33×10^{11}
778	2.25×10^{-5}	1.63×10^{13}
800	5.94×10^{-5}	4.26×10^{13}
900	2.69×10^{-3}	1.82×10^{15}
1000	5.61×10^{-2}	3.59×10^{16}

At steady state, Eq. (1) reduces to

$$\nabla \cdot (\lambda(T)\nabla T) + \rho_e(T)|\mathbf{j}(x, z; I, l)|^2 - Q_{\mathrm{loss}}(T) = 0.$$

The in-plane free boundaries are thermally insulated. Radiation and evaporation act through Q_{loss}, not through those edge conditions.

2.4. Evaporation flux from the temperature field

Once the stationary temperature is known, the thulium flux follows directly from the local surface temperature.

For solid thulium, the saturated vapor pressure is estimated using the CRC vapor-pressure relation [9]

$$\log_{10}\left(\frac{P_{\mathrm{sat}}}{\mathrm{Pa}}\right) = 13.888 - \frac{12270}{T} - 0.9564 \log_{10} T, \qquad 298\ \mathrm{K} \le T \le 1400\ \mathrm{K}. \tag{3}$$

We calculate the equilibrium flux from the Hertz–Knudsen relation

$$\Gamma(T) = \frac{P_{\mathrm{sat}}(T)}{\sqrt{2\pi m_{\mathrm{Tm}} k_B T}},$$

where k_B is Boltzmann's constant and $m_{\mathrm{Tm}} = 168.934\,21$ u is the atomic mass of thulium. We set the evaporation coefficient to unity, so $\Gamma(T)$ is an equilibrium upper estimate.

Table 1 shows the strong temperature dependence. Values below 298 K are formal extrapolations of Eq. (3).

For a prescribed wing length l and electric current I, the total evaporation flux from one large surface of the foil is defined as

$$\Phi(l; I) = \int_{\Omega_l} \Gamma\left(T_{l,I}(x, z)\right)\, dx\, dz.$$

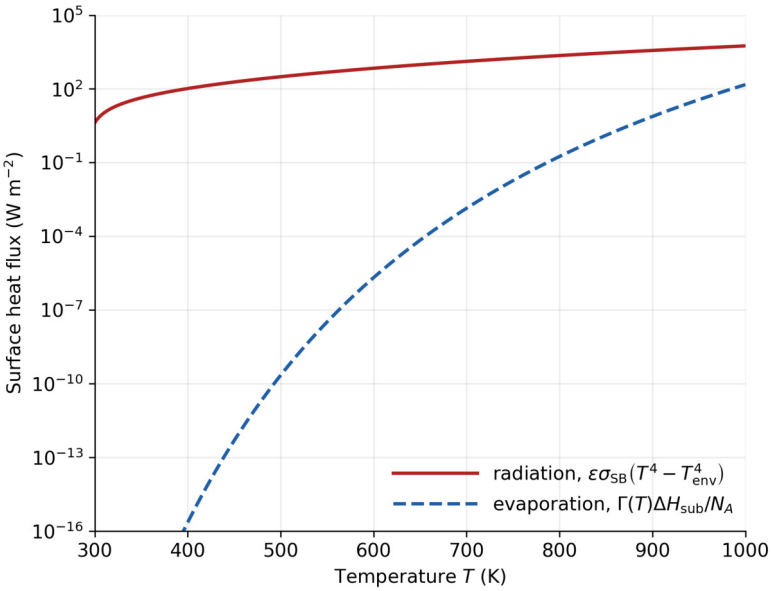


Figure 2. Radiative and evaporative surface heat fluxes of the thulium foil versus temperature. Solid line: radiation, $\varphi_{rad} = \varepsilon\sigma_{SB}(T^4 - T_{env}^4)$ with $\varepsilon = 0.10$; dashed line: evaporation, $\varphi_{evap} = \Gamma(T)\,\Delta H_{sub}/N_A$, with $\Gamma(T)$ from the Hertz–Knudsen relation. Below 1000 K radiation exceeds evaporation by more than three orders of magnitude and dominates the surface energy balance

This definition refers to one face of the foil.

Since the numerical calculation is performed only in one quarter of the domain, the full one-side evaporation flux is reconstructed as

$$\Phi(l;I) = 4\int_{\Omega_l^{(1/4)}} \Gamma\left(T_{l,I}(x,z)\right)\,dx\,dz. \tag{4}$$

The total from both faces is 2Φ.

The number of atoms that ultimately reach the ionization region will be lower than this equilibrium estimate. It also depends on source geometry, transport conductance, background pressure, and deposition on surrounding surfaces.

2.5. Relative importance of radiation and evaporation

Figure 2 compares the two surface-loss channels. Below 1000 K the radiative flux $\varphi_{rad} = \varepsilon\sigma_{SB}(T^4 - T_{env}^4)$ exceeds the evaporative flux $\varphi_{evap} = \Gamma(T)\,\Delta H_{sub}/N_A$ by at least three orders of magnitude and is therefore the principal loss term. The approximate balance $q_J \simeq \varepsilon\sigma_{SB}T^4$ gives $T_{max} \propto \varepsilon^{-1/4}$. In the numerical model, T_{max} changes from 985 K at $\varepsilon = 0.05$ to 700 K at $\varepsilon = 0.20$, compared with 830 K at the baseline value $\varepsilon = 0.10$. This relatively weak fourth-root dependence supports the use of a single effective emissivity.

Although evaporation contributes little to cooling below 1000 K, we retain it because $\Gamma(T)$ is the quantity needed in the subsequent optimization over wing length and operating current. In the regime studied here it uses for diagnostic rather than for cooling.

2.6. Direct problem

For each prescribed pair (l, I), we compute the transient field $T(x, z, t)$ and its stationary limit $T_{l,I}(x, z)$.

The prescribed wing length is aligned with the computational grid:

$$l = k_l \Delta z, \quad k_l = 0, 1, \dots, N_z,$$

so that the wing edge coincides with a grid line. The current remains fixed during each run.

For the computed stationary temperature field, the following output quantities are evaluated:

$$T_{\max}(l, I) = \max_{(x,z)\in\Omega_l} T_{l,I}(x, z),$$

and the total evaporation rate of the surface (4). Optimization over l and selection of a current subject to a maximum- temperature constraint are left to an outer procedure and are not considered here.

3. Thermophysical coefficients used in the numerical calculations

The model requires $\rho_m(T)$, $\lambda(T)$, $c_p(T)$, and $\rho_e(T)$ over the operating range of the foil. Earlier calculations used room-temperature constants [2]; here we construct temperature-dependent functions from experimental and reference data over approximately 60 K to 800 K.

3.1. Mass density

We reconstructed the density from the linear-expansion data in the TPRC compilation [10], which for thulium draws on the measurements of Singh, Khanduri and Tiang between 90 K and 300 K [11].

Taking

$$\rho_m(293\,\mathrm{K}) = 9.33\,\mathrm{g\,cm^{-3}},$$

as the reference density, the density at temperature T was calculated as

$$\rho_m(T) = \frac{\rho_m(293\,\mathrm{K})}{\left[1 + \Delta L(T)/L_0\right]^3},$$

where $\Delta L(T)/L_0$ is measured relative to room temperature. We assume isotropic expansion, as no crystallographic texture is specified for the polycrystalline foil. The resulting correction is small but is retained in the calculations (Table 2).

Table 2

Mass density of metallic thulium reconstructed from thermal expansion data [10, 11].

T (K)	$\Delta L/L_0$ (%)	ρ_m (g cm^{-3})
60	−0.163	9.376
78	−0.153	9.373
100	−0.140	9.369
200	−0.083	9.353
293	0.000	9.330
400	0.142	9.290
500	0.266	9.256
600	0.386	9.223
700	0.505	9.190
778	0.599	9.164
800	0.625	9.157

3.2. Thermal conductivity

Single-crystal thulium is anisotropic because of its hexagonal close-packed structure. Ho, Powell and Liley report recommended conductivities parallel and perpendicular to the c axis, together with a polycrystalline value [12]. We use the latter for the foil.

The source values, originally in $\mathrm{W\,cm^{-1}\,K^{-1}}$, were converted using $1\,\mathrm{W\,cm^{-1}\,K^{-1}} = 100\,\mathrm{W\,m^{-1}\,K^{-1}}$. No additional Voigt–Reuss–Hill averaging was applied.

Because the recommended data end near room temperature, the code uses the following smooth continuation rather than a piecewise-constant extension:

$$\lambda(T) = \lambda_0 + A\frac{T_{\mathrm{eff}}^{p}}{\rho_e(T_{\mathrm{eff}})}, \tag{5}$$

where

$$\lambda_0 = -0.821\,188\,775\,\mathrm{W\,m^{-1}\,K^{-1}}, \qquad A = 1.07573654\times10^{-7}, \qquad p = 0.829022226.$$

The effective temperature is limited by

$$T_{\mathrm{eff}} = \min(T, T_{\lambda}^{\max}), \qquad T_{\lambda}^{\max} = \frac{p\rho_0}{b(1-p)},$$

where ρ_0 and b are defined in the resistivity model below. The cap prevents an unphysical decrease beyond the maximum of the fitted curve. This continuation is a modelling assumption introduced to keep the nonlinear coefficient smooth.

3.3. Specific heat capacity

Below 360 K, the heat capacity is taken from the measurements of Jennings, Hill and Spedding [13], which cover 15 K to 360 K.

The original data are given as molar heat capacity $C_{p,m}(T)$ in $\mathrm{J\,mol^{-1}\,K^{-1}}$. They were converted to mass specific heat by

$$c_p(T) = \frac{C_{p,m}(T)}{M_{\mathrm{Tm}}}, \qquad M_{\mathrm{Tm}} = 168.94\,\mathrm{g\,mol^{-1}}.$$

The difference between c_p and c_V is small relative to other model uncertainties, so Eq. (1) uses $c_p(T)$.

Above 360 K, we extend the table using the trend reported in the TPRC compilation [14]. This continuation is less direct than the low-temperature measurements and is used only to cover the foil's operating range. A constant value $c_p = 160\,\mathrm{J\,kg^{-1}\,K^{-1}}$ is retained for comparisons with the earlier constant-coefficient model.

3.4. Electrical resistivity

Electrical resistivity directly controls the Joule source:

$$q_J(x,z,T) = \rho_e(T)|\mathbf{j}(x,z;I,l)|^2.$$

For 60 K to 300 K we use the polycrystalline measurements of Colvin, Legvold and Spedding [15]; these data are more appropriate for a foil of unspecified texture than single-crystal values.

Above 300 K, we extrapolate from the approximately linear trend in the single-crystal measurements of Edwards and Legvold [16], which provide $\rho_a(T)$, $\rho_b(T)$, and $\rho_c(T)$ up to room temperature.

The single-crystal data distinguish the basal-plane and c-axis directions. To obtain a scalar polycrystalline estimate, the conductivity was averaged as

$$\sigma_i(T) = \frac{1}{\rho_i(T)},$$

Table 3
Recommended thermal conductivity of metallic thulium from Ho, Powell and Liley [12]. Original values are given in W cm^{-1} K^{-1} and converted here to W m^{-1} K^{-1}. The column k_{poly} was used in the numerical calculations.

T (K)	$k_{\parallel c}$ (W m^{-1} K^{-1})	$k_{\perp c}$ (W m^{-1} K^{-1})	k_{poly} (W m^{-1} K^{-1})
50	14.2	9.18	10.2
58	17.0	10.4	11.0
60	17.9	10.4	11.2
70	21.4	10.9	11.8
80	25.4	10.7	12.7
90	24.8	10.5	13.1
100	24.6	11.1	13.5
123.2	24.4	11.7	14.4
150	24.3	12.6	15.3
173.2	24.8	13.0	15.8
200	23.2	13.4	16.2
223.2	22.1	13.8	16.4
250	20.2	13.9	16.7
273.2	16.8	14.0	16.8
298.2	13.8	14.0	16.9
300	12.3	14.1	16.9
400	—	—	16.9
500	—	—	16.9
600	—	—	16.9
700	—	—	16.9
778	—	—	16.9
800	—	—	16.9

$$\sigma_{\mathrm{eff}}(T) = \frac{2\sigma_{a/b}(T) + \sigma_c(T)}{3},$$

and then inverted:

$$\rho_{\mathrm{eff}}(T) = \frac{1}{\sigma_{\mathrm{eff}}(T)}.$$

The values appear in Table 5; the code represents them by the smooth linear fit

$$\rho_e(T) = \rho_0 + bT,$$

with

$$\rho_0 = 1.662\,774\,21 \times 10^{-7}\,\Omega\,\mathrm{m}, \qquad b = 1.730\,384\,89 \times 10^{-9}\,\Omega\,\mathrm{m\,K^{-1}}.$$

The same differentiable fit is used in the Joule source and in Eq. (5).

Table 4
Specific heat capacity of metallic thulium used in the numerical calculations. Values below 360 K are based on the measurements of Jennings, Hill and Spedding [13]; the high-temperature continuation is based on reference data [14].

T (K)	$C_{p,m}$ (J mol^{-1} K^{-1})	c_p (J g^{-1} K^{-1})	c_p (J kg^{-1} K^{-1})
60	24.22	0.143	143
70	24.51	0.145	145
75	24.67	0.146	146
78	24.77	0.147	147
80	24.83	0.147	147
90	25.12	0.149	149
100	25.25	0.150	150
150	25.91	0.153	153
200	26.52	0.157	157
250	26.75	0.158	158
273.15	26.88	0.159	159
298.15	27.02	0.160	160
300	27.03	0.160	160
360	27.37	0.162	162
400	—	0.160–0.165	160–165
500	—	0.165	165
600	—	0.171	171
700	—	0.177	177
778	—	0.180	180
800	—	0.182	182

4. ADI finite-difference scheme on the quarter domain

Symmetry about the longitudinal and transverse axes reduces the calculation to the quarter-domain

$$\Omega_l^{(1/4)} = \{(x,z) : 0 \le z \le L, \quad 0 \le x \le W_l(z)\}.$$

Zero normal heat flux is imposed at $x = 0$ and $z = 0$. At the terminal,

$$T_{i,N_z} = T_0, \quad 0 \le i \le i_{\min},$$

with $T_0 = 78$ K. The other in-plane boundaries are insulated.

A uniform Cartesian grid is introduced in the enclosing rectangle $[0, W_{\max}] \times [0, L]$:

$$x_i = i\Delta x, \quad i = 0, \dots, N_x,$$

$$z_k = k\Delta z, \quad k = 0, \dots, N_z.$$

The grid is chosen so that

$$W_{\min} = i_{\min}\Delta x, \qquad W_{\max} = i_{\max}\Delta x, \qquad l = k_l\Delta z.$$

Table 5
Electrical resistivity of metallic thulium used in the numerical calculations. Values up to 300 K are based on polycrystalline data [15]; values above 300 K are model extrapolations based on single-crystal data [16].

T (K)	ρ_e (μΩ cm)	ρ_e (Ω m)	Origin
60	26.5	2.65×10^{-7}	polycrystalline data
70	28.0	2.80×10^{-7}	polycrystalline data
78	29.5	2.95×10^{-7}	polycrystalline data
80	30.0	3.00×10^{-7}	polycrystalline data
100	34.0	3.40×10^{-7}	polycrystalline data
120	37.5	3.75×10^{-7}	polycrystalline data
160	44.5	4.45×10^{-7}	polycrystalline data
200	52.0	5.20×10^{-7}	polycrystalline data
240	59.0	5.90×10^{-7}	polycrystalline data
280	65.5	6.55×10^{-7}	polycrystalline data
300	69.0	6.90×10^{-7}	polycrystalline data / joining point
400	86.1	8.61×10^{-7}	extrapolation
500	103.2	1.032×10^{-6}	extrapolation
600	120.4	1.204×10^{-6}	extrapolation
700	137.6	1.376×10^{-6}	extrapolation
778	151.0	1.510×10^{-6}	extrapolation
800	154.7	1.547×10^{-6}	extrapolation

We normally set $i_{\max} = N_x$. Active rows contain

$$i = 0, \dots, i_{\text{end}}(k), \text{ where } i_{\text{end}}(k) = \begin{cases} i_{\max}, & 0 \le k \le k_l, \\ i_{\min}, & k_l < k \le N_z \end{cases},$$

and the active part of a column is

$$k = 0, \dots, k_{\text{end}}(i), \text{ where } k_{\text{end}}(i) = \begin{cases} N_z, & 0 \le i \le i_{\min}, \\ k_l, & i_{\min} < i \le i_{\max} \end{cases}.$$

Before time integration, the current field is stored as

$$j_{i,k}^2 = |\mathbf{j}(x_i, z_k; I, l)|^2.$$

At a Picard iterate $\widetilde{T}$, the thermal coefficients are

$$C_{i,k}(\widetilde{T}) = \rho_m(\widetilde{T}_{i,k}) c_p(\widetilde{T}_{i,k}),$$

$$\lambda_{i,k}(\widetilde{T}) = \lambda(\widetilde{T}_{i,k}),$$

and

$$q_{\text{eff},i,k}(\widetilde{T}) = j_{i,k}^2 \rho_e(\widetilde{T}_{i,k}) - Q_{\text{loss}}(\widetilde{T}_{i,k}).$$

Here

$$Q_{\mathrm{loss}}(T_{i,k}^n) = \frac{2}{h}\left[\varepsilon\sigma_{\mathrm{SB}}\left((T_{i,k}^n)^4 - T_{\mathrm{env}}^4\right) + \Gamma(T_{i,k}^n)\frac{\Delta H_{\mathrm{sub}}}{N_A}\right].$$

We discretize diffusion in conservative flux form. At an active node (i,k), the contributions through the vertical faces are

$$F_{i+1/2,k}^x = \begin{cases} \lambda_{i+1/2,k}^n\left(T_{i+1,k} - T_{i,k}\right), & (i+1,k) \in \Omega_l^{(1/4)}, \\ 0, & (i+1,k) \notin \Omega_l^{(1/4)} \end{cases},$$

and

$$F_{i-1/2,k}^x = \begin{cases} \lambda_{i-1/2,k}^n\left(T_{i,k} - T_{i-1,k}\right), & (i-1,k) \in \Omega_l^{(1/4)}, \\ 0, & (i-1,k) \notin \Omega_l^{(1/4)} \end{cases}.$$

Similarly, the fluxes through the horizontal faces are

$$F_{i,k+1/2}^z = \begin{cases} \lambda_{i,k+1/2}^n\left(T_{i,k+1} - T_{i,k}\right), & (i,k+1) \in \Omega_l^{(1/4)}, \\ 0, & (i,k+1) \notin \Omega_l^{(1/4)} \end{cases},$$

and

$$F_{i,k-1/2}^z = \begin{cases} \lambda_{i,k-1/2}^n\left(T_{i,k} - T_{i,k-1}\right), & (i,k-1) \in \Omega_l^{(1/4)}, \\ 0, & (i,k-1) \notin \Omega_l^{(1/4)} \end{cases}.$$

When both neighboring nodes are active, face conductivities are arithmetic means:

$$\lambda_{i+1/2,k}^n = \frac{\lambda(T_{i,k}^n) + \lambda(T_{i+1,k}^n)}{2},$$

$$\lambda_{i,k+1/2}^n = \frac{\lambda(T_{i,k}^n) + \lambda(T_{i,k+1}^n)}{2}.$$

If the neighboring node lies outside the foil, the corresponding flux is zero; no ghost temperature is introduced. The corner $(i_{\min}, k_l)$ requires no special condition.

The discrete operators are then written as

$$L_x^{(n)} T_{i,k} = \frac{F_{i+1/2,k}^x - F_{i-1/2,k}^x}{\Delta x^2},$$

and

$$L_z^{(n)} T_{i,k} = \frac{F_{i,k+1/2}^z - F_{i,k-1/2}^z}{\Delta z^2}.$$

Time integration uses a Peaceman–Rachford ADI scheme [17–19], with Picard iteration at each half-step. The first half-step is implicit in x and explicit in z:

$$C_{i,k}^{n+1/2,(s)} \frac{T_{i,k}^{n+1/2,(s+1)} - T_{i,k}^n}{\Delta t/2} = L_x^{n+1/2,(s)} T_{i,k}^{n+1/2,(s+1)} + L_z^n T_{i,k}^n + q_{\mathrm{eff},i,k}^{n+1/2,(s)}. \tag{6}$$

For each fixed k, Eq. (6) gives a tridiagonal system along the active row $i = 0, \dots, i_{\mathrm{end}}(k)$:

$$a_{i,k}^x T_{i-1,k}^{n+1/2,(s+1)} + b_{i,k}^x T_{i,k}^{n+1/2,(s+1)} + c_{i,k}^x T_{i+1,k}^{n+1/2,(s+1)} = r_{i,k}^x. \tag{7}$$

For ordinary active nodes,

$$a_{i,k}^x = -\frac{\lambda_{i-1/2,k}^{n+1/2,(s)}}{\Delta x^2}, \qquad c_{i,k}^x = -\frac{\lambda_{i+1/2,k}^{n+1/2,(s)}}{\Delta x^2},$$

$$b^x_{i,k} = \frac{2C^{n+1/2,(s)}_{i,k}}{\Delta t} + \frac{\lambda^{n+1/2,(s)}_{i-1/2,k} + \lambda^{n+1/2,(s)}_{i+1/2,k}}{\Delta x^2},$$

and

$$r^x_{i,k} = \frac{2C^{n+1/2,(s)}_{i,k}}{\Delta t} T^n_{i,k} + L^n_z T^n_{i,k} + q^{n+1/2,(s)}_{\mathrm{eff},i,k}. \tag{8}$$

If a neighboring node in the x direction is absent, the corresponding coefficient $a^x_{i,k}$ or $c^x_{i,k}$ is set to zero. In particular, at $x = 0$ the symmetry condition gives $a^x_{0,k} = 0$, while at the right end of an active row $c^x_{i_{\mathrm{end}}(k),k} = 0$.

The row $k = N_z$ is not advanced by the x-sweep. It belongs to the current terminal for $0 \le i \le i_{\min}$ and is fixed as

$$T^{n+1/2}_{i,N_z} = T_0, \quad 0 \le i \le i_{\min}.$$

The second half-step is implicit in z. The accepted intermediate field provides the explicit x contribution, while Picard iteration updates the implicit coefficients:

$$C^{n+1,(s)}_{i,k} \frac{T^{n+1,(s+1)}_{i,k} - T^{n+1/2}_{i,k}}{\Delta t/2} = L^{n+1,(s)}_z T^{n+1,(s+1)}_{i,k} + L^{n+1/2}_x T^{n+1/2}_{i,k} + q^{n+1,(s)}_{\mathrm{eff},i,k}. \tag{9}$$

For each fixed i, Eq. (9) gives a tridiagonal system along the active column $k = 0, \dots, k_{\mathrm{end}}(i)$:

$$a^z_{i,k} T^{n+1,(s+1)}_{i,k-1} + b^z_{i,k} T^{n+1,(s+1)}_{i,k} + c^z_{i,k} T^{n+1,(s+1)}_{i,k+1} = r^z_{i,k}. \tag{10}$$

For ordinary active nodes,

$$a^z_{i,k} = -\frac{\lambda^{n+1,(s)}_{i,k-1/2}}{\Delta z^2}, \qquad c^z_{i,k} = -\frac{\lambda^{n+1,(s)}_{i,k+1/2}}{\Delta z^2},$$
$$b^z_{i,k} = \frac{2C^{n+1,(s)}_{i,k}}{\Delta t} + \frac{\lambda^{n+1,(s)}_{i,k-1/2} + \lambda^{n+1,(s)}_{i,k+1/2}}{\Delta z^2},$$

and

$$r^z_{i,k} = \frac{2C^{n+1,(s)}_{i,k}}{\Delta t} T^{n+1/2}_{i,k} + L^{n+1/2}_x T^{n+1/2}_{i,k} + q^{n+1,(s)}_{\mathrm{eff},i,k}.$$

At $z = 0$, the symmetry condition gives $a^z_{i,0} = 0$. For columns inside the side wing, $i > i_{\min}$, the active segment ends at $k = k_l$, and the upper face is insulated; therefore $c^z_{i,k_l} = 0$. For columns inside the central part, $0 \le i \le i_{\min}$, the active segment extends to $k = N_z$, where the Dirichlet condition is imposed by replacing the last equation with

$$T^{n+1}_{i,N_z} = T_0, \quad 0 \le i \le i_{\min}.$$

Equivalently,

$$a^z_{i,N_z} = 0, \qquad b^z_{i,N_z} = 1, \qquad c^z_{i,N_z} = 0, \qquad r^z_{i,N_z} = T_0.$$

The Picard iteration in each half-step is stopped when both an absolute and a relative update criterion are satisfied,

$$\max_{(i,k)\in\Omega_l^{(1/4)}} \left| T^{(s+1)}_{i,k} - T^{(s)}_{i,k} \right| < \varepsilon_{\mathrm{nl,abs}},$$
$$\frac{\max_{(i,k)\in\Omega_l^{(1/4)}} \left| T^{(s+1)}_{i,k} - T^{(s)}_{i,k} \right|}{\max\left(1, \max_{(i,k)\in\Omega_l^{(1/4)}} |T^{(s+1)}_{i,k}|\right)} < \varepsilon_{\mathrm{nl,rel}}. \tag{11}$$

After each full step, stationarity is tested with the maximum temperature rate,

$$R^n_T = \max_{(i,k)\in\Omega_l^{(1/4)}} \left| \frac{T^{n+1}_{i,k} - T^n_{i,k}}{\Delta t} \right|. \tag{12}$$

The loop ends when $R^n_T < \varepsilon_{\mathrm{rate}}$ or $t_n \ge t_{\max}$. The default $t_{\max} = \mathrm{DBL_MAX} - 10\Delta t$ effectively disables the time limit, so production runs normally stop on the rate criterion. The elapsed physical time then estimates the foil's approach time to steady operation.

5. GPU implementation of the ADI solver

We implemented the ADI scheme in CUDA C for a single GPU. The row systems in Eq. (7) and the column systems in Eq. (10) are independent within their respective half-steps. We compare several ways of solving these systems and dispatching the associated kernels; all produce the same discrete solution. Figure 3 summarizes the implementation.

5.1. Overall organization

All field arrays, including the two temperature layers, squared current density $j^2_{i,k}$, and the temperature-dependent coefficients $C_{i,k}$, $\lambda_{i,k}$ and $q_{\mathrm{eff},i,k}$, are stored on the device in row-major order over the enclosing rectangle, $\mathrm{IDX}(i,k) = k(N_x+1)+i$. The auxiliary electric-current problem is linear and is solved once on the host before the time loop; only the resulting field $j^2_{i,k}$ is copied to the device. The transient integration then runs entirely on the GPU. Host-device transfers during integration are limited to the maximum temperature change and maximum temperature, and occur only when a convergence test is evaluated.

Each time step is carried out by a small set of kernels: a coefficient kernel that evaluates $C_{i,k}$, $\lambda_{i,k}$ and $q_{\mathrm{eff},i,k}$ from the current temperature estimate with one thread per node; the two sweep kernels that assemble and solve the tridiagonal systems of the first and second half-steps; and reduction kernels that return rates for the Picard test (11) and for the stationary-rate test (12). The two temperature layers are kept in two device buffers that are exchanged by pointer swap after each accepted step, so that no full-field copy is performed inside the time loop.

5.2. Mapping of the tridiagonal systems onto the device

Each tridiagonal system is assigned to *one CUDA block*, and the threads of that block cooperate on that single system rather than each thread owning a complete system. This keeps the three diagonals and the right-hand side of a given system in a contiguous span of device memory, so that the parallel assembly and scatter phases issue coalesced accesses, and it allows the block to use `__syncthreads()` to separate the assembly, the solve and the scatter phases. The block dimension is fixed at 256 threads.

Because the quarter domain is L-shaped, the systems do not all have the same length. The rows split into long rows in the wide central part ($0 \le k \le k_l$, length $i_{\max}+1$) and short rows in the side wing ($k_l < k < N_z$, length $i_{\min}+1$); the columns split analogously into long columns in the central part ($0 \le i \le i_{\min}$, length N_z+1) and short columns in the side wing ($i_{\min} < i \le i_{\max}$, length k_l+1). Each group is handled by a separate kernel launch, so that a launch processes a batch of equal-length systems and the storage for that batch is sized to the exact system length rather than to the largest system in the domain. For the grid used here ($N_x = 50$, $N_z = 400$, $i_{\max} = 50$, $i_{\min} = 20$, $k_l = 280$) the four batches contain 281, 119, 21 and 30 systems of length 51, 21, 401 and 281, respectively. For a batch of N_{sys} systems of length $n_{\max}$, four device arrays of size $N_{\mathrm{sys}}\, n_{\max}$ hold the sub-, main- and super-diagonals and the right-hand side; system s occupies the contiguous span starting at $s\, n_{\max}$, and its solution overwrites the right-hand side in place.

5.3. Assembly, solve and scatter within a block

Within a block the work proceeds in three barrier-separated phases. In the *assembly* phase the threads stride over the active nodes of the system, *count* = tid, tid + blockDim, …, and each thread writes the coefficients a, b, c and the right-hand side r of its nodes according to Eqs. (7)–(8) for the x-sweep and the analogous relations for the z-sweep. The face conductivities are evaluated by arithmetic averaging of the neighbouring nodal values, and a neighbour outside the quarter domain contributes a zero flux, so that the corresponding off-diagonal coefficient vanishes. The symmetry conditions at $x = 0$ and $z = 0$ enter as a vanishing lower diagonal at *count* $= 0$, and the end of each active segment as a vanishing upper diagonal at *count* $= n-1$; the Dirichlet terminal node (i, N_z) with $i \le i_{\min}$ is

assembled directly as $a^z = 0$, $b^z = 1$, $c^z = 0$, $r^z = T_0$, i.e. the last equation of the affected columns is replaced rather than eliminated.

After a barrier the *solve* phase reduces each system to its solution, and after a second barrier the *scatter* phase writes the computed line back into the two-dimensional temperature array, again with the threads striding over the nodes of the system. The same kernel structure is used for both half-steps; only the index running along the system (the row index i for the x-sweep, the column index k for the z-sweep) and the direction of the implicit and explicit operators differ. The assembly and scatter phases are identical across all variants considered below; the variants differ only in the algorithm that implements the solve phase.

5.4. Tridiagonal-solve algorithms

We compared four solvers that differ in how elimination is distributed across the block [20]. Their solutions agree to round-off.

(i) Serial Thomas sweep (baseline). Thread 0 executes the classical Thomas algorithm [21]: forward elimination followed by backward substitution. A pivot smaller than 10^{-300} marks the solution as `NaN`. The guard was never triggered because the transient term $2C_{i,k}/\Delta t$ makes these systems strongly diagonally dominant. This implementation matches the serial CPU sweep bit-for-bit, but the device is under-utilized during this phase because the other block threads remain idle.

(ii) Two-sided Thomas algorithm. This variant applies Thomas elimination simultaneously from both ends of the system [22, 23]. The two elimination fronts advance towards a central index, after which substitution proceeds outwards. Two threads per block carry out the sweeps, halving the length of the inherently sequential dependency chain.

(iii) Austin-Berndt-Moulton partition method. Production runs use the memory-efficient partitioning scheme of Austin, Berndt, and Moulton (ABM) [24]. A system of N rows is divided into N_P contiguous partitions, each of length $N_k \approx N/N_P$. Each thread eliminates the interior unknowns of one partition and expresses them in terms of two interface unknowns. These interface unknowns form a reduced tridiagonal system of order $2N_P$. After this system is solved by thread 0 using the serial Thomas algorithm, the threads recover the interior unknowns of their respective partitions in parallel. The ABM method stores only the boundary-coupling coefficients rather than the full fill-in vectors, requiring approximately 6 kB of shared memory in our kernels. The partition method is applied to systems with $N > 100$. Smaller systems containing 21 and 51 unknowns, are solved using two-sided elimination.

(iv) Vendor batched solver (cuSPARSE). For an external comparison, the batched solve was delegated to the NVIDIA `cuSPARSE` library [25] routine `cusparseDgtsv2StridedBatch`, which solves a batch of equal-length tridiagonal systems stored in the strided layout already used by the assembly phase. This variant reuses the same assembly and scatter kernels and replaces only the solve, so it measures the cost of a production-quality library solver on the identical data layout.

5.5. Kernel launch strategy

We also compared two launch strategies. In *plain* mode every kernel of a step — the coefficient kernel, the four assembly/solve batches of each sweep, and the reductions — is launched individually through the ordinary runtime API. Because a single step of the present problem issues of the order of a few tens of very short kernels (each system is at most 401 unknowns long, so a kernel runs only for microseconds), the fixed CPU-side cost of launching each kernel becomes comparable to the kernel's own execution time, and over the $\sim 8 \times 10^4$ steps of a full run this launch overhead accumulates into a noticeable fraction of the wall time.

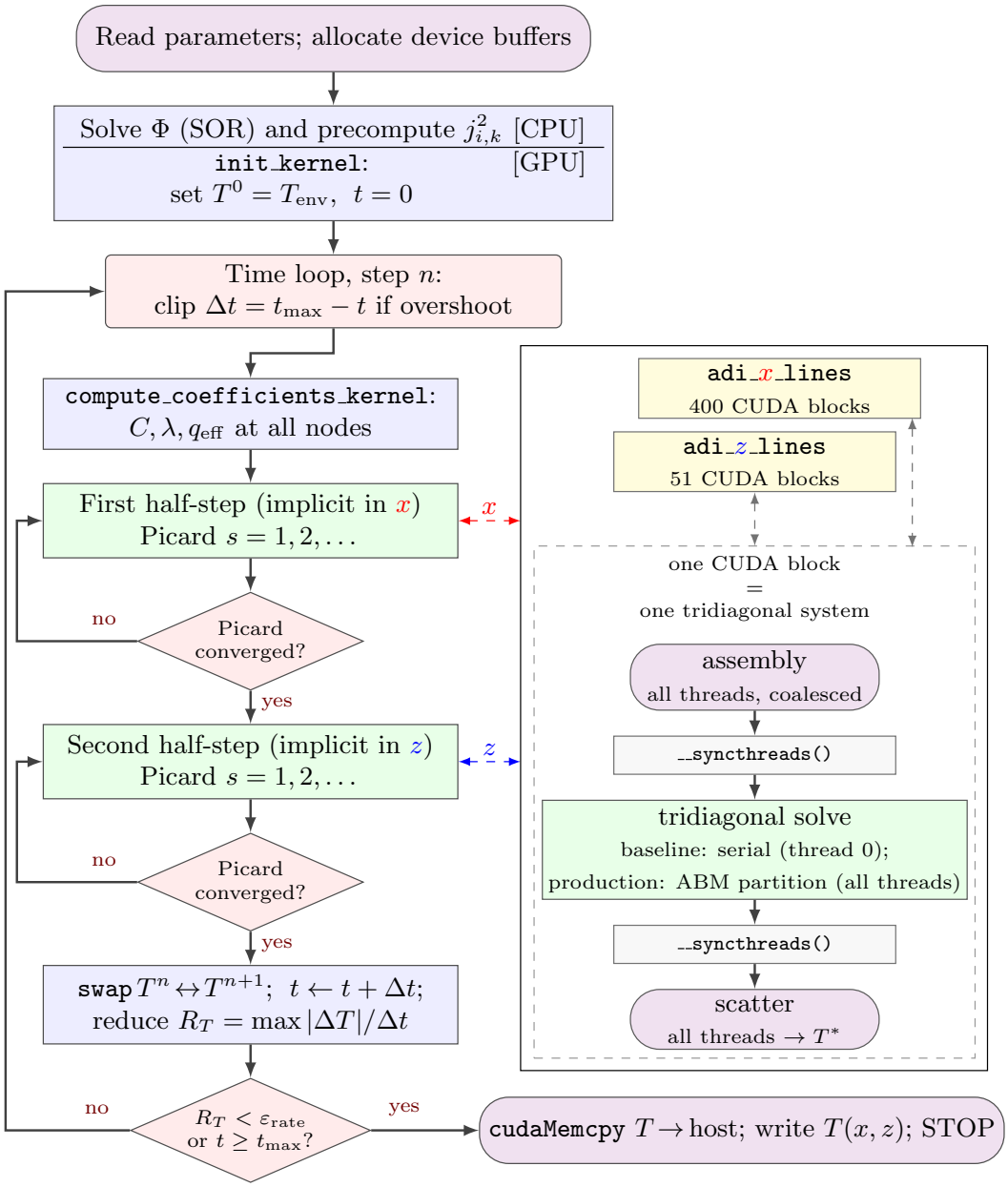
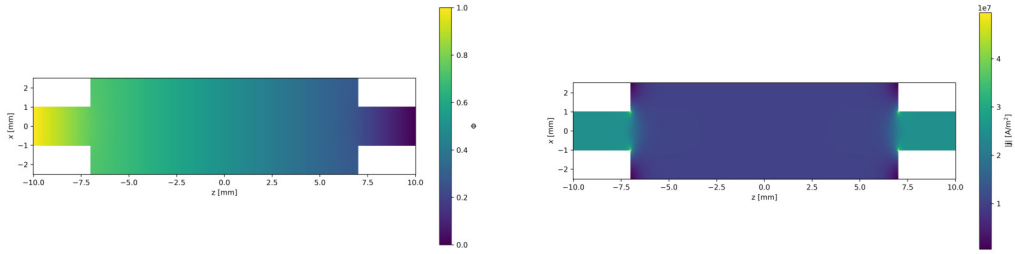


Figure 3. Structure of the GPU implementation of the ADI solver. The host solves the electric problem once; the transient loop runs entirely on the device. Each ADI half-step launches one kernel per batch of equal-length tridiagonal systems (the x-sweep is shown exploded on the right: 281 long rows of length 51 and 119 short rows of length 21; the z-sweep is organized analogously into 21 long and 30 short columns). Every tridiagonal system is mapped to a single CUDA block, whose threads cooperate in three barrier-separated phases - parallel assembly, the tridiagonal solve, and parallel scatter of the solution. The solve phase is interchangeable: the baseline runs a serial Thomas sweep in thread 0, whereas the production configuration distributes it across the threads of the block through the ABM partition method (Section 5)



(a) Electric potential $\phi(x, z)$ for the full left-to-right problem. The potential decreases monotonically from the left contact, where $\phi = 1$, to the right contact, where $\phi = 0$. The central value $\phi \simeq 0.5$ corresponds to the symmetry plane used in the quarter-domain calculation

(b) Distribution of the electric-current-density magnitude $|\mathbf{j}(x, z)|$ in the full plate domain. The current density increases in the narrow end regions because of the reduced cross-sectional width and exhibits local concentrations near the width-transition corners

Figure 4. Electric properties of the full plate geometry: (a) electric potential and (b) magnitude of the electric current density

The second mode uses *CUDA task graphs* [26]. The kernel-call flow within one time step is represented as a task graph and submitted as a single GPU operation. We construct the graph implicitly by capturing the stream workflow with `cudaStreamBeginCapture` and `cudaStreamEndCapture`, instantiate it with `cudaGraphInstantiate`, and execute it with `cudaGraphLaunch`. This approach is particularly effective for short kernels, whose execution time can be comparable to their launch latency, because it reduces the gaps between successive kernel launches [27]. Since Δt, the grid, and the batch structure remain fixed, the same graph is used throughout a run. A shortened final step, if needed to reach $t_{\max}$ exactly, is launched separately.

5.6. Time loop and stopping

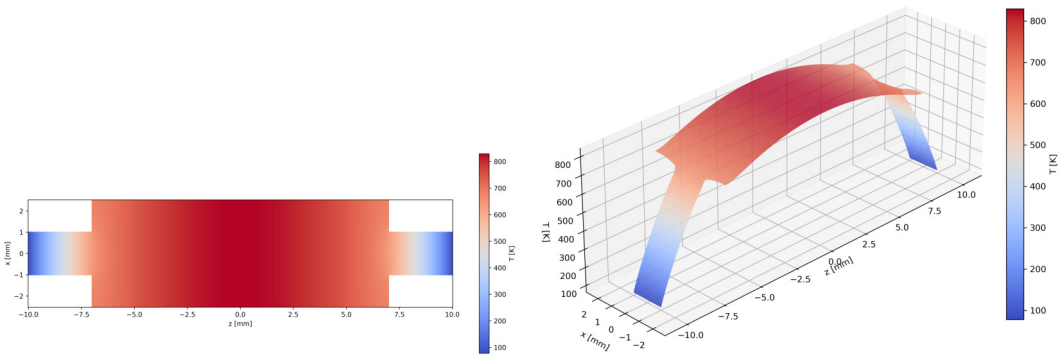
The Picard iterations of each half-step reuse the coefficient and sweep kernels: the coefficients are re-evaluated from the latest temperature estimate, the tridiagonal systems are re-assembled and re-solved, and the maximum update is reduced on the device. To limit host-device synchronization, the update norm is copied back and tested only on every third iteration and on the last allowed iteration. After a full step the maximum temperature change is reduced on the device and divided by Δt to form the stationary rate R_T^n of Eq. (12). The time loop terminates when $R_T^n < \varepsilon_{\text{rate}}$ or when the accumulated physical time reaches the prescribed bound $t_{\max}$; when the next step overshoot $t_{\max}$, the step size is reduced to $\Delta t = t_{\max} - t_n$ for that final step in order to land exactly on $t_{\max}$.

6. Numerical results

We solved the coupled problem for a total current $I = 2.5\,\text{A}$, with the cold contacts held at $T_0 = 78\,\text{K}$, the surrounding medium at $T_{\text{env}} = 293\,\text{K}$, and a surface emissivity $\varepsilon = 0.10$. The grid used $N_x = 50$, $N_z = 400$ (grid_scale $= 1$), with the wing transition at $k_l = 280$ and $i_{\min} = 20$. The time step was $\Delta t = 1 \times 10^{-3}\,\text{s}$, and each Picard update used at most 20 iterations per half-step with tolerances $\varepsilon_{nl,\text{abs}} = 10^{-6}$ and $\varepsilon_{nl,\text{rel}} = 10^{-10}$.

The potential decreases monotonically between the contacts (Figure 4a). As expected, the current density is largest in the narrow end regions and shows additional crowding near the re-entrant corners (Figure 4b). This nonuniform $|\mathbf{j}|^2$ field is used in the Joule source.

Starting from $T_0 = 78\,\text{K}$, the calculation reached the criterion $R_T = \max_{i,k} |T_{i,k}^{n+1} - T_{i,k}^n|/\Delta t < \varepsilon_{\text{rate}}$ with $\varepsilon_{\text{rate}} = 1 \times 10^{-2}\,\text{K s}^{-1}$ after 77 397 steps, or 77.397 s of simulated time. The maximum temperature was 829.803 K. Figures 5a and 5b show the stationary field. The cold contacts keep the narrow ends near 78 K, while the maximum lies in the broad central region. Changes in the field near the width transitions reflect the redistribution of current there.



(a) Two-dimensional temperature map of the stationary regime in the full symmetric thulium plate domain. The narrow end regions are maintained close to the prescribed contact temperature $T_0 = 78$ K, whereas the central wide part reaches the highest temperature

(b) Three-dimensional representation of the stationary temperature field $T(x, z)$ in the full symmetric thulium plate domain. Local distortions near the width-transition zones reflect current redistribution and the associated spatial variation of Joule heating

Figure 5. Stationary temperature distribution in the full symmetric thulium plate domain: a two-dimensional temperature map and b three-dimensional representation of the temperature field. The temperature decreases toward the narrow cold-contact regions, while the maximum occurs in the central part of the wider section

All tridiagonal solvers produced the same converged field and maximum temperature, allowing their execution times to be compared directly.

7. Performance of the tridiagonal-solver strategies

We benchmarked the batched solvers on one NVIDIA V100 against a serial CPU implementation. Every variant used $N_x = 50$, $N_z = 400$, $k_l = 280$, and $\Delta t = 1 \times 10^{-3}$ s, stopped at step 77 397, and produced a bit-for-bit identical $T_{\max} = 829.803$ K. Wall-clock differences therefore arise from the solver and launch strategy rather than from different stopping histories.

The tested configurations comprise the one-thread Thomas baseline, the two-sided Thomas algorithm, the ABM partition solver, and `cusparseDgtsv2StridedBatch`. Each in-house solver was measured with ordinary kernel launches and with CUDA task graphs. We also tested device intrinsics in the partition sweep. Each configuration was run five times; Table 6 reports the mean and standard deviation; Figure 6 and 7 show the same data graphically.

The serial CPU run took 876 s. ABM partitioning achieved 21-24× speedup (Figure 7), roughly twice that of the serial and two-sided Thomas algorithms (11-12×), because the elimination work is shared across the block. CUDA task graphs reduced runtime by about ten percent over the 77 397 time steps. Explicit use of FMA intrinsics produced no speedup because nvcc enables contraction of eligible multiply-add operations by default (–fmad=true). The fastest configuration, ABM partitioning with a CUDA task graph, completed in 36.3 s (24.1×; Figure 6), about ten percent faster than `cuSPARSE` at 40.2 s (21.8×).

The GPU computations were performed on an NVIDIA Tesla V100-SXM2 (16 GB) accelerator of the "Govorun" supercomputer at the HybriLIT heterogeneous computing platform [28], using code built with the CUDA 11.2 toolkit and GCC 9.5.0 as the host compiler (`-arch=sm_70 -O3`). For comparison, the CPU version was run on the same platform, on Intel Xeon Platinum 8268 processors (24 cores, 2.9 GHz, 192 GB DDR4) and built with the same compiler.

8. Discussion

The calculated temperature field reflects the combined effects of the nonuniform current distribution and heat removal through the cold contacts. The maximum temperature occurs in the broad central

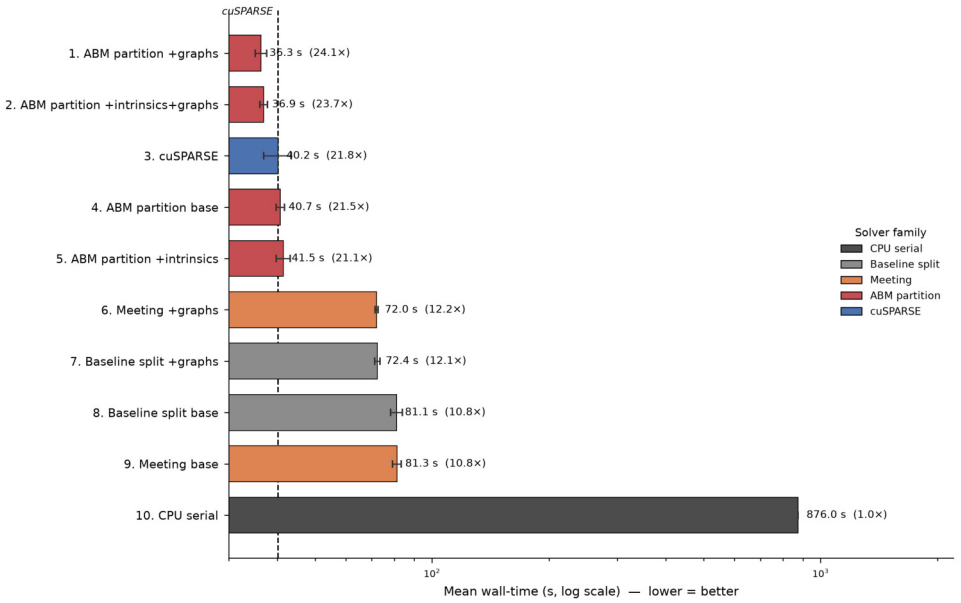


Figure 6. Mean wall-clock time of the tridiagonal-solver configurations on an NVIDIA V100 (logarithmic scale; lower is better; error bars show the standard deviation over five runs). The dashed line shows the cuSPARSE timing. Colours distinguish the tridiagonal algorithms. All configurations converge to the same $T_{\max} = 829.803\,\mathrm{K}$ at step 77 397

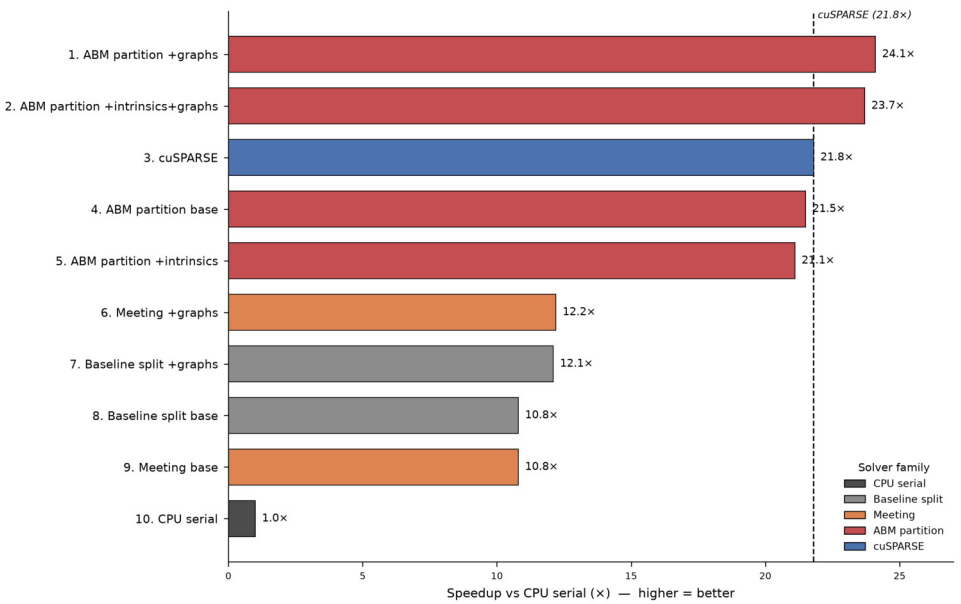


Figure 7. Speedup of the GPU configurations relative to the single-thread CPU run (linear scale; higher is better). The dashed line shows the cuSPARSE result. The ABM partition configurations reach 21-24× speedup; the two configurations that use CUDA task graphs outperform the vendor routine

Table 6
Wall-clock time (mean ± standard deviation over five runs) and speedup relative to the single-thread CPU run for the tridiagonal-solver strategies on an NVIDIA V100. All configurations converge at step 77 397 to $T_{\max} = 829.803$ K.

Configuration	**Wall time** (s)	**Speedup**
ABM partition, + task graph	36.3 ± 1.2	24.1×
ABM partition, + intrinsics + task graph	36.9 ± 0.8	23.7×
cuSPARSE	40.2 ± 3.3	21.8×
ABM partition, plain	40.7 ± 1.0	21.5×
ABM partition, + intrinsics	41.5 ± 1.7	21.1×
Two-sided Thomas, + task graph	72.0 ± 0.6	12.2×
Serial Thomas, + task graph	72.4 ± 1.1	12.1×
Serial Thomas, plain	81.1 ± 2.8	10.8×
Two-sided Thomas, plain	81.3 ± 2.1	10.8×
CPU serial	876.0	1.0×

region, whereas the narrow end regions remain close to the prescribed contact temperature. The local changes in the temperature field near the width transitions are associated with current crowding at the re-entrant corners. This behaviour confirms the need for a two-dimensional electric model, since the one-dimensional approximation cannot resolve these local variations in the current density.

The present results should be considered in the context of the model assumptions. The electric-current distribution is calculated using constant conductivity and is subsequently scaled to the prescribed total current, while the temperature dependence of the electrical resistivity is included in the Joule heat source. In addition, a constant effective emissivity is used, and some thermophysical properties are extrapolated beyond the available experimental ranges. The numerical results therefore characterize the selected foil geometry and operating conditions rather than providing a universal optimum.

The ADI discretization produces batches of independent tridiagonal systems. Mapping each system to a CUDA block makes it possible to change the solution algorithm without modifying the assembly procedure or data layout. For the grid considered here, ABM partitioning approximately doubled the performance relative to the serial and two-sided Thomas algorithms. CUDA task graphs provided a further improvement of about ten percent, whereas device intrinsics changed the execution time by less than the run-to-run variation. The fastest configuration, ABM partitioning combined with a CUDA task graph, completed the calculation in 36.3 s and achieved a 24.1× speedup over the single-thread CPU implementation. It was also approximately ten percent faster than `cuSPARSE`.

Compared with the earlier formulation [2], which ranked candidate geometries according to the area within a prescribed temperature interval, the present model provides the evaporation flux as a more direct measure of ion-source performance. The computational efficiency of the GPU implementation makes the direct solver suitable for repeated calculations in an optimization procedure in which the foil geometry and operating current are varied. Future development of the model will couple the electric field to the evolving temperature-dependent conductivity.

9. Conclusions

A two-dimensional electric-thermal model of a wing-shaped thulium foil was developed. The model accounts for temperature-dependent material properties, nonuniform Joule heating, radiation, and evaporation. The numerical results show that the proposed approach can determine the stationary temperature field and provide the quantities needed to evaluate the foil performance. All tested

tridiagonal solvers produced the same converged solution, while the GPU implementation substantially reduced the computation time. The resulting solver can therefore be used for repeated calculations when optimizing the foil geometry and operating current.

Author Contributions: A. Ayriyan: Conceptualization (physical and mathematical model, formulation of mathematical problem), Methodology, Software, Investigation (numerical computations), Writing, Supervision. E. Ayryan: Methodology (numerical solution of the elliptic equation). E. E. Donets: Conceptualization (physical problem). M. Veneva: Software (parallel tridiagonal solver and CUDA implementation), Methodology (GPU optimization). All authors have read and agreed to the published version of the manuscript.

Data Availability Statement: All data and parameters required to reproduce the results of this study are provided within the article. No additional datasets are required.

Acknowledgments: The authors thank *Hovik Grigorian* and *Jan Buša Jr.* for helpful discussions and technical assistance. Computations were held on the basis of the HybriLIT heterogeneous computing platform (MLIT, JINR).

Conflicts of Interest: The authors declare no conflict of interest.

Declaration on Generative AI: Claude (Anthropic) was used solely to improve the language and readability of text originally written by the authors and to assist in preparing Figures 6 and 7 from the numerical data reported in Table 6. The authors reviewed and approved all AI-assisted changes and take full responsibility for the content of the manuscript.

References

[1] D. E. Donets, E. D. Donets, E. E. Donets, V. V. Salnikov, and V. B. Shutov, "Production of highly charged ion beams Kr32+, Xe44+, Au54+ with Electron String Ion Source (ESIS) Krion-2 and corresponding basic and applied studies," *JINST*, vol. 5, p. C09001, 2010. DOI: 10.1088/1748-0221/5/09/C09001

[2] A. Ayriyan, E. Donets, H. Grigorian, N. Kolkovska, and A. Lebedev, "Algorithm for Solving an Optimization Problem for the Temperature Distribution on a Plate," *EPJ Web of Conferences*, vol. 108, p. 02 010, 2016. DOI: 10.1051/epjconf/201610802010

[3] A. H. Persad and C. A. Ward, "Expressions for the Evaporation and Condensation Coefficients in the Hertz-Knudsen Relation," *Chemical Reviews*, vol. 116, no. 14, pp. 7727–7767, 2016. DOI: 10.1021/acs.chemrev.5b00511

[4] Y. B. Zudin, *Non-equilibrium Evaporation and Condensation Processes*. Cham, Switzerland: Springer, 2017. DOI: 10.1007/978-3-319-67306-6

[5] V. P. Carey, *Liquid-Vapor Phase-Change Phenomena*, 3rd ed. Boca Raton, FL: CRC Press, 2020.

[6] D. M. Young, "Iterative Methods for Solving Partial Difference Equations of Elliptic Type," *Transactions of the American Mathematical Society*, vol. 76, no. 1, pp. 92–111, 1954. DOI: 10.1090/S0002-9947-1954-0059635-7

[7] A. A. Samarskii and E. S. Nikolaev, *Numerical Methods for Grid Equations, Volume II: Iterative Methods*. Basel: Birkhäuser, 1989. DOI: 10.1007/978-3-0348-9142-4

[8] T. L. Bergman, A. S. Lavine, F. P. Incropera, and D. P. DeWitt, *Fundamentals of Heat and Mass Transfer*, 8th ed. Hoboken, NJ: Wiley, 2017.

[9] D. R. Lide, Ed., *CRC Handbook of Chemistry and Physics*, 84th ed. Boca Raton: CRC Press, 2003, Section 6, Fluid Properties; vapor-pressure data for the elements.

[10] Y. S. Touloukian, R. K. Kirby, R. E. Taylor, and P. D. Desai, Eds., *Thermal Expansion: Metallic Elements and Alloys* (Thermophysical Properties of Matter: The TPRC Data Series). New York: IFI/Plenum, 1975, vol. 12.

[11] S. Singh, N. C. Khanduri, and T. Tiang, "Thermal Expansions of Thulium and Lutetium, 90–300 K," *Solid State Communications*, vol. 5, no. 3, pp. 167–173, 1971.

[12] C. Y. Ho, R. W. Powell, and P. E. Liley, "Thermal Conductivity of the Elements," *Journal of Physical and Chemical Reference Data*, vol. 1, no. 2, pp. 279–421, 1972.

[13] L. D. Jennings, E. Hill, and F. H. Spedding, "Heat Capacity of Thulium from 15 Degrees to 360 Degrees K," *The Journal of Chemical Physics*, vol. 34, no. 6, pp. 2082–2088, 1961. DOI: 10.1063/1.1731825

[14] Y. S. Touloukian and E. H. Buyco, Eds., *Specific Heat: Metallic Elements and Alloys* (Thermophysical Properties of Matter: The TPRC Data Series). New York: IFI/Plenum, 1970, vol. 4.
[15] R. V. Colvin, S. Legvold, and F. H. Spedding, "Electrical Resistivity of the Heavy Rare-Earth Metals," *Physical Review*, vol. 120, no. 3, pp. 741–745, 1960. DOI: 10.1103/PhysRev.120.741
[16] L. R. Edwards and S. Legvold, "Transport Properties of Thulium Single Crystals," *Physical Review*, vol. 176, no. 3, pp. 753–758, 1968. DOI: 10.1103/PhysRev.176.753
[17] D. W. Peaceman and H. H. Rachford, "The Numerical Solution of Parabolic and Elliptic Differential Equations," *Journal of the Society for Industrial and Applied Mathematics*, vol. 3, no. 1, pp. 28–41, 1955. DOI: 10.1137/0103003
[18] A. A. Samarskii and P. N. Vabishchevich, *Computational Heat Transfer*. Chichester; New York: Wiley, 1995, vol. 1–2.
[19] A. A. Samarskii, *The Theory of Difference Schemes*. New York: Marcel Dekker, 2001, Russian original: *Teoriya raznostnykh skhem*, Nauka, Moscow, 1977.
[20] Y. Zhang, J. Cohen, and J. D. Owens, "Fast Tridiagonal Solvers on the GPU," *ACM SIGPLAN Notices (PPoPP '10)*, vol. 45, no. 5, pp. 127–136, 2010. DOI: 10.1145/1837853.1693472
[21] L. H. Thomas, "Elliptic Problems in Linear Difference Equations over a Network," *Watson Sci. Comput. Lab. Report, Columbia University, New York*, 1949.
[22] I. Babuška, "Numerical Stability in Problems of Linear Algebra," *SIAM Journal on Numerical Analysis*, vol. 9, no. 1, pp. 53–77, 1972. DOI: 10.1137/0709008
[23] H. A. van der Vorst, "Large Tridiagonal and Block Tridiagonal Linear Systems on Vector and Parallel Computers," *Parallel Computing*, vol. 5, no. 1–2, pp. 45–54, 1987. DOI: 10.1016/0167-8191(87)90005-6
[24] T. M. Austin, M. Berndt, and J. D. Moulton, "A Memory Efficient Parallel Tridiagonal Solver," Los Alamos National Laboratory, Tech. Rep. LA-UR-03-4149, 2004.
[25] N. Corporation, *cuSPARSE Library*, https://docs.nvidia.com/cuda/cusparse/, NVIDIA CUDA Toolkit documentation.
[26] N. Corporation, *CUDA C++ Programming Guide*, https://docs.nvidia.com/cuda/cuda-c-programming-guide/, Section on CUDA Graphs.
[27] M. Veneva, "GPU-Based Optimizations for waLBerla: Porting waLBerla to CUDA Task Graphs," in *JSC Guest Student Programme Proceedings 2021*, I. Kabadshow, Ed., ser. IAS Series, vol. 52, Forschungszentrum Jülich GmbH, Zentralbibliothek, Verlag, 2023, pp. 59–82.
[28] A. Anikina, D. Belyakov, T. Bezhanyan, et al., "Structure and Features of the Software and Information Environment of the HybriLIT Heterogeneous Platform," in *Distributed Computer and Communication Networks (DCCN 2024)*, ser. Lecture Notes in Computer Science, vol. 15460, Springer, Cham, 2025, pp. 444–457. DOI: 10.1007/978-3-031-80853-1_33

Information about the authors

Ayriyan, Alexander S.—Candidate of Physical and Mathematical Sciences, Head of the Nonlinear Systems Modeling Methods Sector, Scientific Department of Computational Physics, Meshcheryakov Laboratory of Information Technologies (MLIT), Joint Institute for Nuclear Research (JINR); Research Scientist at the Division of Computational Physics and Information Technologies, A. Alikhanyan National Science Laboratory (Yerevan) (e-mail: ayriyan@jinr.ru, ORCID: 0000-0002-5464-4392)

Ayryan, Edik A.—Candidate of Physical and Mathematical Sciences, Assistant to the Director of the Meshcheryakov Laboratory of Information Technologies (MLIT), Joint Institute for Nuclear Research (JINR) (e-mail: ayrjan@jinr.ru, ORCID: 0000-0001-6478-4041)

Donets, Eugeny E.—Candidate of Physical and Mathematical Sciences, Head of the Electron Beam Ion Source Sector, Scientific and Experimental Department of Injection and the Nuclotron Ring, Veksler and Baldin Laboratory of High Energy Physics (VBLHEP), Joint Institute for Nuclear Research (JINR) (e-mail: edonets@jinr.ru)

Veneva, Milena P.—Student Trainee at the RIKEN Center for Computational Science (e-mail: milena.p.veneva@gmail.com, ORCID: 0000-0002-6421-4716)

RUSSIAN METADATA

УДК 519.63, 536.2
PACS 44.10.+i, 07.05.Tp, 02.70.Bf
DOI: 10.22363/2658-4670-2026-34-3-408-429 EDN: QXTTKT

Моделирование теплопроводности в тулиевой фольге крыловидной формы для источника ионов

А. С. Айриян[1, 2], Э. А. Айрян[1], Е. Е. Донец[1], М. П. Венева[3]

[1] *Объединённый институт ядерных исследований, ул. Жолио-Кюри, д. 6, г. Дубна, 141980, Российская Федерация*

[2] *Национальная научная лаборатория им. А. Алиханяна, ул. Братьев Алиханян, д. 2, г. Ереван, 0036, Армения*

[3] *Центр вычислительных наук RIKEN, Минатодзима-минами-мати 7-1-26, район Тюо, г. Кобе, префектура Хёго, 650-0047, Япония*

Аннотация. *Актуальность.* Металлическая фольга, нагреваемая электрическим током, широко применяется в качестве испарительных элементов источников ионов. Поскольку скорость испарения сильно зависит от температуры, точное и эффективное определение распределения температуры необходимо для выбора геометрии фольги и рабочих условий. *Цель.* Разработать двумерную электротепловую модель тулиевой фольги крыловидной формы и оценить численные методы для многократного проведения расчётов. *Методы.* Благодаря симметрии в расчётную область включается только одна четверть фольги. Траектории электрического тока определяются посредством решения задачи Лапласа при постоянной электропроводности. Полученное поле нормируется на заданный полный ток и используется для вычисления пространственно-неоднородного источника джоулева тепла. Нестационарное уравнение теплопроводности учитывает температурные зависимости плотности, теплоёмкости, теплопроводности и удельного электрического сопротивления, а также радиационные и испарительные тепловые потери с обеих поверхностей фольги. Уравнение дискретизируется на декартовой сетке с маской расчётной области и интегрируется методом переменных направлений; на каждом полушаге применяется метод простых итераций. *Результаты.* При токе 2,5 A и температуре контактов 78 K максимальная температура в стационарном состоянии составляет 829,803 K. Все исследованные методы решения трёхдиагональных систем дают одно и то же температурное поле после достижения сходимости. Самый быстрый метод разбиения в сочетании с графом задач CUDA выполняет расчёт за 36,3 s, обеспечивая ускорение в 24,1 раза по сравнению с последовательной реализацией на центральном процессоре. *Заключение.* Разработанная модель учитывает неоднородный электрический нагрев и нелинейные тепловые потери в фольге. Реализация на графическом процессоре обладает достаточной производительностью для проведения многократных расчётов при оптимизации геометрии фольги и рабочего тока.

Ключевые слова: нелинейная теплопроводность, джоулев нагрев, метод переменных направлений, метод прогонки, метод разбиения, CUDA